

DISSERTATION

---

**Radiative and Non-Radiative Phenomena During Gate-Switching in  
Silicon Carbide Power MOSFETs**

---

zur Erlangung des akademischen Grades  
**Doktor der technischen Wissenschaften**

EINGEREICHT AN DER  
**Technischen Universität Wien**  
Fakultät für Elektrotechnik und Informationstechnik

VON  
M.Sc. **Maximilian Wolfgang Feil**

UNTER BETREUUNG VON  
Univ.Prof. Dipl.-Ing. Dr.techn. **Tibor Grasser**

Villach, 8. Juli 2024



# Acknowledgements

First and foremost, I would like to express my deepest gratitude to PROFESSOR TIBOR GRASSER for his supervision and guidance throughout the time of this work. Aside from always being outstandingly kind and supportive, he has a tremendous knowledge and invaluable expertise in this research field, which was foundational for the success of this work. Nobody could expect to have a nicer and better supervising professor. I would like to thank him in particular for his trust and belief with respect to my person and abilities.

In the same breath, I want to thank HANS REISINGER, my supervisor at Infineon Technologies AG. I feel infinite gratitude for him. During the time of this work, his boundless enthusiasm for this research field has always been a great inspiration and his advice in personal matters was indispensable. His ability to bring electronics and physics in an industrial environment together is absolutely unique. He designed and built extraordinary measurement equipment that was essential for the success of this work.

Once more in the same breath, I want to express my gratitude to THOMAS AICHINGER from Infineon Technologies Austria AG for his enormous support and trust. His way of turning scientific thinking into entrepreneurial success has been a great source of motivation and inspiration. His personality and competence make him undoubtedly to one of my primary role models.

I would also like to acknowledge the great and outstanding support of my former managers WOLFGANG GUSTIN and BASTIAN HENNE from Infineon Technologies AG. Their visionary attitude, enormous support, and trust in the success of this work made this work actually possible – this cannot be emphasized enough.

Next, I would like to thank an extraordinary professor and friend: PROFESSOR MICHAEL WATTL. I thank him for his trust and belief. Besides his outstanding skills in this scientific field, you just have to love his beautiful smile, his kindness, and his way of looking at life.

Many thanks to my lab mates CHRISTIAN BOGNER and SVEN PRIGANN and to a close colleague CHRISTIAN SCHLÜNDER for the stimulating discussions, inspiring contributions, and fun moments.

Another remarkable person of this time was my predecessor KATJA WASCHNECK, who was an outstanding supporter and friend.

## CHAPTER 0. ACKNOWLEDGEMENTS

---

I also would like to thank GREGOR POBEGEN from KAI Kompetenzzentrum Automobil- und Industrieelektronik GmbH for his outstanding contributions, support, and trust at any point in time of this work.

Furthermore, my sincere thanks go to PROFESSOR MICHEL BOCKSTEDTE from Johannes Kepler University Linz for his kindness, unique contributions, and support.

Over the past years, I had the luck to meet and work with other outstanding PhD candidates. I would like to thank each of them for their kindness and collaboration, in particular MAGDALENA WEGER, DOMINIC WALDHÖR, CHRISTIAN SCHLEICH, ALEXSANDR VASILEV, and ALEXANDER KINSTLER.

Attending conferences becomes a lot more enjoyable, once you travel and attend the conference together with great people. Therefore, I would like to thank ALEXANDER HIRLER, ANDREAS MARTIN, INSAF LAHBIB, GRAZVYDAS ZIEMYS, SABINA SUSNIK, MAXIMILIAN MOSER, VICE SODAN, REIMUND ENGL, PAUL SALMEN, JUDITH BERENS, GERALD RESCHER, and BETTINA FINDENIG.

I would also like to thank my very first and unforgettable session chair DANIEL J. LICHTENWALNER and the organizing committees of the conferences I had the chance to attend during my time as PhD candidate. In particular, I want to thank the committee of the IEEE 2023 International Reliability Physics Symposium for the great recognition in the form of the Best Student Paper Award and the editorial board and editorial team of Communications Engineering for selecting one of our publications as “Editors Choice 2023”.

There have been numerous colleagues at Infineon that I deeply appreciate and thank for their support. Among them are MARKUS SCHWERD, ERWIN HAMMERL, GÜNTHER SCHINDLER, PETER FRIEDRICHS, PHILIPP KOHLER-REDLICH, FLORIAN GRASSE, ANDRÉ KABAKOW, RICHARD NEUMANN, ANDREAS HÜRNER, STEFANO ARESU, RASSO OSTERMEIR, FLORIAN HOLLEY, MARKUS KLEINHANS, INSAF LAHBIB, MANUEL KOLLMUSS, HANNO MELZNER, JOHANNES SCHLIPF, CHRISTIAN WEINDL, ANTOINE CHANUEL, SEBASTIAN DIETL, ANDREAS JAKOWETZ, PUSHPENDRA KUMAR, ROSINA MENDITTO, SEBASTIAN MÜLLER, LORI ALTENMÜLLER, ULRICH BRUNNER, and MAX STELZER.

I also thank my non-technical colleagues REGINA MARIA REITER and RENATE WOLF that always supported in organizing conference trips or procurement of technical equipment.

There have been many more people in my life that I would like to thank, among which are INKA, RAPHAEL, HANNAH, SONJA, MATTHIAS, MARTIN, TIM, BENJAMIN, FLORIAN, and TOBIN.

Finally, I thank my parents THOMAS and INGE who have been my biggest supporters throughout this work. My gratitude goes also to my personal sources of encouragement and motivation: my sister PAOLA, my best friend NIKOLAI, and my girlfriend LARA.

# Abstract

Climate change mitigation is a prominent topic in politics and society today. Green energy generation, its use and improving and developing new technologies is hereby of central importance. This includes energy storage systems, wind turbines, solar power plants, electric vehicles, and associated charging infrastructure. Most – if not all – green technologies require power conversion systems. A central device in these power conversion systems is “a simple switch”. In the past, the premier solution for this switch has been the silicon (Si)-based insulated gate bipolar transistor (IGBT). However, a new class of materials is becoming increasingly important: wide-bandgap semiconductors. In particular the 4H-silicon carbide (SiC) metal-oxide-semiconductor field-effect transistor (MOSFET) is currently the most suited solution for high power and high voltage power conversion applications because of its ability to reduce weight and size of these systems, while improving their energy efficiency. In these applications, a SiC MOSFET is in an operation mode where it is continuously switched at high frequencies up to hundreds of kilohertz between its conductive and non-conductive state. As for any other technology, it is of major importance to guarantee excellent reliability. This includes limiting gradual shifts of device parameters over operation time.

A known mechanism leading to such gradual shifts of device parameters is bias temperature instability (BTI), which is caused by the collective response of point defects close to the semiconductor-insulator interface. These defects act as traps for charge carriers from the semiconductor. Consequently, understanding the trapping and detrapping kinetics of these defects must be of central importance to the research field of reliability physics. The kinetics of BTI in SiC MOSFETs differs considerably from the kinetics in conventional Si-based devices, whereby the most important difference is the higher density of a distribution of defects with very short capture and emission time constants, that is summarized under the term “recoverable component”.

The all-embracing goal of the experiments and investigations conducted in the course of this work was to deepen the understanding of the trapping and detrapping kinetics at the SiC/silicon dioxide (SiO<sub>2</sub>) interface in the context of BTI, but also to reveal and investigate new mechanisms and processes.

First, the focus was placed on single-value apparent activation energies that are commonly used in reliability modeling. As BTI is the result of a large population of defects, only distributions of activation energies must exist and single values can at best be used as a crude approximation. Two different extraction methods for the apparent activation energy were analyzed with respect to their validity and dependence on measurement parameters, such as the extraction point in the drift curve or the recovery time. Analytic approximations for the parameter dependencies were deduced. Besides affecting the extraction of apparent activation energies, the recoverable component in SiC MOSFETs can introduce short-term shifts in the

threshold voltage, which make correct device parameter measurements challenging. Using several commercially available devices of different designs, the effect of the recoverable component in such measurements is evaluated. Also, the advantage of using device conditioning to bring a device faster back to a close-to-equilibrium state is presented.

A central topic of this work is a new type of instability, the so-called gate switching instability (GSI), which arises only upon extensive switching between gate-source voltage levels situated in inversion and accumulation, respectively. However, as this is exactly the operation mode the devices face in power conversion systems, GSI is highly relevant for reliability evaluations. The defining experimental characteristics of GSI are presented and it is shown that the gate switching creates active, acceptor-like interface defects that are responsible for the degradation. Furthermore, these findings are used to disprove a recently proposed mechanism based on increased electron trapping upon a locally-enhanced electric field. In fact, experimental evidence is shown that the underlying physical mechanism responsible for the observed trapping kinetics is based on recombination-enhanced defect reactions (REDRs), which is subsequently used to create a detailed physics-based model that fully agrees with all available experimental results presented so far.

Finally, SiC power MOSFETs are shown to emit light under the exact same operation condition where GSI is encountered. Hereby, the field effect stimulates defect-assisted recombination at the SiC/SiO<sub>2</sub> interface. Within the course of this work, methods to characterize this light emission in fully-processed SiC power MOSFETs are presented. This includes the measurement of only a few hundreds of photons from a single transition of the gate-source voltage, optical spectroscopy, and time-gated optical spectroscopy. Based on a pump-probe scheme, a one-to-one correlation between the light emission and the recovery of the threshold voltage shift after microsecond gate pulses could be revealed. This correlation was equally observed in the voltage level dependence and even upon extended gate stress. Overall, this links the emission of photons also to the recoverable component of BTI in SiC MOSFETs and shows that BTI is not exclusively governed by non-radiative transitions – also radiative transitions can occur. Furthermore, the spectrum of the emitted photons provides valuable information on the involved defects. In particular time-gated optical spectroscopy enabled to reveal the presence of two different spectral components. Based on fitting one of these components with a quantum mechanical model, the component could be assigned to a carbon cluster-like defect with a local vibrational mode (LVM) of 220 meV – this is significantly higher than the highest phonon mode in 4H-SiC or SiO<sub>2</sub>. Other transitions could be assigned to EH<sub>6/7</sub>-assisted, EK<sub>2</sub>-D, and nitrogen-aluminum donor-acceptor-pair recombination. These novel insights do not only broaden the perspective on experimental characterization techniques of interface defects, but will in the future contribute to an improved reliability and performance of these devices.

# Kurzfassung

Die Eindämmung des Klimawandels ist aktuell ein wichtiges Thema in Politik und Gesellschaft. Grüne Energieerzeugung, ihre Nutzung und die Verbesserung und Entwicklung neuer Technologien sind dabei von zentraler Bedeutung. Dazu gehören Energiespeichersysteme, Windturbinen, Solarkraftwerke, Elektrofahrzeuge und die dazugehörige Ladeinfrastruktur. Die meisten – wenn nicht alle – grünen Technologien benötigen Stromumwandlungssysteme. Ein zentrales Bauteil in diesen Stromumwandlungssystemen ist „ein einfacher Schalter“. In der Vergangenheit war hierfür der Silizium (Si)-basierte insulated gate bipolar transistor (IGBT) die beste Lösung. Eine neue Materialklasse gewinnt jedoch rasant an Bedeutung: Halbleiter mit breiter Bandlücke. Insbesondere der 4H-Siliziumkarbid (SiC) Metall-Oxid-Halbleiter-Feldeffekttransistor (MOSFET) ist derzeit die beste Lösung für Anwendungen mit hoher Leistung und Spannung, da er Gewicht und Größe dieser Systeme reduziert und gleichzeitig ihre Energieeffizienz verbessert. In diesen Anwendungen befindet sich ein SiC MOSFET in einem Betriebsmodus, in dem er kontinuierlich bei hohen Frequenzen von bis zu Hunderten von Kilohertz zwischen seinem leitenden und nichtleitenden Zustand umgeschaltet wird. Wie bei jeder anderen Technologie auch, ist es hier von großer Bedeutung, eine hohe Zuverlässigkeit zu gewährleisten. Das beinhaltet auch allmähliche Verschiebungen der Bauteilparameter über die Betriebszeit zu limitieren.

Ein bekannter Mechanismus, der zu solchen Veränderungen der Bauteilparameter führt, ist die *bias temperature instability* (BTI), die durch das kollektive Verhalten von Punktdefekten nahe der Halbleiter-Isolator-Grenzfläche verursacht wird. Diese Defekte wirken als Fallen für Ladungsträger aus dem Halbleiter. Daher ist das Verständnis der Einfang- und Emissionskinetik dieser Defekte von zentraler Bedeutung für das Forschungsgebiet der Zuverlässigkeitsphysik. Die Kinetik von BTI in SiC-MOSFETs unterscheidet sich erheblich von der Kinetik in konventionellen Si-basierten Bauelementen, wobei der wichtigste Unterschied in der ausgeprägteren Verteilung von Defekten mit sehr kurzen Einfang- und Emissionszeitkonstanten besteht, die unter dem Begriff *recoverable component* zusammengefasst sind.

Das Ziel der im Rahmen dieser Arbeit durchgeführten Experimente und Untersuchungen war es, das Verständnis der Einfang- und Emissionskinetik an der SiC/SiO<sub>2</sub>-Grenzfläche im Zusammenhang mit BTI zu vertiefen, aber auch neue Mechanismen und Prozesse aufzudecken und zu untersuchen.

Zunächst wurde der Fokus auf einwertige Aktivierungsenergien gelegt, die üblicherweise in der Zuverlässigkeitsmodellierung verwendet werden. Da BTI das Ergebnis einer großen Population von Defekten ist, kann es nur Verteilungen von Aktivierungsenergien geben und Einzelwerte können bestenfalls als grobe Näherung dienen. Zwei verschiedene Extraktionsmethoden für die einwertige Aktivierungsenergie wurden im Hinblick auf ihre Gültigkeit und ihre Abhängigkeit von Messparametern wie dem Extraktionspunkt in der Driftkurve

oder der Erholungszeit analysiert. Analytische Näherungen für die Parameterabhängigkeiten wurden hergeleitet. Neben der Beeinflussung der Extraktion von einwertigen Aktivierungsenergien kann die *recoverable component* in SiC-MOSFETs zu kurzfristigen Verschiebungen der Schwellenspannung führen, was die korrekte Messung der Bauteilparameter zu einer Herausforderung macht. Anhand mehrerer handelsüblicher Bauelemente unterschiedlicher Bauart werden die Auswirkungen der *recoverable component* bei solchen Messungen untersucht. Außerdem wird der Vorteil der Konditionierung vorgestellt, mit der ein Bauelement schneller nah an das thermische Gleichgewicht gebracht werden kann.

Ein zentrales Thema dieser Arbeit ist eine neue Art von Instabilität, die so genannte *gate switching instability* (GSI), die nur beim häufigen Schalten zwischen Gate-Source Spannungspegeln auftritt, die sich in Inversion bzw. Akkumulation befinden. Da dies der Betriebsmodus ist, mit dem die Bauelemente in Stromumwandlungssystemen konfrontiert sind, ist GSI für die Zuverlässigkeit von großer Bedeutung. Die entscheidenden experimentellen Merkmale von GSI werden vorgestellt und es wird gezeigt, dass das häufige Schalten aktive, akzeptorähnliche Grenzflächendefekte erzeugt, die für die Degradation verantwortlich sind. Darüber hinaus werden diese Ergebnisse genutzt, um einen kürzlich vorgeschlagenen Mechanismus zu widerlegen, der auf verstärktem Elektroneneinfang durch lokal verstärktes elektrisches Feld beruht. Tatsächlich wird experimentell nachgewiesen, dass der zugrundeliegende physikalische Mechanismus, der für die beobachtete Degradation verantwortlich ist, auf *recombination-enhanced defect reactions* (REDRs) basiert, was anschließend zur Erstellung eines physikalischen Modells verwendet wird, das mit allen vorliegenden experimentellen Ergebnissen übereinstimmt.

Schließlich wird gezeigt, dass SiC-Leistungs-MOSFETs unter denselben Betriebsbedingungen, bei denen GSI auftritt, Licht emittieren. Dabei verursacht der Feldeffekt Defekt-unterstützte Rekombination an der SiC/SiO<sub>2</sub>-Grenzfläche. Im Rahmen dieser Arbeit werden Methoden zur Charakterisierung dieser Lichtemission in vollständig prozessierten SiC-Leistungs-MOSFETs vorgestellt. Dazu gehört die Messung von nur einigen hundert Photonen aus einem einzigen Übergang der Gate-Source-Spannung, die optische Spektroskopie und die zeitabhängige optische Spektroskopie. Basierend auf einem Pump-Probe-Schema konnte eine Eins-zu-Eins-Korrelation zwischen der Lichtemission und der Erholung der Schwellenspannungsverschiebung nach Mikrosekunden-Gate-Pulsen nachgewiesen werden. Diese Korrelation wurde auch bei der Abhängigkeit vom Spannungsniveau und sogar bei längerem Gate-Stress beobachtet. Insgesamt ergibt sich damit ein Zusammenhang zwischen der Emission von Photonen und der *recoverable component* der BTI in SiC-MOSFETs und es zeigt sich, dass die BTI nicht ausschließlich aus nicht-strahlenden Übergängen besteht - auch strahlende Übergänge können auftreten. Außerdem liefert das Spektrum der emittierten Photonen wertvolle Informationen über die beteiligten Defekte. Insbesondere die zeitabhängige optische Spektroskopie ermöglichte es, das Vorhandensein von zwei verschiedenen Spektralkomponenten aufzudecken. Basierend auf dem Fitten einer dieser Komponenten mit einem quantenmechanischen Modell konnte die Komponente einem kohlenstoffclusterähnlichen Defekt mit einer lokalen Schwingungsmode von 220 meV zugeordnet werden - das ist höher als jede Phononenmode in 4H-SiC oder SiO<sub>2</sub>. Andere Übergänge konnten der EH<sub>6/7</sub>-unterstützten, EK<sub>2</sub>-D- und Stickstoff-Aluminium-Donor-Akzeptor-Paar-Rekombination zugeordnet werden. Diese neuen Erkenntnisse erweitern nicht nur den Blickwinkel auf Charakterisierungsmethoden von Grenzflächendefekten, sondern werden in Zukunft auch zu einer verbesserten Zuverlässigkeit und Leistung dieser Bauelemente beitragen.



# Contents

|  |             |
|--|-------------|
| <b>Acknowledgements</b>  | <b>iii</b>  |
| <b>Abstract</b>  | <b>v</b>    |
| <b>Kurzfassung</b>   | <b>vii</b>  |
| <b>Contents</b>  | <b>ix</b>   |
| <b>List of Figures</b>   | <b>xiii</b> |
| <b>List of Tables</b>  | <b>xvii</b> |
| <b>List of Abbreviations</b>   | <b>xix</b>  |
| <b>1 Introduction</b>  | <b>1</b>    |
| 1.1 Motivation for Silicon Carbide Technology . . . . .                      | 1           |
| 1.2 The History of Silicon Carbide and its Devices . . . . .                 | 3           |
| 1.3 Silicon Carbide: From the Crystal to the Wafer . . . . .                 | 5           |
| 1.3.1 Crystal Structure . . . . .  | 6           |
| 1.3.2 Crystal growth . . . . .   | 8           |
| 1.3.3 Band Structure . . . . .   | 9           |
| 1.3.4 Lattice Vibrations . . . . .   | 9           |
| 1.3.5 Localized Vibrations . . . . .   | 10          |
| 1.4 Applications of Silicon Carbide Devices . . . . .                        | 12          |
| 1.5 The Designs of Modern Silicon Carbide Field-Effect Transistors . . . . . | 13          |
| 1.5.1 The Planar Designs . . . . .   | 14          |
| 1.5.2 The Trench Designs . . . . .   | 15          |
| 1.6 Reliability of Silicon Carbide Field-Effect Transistors . . . . .        | 16          |
| 1.6.1 Gate Oxide Reliability . . . . .                                       | 16          |
| 1.6.2 Bipolar Degradation of the Body Diode . . . . .                        | 16          |
| 1.6.3 Bias Temperature Instability . . . . .                                 | 17          |
| 1.7 Motivation for This Work . . . . .                                       | 18          |

|          |  |           |
|----------|--|-----------|
| <b>2</b> | <b>The Physics of Charge Trapping in Defects and Defect-Assisted Recombination</b> | <b>21</b> |
| 2.1      | Non-Radiative Transitions . . . . .  | 21        |
| 2.1.1    | Shockley-Read-Hall Theory . . . . .  | 21        |
| 2.1.2    | Non-Radiative Multiphonon Theory . . . . .   | 23        |
| 2.1.3    | Recombination Enhanced Defect Reactions . . . . .                                  | 26        |
| 2.2      | Radiative Transitions . . . . .  | 28        |
| 2.3      | Competition Between Radiative and Non-Radiative Transitions . . . . .              | 31        |
| <b>3</b> | <b>Optical and Electrical Measurement Methodology</b>                              | <b>33</b> |
| 3.1      | Transfer Characteristic . . . . .  | 33        |
| 3.2      | Impedance Characterization . . . . .   | 35        |
| 3.3      | Ultra-fast Threshold Voltage Measurement . . . . .                                 | 37        |
| 3.4      | Charge Pumping . . . . .   | 39        |
| 3.5      | Measurement of Photon Emission of Single-Gate Voltage Transients . . . . .         | 41        |
| 3.6      | Optical Spectroscopy . . . . .   | 44        |
| 3.7      | Time-Gated Optical Spectroscopy . . . . .  | 45        |
| 3.7.1    | Wavelength and Intensity Calibration . . . . .                                     | 46        |
| 3.8      | Photon Emission Microscopy . . . . .   | 48        |
| <b>4</b> | <b>Measurements and Results</b>  | <b>51</b> |
| 4.1      | Single-Value Apparent Activation Energies in Silicon and Silicon Carbide MOSFETs   | 52        |
| 4.1.1    | The Analytic Activation Energy Map . . . . .                                       | 53        |
| 4.1.2    | Basic Principle of Vertical Extraction . . . . .                                   | 55        |
| 4.1.3    | Basic Principle of Horizontal Extraction . . . . .                                 | 56        |
| 4.1.4    | Analytic Formulations of Apparent Activation Energies . . . . .                    | 57        |
| 4.1.5    | Relation Between Horizontally and Vertically Extracted Energies . . . . .          | 58        |
| 4.1.6    | Examples for the Dependencies of Apparent Activation Energies . . . . .            | 59        |
| 4.2      | The Recoverable Component in SiC MOSFETs and its Impact on Measurements .          | 64        |
| 4.2.1    | Threshold Voltage Shift after Short Gate Pulses . . . . .                          | 66        |
| 4.2.2    | Impact of the Recoverable Component on the Pulsed Transfer Characteristics         | 69        |
| 4.2.3    | Conditioning of Threshold Voltage Measurements . . . . .                           | 71        |
| 4.3      | Gate Switching Instability . . . . .   | 75        |
| 4.3.1    | A Brief Historic Review of Gate Switching Instability . . . . .                    | 75        |
| 4.3.2    | Measuring Gate Switching Instability . . . . .                                     | 76        |
| 4.3.3    | Switching Frequency . . . . .  | 78        |
| 4.3.4    | Origin of Gate Switching Instability: Acceptor-Like Interface Defects . . .        | 84        |
| 4.3.5    | Voltage Levels . . . . .   | 86        |
| 4.3.6    | Junction Temperature . . . . .   | 88        |
| 4.3.7    | Transition Times . . . . .   | 89        |
| 4.3.8    | Similarity to Charge Pumping . . . . .   | 90        |
| 4.3.9    | Overshoots and Undershoots . . . . .   | 92        |
| 4.3.10   | Impact on the Hysteresis . . . . .   | 93        |
| 4.3.11   | Recovery and Annealing . . . . .   | 95        |
| 4.3.12   | The Physics of Gate Switching Instability . . . . .                                | 95        |
| 4.3.13   | Gate Switching Instability in Silicon MOSFETs? . . . . .                           | 102       |
| 4.3.14   | Mathematical Model based on Recombination-Enhanced Defect Reactions                | 104       |

|          |  |            |
|----------|--|------------|
| 4.4      | Field-Effect Stimulated Optical Spectroscopy of Interface Defects . . . . .                          | 110        |
| 4.4.1    | Light Emission from the Active Area of a Silicon Carbide Power MOSFET                                | 111        |
| 4.4.2    | Light Emission from Single Gate Voltage Transitions . . . . .  | 114        |
| 4.4.3    | Voltage Level Dependence . . . . .   | 117        |
| 4.4.4    | Field-Effect-Based Pump-Probe Scheme . . . . .   | 121        |
| 4.4.5    | Impact of Extended Gate Stress onto the Photon Emission . . . . .                                    | 127        |
| 4.4.6    | Optical Spectroscopy . . . . .   | 128        |
| 4.4.7    | Time-Gated Optical Spectroscopy . . . . .  | 132        |
| 4.4.8    | Relation Between Gate Switching Instability and Field-Effect Stimulated<br>Photon Emission . . . . . | 150        |
| <b>5</b> | <b>Summary and Outlook</b>   | <b>153</b> |
| 5.1      | Summary . . . . .  | 153        |
| 5.2      | Outlook . . . . .  | 155        |
|          | <b>References</b>  | <b>157</b> |
|          | <b>List of Publications</b>  | <b>187</b> |
|          | <b>Curriculum Vitae</b>  | <b>191</b> |

Die approbierte gedruckte Originalversion dieser Dissertation ist an der TU Wien Bibliothek verfügbar.  
The approved original version of this doctoral thesis is available in print at TU Wien Bibliothek.



Die approbierte gedruckte Originalversion dieser Dissertation ist an der TU Wien Bibliothek verfügbar.  
The approved original version of this doctoral thesis is available in print at TU Wien Bibliothek.



# List of Figures

|      |  |    |
|------|--|----|
| 1.1  | Comparison between Si and SiC devices with respect to specific on-state resistance and efficiency . . . . .  | 3  |
| 1.2  | The first SiC-based devices . . . . .  | 4  |
| 1.3  | Evolution of specific on-state resistance and cell pitch over time . . . . .   | 5  |
| 1.4  | The crystal structure of 4H-SiC . . . . .  | 6  |
| 1.5  | The primitive unit cells of different SiC polytypes . . . . .  | 7  |
| 1.6  | Band structure of 4H-SiC and its phonon dispersion . . . . .   | 9  |
| 1.7  | Phonon dispersion of mono and diatomic chains and a local vibrational mode . .   | 11 |
| 1.8  | A basic full-bridge converter . . . . .  | 13 |
| 1.9  | Band alignment of the 4H-SiC/SiO <sub>2</sub> interface and doping ionization energies in 4H-SiC . . . . .   | 14 |
| 1.10 | The planar designs of SiC MOSFETs . . . . .  | 14 |
| 1.11 | The trench designs of SiC MOSFETs . . . . .  | 15 |
| 2.1  | Shockley-Read-Hall trapping processes . . . . .  | 22 |
| 2.2  | Adiabatic and diabatic potentials and non-radiative multiphonon trapping and detrapping processes . . . . .  | 24 |
| 2.3  | Configuration coordinate diagram of a recombination-enhanced defect reaction and the relation between its activation energy and the phonon kick energy . . . . | 27 |
| 2.4  | Potentials, eigenstates, and eigenvalues for radiative transitions between two electronic states and the corresponding emission spectrum . . . . .             | 29 |
| 2.5  | Thermal quenching: competition between radiative and non-radiative transitions   | 32 |
| 3.1  | Transfer curve of a SiC DMOSFET . . . . .  | 34 |
| 3.2  | Parallel equivalent circuit in impedance characterization . . . . .  | 35 |
| 3.3  | Calibration of an impedance measurement . . . . .  | 36 |
| 3.4  | Capacitance-voltage and conductance-voltage curves of a SiC DMOSFET . . . . .  | 37 |
| 3.5  | Simplified circuit diagram of the ultra-fast $V_{th}$ measurement setup . . . . .  | 38 |
| 3.6  | Illustration of the charge pumping technique . . . . .   | 40 |
| 3.7  | Illustration of constant high level and constant low level techniques in charge pumping experiments . . . . .  | 41 |
| 3.8  | Characteristics of a silicon photomultiplier . . . . .   | 42 |
| 3.9  | Schematic and picture of a measurement setup based on a silicon-photomultiplier  | 43 |

## LIST OF FIGURES

---

|      |   |    |
|------|---|----|
| 3.10 | Schematic of a measurement setup for optical spectroscopy based on a compact CCD spectrometer . . . . .   | 44 |
| 3.11 | Illustration of a measurement setup for time-gated optical spectroscopy, its timing, and working principle . . . . .  | 46 |
| 3.12 | Calibration of the measurement setup for time-gated optical spectroscopy . . . . .  | 48 |
| 4.1  | Stress and recovery time dependence of the threshold voltage drift in a Si technology   | 53 |
| 4.2  | Activation energy map and capture emission time map of a Si technology . . . . .  | 54 |
| 4.3  | Schematic representation of apparent activation energy extraction methods . . . . .   | 56 |
| 4.4  | Analytic approximations for apparent activation energies . . . . .  | 58 |
| 4.5  | Activation energy map and capture emission time map of a SiC technology . . . . .   | 59 |
| 4.6  | Vertical extraction method and its dependence on the stress time . . . . .  | 60 |
| 4.7  | Horizontal extraction method and its dependence on the threshold voltage drift . . . . .  | 60 |
| 4.8  | Recovery time and stress voltage dependence of the horizontal extraction method . . . . .   | 61 |
| 4.9  | Stress and recovery time dependence of the threshold voltage drift in a SiC technology . . . . .  | 62 |
| 4.10 | Threshold voltage drift and recovery time dependence of the horizontal extraction method in a SiC technology . . . . .  | 63 |
| 4.11 | Threshold voltage shift during a continuous threshold voltage measurement . . . . .   | 65 |
| 4.12 | Temporal evolution of the drain-source current during a gate pulse in SiC and Si technologies . . . . .   | 65 |
| 4.13 | Measurement schemes for recovery after short gate pulses and for the gate-pulsed transfer characteristic . . . . .  | 66 |
| 4.14 | Recovery traces after short gate pulses . . . . .   | 67 |
| 4.15 | The pulse length dependence of the recoverable threshold voltage shift . . . . .  | 67 |
| 4.16 | The pulse voltage dependence of the recoverable threshold voltage shift . . . . .   | 68 |
| 4.17 | Time to full recovery versus the pulse voltage . . . . .  | 68 |
| 4.18 | Impact of different pulse lengths on the parameter curves . . . . .   | 69 |
| 4.19 | Impact of different pulse voltages on the parameter curves . . . . .  | 71 |
| 4.20 | Low level dependence of the drain-source current shift . . . . .  | 72 |
| 4.21 | Transfer curves with different starting voltages under high drain-source voltage . . . . .  | 73 |
| 4.22 | Recovery curves after device conditioning . . . . .   | 74 |
| 4.23 | Time to full recovery using device conditioning . . . . .   | 74 |
| 4.24 | Measure-stress-measure scheme and recovery curves of a gate switching instability experiment . . . . .  | 77 |
| 4.25 | Stress and measurement modes of a gate switching instability experiment . . . . .   | 77 |
| 4.26 | Frequency dependence of the threshold voltage drift upon gate switching stress . . . . .  | 78 |
| 4.27 | Frequency dependence of the threshold voltage drift upon gate switching stress in a double logarithmic plot . . . . .   | 79 |
| 4.28 | Frequency dependence of the threshold voltage drift upon gate switching stress – extraction of bias temperature instability and gate switching instability components . . . . . | 80 |
| 4.29 | Frequency dependence of the gate switching instability component . . . . .  | 80 |
| 4.30 | Capacitance-voltage and conductance-voltage curves before and after gate switching stress . . . . .   | 82 |
| 4.31 | Gate switching stress induced change of capacitance and conductance curves . . . . .  | 83 |

|      |  |     |
|------|--|-----|
| 4.32 | Gate switching stress induced change in the hysteresis of capacitance and conductance curves . . . . .   | 83  |
| 4.33 | Interface state capacitance and its change upon gate switching stress . . . . .  | 84  |
| 4.34 | Creation of acceptor-like interface states upon gate switching stress . . . . .  | 85  |
| 4.35 | Voltage level dependence of gate switching instability . . . . .   | 86  |
| 4.36 | Temperature dependence of gate switching instability . . . . .   | 87  |
| 4.37 | Horizontal activation energy of the threshold voltage drift upon gate switching stress . . . . .   | 88  |
| 4.38 | Transition time dependence of gate switching instability: I . . . . .  | 89  |
| 4.39 | Transition time dependence of gate switching instability: II . . . . .   | 90  |
| 4.40 | Transition time dependence of the charge pumping current and the GSI-related drift   | 91  |
| 4.41 | Impact of undershoots on the gate switching instability . . . . .  | 93  |
| 4.42 | Impact of gate switching stress on the hysteresis of the recoverable threshold voltage shift . . . . .   | 94  |
| 4.43 | Illustration of locally-enhanced electric field as the cause of gate switching instability   | 96  |
| 4.44 | Schematic illustration of recombination-enhanced defect reactions as the cause of gate switching instability . . . . .                                 | 99  |
| 4.45 | Comparison of low-level dependence between charge pumping current, recoverable threshold voltage shift, and drift upon gate switching stress . . . . . | 102 |
| 4.46 | Comparison between two state model and three state model as the cause of gate switching instability . . . . .  | 104 |
| 4.47 | Configuration coordinate diagram and state diagram of the mathematical model for gate switching instability . . . . .                                  | 105 |
| 4.48 | Parameter dependencies of mathematical model for gate switching instability . .  | 108 |
| 4.49 | Comparison between the mathematical model for gate switching instability and experimental data . . . . .   | 109 |
| 4.50 | Comparison between topside and backside detection of light emission from SiC MOSFETs . . . . .   | 112 |
| 4.51 | Pictures of light emission from the active area of a SiC MOSFET upon continuous gate switching . . . . .   | 112 |
| 4.52 | Emission microscopy of a 4H-SiC power MOSFET under continuous gate switching   | 113 |
| 4.53 | Light emission during continuous gate switching detected with a silicon photomultiplier . . . . .  | 115 |
| 4.54 | Deconvolution of the photo current measured with a silicon photomultiplier . .   | 116 |
| 4.55 | Double pulses for the measurement of the voltage level dependence of the light emission with a silicon photomultiplier . . . . .                       | 118 |
| 4.56 | Voltage level dependence of the light emission measured using a silicon photomultiplier . . . . .  | 119 |
| 4.57 | Illustration of the different contributions to the threshold voltage shift depending on the type of measurement . . . . .                              | 122 |
| 4.58 | Transitions and potential energy surfaces of processes involved in the pump-probe measurement scheme of the light emission . . . . .                   | 123 |
| 4.59 | Pump-probe measurement scheme using short gate-source voltage pulses . . . .   | 123 |
| 4.60 | Photo current peaks measured using a pump-probe scheme with different recovery times . . . . .   | 124 |

## LIST OF FIGURES

---

|      |  |     |
|------|--|-----|
| 4.61 | Number of emitted photons measured with a pump-probe scheme versus the recovery time . . . . .   | 125 |
| 4.62 | Recovery of the threshold voltage shift following different pump pulses . . . . .  | 126 |
| 4.63 | Correlation between number of emitted photons and the threshold voltage shift in a pump-probe experiment . . . . .   | 126 |
| 4.64 | Photo charge shift and threshold voltage shift upon extended gate stress . . . . .   | 127 |
| 4.65 | Correlation between photo charge shift and the threshold voltage shift upon extended gate stress . . . . .   | 128 |
| 4.66 | Emission spectrum of a SiC DMOSFET upon continuous gate switching and its transformation into energy space . . . . .   | 129 |
| 4.67 | Fit of the emission spectrum of a SiC DMOSET with Gaussian lineshape functions and comparison to results from density-functional theory . . . . .  | 130 |
| 4.68 | Schematic illustration of recombination processes occurring at the rising and falling transitions of the gate-source voltage . . . . .   | 131 |
| 4.69 | Comparison of capacitance-voltage curves of differently prepared SiC DMOSFETs  | 133 |
| 4.70 | Timing and emission spectra in a time-gated optical spectroscopy experiment to distinguish between light emission at the rising and falling transitions . . . . .  | 134 |
| 4.71 | Schematic illustration of recombination processes and light emission spectra related to a forward current through the body diode . . . . .   | 135 |
| 4.72 | Emission spectra of the rising and falling transitions and the forward biased body diode . . . . .   | 136 |
| 4.73 | Model and corresponding fit of the red component . . . . .   | 137 |
| 4.74 | Schematic illustration of the processes involved in the mechanisms creating the red and blue components . . . . .  | 139 |
| 4.75 | Emission spectra obtained by the constant low level technique . . . . .  | 140 |
| 4.76 | Emission spectra obtained by the constant high level technique . . . . .   | 141 |
| 4.77 | Constant low and constant high level curves of the red and blue components . .   | 142 |
| 4.78 | Impact of switching frequency and duty cycle on the emission spectra at the rising and falling transitions . . . . .   | 144 |
| 4.79 | Transition time dependence of the red and blue components . . . . .  | 145 |
| 4.80 | Temporal evolution of the emission spectrum over an entire gate-source voltage period: I . . . . .   | 147 |
| 4.81 | Temporal evolution of the emission spectrum over an entire gate-source voltage period: II . . . . .  | 148 |
| 4.82 | Schematic illustration of combined model for gate switching instability and field-effect stimulated light emission and change of field-effect stimulated light emission upon continuous gate switching . . . . . | 151 |



# List of Tables

|     |   |     |
|-----|---|-----|
| 1.1 | Material parameters and figure-of-merits of different semiconductor materials . . .   | 2   |
| 1.2 | Lattice constants, bandgaps, and electron mobilities of selected SiC polytypes . . .  | 8   |
| 1.3 | Energies of various local vibrational modes of asymmetric carbon split-interstitials<br>in 4H-SiC . . . . .                                   | 11  |
| 1.4 | Energies of various local vibrational modes of carbon clusters in 4H-SiC . . . . .  | 12  |
| 3.1 | Comparison between different experimental setups for the analysis of light emitted<br>from SiC MOSFETs. . . . .                               | 47  |
| 4.1 | Parameters of two bivariate Gaussian distributions from a silicon technology . . .  | 54  |
| 4.2 | Datasheet values and the Baliga high-frequency figure of merit of tested devices  | 64  |
| 4.3 | List of experimental findings related to gate switching instability . . . . .   | 95  |
| 4.4 | Parameters of two bivariate Gaussian distributions from a silicon technology . . .  | 120 |
| 4.5 | Parameters of a fit of the emission spectrum of a SiC DMOSFET with Gaussian<br>lineshape functions . . . . .                                  | 130 |
| 4.6 | Model parameters obtained by fitting the red component . . . . .  | 138 |
| 4.7 | Biexponential parameters of the red and blue components . . . . .   | 149 |
| 4.8 | Comparison of defect parameters experimentally obtained by the red component<br>and theoretically calculated values from literature . . . . . | 149 |



# List of Abbreviations

|                        |                                       |
|------------------------|---------------------------------------|
| $C_{iss}$              | input capacitance                     |
| $\Delta V_{th}$        | threshold voltage shift               |
| $E_G$                  | bandgap                               |
| $f_{sw}$               | switching frequency                   |
| $g_m$                  | transconductance                      |
| $I_{CP}$               | charge-pumping current                |
| $I_{DS}$               | drain-source current                  |
| $R_{on}$               | on-state resistance                   |
| $t_r$                  | recovery time                         |
| $t_s$                  | stress time                           |
| $V_{DS}$               | drain-source voltage                  |
| $V_{fb}$               | flatband voltage                      |
| $V_{GS}$               | gate-source voltage                   |
| $V_H$                  | high level                            |
| $V_L$                  | low level                             |
| $V_{th}$               | threshold voltage                     |
| <b>SiC</b>             | silicon carbide                       |
| <b>SiO<sub>2</sub></b> | silicon dioxide                       |
| <b>Si</b>              | silicon                               |
| <b>AC</b>              | alternating current                   |
| <b>AE</b>              | activation energy                     |
| <b>BHFFOM</b>          | Baliga high-frequency figure of merit |
| <b>BTI</b>             | bias temperature instability          |
| <b>CCD</b>             | charge-coupled device                 |
| <b>CET</b>             | capture-emission-time                 |
| <b>Comphy</b>          | compact-physics framework             |
| <b>CP</b>              | charge pumping                        |
| <b>CTL</b>             | charge transition level               |
| <b>CV</b>              | capacitance-voltage                   |
| <b>CVD</b>             | chemical vapor deposition             |
| <b>DAP</b>             | donor-acceptor-pair                   |
| <b>DC</b>              | direct current                        |
| <b>DFT</b>             | density functional theory             |
| <b>DLTS</b>            | deep-level transient spectroscopy     |
| <b>DMOS</b>            | double-diffused MOS                   |
| <b>DMOSET</b>          | double-diffused MOSFET                |

|                  |   |
|------------------|---|
| <b>DUT</b>       | device under test                                 |
| <b>EL</b>        | electroluminescence                               |
| <b>FinFET</b>    | fin field-effect transistor                       |
| <b>FOM</b>       | figure of merit                                   |
| <b>FWHM</b>      | full width at half maximum                        |
| <b>GaN</b>       | gallium nitride                                   |
| <b>GSI</b>       | gate switching instability                        |
| <b>GSS</b>       | gate switching stress                             |
| <b>GV</b>        | conductance-voltage                               |
| <b>HR-factor</b> | Huang-Rhys factor                                 |
| <b>ICCD</b>      | intensified charge-coupled device                 |
| <b>IGBT</b>      | insulated gate bipolar transistor                 |
| <b>IPCC</b>      | Intergovernmental Panel on Climate Change         |
| <b>JEDEC</b>     | Joint Electron Device Engineering Council         |
| <b>JFET</b>      | junction field-effect transistor                  |
| <b>JFOM</b>      | Johnson's figure of merit                         |
| <b>KFOM</b>      | Keyes figure of merit                             |
| <b>LED</b>       | light-emitting diode                              |
| <b>LVM</b>       | local vibrational mode                            |
| <b>MCP</b>       | microchannel plate                                |
| <b>MOSCAP</b>    | metal-insulator-semiconductor capacitor           |
| <b>MOSFET</b>    | metal-oxide-semiconductor field-effect transistor |
| <b>MSM</b>       | measure-stress-measure                            |
| <b>NBTI</b>      | negative bias temperature instability             |
| <b>NMP</b>       | non-radiative multiphonon                         |
| <b>NO</b>        | nitric oxide                                      |
| <b>PBTI</b>      | positive bias temperature instability             |
| <b>PCB</b>       | printed circuit board                             |
| <b>PDE</b>       | photodetection efficiency                         |
| <b>PEC</b>       | potential energy curve                            |
| <b>PES</b>       | potential energy surface                          |
| <b>PID</b>       | proportional–integral–derivative                  |
| <b>PWM</b>       | pulse-width modulation                            |
| <b>RAM</b>       | random-access memory                              |
| <b>REDG</b>      | recombination-enhanced defect glide               |
| <b>REDR</b>      | recombination-enhanced defect reaction            |
| <b>RTN</b>       | random-telegraph noise                            |
| <b>SBD</b>       | Schottky-barrier diode                            |
| <b>SiPM</b>      | silicon-photomultiplier                           |
| <b>SPAD</b>      | single-photon avalanche diode                     |
| <b>SRH</b>       | Shockley-Read-Hall                                |
| <b>TAT</b>       | trap-assisted tunneling                           |
| <b>TDDDB</b>     | time-dependent dielectric breakdown               |
| <b>TO</b>        | transistor outline                                |
| <b>UMOSFET</b>   | trench MOSFET                                     |

---

**USB**  
**WKB**  
**ZPL**

universal serial bus  
Wentzel-Kramers-Brillouin  
zero-phonon line

Die approbierte gedruckte Originalversion dieser Dissertation ist an der TU Wien Bibliothek verfügbar.  
The approved original version of this doctoral thesis is available in print at TU Wien Bibliothek.



# Introduction

In the year 2021, Syukuro Manabe, Klaus Hasselmann, and Giorgio Parisi were jointly awarded the Nobel Prize in physics, predominantly for their contributions to the understanding and forecasting of climate change [1]. In the same year, the Intergovernmental Panel on Climate Change (IPCC) released a report that clearly demonstrated the necessity of global warming mitigation via a reduction of global carbon-dioxide emission to a net-zero level [2]. In consequence, technologies that support the efforts to achieve this goal are highly needed. This comprises electric vehicles [3], solar power plants [4], wind turbines [5], hydro power generation [6], systems for energy storage [7] and numerous others. A recurring challenge is hereby the conversion of input power  $P_{in}$  into an output power  $P_{out}$ , whereby the conversion is either from alternating current (AC) to direct current (DC) (power supply), DC to AC (inverter), DC to DC (converter), or AC to AC (frequency changer). All of these power conversions have an inherent power conversion efficiency

$$\eta = \frac{P_{out}}{P_{in}}, \quad (1.1)$$

that should be as close as possible to 100 % to minimize the total losses of the application. Apparently, an increase in energy efficiency could directly convert into a reduction of associated carbon-dioxide emission.

In this chapter, the potential of silicon carbide (SiC) metal-oxide-semiconductor field-effect transistors (MOSFETs) for increased efficiency of power conversion applications is introduced, followed by a brief summary of the history of this technology. Next, the physical properties of SiC are outlined, including its crystal structure, growth, band structure, lattice vibrations, and potential for localized vibrations. Furthermore, the applications and prevalent designs of modern SiC MOSFETs are presented. Finally, particular reliability issues of these devices are summarized and the motivation and context of this work is outlined.

## 1.1 Motivation for Silicon Carbide Technology

There are various circuit topologies for power conversion in electronics, however, they all require some sort of switch [8]. Semiconductor switches can be based on different materials, whereby the potential of corresponding devices can be estimated by using so-called figure of merits (FOMs). Two well-known FOMs are the Keyes figure of merit (KFOM) [9] and the

| Material | $E_G$ [eV] | $\epsilon_r$ | $E_{\text{crit}}$ [MV cm <sup>-1</sup> ] | $v_s$ [cm $\mu\text{s}^{-1}$ ] | $\lambda_{\text{th}}$ [W cm <sup>-1</sup> K <sup>-1</sup> ] | JFOM | KFOM  |
|----------|------------|--------------|--|--------------------------------|---|------|-------|
| Si       | 1.12       | 11.7         | 0.3                                      | 23                             | 1.48  | 1    | 1     |
| GaAs     | 1.42       | 13.1         | 0.4                                      | 44                             | 0.52  | 2.55 | 0.486 |
| GaP      | 2.26       | 11.1         | 1  | 20                             | 1.1   | 2.9  | 0.693 |
| GaN      | 3.49       | 9            | 3  | 15                             | 1.3   | 6.52 | 0.709 |
| 6H-SiC   | 3.0        | 9.66         | 2.4                                      | 19                             | 7   | 6.61 | 4.3   |
| 4H-SiC   | 3.26       | 9.7          | 3.18                                     | 22                             | 7   | 10.1 | 4.63  |
| diamond  | 5.0        | 5.7          | 5.17                                     | 27                             | 20  | 22.3 | 14.6  |

**Table 1.1.** The bandgap  $E_G$ , other material parameters entering Equations 1.2 and 1.3, and the figure of merits (FOMs) of different semiconductor materials. Both Johnson’s figure of merit (JFOM) and Keyes figure of merit (KFOM) are given for room temperature and normalized to their respective value for Si. Redrawn from [12].

Johnson’s figure of merit (JFOM) [10], relating to the thermal limit and the high-frequency limit, respectively. These FOMs are given by the equations

$$\text{KFOM} = \lambda_{\text{th}} \sqrt{\frac{c v_s}{4\pi\epsilon_r}} \quad \text{and} \quad (1.2)$$

$$\text{JFOM} = \frac{E_{\text{crit}} v_s}{2\pi}. \quad (1.3)$$

Hereby, the parameter  $\lambda_{\text{th}}$  is the thermal conductivity,  $c$  is the speed of light,  $v_s$  is the minority-carrier saturated drift-velocity,  $\epsilon_r$  is the relative dielectric constant, and  $E_{\text{crit}}$  is the critical electric field strength. Table 1.1 summarizes material parameters and FOMs of various semiconductors. A traditional choice for a power switch is the insulated gate bipolar transistor (IGBT), that is based on silicon (Si) [11]. However, the values of the two FOMs in Table 1.1 reveal that 4H-SiC could potentially outperform silicon based devices by far – only diamond performs better. Due to its wide bandgap, the critical electric field strength is roughly ten times higher than the one of Si, which subsequently increases the JFOM. Additionally, a higher thermal conductance and a smaller dielectric constant lead to an approximately five times higher KFOM of 4H-SiC compared to Si.

As the above mentioned power conversion circuits require continuous switching of the semiconductor switch, the total power loss  $P_{\text{loss}}$  is constituted by the conduction loss and by the switching loss via

$$P_{\text{loss}} = \underbrace{I^2 R_{\text{on}}}_{\text{conduction loss}} + \underbrace{C_{\text{iss}} V_{\text{GS}}^2 f_{\text{sw}}}_{\text{switching loss}}, \quad (1.4)$$

which assumes that the switching loss is solely caused by charging and discharging of the input capacitance ( $C_{\text{iss}}$ ) [13]. Hereby,  $I$  is the average conducted current,  $R_{\text{on}}$  is the on-state resistance,  $V_{\text{GS}}$  is the gate-source voltage and  $f_{\text{sw}}$  is the switching frequency. Based on Equation 1.4, Baliga proposed another FOM [13], which was termed Baliga high-frequency figure of merit (BHFFOM) and follows

$$\text{BHFFOM} = \frac{1}{R_{\text{on,sp}} C_{\text{iss,sp}}}. \quad (1.5)$$

In the above equation, the two parameters are the specific values of the on-state resistance  $R_{\text{on,sp}} = R_{\text{on}}/A$  and of the input capacitance  $C_{\text{iss,sp}} = C_{\text{iss}}/A$ , whereby  $A$  is the device area. In



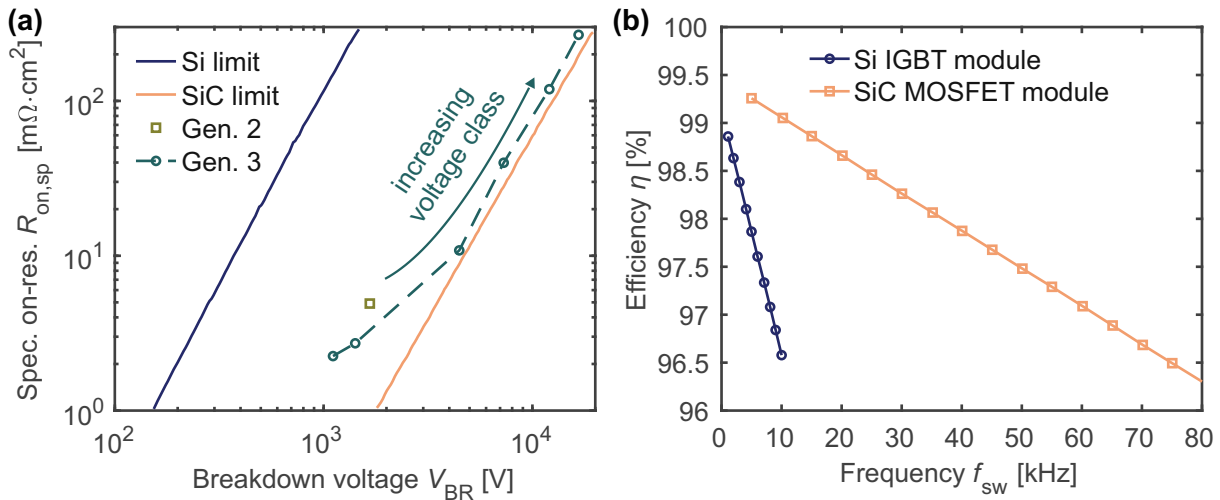


**Figure 1.1.** (a) The specific on-state resistance versus the breakdown voltage at  $V_{GS} = 20$  V and a temperature of  $25^\circ\text{C}$ . All samples are from the second or third generation of the planar power technology from Cree Inc. Redrawn from [15]. (b) Efficiency of a Si IGBT module and a SiC MOSFET module. Within the shown frequency range, the SiC module shows a higher efficiency, particularly at higher frequencies. Redrawn from [16].

this context, Baliga already recognized in 1989 that SiC offers great potential for the creation of energy-efficient high-power switching applications [13]. SiC technology can achieve an approximately 100-times lower specific on-state resistance compared to Si, which is illustrated in Fig. 1.1a. Consequently, 4H-SiC can achieve higher BHFFOM values than Si, which was for example quantified by Li *et al.* with an increase by a factor of 556 [14].

Experimentally, this superior performance of SiC devices becomes ultimately evident by comparing the performance of SiC MOSFET-based with Si IGBT-based power modules [16]. As shown in Fig. 1.1b, the efficiency of the SiC module is well above the efficiency of the IGBT module. Most importantly, the difference in efficiency increases with increasing frequency.

Consequently, SiC has the potential to reduce the energy consumption of power electronic converters compared to conventional Si-based technology, particularly at higher frequencies. Many technologies that are used for climate change mitigation, some of them pointed out at the beginning of this chapter, are related to electric power-conversion and high-frequency switching. Hence, SiC devices could indeed contribute significantly to the reduction of global carbon-dioxide emissions in the future.

## 1.2 The History of Silicon Carbide and its Devices

SiC has a history that covers more than a century in time. Unlike other materials that have been under focus of researchers decades before their first commercial applications have been released, SiC has from the very first moment attracted both scientific and commercial interests. Furthermore, some important technological developments were closely linked to SiC.

The story of SiC started in the year 1891 with Edward Goodrich Acheson, an American born in Washington, Pennsylvania, who synthesized SiC for the first time without knowing about the material composition [17], [18]. He named the new material “carborundum” and commercialized it as an abrasive material. An employee of his company, Otto Mulhaeuser, was later able to determine the composition of “carborundum” to be SiC. Furthermore, Acheson

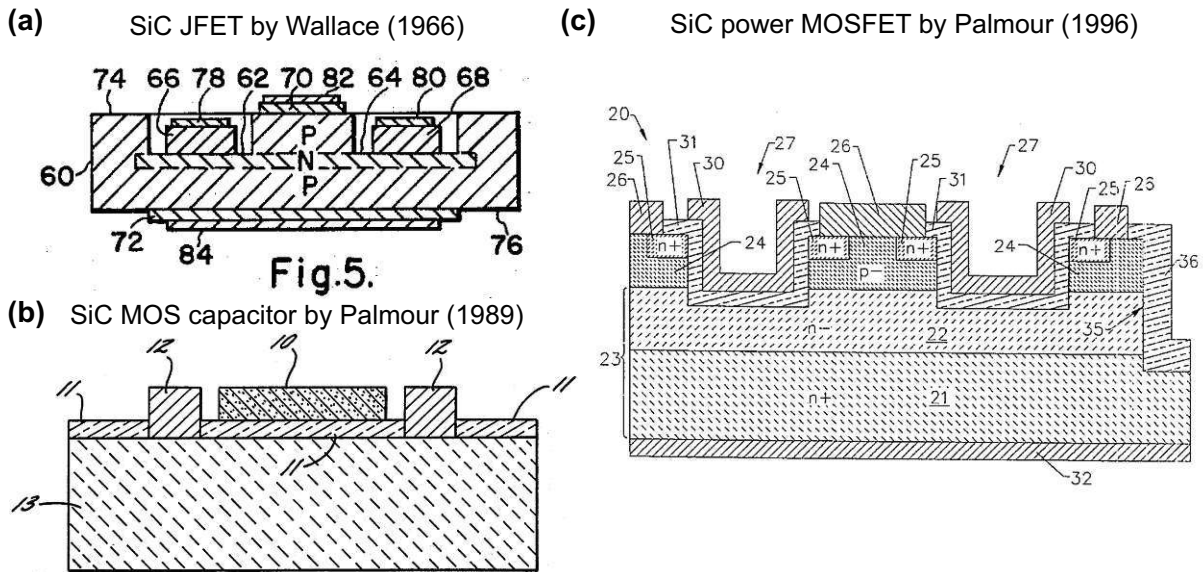


**Figure 1.2.** (a) The SiC junction field-effect transistor (JFET) patented by Lloyd F. Wallace in 1966. Taken from [31]. (b) The SiC metal-insulator-semiconductor capacitor (MOSCAP) patented by John W. Palmour in 1989. Taken from [32]. (c) The SiC power MOSFET patented by John W. Palmour in 1996. Taken from [33].

asked B.W. Frazier, a professor for mineralogy and metallurgy from Lehigh University in South Bethlehem, to analyze the “carborundum” crystal [19]. Indeed, Frazier effectively discovered the polytypism of SiC. Around the same time in 1893, Henri Moissan discovered natural SiC in a meteorite in the Diablo Canyon, Arizona [20]. As a result, in 1905, George F. Kunz suggested to term SiC “moissanite” to the honor of Moissan’s discovery [21], which is why the name “moissanite” is still occasionally in use nowadays.

Most interestingly, the history of light-emitting diodes (LEDs) is also closely linked to SiC [22]. In 1907, Henry Joseph Round published the first general report of electroluminescence (EL), whereby his samples were made of SiC (“carborundum”) [23]. His scientific note was only 24 lines in length, in which he briefly described his observations. Later in 1927, Oleg Vladimirovich Losev published similar observations [24] followed by other related contributions, that are summarized in [25].

The first steps towards industrial manufacturing of SiC crystals were done by Jan Anthony Lely in the year 1955, when he filed a patent of a sublimation growth process for bulk SiC crystals [26] that is still being used nowadays in industry in a modified version [27]–[30].

This was the start of SiC device development. In 1963, Lloyd F. Wallace filed a patent on the first reported SiC transistor [31], which basically was a junction field-effect transistor (JFET). The device is illustrated in Fig. 1.2a. The current flow between the source and drain terminals is controlled via gate electrodes by changing the spatial spread of the depletion layer. More than a decade later, in 1977, the first SiC bipolar transistors were presented by W. von Muench [35].

Commercialization of SiC devices was significantly boosted once John W. Palmour, at that time PhD student at the North Carolina State University, filed a patent in the year 1987 for a SiC metal-insulator-semiconductor capacitor (MOSCAP), shown in Fig. 1.2b [32]. In the very same year, together with others, he founded the company Cree Research, Inc. In 1989, Cree Research even filed a patent for the first SiC LED [36]. Shortly after that in 1992, the company filed a

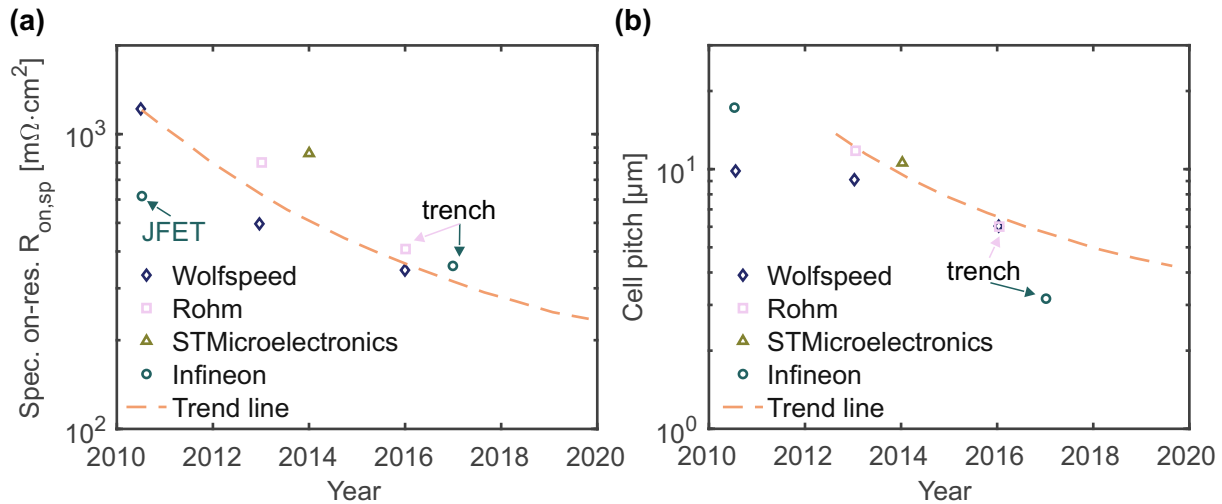


**Figure 1.3.** (a) Temporal evolution of specific on-state resistance of 1200 V commercial SiC MOSFETs. Redrawn from [34]. (b) Temporal evolution of the cell pitch of 1200 V commercial SiC MOSFETs. Redrawn from [34].

patent for the first SiC power MOSFET [33]. This device had a vertical design (see Fig. 1.2c and Section 1.5.2 for more details on such a device design).

In 1991 and 1993, both a 1 kV pn diode and a Schottky-barrier diode (SBD) have been demonstrated on 6H-SiC [37], [38]. Shortly afterwards in 1995, the superior on-resistance of SBDs based on 4H-SiC has been shown [39].

Initially, the interface quality between silicon dioxide ( $SiO_2$ ) and SiC was a limiting factor for the inversion channel mobility in SiC-based MOSFETs, until it was found that an anneal in nitric oxide (NO) significantly reduces the density of interface defects by roughly a factor of ten and subsequently also increases the effective channel mobility by roughly one order of magnitude [40], [41].

In 2001, Infineon Technologies released the first commercial SiC power device, which was a Schottky diode [42]. In the following, Cree further focused on the commercialization of SiC MOSFETs [43], finally leading to the very first lateral commercial SiC power MOSFET CMF20120D in 2011 [44]. Around the same time, Rohm released its own SiC MOSFET technology [45]. In the year 2014, STMicroelectronics followed and released their first SiC MOSFET [46], [47]. A few years later, after Infineon Technologies had initially produced a SiC JFET [48], [49], it finally released the first asymmetric trench SiC MOSFET, announced at the PCIM Europe 2016 [50].

The commercial vendors of SiC MOSFETs are continuously improving their devices. Fig. 1.3 shows the temporal evolution of both specific on-state resistance and cell pitch, whereby the former is reduced by a factor of 0.7 within every three years [34]. Consequently, there is a clear trend towards lower prices and improved performance.

### 1.3 Silicon Carbide: From the Crystal to the Wafer

In order to understand the working principle of semiconductor devices, it is important to understand the physical properties of the employed materials. Therefore, this section introduces the crystal structure of SiC, its polytypism, and its growth techniques. In particular in the context of defect-related phenomena such as bias temperature instability (BTI), the band structure and lattice vibrations become important. After having presented them, localized vibrations are

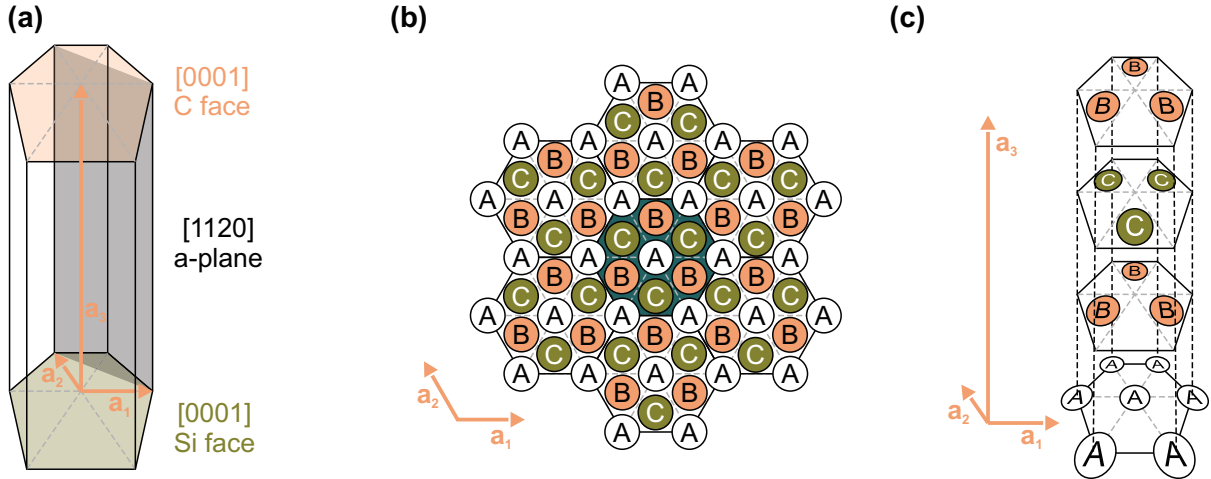


**Figure 1.4.** (a) The conventional hexagonal unit cell and the primitive lattice vectors  $a_i$  spanning the primitive hexagonal unit cell. (b) The positions associated with the layers A, B, and C. (c) Illustration of the stacking-order of the layers for the example of 4H-SiC.

introduced, that can be created by crystal point defects and become particularly important in the context of Section 4.4.7.

### 1.3.1 Crystal Structure

SiC is a stable crystal up to about 2800 K at ambient pressure, however, there is still ongoing research regarding the stability of the crystal at higher pressure [51]. As described in detail in any introductory solid state physics textbook, such as from Kittel [52], a crystal structure is described using a lattice and a basis of atoms. The defining property of a lattice is its translation invariance. From any point  $r$ , there are vectors  $a_1$ ,  $a_2$ , and  $a_3$ , such that the arrangement of lattice points is exactly the same from any other point

$$\mathbf{r}' = \mathbf{r} + u_1\mathbf{a}_1 + u_2\mathbf{a}_2 + u_3\mathbf{a}_3. \quad (1.6)$$

Hereby, the scalars  $u_1$ ,  $u_2$ , and  $u_3$  denote arbitrary integer numbers. At each grid point, there is a basis of atoms that are equally located with reference to each lattice point. The vectors  $a_i$  are called primitive, if all points  $r$  and  $r'$  from which the arrangement of atoms is identical follow Equation 1.6. Consequently, the corresponding primitive unit cell, which is the volume spanned by the vectors  $a_i$ , contains exactly a single lattice point. Different lattices can be transformed into other lattices by symmetry operations such as rotation, mirror reflection, and inversion. This leads to the definition of fundamental lattice types, so-called Bravais lattices. Crystal directions are indicated using the projected coordinates  $[hkl]$  (Miller indices) in the system of the lattice vectors. Apart from that, crystal planes are indicated by naming the three inverse intersection coordinates  $(hkl)$  with the lattice axes.

For the hexagonal Bravais lattice, it is common to use four so-called Bravais-Miller indices

$$[hkil] = [hk(-h-k)l] \quad (1.7)$$

instead of three Miller indices [53]. Analogously, four indices for lattice planes can be defined. Despite the redundancy of information, this notation considers the hexagonal symmetry. Subse-

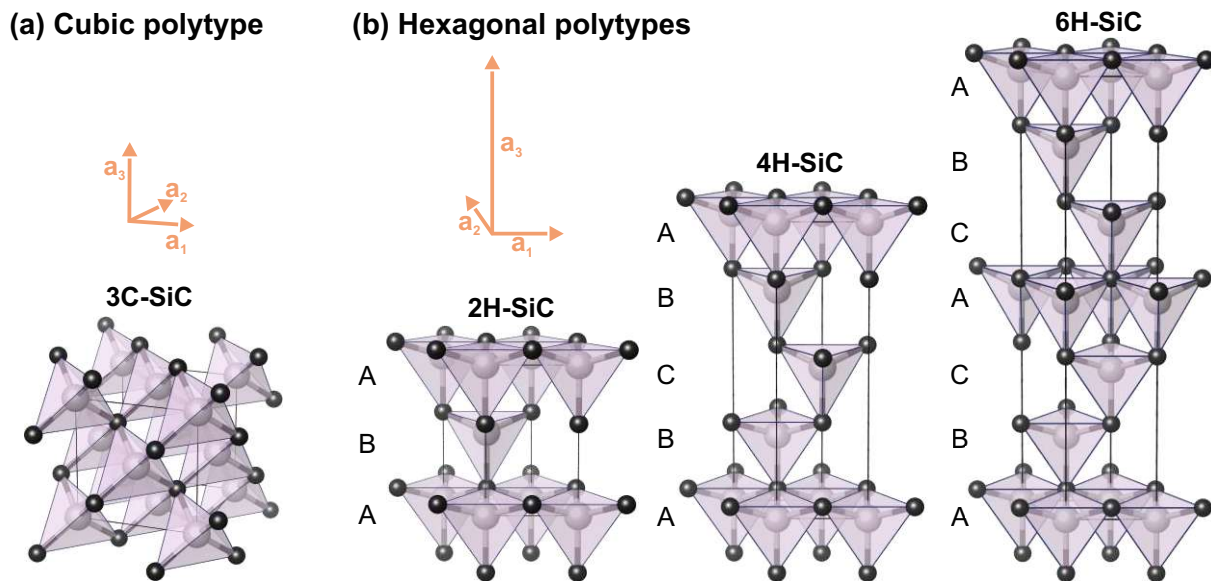


**Figure 1.5.** (a) The primitive unit cell of a cubic polytype of SiC. (b) The primitive unit cells of three selected hexagonal polytypes of SiC. The schematics were created using VESTA [60].

quent equivalence of planes can easily be recognized as two equivalent planes are permutations of each other in the first three indices.

SiC as a crystal exhibits polymorphism, or more precisely polytypism, which means different polytypes with different primitive unit cells can be created by varying the stacking order of certain layers [54], [55]. Apparently, both silicon and carbon have four unpaired outer electrons, leading to the formation of typical  $sp^3$ -hybridized tetrahedrons of carbon atoms with a silicon atom in the center. Starting with a hexagonal Bravais lattice (see illustration of primitive unit cell within conventional unit cell in Fig. 1.4a), the initial layer A is defined as the layer where the silicon atoms are placed at the  $(0,0,0)$  position (see Fig. 1.4b). The subsequent positions of the layers, consisting of tetrahedra, determine the SiC polytype. Apart from the position related to layer A, the tetrahedra can be placed in the positions associated with layers B and C. Conventionally, the naming of the different polytypes of SiC is based on the Ramsdell notation consisting of the number of layers in the primitive unit cell and a letter indicating the Bravais lattice (C for cubic, H for hexagonal, and R for rhombohedral). Fig. 1.4c exemplarily shows the stacking order of 4H-SiC. The primitive unit cells of a selection of polytypes are shown in Fig. 1.5.

As can be seen in Fig. 1.5, there are layers in the primitive unit cell that have different local symmetry leading to inequivalent lattice sites for the polyhedra. 3C-SiC has only cubic symmetry sites, whereas 2H-SiC has only hexagonal symmetry sites. However, 4H-SiC has both a local cubic symmetry as well as a hexagonal symmetry site. This inequivalence of lattice sites has an impact on doping levels [56] and bulk defect levels [57]–[59]. In 6H-SiC, there is even a second cubic symmetry site.

Regarding applications in electronics, the polytypes 3C-SiC, 4H-SiC, and 6H-SiC turned out to be most suitable. Although the thermal properties of the polytypes are similar, e.g. the thermal conductivity is always in the range  $3.3\text{--}4.9\text{ W cm}^{-1}\text{ K}^{-1}$  [55], the band structure and hence the electrical properties differ strongly. Consequently, the SiC base material for electronic devices has to be of a single polytype only. As will be outlined in Section 1.3.2, growing a SiC crystal of a single polytype was one of the challenges for the manufacturability of SiC-based

| Polytype | $a$ [Å] | $c/n$ [Å] | inequiv. sites | $E_G$ [eV] | $\mu_{\parallel c} / \mu_{\perp c}$ [cm <sup>2</sup> V <sup>-1</sup> s <sup>-1</sup> ] |
|----------|---------|-----------|----------------|------------|--|
| 3C       | 4.359   | –         | 1              | 2.38       | 750  |
| 2H       | 3.076   | 2.524     | 1              | 3.33       | –/–  |
| 4H       | 3.081   | 2.521     | 2              | 3.26       | 800/800  |
| 6H       | 3.081   | 2.520     | 3              | 3.02       | 60/400   |

**Table 1.2.** Lattice constants, number of inequivalent lattice sites, bandgap  $E_G$ , and electron mobilities parallel ( $\parallel$ ) and perpendicular ( $\perp$ ) to the  $c$ -axis of selected SiC polytypes. The mobility refers to a donor-doping concentration of  $10^{16}$  cm<sup>-3</sup>. The lattice constants are  $a = |\mathbf{a}_1| = |\mathbf{a}_2|$  and  $c = |\mathbf{a}_3|$  and  $n$  is the number of SiC bilayers. Data taken from [61]–[66].

devices in the past. As can be seen in Table 1.2, with regard to the electron mobility, 4H-SiC has proven to be the most suitable polytype, particularly in comparison to 6H-SiC with its strong anisotropy in electron mobility.

### 1.3.2 Crystal growth

Bulk growth of SiC boules is not easy. The state-of-the-art industrial method for bulk growth is the seeded sublimation growth (modified Lely method) with which the production of high-quality crystals has been achieved [67]–[69]. The growth system is based on a graphite crucible, which also works as a susceptor for inductive heating [70]. The crucible is surrounded by a double-wall quartz tube and the inductive heating coils. Additionally, it is loaded with SiC charge material. After degassing, the crucible is flooded with argon while maintaining vacuum pressure conditions, followed by heating up to a operation temperature of 1800–2600 °C [28], [70]. The SiC charge material sublimates and decomposes into the species Si, C, Si<sub>2</sub>C, and SiC<sub>2</sub>, which are subsequently transferred to the seed where the material crystallizes [70]. The seed is either a high-quality platelet or a wafer from a previously manufactured boule. Furthermore, the temperature distribution which also heavily influences the spatial growth behavior is adapted by changing the position of the heating coils, while pre-knowledge about the explicit dependencies from computer simulations is required [70], [71]. Doping of the bulk crystal, predominantly via the use of nitrogen for n-doping and aluminum for p-doping, is achieved by either adding the dopants to the SiC charge material or by inserting it in a gaseous form [72]. The growth of bulk 4H-, and 6H-SiC has been achieved by the modified Lely method [68], [73], however, the growth of 3C-SiC is challenging because it transforms into hexagonal polytypes beyond 2000 °C and requires a high vapor-concentration of Si [74]–[76]. Consequently, 3C-SiC does not yield suitable quality at adequate growth rates, however, it can be grown heteroepitaxially on Si-substrates, e.g. for the fabrication of pn-diodes [77], [78].

Apart from heteroepitaxy of 3C-SiC on Si-substrates, high-quality homoepitaxy is an essential prerequisite for electronic device fabrication. This can be realized using chemical vapor deposition (CVD), with silane as Si source and a hydrocarbon as C source, and the so-called “step-controlled epitaxy”, which in particular works with both 4H- and 6H-SiC [79], [80]. The latter is based on off-orientation of the  $\{0001\}$  substrates by a small angle, typically 0.1–10°. The off-oriented substrate allows to transfer the full information on the crystal structure, including the specific polytype, from the substrate to the epitaxial layer. In situ doping of the epitaxial layer can be achieved by adding gases containing the respective dopants: nitrogen or phosphorous (PH<sub>3</sub>) for n-type doping and trimethyl aluminum or diborane (B<sub>2</sub>H<sub>6</sub>) for p-type doping [81].

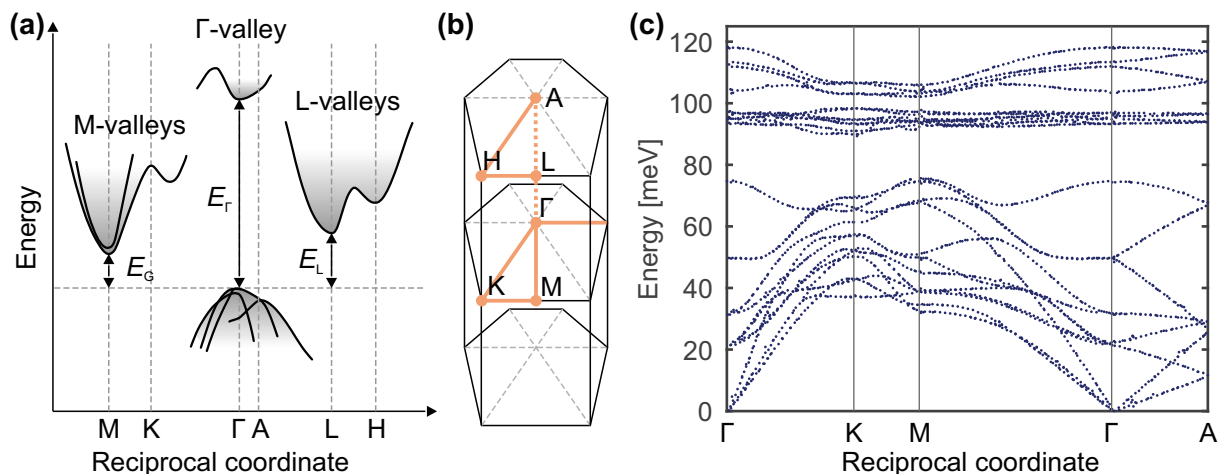


**Figure 1.6.** (a) The band structure of 4H-SiC obtained by theoretical density functional theory (DFT) calculations.  $E_G = 3.23$  eV,  $E_\Gamma = 5-6$  eV, and  $E_L \approx 4$  eV. Redrawn from [85]. (b) Brillouin zone of 4H-SiC indicating the symmetry points from (a). (c) Phonon dispersion in 4H-SiC. Redrawn from [86].

Apart from varying the flow of the respective gas, the doping concentration of the epitaxial layer can be altered by changing the Si/C ratio, which is referred to as “site-competition epitaxy” [82].

In summary, 4H-SiC appears to be the polytype of choice for electronic applications because of the high critical electric field (see Table 1.1), good isotropic electron-mobility (see Table 1.2) and its excellent manufacturability in both bulk crystal growth and epitaxial layer growth. Indeed, 4H-SiC is therefore the polytype that is most frequently used in industry [66], [83]. As a consequence, the following chapters will exclusively discuss the 4H-SiC polytype.

### 1.3.3 Band Structure

4H-SiC is an indirect semiconductor, which means the conduction band minimum and the valence band maximum are separated in reciprocal space. The band diagram is illustrated in Fig. 1.6a, whereas the corresponding symmetry points are illustrated in Fig. 1.6b. The conduction band minimum is located in the M-valleys, whereby the indirect bandgap was measured to be 3.26 eV [64]. Band-to-band transitions between conduction band minimum and valence band maximum hence require additional quasi-momentum provided either by absorption or emission of a phonon, which means that band-to-band optical absorption and emission is suppressed [84, Chapter 3.4]. Typically, light emission in indirect semiconductors occurs therefore via recombination centers that are energetically located inside the bandgap.

### 1.3.4 Lattice Vibrations

Aside from electronic properties, vibrational properties are important with regard to thermal activation in charge transfer reactions. The  $N$  atoms in a crystal can vibrate around their equilibrium positions in harmonically approximated Born-Oppenheimer potentials with the corresponding Hamilton operator

$$\hat{H} = \sum_{i=1}^N \left( \frac{\hat{p}_i^2}{2m_i} + \frac{1}{2} \kappa_i q^2 \right) \quad (1.8)$$

with displacement  $q$  and force constants  $\kappa_i$  [87, Chapter 2]. The behavior of lattice vibrations can indeed be described as a system of  $3N$  independent harmonic oscillators. Collective lattice vibrations are quantized in energy [52, Chapter 4], which leads to the definition of phonon quasi-particles with energy  $\hbar\omega$ . A vibrational mode with energy

$$\epsilon = \hbar\omega \left( n + \frac{1}{2} \right) \quad (1.9)$$

is consequently occupied by  $n$  phonons [87, Chapter 4]. Furthermore, the occupancy of the vibrational modes follows Bose-Einstein-statistics with average occupancy

$$\bar{n}(\hbar\omega) = \frac{1}{\exp\left(\frac{\hbar\omega}{k_B T}\right) - 1}. \quad (1.10)$$

As in the case of 4H-SiC, if the crystal basis contains more than 1 atom, several branches appear in the phonon dispersion relation that are referred to as optical and acoustical phonon branches. In 4H-SiC, they could be determined experimentally. Besides the use of Raman scattering experiments [88], the entire Brillouin zone can be experimentally accessed via inelastic x-ray scattering [86], [89]. In agreement with theory, these experiments show that the maximum energy of the various phonon modes in 4H-SiC is close to 120 meV (see Fig. 1.6c), which is far away from  $k_B T \approx 26$  meV at 300 K ( $\bar{n}(120 \text{ meV}) \approx 0.01$ ). As will be outlined in the following section, there are vibrational modes with even higher energies than the highest phonon mode. The aspect that systems at typical temperatures are in their vibrational ground state becomes then important in Section 4.4.

### 1.3.5 Localized Vibrations

Apart from collective lattice vibrations, crystal point defects can introduce so-called local vibrational modes (LVMs) [90]. These vibrations are localized in real space while they are delocalized in reciprocal space.

For the introduction of the concept of LVMs, consider a linear chain of silicon atoms with lattice constant  $a$ , spring constant  $k$ , and mass  $m_{\text{Si}}$  that gives a dispersion relation in a classical calculation of

$$\omega_{\text{mono}}^2 = \omega_{\text{mono,max}}^2 \sin^2\left(\frac{qa}{2}\right) \quad (1.11)$$

with  $\omega_{\text{mono,max}} = \sqrt{4k/m_{\text{Si}}}$  and the reciprocal lattice coordinate  $q$  [52]. The corresponding energy  $\hbar\omega_{\text{mono}}$  is plotted in Fig. 1.7a, which exhibits a single branch.

In contrast to that, a diatomic chain of silicon and carbon atoms with the same spring constant  $k$  and lattice constant  $a$  gives two branches, the optical and acoustical branches, that are plotted in Fig. 1.7a. The dispersion relation is given by

$$\omega_{\text{diatomic}}^2 = k\mu \pm k \sqrt{\mu^2 - \frac{4 \sin^2\left(\frac{qa}{2}\right)}{m_{\text{Si}}m_{\text{C}}}} \quad (1.12)$$



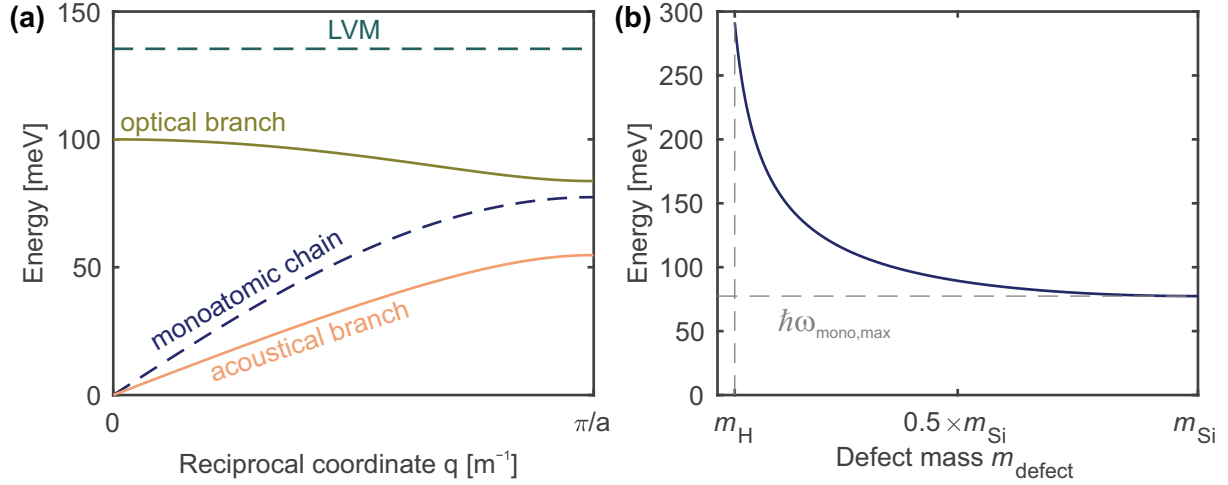


**Figure 1.7.** (a) The dispersion relations of the one dimensional monoatomic chain, the diatomic chain and the energy of an exemplary LVM of a defect atom with a mass of five times the mass of a hydrogen atom. (b) The dependence of the energy of the LVM on the defect mass.

with  $\mu = (m_{Si} + m_C) / (m_{Si}m_C)$  [52]. In three dimensions with  $p$  atoms in the basis, there are  $3p$  branches in total, consisting of 3 acoustical and  $3p - 3$  optical branches.

So far, the considered vibrational modes were collective lattice vibrations related to phonons. Consider again the monoatomic chain of silicon atoms and replace one of the silicon atoms in the chain by another atom with mass  $m_{\text{defect}}$ . This can be considered as a point defect. This point defect then introduces an additional vibrational mode [90], the LVM with a frequency following

$$\omega_{\text{LVM}}^2 = \omega_{\text{mono,max}}^2 \frac{m_{Si}^2}{2m_{Si}m_{\text{defect}} - m_{\text{defect}}^2}. \quad (1.13)$$

Hereby,  $\omega_{\text{LVM}}$  will be higher than  $\omega_{\text{mono,max}}$ , if  $m_{\text{defect}} < m_{Si}$ . The corresponding energy of the LVM for  $m_{\text{defect}} = 5m_H$  with  $m_H$  being the mass of a hydrogen atom, is indicated in Fig. 1.7a. Apparently, the LVM has a much higher energy than the maximum phonon mode in the monoatomic chain. Fig. 1.7b shows the dependence of the LVM on  $m_{\text{defect}}$ . The energy increases with decreasing mass of the defect atom. The energy can easily exceed the maximum phonon frequency by a factor of two or more.

These LVM modes of high energy are known in many material systems featuring various complexes [90]. Most importantly, they have been intensively investigated in a number of polytypes of bulk SiC, both experimentally [91]–[97] as theoretically [98]–[100]. For instance, 6H-SiC exhibits LVMs with energies up to 247 meV related to zero-phonon lines (ZPLs) in the range between 2.36–2.47 eV [93].

| $(C_{sp,k})$ | $(C_{sp,h})$ |
|--------------|--------------|
| 111.3        | 122.5        |
| 186.6        | 124.1        |
| –            | 192.9        |

**Table 1.3.** Calculated energies in meV of various LVMs in 4H-SiC associated with asymmetric carbon split-interstitials. Data taken from [101].

In particular, carbon cluster defects have been investigated as the origin of the various LVMs in SiC [93]. There are various types of carbon clusters, whereby each type of carbon cluster

has a set of LVMs. The basic building block of these defects is the carbon split-interstitial, where two carbon atoms share a carbon lattice site [101]. Depending on its charge state, it exists in a symmetric or an asymmetric configuration. Due to the inequivalence of lattice sites in 4H-SiC, discussed in Section 1.3.1, the split-interstitial can either be at a hexagonal or a cubic lattice site. Of course, the lattice site affects the energy of the LVMs, which are listed for the asymmetric configuration in Table 1.3 for the carbon isotope  $^{12}\text{C}$ . The energies range up to 192.9 meV. Note that the energy of the LVM depends on the involved carbon isotopes, which can lower the energies with increasing mass by several millielectronvolt. Furthermore, even higher energies of 219.2 meV and 183 meV were calculated for the symmetric configuration in the  $2^+$  and neutral states, respectively [98], [99], [101].

| $(\text{C}_{\text{sp}})_{2,\text{kk}}$ | $(\text{C}_{\text{sp}})_{2,\text{hk,cub}}$ | $(\text{C}_{\text{sp}})_{2,\text{hh}}$ | $(\text{C}_{\text{sp}})_{2,\text{kk,lin}}$ | $(\text{C}_2)_{\text{Si},\text{k}}$ | $(\text{C}_3)_{\text{Si},\text{k}}$ | $(\text{C}_4)_{\text{Si},\text{k}}$ | $[(\text{C}_2)_{\text{Si}}]_{2,\text{kh}}$ | $[(\text{C}_2)_{\text{Si}}]_{2,\text{hh}}$ |
|--|--|--|--|-------------------------------------|-------------------------------------|-------------------------------------|--|--|
| 123.7                                  | 128.0                                      | 134.9                                  | 117.1                                      | 102.3                               | 119.0                               | 113.4                               | 114.4                                      | 114.3                                      |
| 126.3                                  | 161.3                                      | 159.9                                  | 120.2                                      | 119.7                               | 130.2                               | 114.3                               | 119.6                                      | 120.4                                      |
| 159.3                                  | 167.1                                      | 168.1                                  | 160.0                                      | 135.0                               | 154.0                               | 114.5                               | 132.2                                      | 130.8                                      |
| 164.6                                  | 189.1                                      | 191.5                                  | 167.0                                      | 139.1                               | 182.3                               | 120.3                               | 147.0                                      | 145.7                                      |
|  |  |  | 203.2                                      | 178.0                               | 254.9                               | 200.1                               | 160.2                                      | 159.7                                      |
|  |  |  |  |                                     |                                     | 201.5                               | 162.4                                      | 161.8                                      |
|  |  |  |  |                                     |                                     | 204.3                               |  |  |
|  |  |  |  |                                     |                                     | 240.7                               |  |  |

**Table 1.4.** Calculated energies in meV of various LVMs in 4H-SiC associated with different carbon clusters. Data taken from [101].

The interstitials discussed above can aggregate and form larger carbon clusters, such as the di-interstitial complexes  $(\text{C}_{\text{sp}})_{2,\text{kk}}$ ,  $(\text{C}_{\text{sp}})_{2,\text{hk,cub}}$ ,  $(\text{C}_{\text{sp}})_{2,\text{hh}}$ , and  $(\text{C}_{\text{sp}})_{2,\text{kk,lin}}$  [101], [102]. Their properties depend on the properties of the building blocks. For instance,  $(\text{C}_{\text{sp}})_{2,\text{kk}}$  is a complex of two neighboring split interstitials at cubic lattice sites. Besides di-interstitials, it can occur that a carbon antisite serves as a growth center for carbon clusters. This includes the dicarbon antisite  $(\text{C}_2)_{\text{Si},\text{k}}$ , where two carbon atoms replace a silicon atom of the crystal. Similar to the formation of di-interstitial clusters by split interstitials, dicarbon antisites can cluster and form dicarbon-antisite pairs, such as  $[(\text{C}_2)_{\text{Si}}]_{2,\text{kh}}$  and  $[(\text{C}_2)_{\text{Si}}]_{2,\text{hh}}$ . Besides that, a dicarbon antisite can capture carbon interstitials, forming antisite complexes such as  $(\text{C}_3)_{\text{Si},\text{k}}$  and  $(\text{C}_4)_{\text{Si},\text{k}}$  of three and four carbon atoms, respectively. Table 1.4 shows the calculated energies of LVMs of the mentioned carbon clusters in 4H-SiC. Energies up to 254.9 meV are reached.

## 1.4 Applications of Silicon Carbide Devices

As already pointed out in Section 1.1, SiC-based devices feature much lower switching losses compared to Si-based technologies. The reason is the higher critical electric field strength (see Table 1.1), that allows SiC devices of the same voltage and on-state resistance class to be designed smaller in size, which in turn reduces parasitic capacitances. The benefit of a reduction in parasitic capacitance particularly appears at high switching frequency (see Fig. 1.1).

Applications with high switching frequency and high power density can be found in power conversion circuits, unavoidably present in electric vehicles and numerous green industrial power applications. These comprise solar inverters, uninterruptible power supplies, railway traction inverters, electric vehicles, induction heating, or solid state transformers [104]. Consider the example of a full bridge DC-DC converter circuit, as illustrated in Fig. 1.8. This circuit

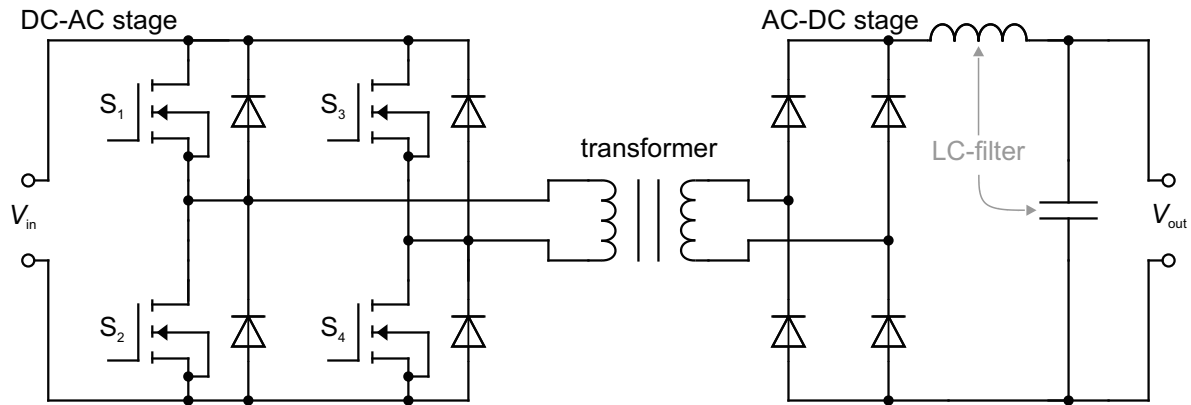


Figure 1.8. Full bridge DC-DC converter circuit. Redrawn from [103].

converts a DC input voltage  $V_{in}$  into a DC output voltage  $V_{out}$  [105]. It consists of a first DC-AC stage converting the DC input into an AC voltage at the left-hand side of the transformer. This stage uses four MOSFET switches ( $S_1$  to  $S_4$ ) that are continuously switching at high frequency between their conductive and non-conductive states. Switch  $S_1$  switches synchronously with switch  $S_4$ , and switch  $S_2$  switches synchronously with switch  $S_3$ . Consequently, the transformer receives an AC voltage with levels  $+V_{in}$  and  $-V_{in}$ , which is subsequently transformed according to the winding ratio of the transformer. On the right-hand side of the transformer, the resulting AC voltage is rectified and finally passes a low-pass LC-filter. Thanks to the mentioned reduced parasitic capacitances, replacing the Si-based MOSFETs and diodes by SiC-based technology reduces the total loss by around 40 % [106]. Furthermore, for providing the same junction temperature, the cooling components of the SiC-based system can be reduced by 54 % in size and weight. This is supported by the high thermal conductivity of 4H-SiC (see Table 1.1). Finally, a higher switching frequency generally enables the choice of a smaller inductive component in the LC-filter. In summary, SiC-based power conversion systems feature a smaller size, lower weight and increased efficiency.

## 1.5 The Designs of Modern Silicon Carbide Field-Effect Transistors

There are several possibilities to design 4H-SiC power MOSFETs, however, they all have in common the underlying MOS structure. Differences arise e.g. from the choice of deposited versus thermally grown oxide and the crystal interface of SiC, along which the conducting channel is formed. Thermally grown oxides have shown a higher density of interface defects, they are less robust with respect to dielectric breakdown and feature a lower channel mobility [107]. 4H-SiC MOSFETs typically have their channel formed either along the (0001) or the (11 $\bar{2}$ 0) crystal plane. The latter has the highest inversion channel mobility compared to other crystal planes [108], [109], including the (0001) plane [110].

For the design of a MOSFET, the band offsets at the the channel interface are important, because they affect the gate leakage current, e.g. via Fowler-Nordheim tunneling [111], [112]. The band alignment for the 4H-SiC/SiO<sub>2</sub> interface is illustrated in Fig. 1.9a. Note that the offsets for both the valence and conduction bands are very similar, so that the bandgap of 4H-SiC is well-centered in the middle of the bandgap of SiO<sub>2</sub>. Consequently, the potential barrier for Fowler-Nordheim tunneling of electrons and holes from 4H-SiC to SiO<sub>2</sub> is similar.

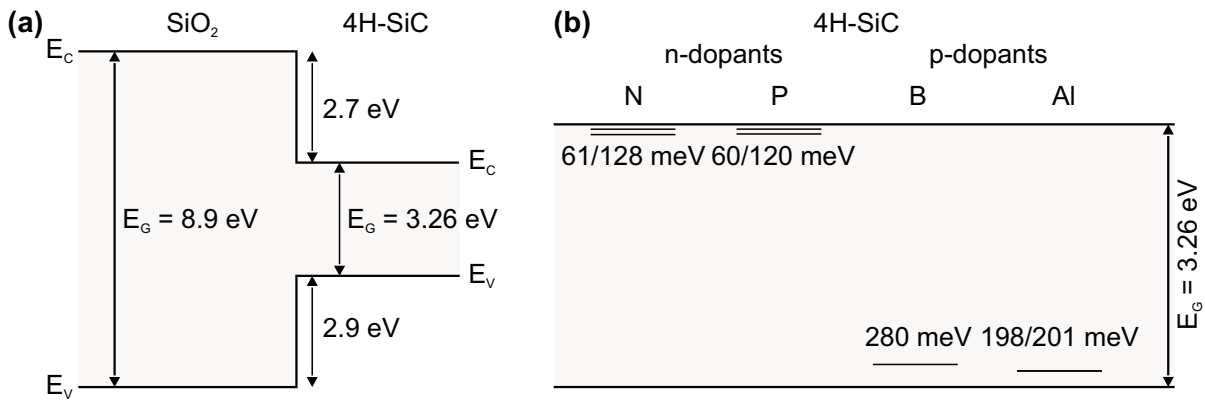


**Figure 1.9.** (a) Band alignment at the 4H-SiC/SiO<sub>2</sub> interface. Data taken from [64]. (b) Ionization energies of nitrogen (N), phosphorus (P), boron (B), and aluminum (Al). The given values are for the hexagonal and cubic lattice sites, respectively. Data taken from [55].

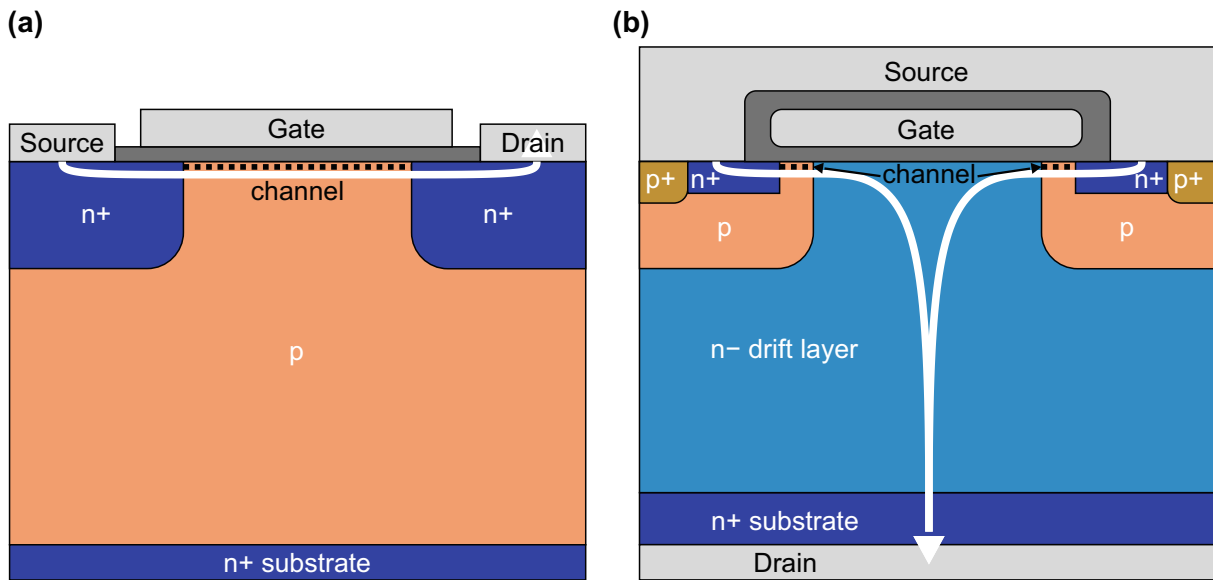


**Figure 1.10.** (a) Planar SiC MOSFET with lateral current-flow, indicated by a white arrow. The channel region is indicated by black dots. (b) The power double-diffused MOSFET (DMOSFET) with a lateral gate, but with vertical current flow. Redrawn from [113].

Of course, doping of 4H-SiC is a prerequisite to design a working MOSFET. Fig. 1.9b shows the ionization energies of four different dopants, two for n-type doping and two for p-type doping. As mentioned in Section 1.3.1, 4H-SiC features lattice sites of either cubic or hexagonal symmetry, which gives rise to two different ionization energies of doping impurities [56]. Typically, commercially available power MOSFETs based on 4H-SiC are n-channel MOSFETs, meaning the channel region is p-type doped. The different designs are presented in the following sections.

### 1.5.1 The Planar Designs

The planar designs of SiC MOSFETs feature a lateral gate oxide, such that the 4H-SiC/SiO<sub>2</sub> is formed at the (0001) crystal plane. The simplest device design is the lateral MOSFET with a lateral current-flow (see Fig. 1.10a). Source and drain terminals are on the upper side of the chip with the gate terminal in the center. Its related power device with a vertical current-flow is the

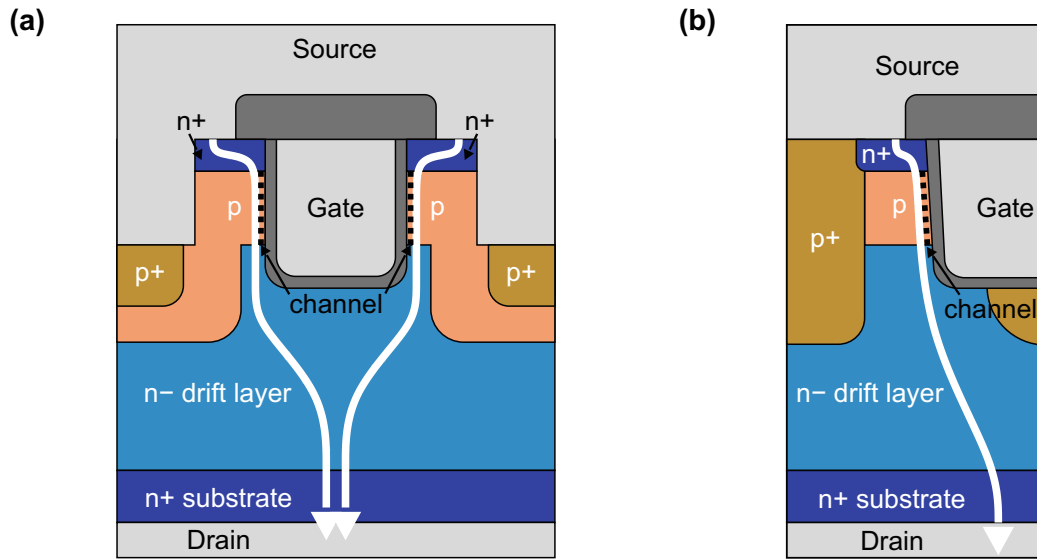


**Figure 1.11.** (a) The double-trench design with vertical current-flow, indicated white arrows. The channel regions are indicated by black dots. Redrawn from [45]. (b) The asymmetric trench design. Redrawn from [113].

double-diffused MOSFET (DMOSFET), illustrated in Fig. 1.10b. Each gate terminal operates two p-type regions where the channels are formed. Furthermore, this structure features two vertical body diodes per cell, which are the vertical pn junctions at the right and left-hand side of the cell that connect source and drain. This is the cell concept of many commercially available SiC power MOSFETs [114], [115]. However, the lateral gate hinders strong down-scaling of the cell structure [108].

### 1.5.2 The Trench Designs

In contrast to the planar designs, the trench MOSFETs (UMOSFETs) have a vertical trench gate, which allows down scaling of the cell size. As for the DMOSFET, the current-flow is vertical with the drain terminal at the backside of the chip. Among the UMOSFETs, the double-trench MOSFET features two channels per cell (see Fig. 1.11a). The channels are located vertically along the left and right-hand side of the trench. Apart from the gate trench, there are also source trenches at the sides of the cell with the vertical body diodes underneath. This concept is employed in commercial SiC MOSFETs with low specific on-state resistance [45]. However, having two channels along the trench unavoidably means that the crystal planes for the left and right-hand side channel differ and therefore have different properties [108].

This drawback of having two different crystal planes for the different channels is eliminated with the asymmetric trench design, shown in Fig. 1.11b. Here, the channel is formed exactly along the  $(11\bar{2}0)$  crystal plane. As mentioned above, this plane features the best inversion channel mobility. Furthermore, the asymmetric trench MOSFET does not have the source trenches of the double-trench MOSFET. The asymmetric trench MOSFET is also a commercially realized design [108], [113].

## 1.6 Reliability of Silicon Carbide Field-Effect Transistors

The term *reliability*, as generally defined in the *IEEE 100 The Authoritative Dictionary of IEEE Standards Terms*, means: “The ability of an item to perform a required function under stated conditions for a stated period of time” [116]. In general, the targeted application dictates all of the three factors: function, conditions and the period of time. In the specific case of a MOSFET, the function is to switch between blocking and non-blocking state, which is switching between inversion and depletion or accumulation. This includes the stability of the entire device, including its characteristic parameters, such as threshold voltage ( $V_{th}$ ),  $R_{on}$ , etc. The set of conditions generally includes any condition that might affect any physical mechanism that could lead to the failure of a device. Typical quantities that are considered in reliability physics are temperature, voltage (including electric field, switching frequency, transition times, etc.), humidity, ionizing radiation, and mechanical stress. The specified period of time is usually given by the life cycle of the application or product, that contains the MOSFET. This could be a battery electric vehicle or an inverter system for a solar power plant. Ideally, the lifetime of the MOSFET exceeds the life cycle of the application.

Besides hard fails, e.g. a short between the gate and source terminals, there could be violations of the mentioned parameter stability. In the following, typical reliability issues in SiC MOSFETs related to the gate oxide, the body diode, and the SiC/SiO<sub>2</sub> interface are discussed.

### 1.6.1 Gate Oxide Reliability

The reliability of the gate oxide is a intensively discussed topic for SiC MOSFETs [108], [117], [118]. Initially, there were concerns about a possibly worse intrinsic reliability compared to Si devices, caused by the lower band offsets from SiC to SiO<sub>2</sub> (see Fig. 1.9a) [119]. These reduced band offsets would lead to a higher Fowler-Nordheim tunneling current [111], which was related to gate oxide reliability [120]. Furthermore, some researchers reported that early failures in DMOSETs with thermally-grown oxides could be caused by trap-assisted tunneling [121] and probably depend more on the oxide growth conditions than on SiC defects [122].

Meanwhile, it has been found that SiC MOSFETs can basically achieve a performance in gate oxide reliability that is comparable to Si-based technology, upon extensive process improvements [117], [123]–[125]. Effectively, the intrinsic behavior equals the intrinsic behavior of Si-based devices. The extrinsic branch is of greater importance and could be caused by any type of defect that can be intuitively understood as a local thinning of the gate oxide [126]. Indeed, SiC MOSFETs show a roughly three to four orders of magnitude higher extrinsic defect density compared to Si-based devices, but aside from just reducing the extrinsic defect density, this can be very efficiently tackled by using gate oxide screening techniques [117]. These techniques are used to identify devices failing early and remove them from the total population.

### 1.6.2 Bipolar Degradation of the Body Diode

An important degradation mechanism in SiC MOSFETs is bipolar degradation of the body diode [127]. The very first investigations have been conducted by ABB Research, starting with the observation of dislocations in pn junctions [128]. The dislocations grew upon current injection and showed electroluminescence around 425 nm. Later, this has been investigated more prominently as a degradation of the diode, where the forward current leads to an increase

in forward voltage [129]. This was then assigned to stacking faults of the 4H-SiC basal plane that reduce the carrier lifetime. There were considerable device-to-device variations in the forward voltage drift dynamics and it was found that this effect accelerates with both current and temperature [130]. At this early time of SiC device development, the degradation was observed in material from all manufacturers [131]. It is important to note that besides bipolar devices, also MOSFETs are affected because of their internal body diode [132]. In addition to an increasing forward voltage of the body diode, the degradation can lead to a higher leakage current in the blocking state. The underlying stacking faults can experimentally be made visible by imaging electroluminescence around 450 nm [133]. In contrast, partial dislocations show light emission around 700 nm. The activation energy of the stacking fault growth was determined to be 0.27 eV, which deviated by about 2.2 eV from the expected value of 2.5 eV. It was therefore concluded that the so-called recombination-enhanced defect glide (REDG) [134] causes the propagation of the stacking faults, which is basically a variant of recombination-enhanced defect reactions (REDRs). Over time, countermeasures have been developed to mitigate this reliability phenomenon [135].

### 1.6.3 Bias Temperature Instability

The general term BTI encompasses the change of any device parameter upon the application of a gate bias, mostly at elevated temperature up but not limited to 200 °C. BTI has been known for a long time, predominantly as negative bias temperature instability (NBTI) in Si-based MOSFETs [136], [137]. Despite discussions about a part of the underlying physical mechanism [138], whether it is reaction or diffusion limited, the underlying physics is basically related to generation of charge traps at or close to the semiconductor-insulator interface and charge trapping in preexisting charge traps [139]–[142]. These charge traps are point defects located in the bulk insulator (bulk defects), in the bulk insulator close to the semiconductor-insulator interface (border defects), or directly at the semiconductor-insulator interface (interface defect). So far, the physics of trapping and detrapping processes were considered to be exclusively non-radiative and described by the non-radiative multiphonon (NMP) theory [143], which will be described in detail in Section 2.1.2.

The fact that the time constants, related to the activation energies, of both charge capture and emission are distributed over multiple decades in time led to the modeling approaches based on capture-emission-time (CET) and activation energy (AE) maps [144], [145], which have proven useful for the understanding of various BTI-related phenomena, such as its occurrence during AC gate bias [146]. Furthermore, it allows to analytically describe and model BTI [147]. Physically more accurate modeling approaches were based on a two-state NMP model, implemented in a compact-physics framework (Comphy) [148].

Over the past two decades, the understanding of BTI in SiC MOSFETs has been catching up to the one in Si-based devices [149]. BTI was soon discovered in SiC based devices as well [150], [151]. Typical n-channel SiC MOSFETs show both positive bias temperature instability (PBTI) and NBTI and the underlying parameter dependencies are comparable to Si-based devices [152]. As for Si, modelling the wide distributions of time constants can be achieved by using the concept of CET and AE maps [153]–[155]. Comphy, previously used for Si devices, also describes the physics of BTI in SiC devices [156], [MFJ1]. Additionally to the usual long-term degradation, there is a significant amount of short-term trapping and detrapping of charges that dynamically affects  $V_{th}$ . Caused by a hundred times higher density of interface defects with respect to the

Si/SiO<sub>2</sub> interface [157], [158], this short-term component leads to a hysteresis in any device characteristic, including the transfer and capacitance-voltage (CV) characteristics [159], [MFC1].

## 1.7 Motivation for This Work

As outlined in the previous sections, 4H-SiC MOSFETs do not only have a high potential for power conversion applications, they are currently revolutionizing power electronics by enabling higher power conversion efficiency at reduced weight and size. Although they are hidden behind the encasing of many green products, such as electric vehicles or wind turbines, SiC MOSFETs are an essential part of a global transformation towards compact and energy efficient use of green technologies.

Within this inspiring context, this work intends to contribute to the understanding of SiC device reliability and the related physical processes occurring at the 4H-SiC/SiO<sub>2</sub> interface. Given the fact that these devices are already in mass production and built in many purchasable products, the understanding of the device physics is already quite advanced. Indeed, there are many similarities to Si-based MOSFETs, however, there are still a number of peculiarities that need to be understood in greater detail. These peculiarities are mostly related to this high density of interfacial point defects that also constitute the recoverable component of BTI. Besides studying their behavior in typical reliability experiments, the premier goal is to identify these defects and to reveal their nature in order to either mitigate them or characterize them in a better fashion.

First, it was studied how this recoverable component influences the acceleration of BTI experiments at higher temperature. This is embedded in the context of a broader study on single-value activation energies in both Si and SiC-based MOSFETs. These single-value activation energies have been widely employed by scientists to discuss the underlying physics of BTI and model its temperature dependence. However, they can at best be an approximation and have to be used carefully. Among other things, analytic approximations for their dependencies on measurement parameters are presented. Afterwards, the reproducibility of parameter measurements is investigated with regard to the impact of the recoverable component on transfer characteristics and  $V_{th}$  measurements.

As discussed in Section 1.4, SiC MOSFETs are primarily used in applications where they are continuously switched between their conductive and non-conductive state at high frequencies up to hundreds of kilohertz. This is precisely the operating mode where the advantages of these devices discussed in Section 1.1 come into play. However, as presented over the course of this work, this operation mode triggers physical processes at the SiC/SiO<sub>2</sub> interface that have never been observed in such a fashion in Si-based devices. First, the switching of the gate terminal, while keeping drain and source terminals grounded, leads to a significant drift of  $V_{th}$  that by far exceeds the drift observed in DC experiments. This mechanism has recently been termed gate switching instability (GSI) and is investigated in the course of this work with the goal to reveal the underlying physical processes that lead to this increased  $V_{th}$  drift. The results were then used to deduce a model that is consistent with all experimental findings.

Besides GSI, there is another phenomenon related to the switching of the gate terminal, while keeping drain and source grounded. In fact, this switching leads to emission of light, or rather photons, from the SiC/SiO<sub>2</sub> interface. These photons must be created by defect-assisted electron-hole recombination and must therefore convey precise information on the involved interface



defects. In the course of this work, the experimental methodology to analyze these photons created in fully-processed SiC power MOSFETs is developed and presented. This includes an approach to measure the light emission from single gate-source voltage transitions and link it to transient shifts in  $V_{th}$ . Besides that, optical spectroscopy and time-gated optical spectroscopy are used to analyze the energy spectrum of these photons, which allows a comparison between experiment and results from ab-initio calculations based on density functional theory (DFT).

Chapter 2 starts with an introduction to the physics of charge trapping and detrapping. This includes non-radiative transitions, following Shockley-Read-Hall (SRH) theory, NMP theory, and REDRs, but also radiative transitions which lead to the emission of photons. Besides that, the competition between non-radiative and radiative transitions is discussed.

Afterwards, Chapter 3 presents the experimental methods used to investigate the trapping and detrapping kinetics at the semiconductor-insulator interface. This includes conventional electrical characterization techniques, such as the transfer characteristic and the impedance measurement, whereby the latter yields the well-known CV and conductance-voltage (GV) characteristics. But also more advanced measurement techniques, such as ultra-fast  $V_{th}$  measurements and the charge pumping technique are presented. Finally, the electrical characterization techniques are complemented by the optical approaches, including the measurement of photon emission by single  $V_{GS}$ -transitions, optical spectroscopy, and time-gated optical spectroscopy. Also a short outline of photon emission microscopy is provided.

Chapter 4 will then present the measurements, results, explanations, and physical models obtained during the course of this work. This starts with the single-value, apparent activation energies and the recoverable component and its impact on device parameter measurements. The most important chapters are about the novel degradation mechanism GSI, followed by the results obtained by studying the light emission under gate switching.

Finally, Chapter 5 provides a summary of all results and gives an outlook on possible future research directions.

Die approbierte gedruckte Originalversion dieser Dissertation ist an der TU Wien Bibliothek verfügbar.  
The approved original version of this doctoral thesis is available in print at TU Wien Bibliothek.



# The Physics of Charge Trapping in Defects and Defect-Assisted Recombination

This chapter introduces the physics of radiative and non-radiative trapping, detrapping, and recombination processes that can occur at the semiconductor-insulator interface of a metal-oxide-semiconductor field-effect transistor (MOSFET). First, the non-radiative transitions in the framework of Shockley-Read-Hall (SRH) theory and non-radiative multiphonon (NMP) theory are introduced. Besides these two commonly-known theories in the context of bias temperature instability (BTI), the mechanism of recombination-enhanced defect reactions (REDRs) is presented. It is known from bipolar degradation as recombination-enhanced defect glide (REDG) (see Section 1.6.2), but even more important, it turned out in the course of this work that REDRs might play an important role in the context of the recently discovered gate switching instability (GSI). Finally, the physics of radiative-transitions featuring the emission of photons is introduced.

## 2.1 Non-Radiative Transitions

In the context of BTI and trapping and detrapping of charge carriers at the semiconductor-insulator interface, all processes have always been considered to be non-radiative, meaning that no processes that involve the emission or absorption of a photon are involved [140]. In this section, the two prevalent theories for non-radiative charge transitions, the SRH theory and the NMP theory, are presented. Finally, the mechanism of REDRs is outlined.

### 2.1.1 Shockley-Read-Hall Theory

As pointed out in the previous section, the SRH theory was originally introduced to describe defect-assisted electron-hole recombination in bulk semiconductors [160] and explain its temperature-dependent impact on the carrier lifetime [161]. The recombination process was described by rate equations of trapping and detrapping events of charge carriers, which is illustrated in Fig. 2.1a. Electrons could be captured from the conduction band and be emitted back. The same behavior is assumed for capture and emission of holes in interaction with the valence band. SRH theory proposes that the capture processes occur with a probability  $c_{n/p} = v_{th}\sigma$  (for an empty trap and an occupied band state) with the mean thermal velocity

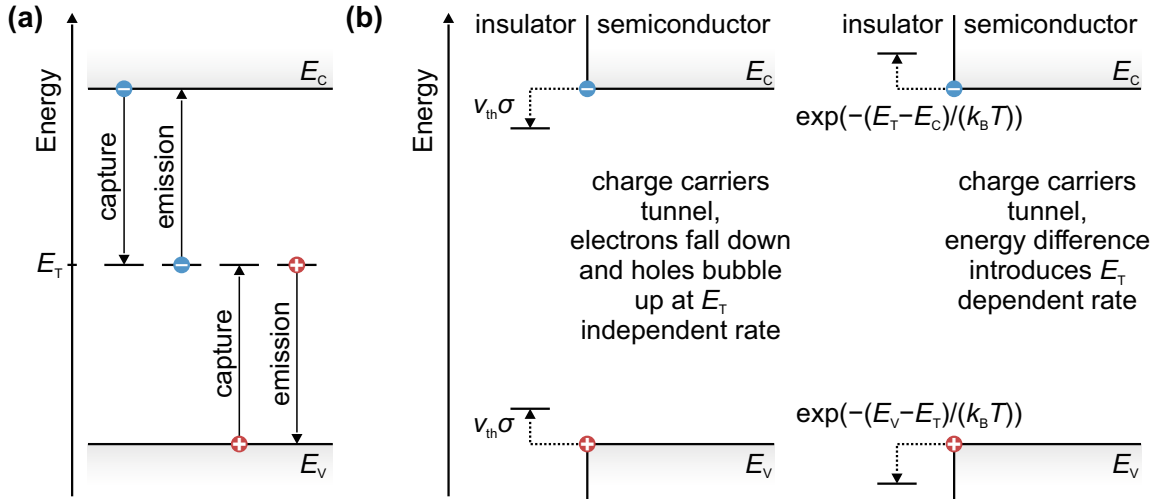


**Figure 2.1.** (a) Illustration of the trapping processes described by the original SRH model [160]. (b) Illustration of trapping processes described by the adapted SRH model for BTI.

$v_{th} = \sqrt{(8k_B T) / (\pi m)}$  given by the Maxwell–Boltzmann distribution [87] and a cross section  $\sigma$ . In contrast to the capture process, during the emission process, a charge carrier must overcome the energy difference between the trap level  $E_T$  and either the conduction band or valence band states, respectively. Neglecting in a crude approximation the occupancy of the states in the valence and conduction bands, the emission probabilities of electrons and holes are simply given by  $e_n^{SRH} = v_{th}\sigma \exp(-(E_C - E_T)/(k_B T))$  and  $e_p^{SRH} = v_{th}\sigma \exp(-(E_T - E_V)/(k_B T))$ , respectively [160]. Here,  $E_C$  and  $E_V$  are the conduction and valence band edges, respectively. In other words, electrons fall down and holes bubble up in energy at a certain capture rate, whereas they have to overcome an energy barrier to get back to the bands again.

The SRH model has been adapted in the past to describe the trapping and detrapping kinetics occurring in pn junctions [162], in random-telegraph noise (RTN), and BTI at the semiconductor-insulator interface [163], [164]. For BTI, the model was essentially extended by a tunneling factor to account for defects located at a certain distance from the channel in the insulator. Based on a few simplifications, the basic behavior of the SRH model for BTI can be obtained [140]. For simplicity, the validity of Boltzmann statistics is assumed, where the hole concentration in the valence band  $p$  and the electron concentration in the conduction band  $n$  follow

$$p = N_V \exp\left(-\frac{E_F - E_V}{k_B T}\right) \quad (2.1)$$

$$n = N_C \exp\left(-\frac{E_C - E_F}{k_B T}\right) \quad (2.2)$$

with  $N_C$  and  $N_V$  being the effective densities of states in the conduction and valence band, respectively. Hereby,  $E_F$  is the Fermi level. To account for the charge transfer into a defect state located at a distance  $x$  away from the interface, a tunneling factor based on the Wentzel-Kramers-Brillouin (WKB) approximation

$$\theta = \exp\left(-\frac{4\sqrt{2m}}{3\hbar qF} ((q\phi - E)^{3/2} - (q\phi_0 - E)^{3/2})\right) \approx \exp\left(-\frac{x}{x_0}\right), \quad x_0 = \frac{\hbar}{\sqrt{2m\phi}} \quad (2.3)$$

was used which can be condensed down to an exponential factor by the use of a Taylor approximation. Hereby,  $m$  is the tunneling mass,  $F$  is the electric field,  $\phi$  the energy barrier at the interface and  $\phi_0$  the barrier at the location of the defect. For hole traps located above the valence band edge the rates follow

$$k_c^{VB} = p v_{th} \sigma_0 \theta \quad \text{and} \quad (2.4)$$

$$k_e^{VB} = N_V v_{th} \sigma_0 \theta \exp\left(-\frac{E_T - E_V}{k_B T}\right) \quad (2.5)$$

whereas hole traps underneath the valence band edge follow

$$k_c^{VB} = p v_{th} \sigma_0 \theta \exp\left(-\frac{E_V - E_T}{k_B T}\right) \quad \text{and} \quad (2.6)$$

$$k_e^{VB} = N_V v_{th} \sigma_0 \theta. \quad (2.7)$$

In these equations,  $\sigma_0$  is the capture cross section. For electron traps, the rates follow

$$k_c^{CB} = n v_{th} \sigma_0 \theta \quad \text{and} \quad (2.8)$$

$$k_e^{CB} = N_C v_{th} \sigma_0 \theta \exp\left(-\frac{E_C - E_T}{k_B T}\right) \quad (2.9)$$

for those located underneath the conduction band edge and

$$k_c^{CB} = n v_{th} \sigma_0 \theta \exp\left(-\frac{E_T - E_C}{k_B T}\right) \quad \text{and} \quad (2.10)$$

$$k_e^{CB} = N_C v_{th} \sigma_0 \theta \quad (2.11)$$

for those located above the conduction band edge. Again, the essential behavior of the SRH model is that electrons fall down and holes bubble up.

The widely distributed time constants faced in BTI experiments have been explained by the spatial distribution of the defects within the insulator [165]–[167]. However, this could be disproved, because scaled MOSFETs with a very thin gate oxide (1.4 nm) can exhibit time constants that are well above the tunneling limit predicted by the tunneling-based SRH model [168], [169]. Nevertheless, the SRH model partly works for some experiments, which was recently investigated by Ruch *et al.* [170].

### 2.1.2 Non-Radiative Multiphonon Theory

Tunneling of charge carriers alone, as used in the SRH theory, cannot explain the widely-distributed time constants observed in BTI experiments [168]. This could later be resolved by NMP theory, which incorporates the potential energy associated with the reconfiguration of a defect within its environment or host lattice upon capture and emission of a charge carrier [171]–[173]. Similar to SRH theory, NMP theory was initially used to describe trapping and recombination of charge carriers in bulk crystals. In physical chemistry, the mechanism is well-known in the context of charge transfer reactions [174], [175] and was first postulated by Marcus [176], who received the Nobel Prize for it in 1992 [177]. This theory was first used to describe RTN associated with trapping of charge carriers in MOSFETs by Kirton and Uren [178] and later ex-

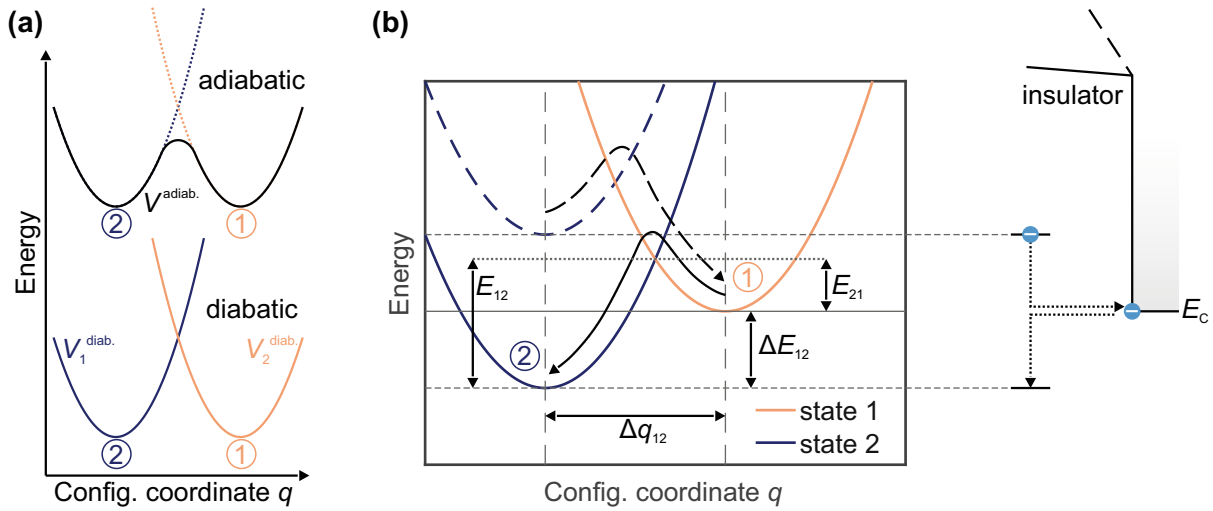


**Figure 2.2.** (a) Configuration coordinate diagram comparing the adiabatic (upper) and the diabatic (lower) potentials. (b) Configuration coordinate diagram of an electron trap interacting with the conduction band. State 1 shows the case of the electron being in the conduction band and case 2 is the electron trapped in the defect. The dashed potential indicates the case of a more negative bias compared to the solid potential. While for the solid potential trapping dominates over detrapping, for the dashed potential this is the other way around.

tended to describe most reliability phenomena, including BTI, RTN, and trap-assisted tunneling (TAT) [140], [143], [179].

In order to describe the quantum mechanical process of trapping or detrapping events in a MOSFET in the framework of NMP theory, it requires a series of simplifications of the full Schrödinger equation that comprises all degrees of freedoms and interactions between electrons and the nuclei of the system [143]. First, the well-known Born-Oppenheimer approximation (or adiabatic approximation) is employed [180], [181], assuming that the electrons move considerably faster than the nuclei, which allows to factorize the wave function and use the nuclear coordinates as a parameter for the electronic part. The resulting electronic Schrödinger equation features a Hamiltonian  $H_{el}$  and a corresponding basis  $\psi_k(\{X_q\})$ , whereby  $\{X_q\}$  is the set of nuclear coordinates. The Hamiltonian has a potential that is referred to as the adiabatic potential energy surface (PES) [143]. Effectively, this PES depends on  $3N$  degrees of freedom and is thus a  $3N$ -dimensional hypersurface. A minimum-energy reaction path on this multidimensional PES can be determined between two local minima (two states) connected by a saddle point [174], [182]. In a first-order approximation, the reaction can then be described by an effective reaction coordinate  $q$  that parametrizes the minimum-energy reaction path [174].

The transition rate along the minimum-energy reaction path can be described by

$$k = k_0 \exp\left(-\frac{E^\ddagger}{k_B T}\right) \quad (2.12)$$

where  $k_0$  is a frequency factor and  $E^\ddagger$  is the energy along the minimum-energy reaction path that needs to be overcome. Consequently, this transition can be illustrated in a two-dimensional configuration coordinate diagram. This is the adiabatic case illustrated in Fig. 2.2a.

In contrast to the adiabatic approximation, which describes a rather gradual charge transfer process on short distances of strongly coupled systems, the diabatic framework is more suited for weakly coupled systems featuring a sudden electron transfer [183]. Here, the two states have

distinct potentials with a diabatic crossing point. If the initial state  $\psi_i$  and the final state  $\psi_f$  were orthogonal ( $S_{if} = \langle \psi_i | \psi_f \rangle = 0$ ), the transition is easily described by a transfer integral

$$H_{if} = \langle \psi_i | H_{el} | \psi_f \rangle. \quad (2.13)$$

The higher the transfer integral  $H_{if}$ , the higher in energy is the avoided crossing. The associated diabatic potentials of the two states are obtained by

$$V_s(\{X_q\}) = \langle \psi_s(\{X_q\}) | H_{el} | \psi_s(\{X_q\}) \rangle, \quad s \in \{i, f\} \quad (2.14)$$

and shown in Fig. 2.2a, that compares them to the adiabatic potential. The diabatic approach is more suitable for the case of trapping of charge carriers at the semiconductor-insulator interface of a MOSFET and consequently used to model BTI [143]. In its simplest form, the diabatic potential can be approximated by a harmonic potential. In the classical limit and the case where photon absorption and emission are not present, the non-radiative transition rates for an electron trap interacting with the conduction band can be written as

$$k_{12}^{CB} = n v_{th} \sigma_0 \theta \exp\left(-\frac{E_{12}}{k_B T}\right) \quad \text{and} \quad (2.15)$$

$$k_{21}^{CB} = N_C v_{th} \sigma_0 \theta \exp\left(-\frac{E_{21}}{k_B T}\right), \quad (2.16)$$

where  $E_{12}$  and  $E_{21}$  are the respective thermal activation energies [140]. Hereby, 12 refers to the process of transfer from state 1 to state 2, whereby state 1 refers to the case of an electron in the conduction band and state 2 to the case of a trap with a captured electron. These states and the associated transitions are illustrated in Fig. 2.2b. In contrast to SRH theory, also the emission process is now linked to an energy barrier that needs to be overcome (compare to Equations 2.4 and 2.5). The harmonic approximations of the diabatic potentials are simple parabolas following

$$V_i(q) = \frac{1}{2} M \omega_i^2 (q - q_i)^2 + E_i, \quad i \in \{1, 2\} \quad (2.17)$$

with effective mass  $M$  [140], [184], vibrational frequencies  $\omega_i$  and positions of the minima at  $(q_i, E_i)$ . For linear electron-phonon coupling ( $R = \omega_1 / \omega_2 = 1$ ,  $\omega_1 = \omega_2 = \omega$ ), the activation energies are given by

$$E_{12} = \frac{(\epsilon_R - \Delta E_{21})^2}{4\epsilon_R} \quad \text{and} \quad E_{21} = \frac{(\epsilon_R + \Delta E_{21})^2}{4\epsilon_R} \quad (2.18)$$

with the relaxation energy  $\epsilon_R = (1/2) M \omega^2 \Delta q_{12}^2 = S \hbar \omega$  [140]. Here,  $S$  is the Huang-Rhys factor (HR-factor) and  $\Delta q_{12} = q_1 - q_2$ .

There are two important cases that need to be highlighted. These are the weak ( $\epsilon_R \ll \Delta E_{12}$ ) and strong electron-phonon ( $\epsilon_R \gg \Delta E_{12}$ ) coupling regimes, where  $\Delta E_{12} = E_1 - E_2$ . These two regimes allow for further simplifications [140]. In the weak-coupling regime, the activation energies roughly depend quadratically on the electric field, whereas in the strong coupling regime, the dependence is linear [140]. This originates from the relation

$$\Delta E_{12}(F) = E_1(F=0) - E_2(F=0) - qxF, \quad (2.19)$$

where  $x$  is the distance between the semiconductor-insulator interface and the location of the trap in the insulator and  $F$  is the electric field.

The above considerations allow to describe the trapping and detrapping processes and provide the involved transition rates. For a simple two-state defect, the stochastic transitions in between the defect states 1 and 2 are described as a Markov process [140], [185], [186], yielding the Master equation

$$\frac{dp_1}{dt}(t) = -k_{12}p_1(t) + k_{21}p_2(t) \quad (2.20)$$

$$\frac{dp_2}{dt}(t) = k_{12}p_1(t) - k_{21}p_2(t) \quad (2.21)$$

for the probabilities  $p_i$  that state  $i$  is occupied. The capture and emission time constants  $\tau_c$  and  $\tau_e$  are the reciprocal values of the rates  $k_{12}$  and  $k_{21}$ , respectively.

### 2.1.3 Recombination Enhanced Defect Reactions

Non-radiative trapping and detrapping of charge carriers in defects, as described in the previous section, is related to overcoming the activation energy for capture and emission by a multiphonon process. If these activation energies are sufficiently large compared to  $k_B T$ , the process becomes unlikely. However, there is a possibility to overcome even very large activation energies by an REDR [187]–[191]. Experimentally, this mechanism was first observed in pn-junctions of gallium arsenide as an enhancement of the annealing rate of electron irradiation induced electron traps upon minority carrier injection [192].

The cause of REDRs is non-radiative recombination of electrons and holes via a defect state [187]. Hereby, a defect is considered as a molecule within an host environment. Such a system features local vibrational modes (LVMs) (see Section 1.3.5), that are local modes that can have a higher energy than the collective lattice vibrations (phonons). The energy that is released non-radiatively upon a recombination event will always dissipate into delocalized phonons, but initially, it can be cast into promoting a defect reaction via the LVMs. LVMs are particularly likely to function as energy accepting modes, because they usually exhibit strong electron-phonon coupling upon a recombination event. The reaction is associated with bringing a certain amount of energy into a critical reaction coordinate, which must be a combination of these LVMs. In general, the more energy is released via the recombination event, the more likely it is that a sufficient amount of energy is cast into the critical reaction coordinate, such that the reaction can occur.

This was first described mathematically by Weeks *et al.* on the basis of the Rice-Ramsperger-Kassel theory [187], [193], [194]. They considered a defect with  $S$  degrees of freedom, an apparent activation energy for the reaction  $E_A \gg (S - 1)k_B T$  (= average thermal energy of the defect), and a recombination event supplying an energy  $E_P$ . If no recombination was involved, the multiphonon transition would follow the usual Arrhenius law

$$k^{\text{NMP}} = k_0 \exp\left(-\frac{E_A}{k_B T}\right) \quad (2.22)$$

with a prefactor  $k_0$ .

In contrast, if recombination was involved, the process can be considered for certain limiting cases, that describe the essential physics. If  $E_P \leq E_A$ , then the case occurs where the apparent



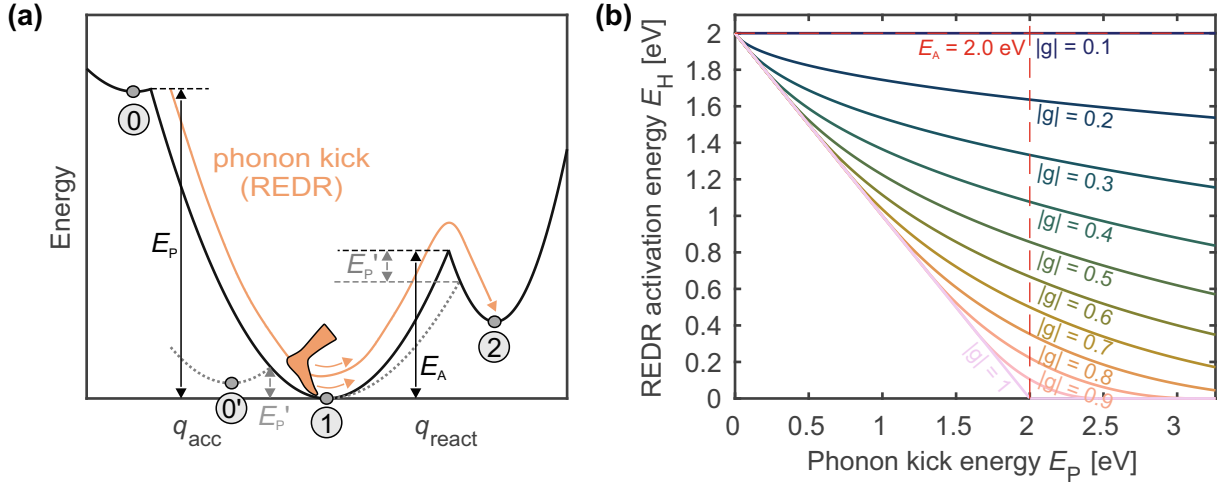


**Figure 2.3.** (a) Configuration coordinate diagram illustrating the principle of REDRs. An energy  $E_P$  is released via a non-radiative recombination event. Here,  $E_P > E_A/g^2$  is valid, which means the released energy from the transition from state 0 to state 1 can be channeled into the reaction that brings the defect from state 0 to state 2. If  $E_A \gg k_B T$ , the transition would be extremely unlikely under thermal equilibrium. The primed state  $0'$  represents a state that leads to a lower energy  $E'_P$ , which is only able to reduce  $E_A$  by  $E'_P$  (if  $E'_P < g^2 E_A$ ). Redrawn from [MFC2]. (b) Effective REDR activation energy  $E_H$  versus the phonon kick energy  $E_P$  for different couplings  $g^2$  and an exemplary activation energy  $E_A = 2$  eV. The higher the coupling  $g^2$  the more  $E_A$  is reduced and can even be pushed down to zero.

activation energy is effectively lowered by the energy supplied by the recombination event. If  $E_A - E_P \gg (S - 1)k_B T$ , the enhanced transition rate is approximately

$$k^{\text{REDR}} \approx R \frac{k_0}{k_{-1}(\bar{E})} \left( \frac{E_A - E_P}{E_A} \right)^{S-1} \exp\left(-\frac{E_A - E_P}{k_B T}\right) \quad (2.23)$$

whereas if  $E_A - E_P \ll (S - 1)k_B T$ , it can be written as

$$k^{\text{REDR}} \approx R \frac{k_0}{k_{-1}(\bar{E})} \frac{(2S - 2)!}{(S - 1)!} \left( \frac{E_A}{k_B T} \right)^{1-S} \exp\left(-\frac{E_A - E_P}{k_B T}\right). \quad (2.24)$$

Hereby,  $k_{-1}(\bar{E})$  is the average rate of energy exchange between the defect molecule and the host environment and  $R$  is the recombination rate.

Particularly for wide-bandgap semiconductors, where  $E_P$  can be high, the case  $E_P > E_A$  becomes important. If  $E_P - E_A \ll (S - 1)k_B T$ , the transition rate is

$$k^{\text{REDR}} \approx R \frac{k_0}{k_{-1}(\bar{E})} \frac{(2S - 2)!}{(S - 1)!} \left( \frac{E_A}{k_B T} \right)^{1-S} \quad (2.25)$$

whereas for  $E_P - E_A \gg (S - 1)k_B T$ , the rate becomes

$$k^{\text{REDR}} \approx R \frac{k_0}{k_{-1}(\bar{E})} \left( \frac{E_P - E_A}{E_P} \right)^{S-1}. \quad (2.26)$$

In the above two cases, the exponential Arrhenius term vanishes and the reaction of the defect can become athermal (independent of temperature). In this context, an REDR can be imagined as a “phonon kick” – the recombination event kicks the defect reaction over its associated activation energy barrier. This is illustrated in Fig. 2.3a.

Overall, it is important to note that the enhanced rate is proportional to the recombination that occurs via the defect state and that it can lower the apparent activation energy of the reaction by the released recombination energy even to the point of making the reaction athermal. Consequently, this mechanism allows a defect to undergo a reaction upon recombination that it would hardly be able to undergo without the presence of recombination.

The above theory was refined later by Sumi [190], who included an efficiency  $g^2$  with which the energy from the recombination event is channeled to the critical reaction coordinate. Here, the quantum yield follows

$$QE_{\text{REDR}} \propto \exp\left(-\frac{E_H}{k_B T}\right) \quad (2.27)$$

with an activation energy

$$E_H = \begin{cases} E_A - E_P, & \text{if } E_P < g^2 E_A \\ \frac{(\sqrt{E_A} - |g|\sqrt{E_P})^2}{1 - g^2}, & \text{if } g^2 E_A < E_P < E_A/g^2 \\ 0, & \text{if } E_P > E_A/g^2 \end{cases} \quad (2.28)$$

that depends on the involved energies and the coupling  $|g| \leq 1$ . The activation energy  $E_H$  is illustrated in Fig. 2.3b as a function of  $E_P$  for different couplings  $g^2$ . For  $|g| = 1$ , this description equals the one of Weeks *et al.*

## 2.2 Radiative Transitions

In the previous sections, radiative transitions involving the absorption or emission of photons have been assumed to be absent. In this section, the energy spectrum of photons created by a transition between two states with their potential energy curves (PECs) is calculated. Again, it is assumed that the multidimensional PES of a state can be approximated by a one-dimensional PEC. The two electronic states are named 1 (ground state) and state 2 (excited state). Each electronic state has its vibrational eigenstates, indicated by the quantum numbers  $n$  (state 1) and  $m$  (state 2). According to the Franck-Condon principle, the absorption and emission of a photon occurs much faster than the movement of the atomic system, which is why radiative transitions in a configuration coordinate diagram occur vertically [195]–[197]. In the context of this work, it is appropriate to assume that radiative transitions that involve the emission of a photon exclusively occur from the ground state ( $m = 0$ ) of state 2. This is justified by the high energy of the investigated LVM, which is above the highest phonon mode. It makes the occupation probability of the state  $m = 1$  negligible (see Section 1.3.5). The two PECs with their vibrational eigenstates are shown in Fig. 2.4a. The potentials of states 1 and 2 are separated by  $\Delta q$  and  $\Delta E_{21}$ .

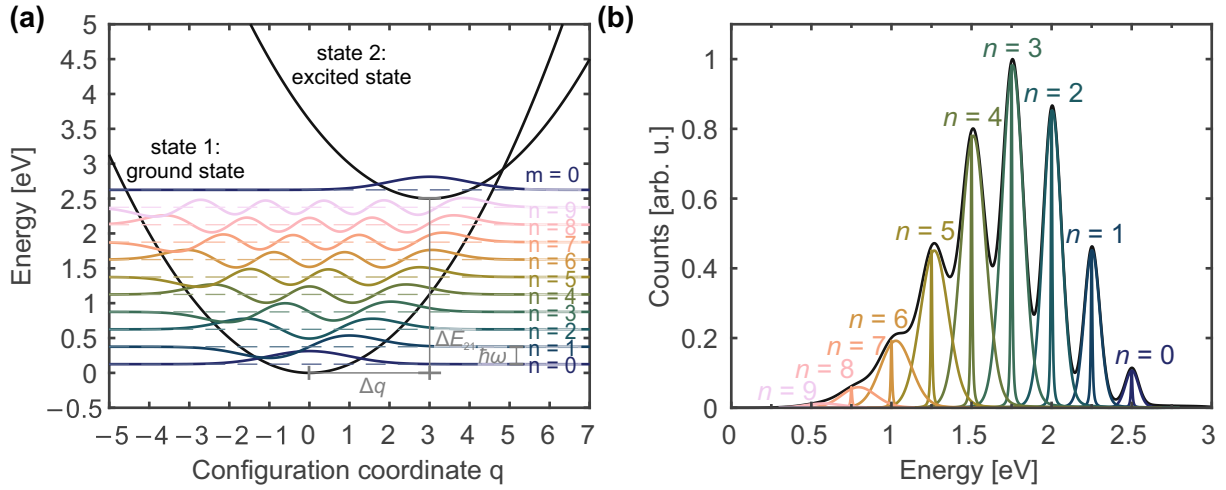


**Figure 2.4.** (a) Configuration coordinate diagram showing the two-dimensional harmonic approximations of the multidimensional PESs. For the ground state 1, the ten lowest eigenstates ( $n \in \{1, 2, \dots, 9\}$ ) are shown together with their eigenvalues (dashed horizontal lines) in an illustrative manner. For the excited state 2, only the ground state ( $m = 0$ ) is shown with its eigenvalue and eigenstate because the system is initially assumed to be in the lowest state possible. (b) The emission spectrum calculated according to Equation 2.43 with the parameters of the PECs from (a). The transitions occur from the vibrational ground state of the electronic state 2 to the ten lowest vibrational states of the electronic state 1, indicated by the quantum number  $n$ .

The transition rate  $k_{mn}$  from the vibrational level  $m$  of electronic state 2 to the vibrational level  $n$  of state 1 is given by Fermi's Golden rule [198], [199]

$$k_{mn} = \frac{2\pi}{\hbar} |\langle \Psi_m^2 | \hat{\mu} | \Psi_n^1 \rangle|^2 \delta(E_m^2 - E_n^1 - \hbar\omega_{\text{ph}}) \quad (2.29)$$

which can be deduced from time-dependent perturbation theory [200]. Hereby,  $\hat{\mu}$  is the perturbation operator, which in the case of photon emission is the dipole operator.

Using the Born-Oppenheimer approximation [180], [181], [201], the total wave function can be approximated by the product of the electronic wave function  $\psi$ , the rotational wave function  $\Phi$ , and the vibrational wave function  $\phi$  as per

$$\Psi_n^i = \underbrace{\psi^i}_{\text{electronic}} \times \underbrace{\Phi^i \phi_n^i}_{\text{nuclear}}. \quad (2.30)$$

In a next step, the dipole operator is assumed to be independent of the nuclear coordinates, which allows to consider only the vibrational component. This is often referred to as the Franck-Condon factor [201]. Additionally, a factor of  $\omega_{\text{ph}}^3$  enters the rate equation [202].

$$k_{mn} \propto \omega_{\text{ph}}^3 |\langle \phi_m^2 | \phi_n^1 \rangle|^2 \delta(E_m^2 - E_n^1 - \hbar\omega_{\text{ph}}) \quad (2.31)$$

The PESs of both states 1 and 2 are approximated by harmonic potentials leading to the simple and well-known Schrödinger equation of the harmonic oscillator

$$-\frac{\hbar^2}{2m_i} \frac{d^2}{dx^2} \phi_n^i(x) + \frac{1}{2} m_i \omega_i^2 x^2 \phi_n^i(x) = E_n^i \phi_n^i(x) \quad (2.32)$$

that needs to be solved for both the eigenvalues  $E_n^i$  and eigenstates  $\phi_n^i(x)$ . Anharmonicity in the underlying multidimensional PESs would make the harmonic approximation inappropriate [97], but could be implemented by replacing the harmonic potential with a Morse potential [90], [203]. However, in the course of this work, the harmonic potential turned out to be sufficient to describe the experimental data, which is why it is further used in the following.

Consequently, the problem can be simplified by conducting a coordinate transformation from the spatial coordinate  $x$  to the configuration coordinate  $q$ , as per

$$x \rightarrow q = \sqrt{\frac{m_i \omega_i}{\hbar}} x. \quad (2.33)$$

The Schrödinger equation changes accordingly to

$$-\frac{1}{2} \hbar \omega_i \frac{d^2}{dq^2} \phi_n^i(q) + \frac{1}{2} \hbar \omega_i q^2 \phi_n^i(q) = E_n^i \phi_n^i(q) \quad (2.34)$$

with a potential

$$V(q) = \frac{1}{2} \hbar \omega_i q^2. \quad (2.35)$$

As can be recognized from Equation 2.35, the curvature of the PECs equals half of the spacing between the energy eigenvalues. The solutions of the Schrödinger equation, in the form of its vibrational eigenstates, are  $\phi_n^i$  of electronic state  $i \in \{1, 2\}$ . The eigenvalues and eigenstates are numbered by the index  $n \in \{0, 1, 2, 3, \dots\}$ , whereby the eigenstates are given by

$$\phi_n^i(q) = \frac{1}{(2^n n!)} \left(\frac{1}{\pi}\right)^{\frac{1}{4}} \exp\left(-\frac{q^2}{2}\right) H_n(q) \quad (2.36)$$

with  $H_n$  being the  $n^{\text{th}}$  Hermite polynomial [204]. The corresponding eigenvalues  $E_n^i$  are equally spaced with a spacing of  $\hbar \omega_i$  and are given by

$$E_n^i = \hbar \omega_i \left(\frac{1}{2} + n\right). \quad (2.37)$$

As the goal of this section is to calculate the emission spectrum obtained by radiative transitions from state 2 to state 1, the lineshape of the emission peaks has to be taken into account. First, the lifetime-limited lineshape follows a Lorentzian peak [205], as per

$$f(E_{\text{ph}}, E_{mn}, \Delta E_L) = \frac{\Delta E_L / (2\pi)}{(E_{\text{ph}} - E_{mn})^2 + (\Delta E_L / 2)^2}. \quad (2.38)$$

Here,  $E_{\text{ph}}$  is the energy of the emitted photon,  $E_{mn} = E_m^2 - E_n^1$ , and  $\Delta E_L$  is the full width at half maximum (FWHM) of the Lorentzian. This lifetime-limited lineshape is subsequently broadened by other effects. First, it is assumed that  $\omega_1$ ,  $\omega_2$  and  $\Delta E_{21}$  are Gaussian distributed. These broadening effects can be justified by variations of the host environment around the defects [142], [206]. Due to the commutativity and associativity of the convolution operation and due to the fact that a convolution of two Gaussian distributions results in a broader Gaussian distribution, the fully broadened lineshape can be calculated by a convolution of a Gaussian

distribution with the lifetime-limited Lorentzian as per

$$L(E_{\text{ph}}, E_{mn}, \sigma_{mn}, \Delta E_L) = \int_{-\infty}^{\infty} G(E', \sigma_{mn}) f(E_{\text{ph}} - E', E_{mn}, \Delta E_L) dE'. \quad (2.39)$$

The width  $\sigma_{mn}$  of the Gaussian is given by

$$\sigma_{mn} = \sqrt{\sigma_1(n)^2 + \sigma_2(m)^2 + \sigma_{\Delta E}^2} \quad (2.40)$$

with the used standard deviations

$$\sigma_i(n) = \sigma_i \left( \frac{1}{2} + n \right) \quad (2.41)$$

that are functions of the vibrational quantum number  $n$ . This dependence on the quantum number is based on the consideration that

$$E_{mn} = E_m^2 - E_n^1 + \Delta E_{21} = \hbar\omega_2 \left( \frac{1}{2} + m \right) - \hbar\omega_1 \left( \frac{1}{2} + n \right) + \Delta E_{21} \quad (2.42)$$

depends on the quantum numbers.

In a last step, a convolution operation leads to the replacement of the Dirac delta distribution in Equation 2.31 by the lineshape function  $L$  calculated above and all considered transitions are summed up, leading to the emission spectrum

$$I(E_{\text{ph}}) \propto \sum_{m,n} \omega_{\text{ph}}^3 |\langle \phi_m^2 | \phi_n^1 \rangle|^2 L(E_{\text{ph}}, E_{mn}, \sigma_{mn}). \quad (2.43)$$

An exemplary emission spectrum for the PECs shown in Fig. 2.4a is presented in Fig. 2.4b. The used parameters were  $\Delta E_{21} = 2.5$  eV,  $\hbar\omega_1 = \hbar\omega_2 = 250$  meV,  $\sigma_1 = \sigma_2 = 12$  meV,  $\Delta q = 3$ ,  $\sigma_{\Delta E} = 30$  meV, and  $\Delta E_L = 10$  meV.

Last but not least, an important and commonly used parameter is the HR-factor  $S$ , that is defined as the number of vibrational quanta that are involved in the radiative transition [207], [208]. In the coordinate  $q$  used here (see Equation 2.33), it is given by

$$S = \frac{1}{2} (\Delta q)^2 \quad (2.44)$$

and can serve for a comparison between the experimental values obtained in the course of this work and values of defects calculated by density functional theory (DFT).

## 2.3 Competition Between Radiative and Non-Radiative Transitions

In many cases, the previously discussed radiative transitions compete with alternative non-radiative NMP transitions. Due to the thermal activation of the non-radiative transition, increasing the temperature leads to an increased share of the non-radiative path with respect to the radiative path. This was described within the Seitz-Mott mechanism [209]–[212] and is often referred to as thermal quenching. As in Equation 2.12, the non-radiative path follows  $k_{\text{NMP}} = k_0 \exp(-E_A / (k_B T))$  with a frequency prefactor  $k_0$  and an activation energy  $E_A$ . Conse-

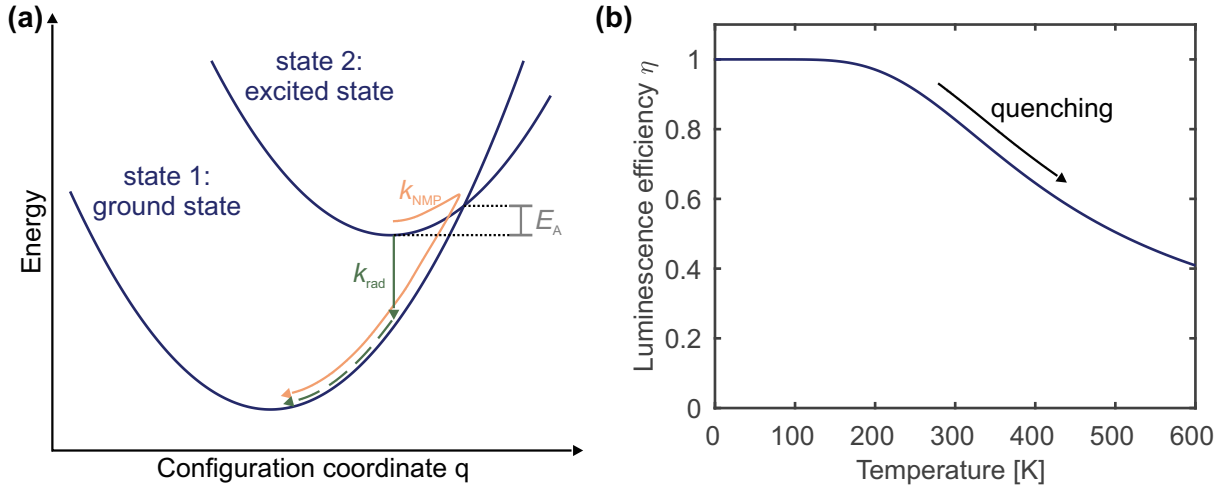


**Figure 2.5.** (a) Configuration coordinate diagram illustrating the competition between a radiative and a non-radiative transition from the excited state 2 to the ground state 1. The non-radiative path is associated with an activation energy  $E_A$ . (b) Luminescence efficiency  $\eta$  as a function of temperature with exemplary values of  $E_A = 100 \text{ meV}$ ,  $k_{\text{rad}} = 10^{-14} \text{ s}^{-1}$ , and  $k_{\text{rad}} = 10^{-13} \text{ s}^{-1}$ . With increasing temperature, the share of non-radiative transitions increases which leads to decreasing luminescence (quenching).

quently, the branching ratio is given by

$$\eta(T) = \frac{k_{\text{rad}}}{k_{\text{rad}} + k_{\text{NMP}}} = \frac{1}{1 + K \exp\left(-\frac{E_A}{k_B T}\right)} \quad (2.45)$$

with  $K = k_0/k_{\text{rad}}$ .

This mechanism is illustrated in a configuration coordinate diagram in Fig. 2.5a and the branching ratio, or rather luminescence efficiency, is shown in Fig. 2.5b using exemplary values for  $k_0$ ,  $E_A$ , and  $k_{\text{rad}}$ . Unfortunately, many systems are more complicated and involve more than those two transitions that might be either radiative or non-radiative. Each case has to be considered carefully and might involve several non-radiative paths with their respective activation energies. Furthermore, it is to note that the presented description does not involve tunnelling effects, which become increasingly important at lower temperatures [213].

# Optical and Electrical Measurement Methodology

In this chapter, the characterization and measurement techniques used in the course of this work are introduced. First, the conventional electrical characterization techniques, such as the measurement of the transfer characteristic or the measurement of the impedance are introduced. This is followed by the presentation of ultra-fast threshold voltage ( $V_{th}$ ) measurements and the charge pumping (CP) technique. After these electrical techniques, the optical measurements are introduced, comprising the measurement of photon emission originating from a single gate-source voltage ( $V_{GS}$ )-transition, optical spectroscopy, and time-gated optical spectroscopy.

## 3.1 Transfer Characteristic

Measuring the transfer characteristic is a common technique to evaluate the charge state of defects at the semiconductor-insulator interface [214]. Hereby, the drain-source current  $I_{DS}$  is measured as a function of the gate-source voltage  $V_{GS}$  for a small drain-source voltage  $V_{DS}$ . This is usually done in the linear regime, where  $V_{DS} \ll V_{GS} - V_{th}$ . Since silicon carbide (SiC) metal-oxide-semiconductor field-effect transistors (MOSFETs) are long-channel devices, in this regime,  $I_{DS}$  can be approximated by

$$I_{DS} = \frac{W}{L} \mu_n C_{ox} \left( V_{GS} - V_{th} - \frac{V_{DS}}{2} \right) V_{DS}, \quad (3.1)$$

whereby  $W$  is the width of the channel,  $L$  is the length of the channel,  $\mu_n$  is the mobility of the channel electrons, and  $C_{ox}$  is the oxide capacitance [215]. This leads to a typical method for the extraction of  $V_{th}$  from a measured transfer characteristic, which is the linear extrapolation to  $I_{DS} = 0$  [216]. However, for the later presented ultra-fast  $V_{th}$  measurement, a constant  $I_{DS}$  criterion is used [217], which allows to measure  $V_{th}$  with a low measurement delay and reproducible timing [218]. In contrast to a constant voltage criterion, the measured quantity does hardly change, which is why no adjustment of the measurement range is needed.

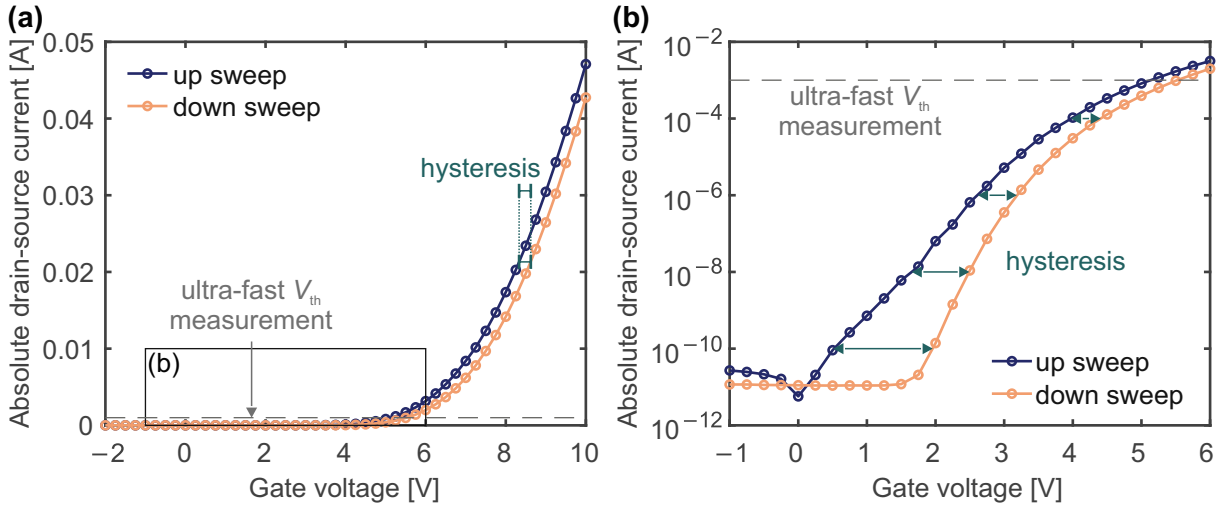


**Figure 3.1.** (a) A transfer curve of a SiC double-diffused MOSFET (DMOSFET) on a linear y-scale measured by slowly sweeping  $V_{GS}$  upwards from  $-15$  V to  $15$  V and back down at  $V_{DS} = 0.1$  V. The current  $I_{DS} = 1$  mA is marked, as it is the current where ultra-fast  $V_{th}$  measurements extract  $V_{th}$ . The characteristic hysteresis between the up and down sweeps is observed, which is typical for SiC MOSFETs. (b) The transfer curve on a logarithmic y-scale from the region (a) that is marked with a rectangle.

By calculating the first derivative of the transfer characteristic, which is referred to as transconductance ( $g_m$ ), it is possible to obtain the mobility of the channel electrons [216] via

$$g_m = \frac{\partial I_{DS}}{\partial V_{GS}} = \frac{W}{L} \mu_n C_{ox} V_{DS} \Leftrightarrow \mu_n = \frac{L}{WC_{ox} V_{DS}} g_m. \quad (3.2)$$

Furthermore, the transfer characteristic allows to obtain the on-state resistance ( $R_{on}$ ) of the MOSFET. By calculating  $R_{on}(V_{GS}, V_{DS}) = V_{DS}/I_{DS}$ ,  $R_{on}$  can be extracted at a typical on-state voltage for SiC power MOSFETs of  $15$  V,  $18$  V, or  $20$  V. It is important to notice that the measured  $R_{on}$  consists of several contributions [55], [219]. Neglecting contact resistances, for a power double-diffused MOSFET (DMOSFET), it follows that

$$R_{on} = R_{ch} + R_{JFET} + R_{epi} + R_{sub} \quad (3.3)$$

where  $R_{ch}$  is the channel resistance,  $R_{JFET}$  is the junction field-effect resistance,  $R_{epi}$  is the resistance of the epitaxial layer, and  $R_{sub}$  is the resistance of the substrate.

However, Equation 3.1 is only valid for an ideal MOSFET without any active charge traps at the semiconductor-insulator interface. In fact, SiC MOSFETs exhibit strong trapping and detrapping of charges at the interface, which heavily affects the measurement of the transfer characteristic [157]. In case it is measured by sweeping  $V_{GS}$  at a constant  $V_{DS}$ , the transfer characteristic is e.g. heavily affected by the voltage, at which the sweep starts, or by the timing of the sweep itself.

This occurs because a charge that is trapped at the semiconductor-insulator interface or in the oxide leads to a shift of the  $V_{GS}$  needed to reach a certain surface potential. Hence, this leads



to a threshold voltage shift ( $\Delta V_{th}$ ) as per

$$\Delta V_{th} = -\frac{qt_{ox}}{\epsilon_r \epsilon_0} \int_0^{t_{ox}} \left(1 - \frac{x}{t_{ox}}\right) \rho(x) dx, \quad (3.4)$$

where  $\epsilon_r$  is the relative permittivity of the insulator,  $\epsilon_0$  is the vacuum permittivity,  $t_{ox}$  is the thickness of the gate oxide, and  $\rho(x)$  is the distribution of charges in the gate oxide as a function of the the distance to the interface [220].  $\Delta V_{th}$  enters Equation 3.1 and thereby shifts the transfer characteristic horizontally. However, as the trapping and detrapping kinetics depend on time,  $V_{GS}$ , and temperature, the  $\Delta V_{th}$ , and hence the transfer characteristic also depends on these parameters. Basically, the entire history of the device affects  $V_{th}$  and hence the measured transfer characteristic. Modeling the transfer characteristic of a SiC MOSFET hence requires the implementation of charge trapping kinetics [159].

A  $\Delta V_{th}$  created by trapped charges also affects the  $R_{on}$  of the MOSFET. Substituting  $V_{th}$  in Equation 3.1 by  $V_{th,0} + \Delta V_{th}$  and considering the limiting case of  $V_{DS} \rightarrow 0$ , the channel resistance can be written as

$$R_{ch} = \frac{L}{\mu_n C_{ox} W (V_{GS,on} - V_{th,0} - \Delta V_{th})}, \quad (3.5)$$

which clearly relates the channel resistance to  $\Delta V_{th}$ . For a power device, this can be inserted into Equation 3.3 to obtain the impact of  $\Delta V_{th}$  on the total  $R_{on}$ .

## 3.2 Impedance Characterization

A powerful characterization technique for MOSFETs is the impedance method [221]–[223]. Its major advantage over the transfer curve is its ability to characterize the device also in accumulation, where it does not conduct current. Typically, the results of an impedance measurement are illustrated in terms of capacitance-voltage (CV) and conductance-voltage (GV) curves, which are just representations of the real and imaginary part of the measured complex small-signal impedance.

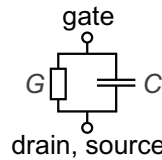


**Figure 3.2.** Parallel equivalent circuit representing the impedance between the gate terminal and the shortened drain and source terminals.

Impedance characterization is conducted using four-terminal sensing to measure the impedance  $Z$  between the gate terminal versus the shortened drain and source terminals. The high current terminal ( $H_C$ ) provides a direct current (DC) voltage modulated by a small alternating current (AC) voltage of a certain frequency. The resulting voltage is measured by the high potential ( $H_p$ ) terminal. At the low side, the low potential terminal ( $L_p$ ) is connected to a null detector creating an output that brings the low side via the low current terminal ( $L_C$ ) to virtual ground, thereby measuring the current flow through the device under test (DUT). In the case of SiC MOSFETs, it is sensible to sweep the DC voltage up and down, so that a

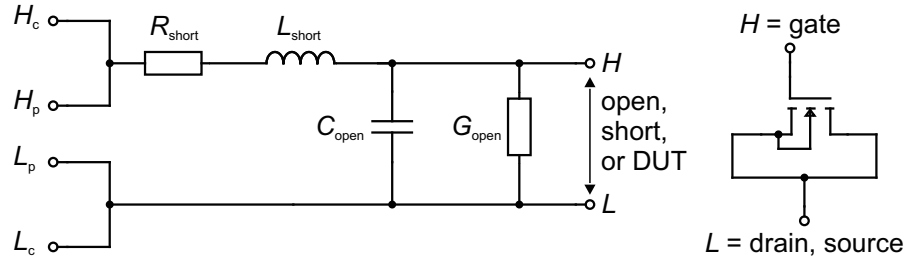


**Figure 3.3.** The left circuit represents the parasitic components occurring between the four-terminal-output of the impedance analyzer and the device under test (DUT). These parasitic components are determined by open and short circuit calibration [224]. The right circuit shows the MOSFET and its connection to the high ( $H$ ) and low ( $L$ ) terminals in the left circuit during a measurement.

defined timing and voltage leads to a reproducible state of the defects in the DUT and capture the hysteresis [MFC1], [225]. As shown in Fig. 3.2, the impedance of a MOSFET is typically interpreted using an equivalent circuit of a capacitor in parallel with a resistor [226]. The associated capacitance and conductance values are then related to the complex impedance via

$$Z^{-1} = G + i\omega C. \quad (3.6)$$

An impedance measurement requires proper de-embedding [224]. Any parasitic impedance, that is not related to the DUT, must be measured and removed from the raw measurement data. This requires a measurement where the two terminals  $H$  and  $L$  of the measurement setup are shortened and a measurement where they are open. The measured impedance can be related to the parasitic components, as illustrated in Fig. 3.3. Once the parasitic components are known, the impedance of the DUT can be calculated according to

$$Z_{\text{DUT}} = \frac{Z_{\text{meas}} - Z_{\text{short}}}{1 - Z_{\text{open}}(Z_{\text{meas}} - Z_{\text{short}})}, \quad (3.7)$$

$$Z_{\text{open}} = G_{\text{open}} + i\omega C_{\text{open}}, \quad (3.8)$$

$$Z_{\text{short}} = R_{\text{short}} + i\omega L_{\text{short}}. \quad (3.9)$$

Any parasitic impedance related to the DUT is assumed to be in series with the MOSFET. It can subsequently be subtracted by assuming that the impedance in strong accumulation is given by the oxide capacitance only [227].

Finally, this yields the CV and GV curves of the MOSFET measured at a certain small-signal frequency, which are illustrated in Fig. 3.4 for a 4H-SiC DMOSET. Based on the same underlying physical mechanism of trapping and detrapping of charges at interface defects during the measurement of a transfer characteristic, these curves show a hysteresis in capacitance and conductance [MFC1]. These shifts can be analyzed and used to extract defect densities, e.g. by the difference between high and low frequency measurements [223]. However, these methods were originally used for silicon (Si)-based technologies. Due to the strong short-term charge trapping in SiC MOSFETs, their usage requires greater care.

The CV curve allows to determine the capacitance of the insulator. The easiest way would be to take the maximum measured capacitance in strong accumulation as the capacitance of the

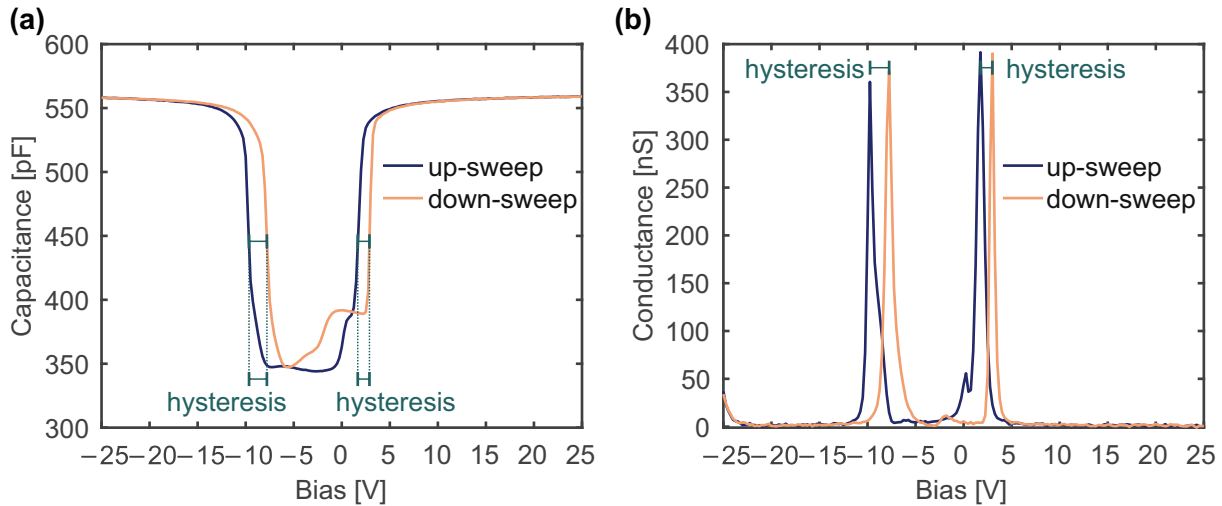


**Figure 3.4.** (a) The CV curves of a 4H-SiC DMOSET measured by either sweeping the gate voltage upwards (up-sweep) from  $-25$  V to  $25$  V or downwards (down-sweep)  $25$  V to  $-25$  V. The small-signal amplitude was  $0.1$  V at a frequency of  $1$  kHz. The  $V_{GS}$ -dependent horizontal shift is due to the hysteresis in these devices. (b) The GV curves from the same impedance measurement as in (a).

insulator. However, a better method has been proposed, where the expression

$$C_{ox} = C \left( 1 - \underbrace{\sqrt{-2 \frac{k_B T}{q} C^{-1} \frac{\partial C}{\partial V}}}_Y \right)^{-1} \quad (3.10)$$

suggests that plotting  $Y$  versus  $C$  gives a curve with slope  $-C_{ox}^{-1}$  and a zero at  $C_{ox}$ , whereby the latter value yields more reliable results [228]–[230].

### 3.3 Ultra-fast Threshold Voltage Measurement

This section introduces ultra-fast  $V_{th}$  measurements that can be used for typical bias temperature instability (BTI) experiments, where  $V_{th}$  is monitored as a device parameter that is prone to instability upon a certain stress. Due to the broad distribution of emission time constants in SiC MOSFETs, ranging down to nanoseconds and below, it is of utmost importance to have precise control over both timing and the applied voltages [231]. A typical measure-stress-measure (MSM) scheme basically consists of three phases: a pre-stress measurement of the pristine state, the stress phase, and the post-stress measurement phase [232], [233].

In order to avoid unwanted recovery, the post-stress measurement phase requires precise timing and ideally a minimized time delay between the end of the stress phase and the first readout [218]. For this purpose, a custom setup based on ultra-fast  $V_{th}$  measurements is used, that features a measurement delay time of only  $1 \mu\text{s}$  [218], [231]. A simplified circuit diagram illustrating the basic functionality of the setup is shown in Fig. 3.5. For the pre-stress measurement, a small drain-source voltage ( $V_{DS}$ ) is applied at the drain terminal and a small voltage  $V_{sense}$  is applied to the sense resistor, which defines a certain  $I_{DS}$ , typically  $1$  mA. Closing the switch that connects the feedback loop to the gate terminal regulates  $V_{GS}$  in such a way that this current flows through the MOSFET and the corresponding  $V_{GS}$ , which is the  $V_{th}$ , can subsequently be measured by an analog-to-digital-conversion.

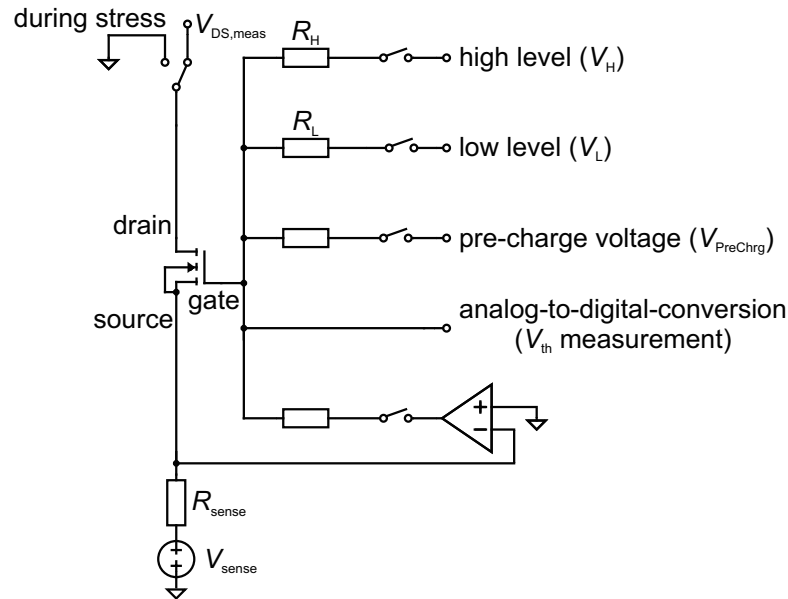


**Figure 3.5.** Simplified circuit diagram of the ultra-fast  $V_{th}$  measurement setup. The drain terminal can either be connected to ground or to voltage  $V_{DS}$ . The gate terminal can be connected to three different voltage sources ( $V_H$ ,  $V_L$ , and  $V_{PreChrg}$ ) or to a feedback loop that forces a current  $V_{sense}/R_{sense}$  by adjusting  $V_{GS}$  – which is then the  $V_{th}$  to be measured.

During stress, both drain and source terminals are grounded and the switch of the feedback loop is open. The setup features three voltage sources: a high level ( $V_H$ ) source, a low level ( $V_L$ ) source, and a pre-charge voltage ( $V_{PreChrg}$ ) source – each of them has its own output resistor  $R$ . They can be selectively connected by closing or opening the corresponding switch. Once one of the switches is closed, the charging of the input capacitance ( $C_{iss}$ ) of the MOSFET occurs with a time constant  $\tau = RC_{iss}$ . By exchanging the output resistor, it is possible to adapt the transition time associated with the respective voltage source. In fact, this setup allows to switch between  $V_H$  and  $V_L$  with a frequency of up to 10 MHz, whereby the rise and fall times of the resulting square waveform can be selectively adapted by exchanging the respective output resistor.

In order to switch from a stress voltage, provided either by the  $V_L$  or  $V_H$  source, to the measurement mode with an active feedback loop, it is necessary to apply a pre-charge voltage  $V_{PreChrg}$  to  $C_{iss}$  first in order to keep control of the transient response of the operational amplifier that is part of the feedback loop. This pre-charging of  $C_{iss}$  is therefore conducted within the measurement delay time by shortly connecting the gate terminal to  $V_{PreChrg} \approx V_{th}$  and assures reproducible readouts.

Each experiment is independently operated by a PIC18F57K42 8-bit microcontroller with a 20 MHz clock. In order to have precise control over the timing, the firmware of the microcontroller is written in assembly language. This allows to control the timing of any set of instructions in units of one clock cycle, which is 50 ns. The reproduction of the timing of a series of actions is thus limited only by the clock. Interrupts or similar advanced features that might unintentionally affect the deterministic execution of the program are not used.

The microcontrollers interact with a computer via a serial communications interface. Before an experiment is conducted, voltages, PWM frequency, etc. are set up. Each experiment is structured as a list of routines. Like a function, each routine is a fixed set of instructions with maximum six 8-bit input parameters. Therefore, the routine itself provides precise timing with the above mentioned precision of the clock. Besides the 6 bytes of input parameters, there is

another byte, consisting of six bits to identify the routine and of two flag bits for arbitrary use. Thus, each routine basically consists of up to 7 bytes and an experiment can be envisioned as a matrix, where each row contains a routine of up to 7 bytes. Before an experiment is started, this matrix is sent to the microcontroller and stored in the internal random-access memory (RAM). Starting the experiment triggers the consecutive execution of the list of routines. During the measurement, acquired measurement data is stored in the RAM and can be sent after the end of the experiment to the computer.

The temperature of the DUTs is regulated by using proportional–integral–derivative (PID) controllers that operate small ovens. The ovens were specifically designed for TO-247 packages. Due to the small size of the ovens, the DUTs can be directly mounted on the board that controls both the stress and the measurement.

### 3.4 Charge Pumping

The CP technique is a method to measure defect-assisted recombination at the semiconductor-insulator interface of a MOSFET [234]–[236]. CP requires a MOSFET that has no internally shortened source and bulk terminals. The basic measurement principle is illustrated in Fig. 3.6a. In a CP measurement, the drain, source, and bulk terminals are grounded, while  $V_{GS}$  is switched between a high level  $V_H$  and a low level  $V_L$ . If  $V_H$  and  $V_L$  are sufficiently high and low, respectively, the MOSFET is continuously switched between inversion and accumulation. Consequently, electrons and holes alternately appear at the semiconductor-insulator interface – during inversion the minority carriers and during accumulation the majority carriers. During inversion, minority carriers from the channel can get trapped in defects at the semiconductor-insulator interface. Once the MOSFET is switched into accumulation, the majority carriers can subsequently recombine with the previously trapped minority carriers. Additionally, majority carriers can equally get trapped in defect states. Once the MOSFET is switched back into inversion, these previously trapped majority carriers can recombine with minority carriers from the channel. Consequently, there are recombination events occurring in response to switching from inversion to accumulation and vice versa. Hence, these recombination events occur at the rising and falling transitions of  $V_{GS}$  and give rise to a current flow from the bulk contact to the drain and source terminals which follows

$$I_{CP} = fAq \times \int_{E_L}^{E_H} D_{it}(E) dE \quad (3.11)$$

where  $f$  is the switching frequency,  $A$  is the area of the channel,  $q$  is the elementary charge, and  $D_{it}$  is the defect density per area and energy [235].  $E_H$  and  $E_L$  correspond to the Fermi levels at  $V_H$  and  $V_L$ , respectively. Note that  $D_{it}$  is the density of defects that actively assist recombination under the specific experimental conditions and does not reflect the entire variety of defects at the interface.

For square pulses, Groeseneken *et al.* deduced the expression

$$I_{CP} = 2q\overline{D_{it}}fA \times k_B T \left( \ln(v_{th}n_i\sqrt{\sigma_n\sigma_p}) + \ln\left(\frac{|V_{fb} - V_{th}|}{|V_H - V_L|} \sqrt{t_{rise}t_{fall}}\right) \right) \quad (3.12)$$

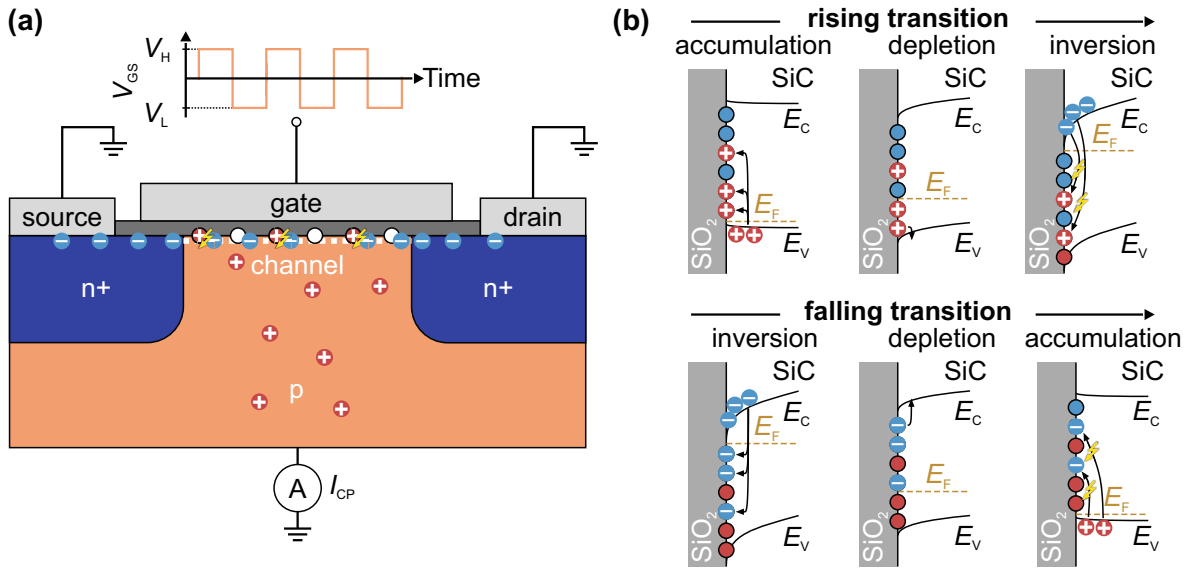


**Figure 3.6.** (a) Illustration of the principle of the CP technique. Drain, source, and bulk terminals are grounded, while the gate terminal is switched between inversion and accumulation. Electrons from the drain and source terminals can undergo defect-assisted recombination with holes coming from the bulk terminal at the semiconductor-insulator interface. The resulting CP current ( $I_{CP}$ ) includes both radiative and non-radiative recombination events. (b) Illustration of the processes occurring at the rising and falling transitions of  $V_{GS}$  for an n-channel MOSFET. During the rising transition from accumulation to inversion, holes get trapped in hole traps (red states) at the interface, which are energetically located above the Fermi level  $E_F$ . During the  $V_{GS}$ -transition, some of the holes detrapp back to the valence band. Once the MOSFET arrives in the inversion regime, channel electrons can recombine with the previously trapped holes which gives rise to the measurable charge-pumping current ( $I_{CP}$ ). For the falling transition, the role of electrons and holes is reversed. Electron traps are indicated by the blue states.

which is actually based on Shockley-Read-Hall (SRH) theory [235]. Hereby,  $\overline{D}_{it}$  is the mean defect density per area and energy between  $E_H$  and  $E_L$ ,  $v_{th}$  is the thermal velocity of the carriers,  $n_i$  is the concentration of minority carriers,  $\sigma_n$  and  $\sigma_p$  are the capture cross sections of electrons and holes, respectively. Furthermore,  $V_{fb}$  is the flatband voltage,  $V_{th}$  the threshold voltage, and  $t_{rise}$  and  $t_{fall}$  are the transition times of the rising and falling transition, respectively. The charge pumping current typically decreases with increasing temperature and increasing transition times. This is due to increased detrapping of charge carriers during the  $V_{GS}$ -transition (see Fig. 3.6b).

It is important to note that the CP technique is sensitive to both radiative and non-radiative transitions – both of them contribute to the bulk current and it is not possible to distinguish between them within such an experiment. Furthermore, recombination processes occurring at the rising transition and the falling transition cannot be distinguished, because the measurement of the bulk current requires integration over several  $V_{GS}$  periods.

There are three commonly used techniques to perform CP measurements [234], [235], [237], [238], in which one voltage parameter is varied while keeping the others constant. Depending on the purpose of the investigation, these techniques, which are listed below for the example of an n-MOSFET, have advantages and disadvantages.

- **Constant high level technique:** The high level  $V_H$  is kept constant in deep inversion. The low level  $V_L$  is gradually decreased until it reaches deep accumulation.

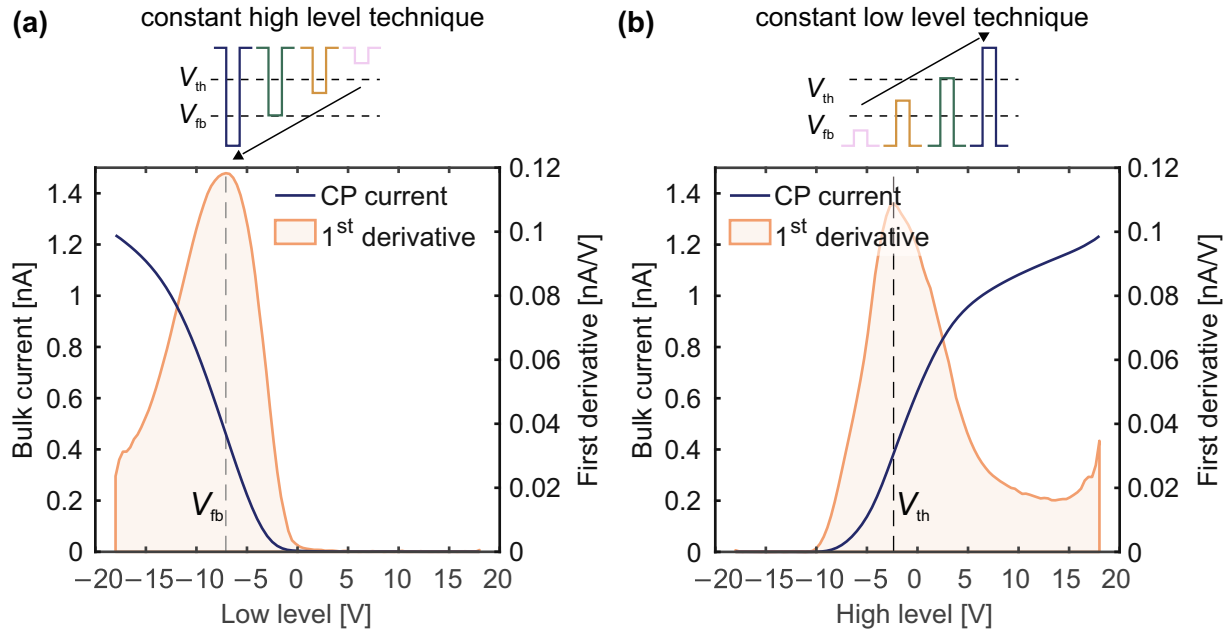


**Figure 3.7.** Illustration of two different charge pumping techniques using a SiC asymmetric trench n-MOSFET. The switching frequency is 10 kHz with a transition time of 500 ns. **(a)** The constant high level technique: CP current (bulk current) versus the low level, while keeping the  $V_H = 18$  V. The peak of the first derivative indicates the CP-related flatband voltage ( $V_{fb}$ ). **(b)** The constant low level technique: CP current (bulk current) versus the high level, while keeping the  $V_L = -18$  V. The peak of the first derivative indicates the CP-related  $V_{th}$ .

- **Constant low level technique:** The low level  $V_L$  is kept constant in deep accumulation. The high level  $V_H$  is gradually increased until it reaches deep inversion.
- **Constant amplitude technique:** The amplitude  $A = V_H - V_L$  is kept constant, while  $V_L$  is increased from deep accumulation into inversion.

The constant high and low level techniques are illustrated for an n-MOSFET in Fig. 3.7a and Fig. 3.7b, respectively. The bulk current increases once the flatband voltage ( $V_{fb}$ ) (constant high level technique) or the  $V_{th}$  (constant low level technique) is passed. Note that due to the recoverable component, both  $V_{fb}$  and  $V_{th}$  are influenced by the switching waveform and hence change dynamically. The corresponding values of  $V_{fb}$  and  $V_{th}$  for charge pumping can be extracted as the peak values of the first derivative of the CP current. The constant amplitude technique is not used within the course of this work, but a detailed description can be found in [238].

### 3.5 Measurement of Photon Emission of Single-Gate Voltage Transients

As found by Macfarlane and Stahlbush [239]–[241], 4H-SiC MOSFETs can emit light in the visible spectral range upon switching between inversion and accumulation. As outlined for CP experiments, the radiative recombination should occur both at the rising and falling transition of  $V_{GS}$ . As the underlying recombination processes are expected to differ significantly, it is desirable to be able distinguish between light emission from the rising and from the falling transition. Furthermore, as known from BTI experiments, the longer a certain  $V_{GS}$  is applied

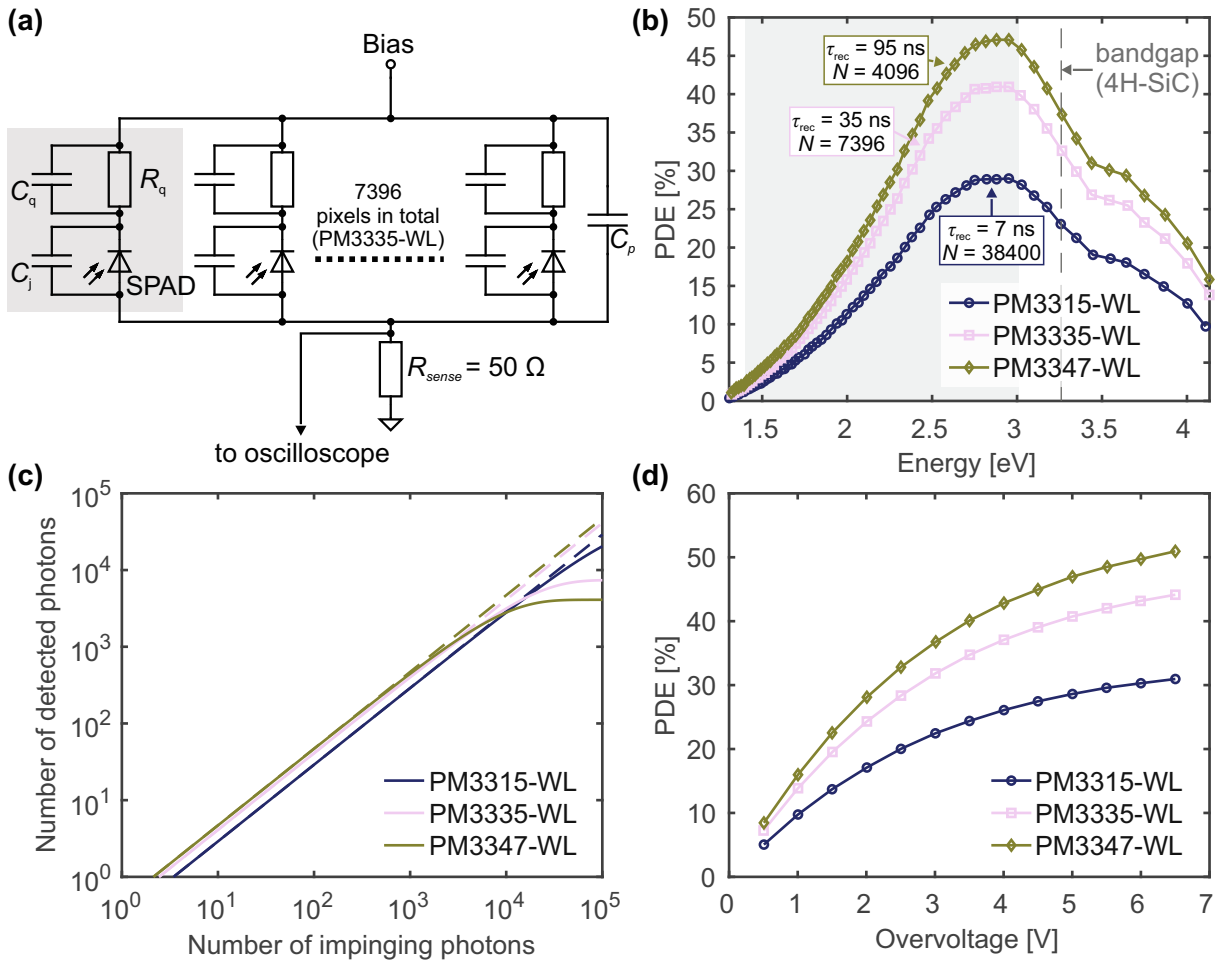


**Figure 3.8.** (a) Equivalent circuit of a silicon-photomultiplier (SiPM), consisting of a two-dimensional array of single-photon avalanche diodes (SPADs). The photocurrent is measured as the voltage-drop at a sense resistor. (b) Photodetection efficiency (PDE) at 5 V overvoltage as a function of photon energy of three silicon-photomultipliers (SiPMs) from the manufacturer Ketek. Data taken from [242]. (c) Relation between the number of detected photons and the number of impinging photons for the three Ketek silicon-photomultipliers (SiPMs). Dashed lines indicate linear relations. (d) Photodetection efficiency (PDE) at 430 nm as a function of overvoltage of three silicon-photomultipliers (SiPMs) from the manufacturer Ketek. Data taken from [242].

to a MOSFET the more charges become trapped in defects. Consequently, it would be very desirable to be able to detect the light emission from a single  $V_{GS}$ -transition between inversion and accumulation. The major challenge is the low light intensity of only up to a few hundreds of photons per transition for a typical active area of  $1.3 \text{ mm}^2$  [MFC3].

A very sensitive photodetector for the visible spectral range is a silicon-photomultiplier (SiPM) [243]. An equivalent circuit of a SiPM is shown in Fig. 3.8a. Generally, a SiPM consists of a two-dimensional array of pixels, whereby each pixel consists of a single-photon avalanche diode (SPAD). An SPAD is basically a diode that operates under a reverse bias above its breakdown voltage – in the so-called Geiger-mode. Each SPAD has its own quenching resistor  $R_q$ , connected in series with the respective SPAD. The SPAD has an associated junction capacitance  $C_j$ . Any capacitance introduced by the quenching resistor is represented by  $C_q$ . Furthermore, the circuit itself introduces a parasitic capacitance  $C_p$ . Once a photon is absorbed in an SPAD, it creates an electron-hole pair that leads to an avalanche process in the respective SPAD. This avalanche



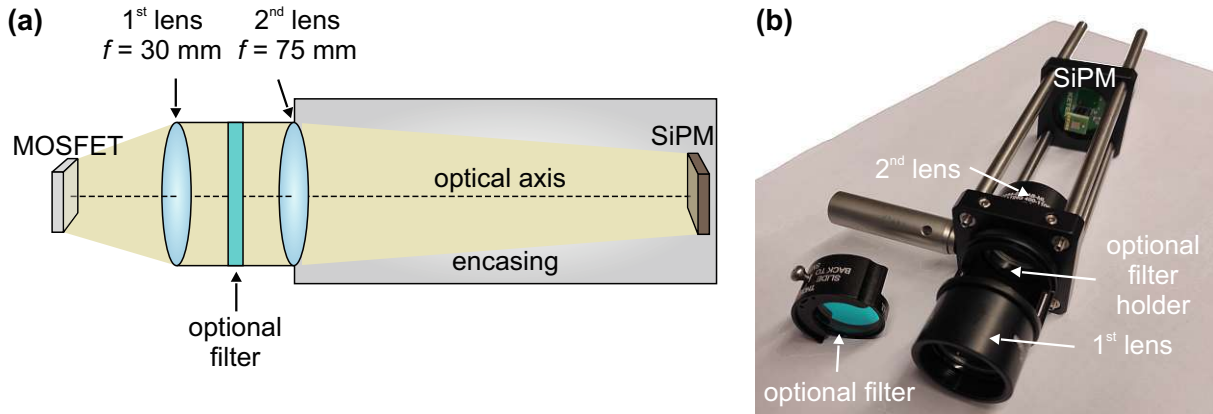


**Figure 3.9.** (a) Schematic illustration of the measurement setup for photon emission from a single  $V_{GS}$ -transition. The first lens has a lower focal length  $f$  (higher numerical aperture) than the second lens. Redrawn from [MFC3]. (b) Image of the setup. The 3D-printed encasing is not shown.

leads to a very high current of up to hundreds of microampere through the SPAD. Due to the quenching resistor, the voltage drop over the SPAD subsequently decreases over time until it reaches the breakdown voltage of the SPAD. At this point, the avalanche stops and the bias of the SPAD increases again with a time constant  $\tau = R_q(C_j + C_q)$  to its initial value above the breakdown voltage, where it is then again ready to detect another photon.

In a SiPM, all these SPADs with their quenching resistors are connected in parallel. Once a photon hits a pixel of the SiPM, it creates a characteristic current signal. The total measured current is always a superposition of the current contributions of all SPADs. The current can be measured as the voltage drop at a sense resistor  $R_{\text{sense}} = 50 \Omega$  by using an oscilloscope.

A SiPM has a certain photodetection efficiency (PDE), which is influenced by many factors, including the geometric fill-factor of the SiPM [244]. For the same active area, there is typically the possibility to choose between different SiPMs that have different pixel sizes and subsequently a different number of pixels and a different geometric fill-factor. In Fig. 3.8b, the PDE of three SiPMs from the manufacturer Ketek are illustrated as a function of the photon energy together with their recovery time constants  $\tau$  and the number of pixels  $N$ . These SiPMs were found to have the most suitable spectral response for the targeted photons located in the grey marked area. All three SiPMs have the same active area of  $9 \text{ mm}^2$ , but different microcell sizes. Apparently, a better PDE comes at the expense of a higher  $\tau$  and lower  $N$ . The higher  $N$  the better the proportionality between number of detected photons  $N_{\text{meas}}$  and number of impinging photons  $N_{\text{photon}}$ . According to [245], this relation can be estimated by

$$N_{\text{meas}} = N \left( 1 - \exp \left( - \frac{N_{\text{photon}} \text{PDE}}{N} \right) \right) \quad (3.13)$$

and is illustrated for the three considered SiPMs in Fig. 3.8c. As illustrated in Fig. 3.8d, the PDE can be increased by increasing the used overvoltage. However, an increase in overvoltage leads to an increased dark count rate, crosstalk probability, and afterpulsing probability [242].

In light of the above discussion, this work uses the Ketek PM3335-WL SiPM, because it is the best compromise between high PDE, linear response, and low  $\tau$ . According to Equation 3.13, for 1000 impinging photons with an energy at maximum PDE, the SiPM deviates only less than 3% from a linear response. At 5 V overvoltage, which is the difference between bias and breakdown voltage of the SiPM, it has a gain of  $4 \times 10^6$ . The gain is the number of charges

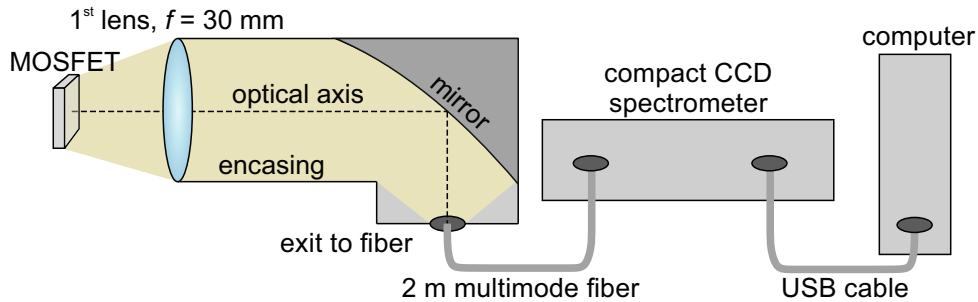


**Figure 3.10.** The measurement setup for optical spectroscopy using a compact CCD spectrometer. Redrawn from [MFC3].

created in a single avalanche event (corresponding to a single photon detection). This high gain allows to detect single photons and very low light intensities.

As many photons as possible emitted from the MOSFET need to reach the SiPM. For this purpose, a setup with two lenses is used, whereby the first lens should ideally have a high numerical aperture. The setup is illustrated in Fig. 3.9. More specifically, two achromatic lenses (Thorlabs AC254-030-AB-ML and AC254-075-AB-ML) with a diameter of 2.54 cm image the light emitted from the MOSFET onto the SiPM. In between the two lenses, a dedicated holder allows to insert an optical filter. The distance between the MOSFET and the first lens is chosen in such a way that the number of detected photons is highest. The SiPM is mounted on a dedicated Ketek printed circuit board (PCB). The bias is supplied by a Ketek bias source dedicated for the used SiPM. The components are mounted on a cage system, which is covered by a black 3D-printed encasing. In general, the entire experiment is conducted in a dark box that further protects the setup from ambient light.

### 3.6 Optical Spectroscopy

The SiPM has a lot of advantages, in particular its high sensitivity that enables the detection of the light emission from only a single  $V_{GS}$  transition. Besides the possibility to use optical filters to select a certain range of photon energies, the setup cannot detect the photon energy itself. For this purpose, a dedicated spectroscopic setup is required. The simplest possible concept is based on a compact charge-coupled device (CCD) spectrometer (Thorlabs CCS200/M), specified for a wavelength range of 200 – 1000 nm [246]. It has a spectral accuracy of less than 2 nm at 633 nm and uses a  $600 \text{ mm}^{-1}$  (800 nm blaze) grating. The setup is illustrated in Fig. 3.10. The emitted light is collected by an achromatic objective lens (Thorlabs AC254-030-AB-ML). Afterwards, a reflective collimator (Thorlabs RC12SMA-P01) couples the light into a multimode fiber (Thorlabs BFL200HS02). Due to the achromaticity of the lens and the wavelength-independent reflection, chromatic aberrations are minimized. As illustrated in Fig. 3.10, the system is protected from ambient light by an encasing. Through the multimode fiber, the light is then directed to the compact CCD spectrometer, which is connected via a universal serial bus (USB) cable to a computer. The spectrometer is intensity and wavelength calibrated by the manufacturer and could only be disturbed by the used fiber.

This setup is sufficient to detect the light from a MOSFET during switching. However, it typically requires long integration times of about 40 s at continuous switching of the gate terminal at a frequency of 1 MHz. Consequently, this setup cannot distinguish between the photons emitted at the falling  $V_{GS}$ -transition and the photons emitted at the rising  $V_{GS}$  transition.

As there is no possibility for gating the detection, the setup collects the light from the entire period of the  $V_{GS}$  switching signal. As the minimum integration time of the spectrometer is  $10\ \mu\text{s}$ , it could be expected that synchronizing the gate switching with the spectrometer integration and summing up the spectra would allow to selectively detect the photons emitted at either the rising or the falling  $V_{GS}$ -transition. However, this leads to significant readout noise, that completely hides the emission spectrum of the MOSFET.

### 3.7 Time-Gated Optical Spectroscopy

The spectroscopic setup described in Section 3.6 has two major disadvantages: the lack of time resolution and the poor sensitivity. This is resolved by another setup with an intensified charge-coupled device (ICCD) camera (Teledyne Princeton Instruments PI-MAX4, PM4-256f-HR-FG-18-P43) as its core component. The setup is illustrated in Fig. 3.11c. The MOSFET is mounted on an XYZ translation stage with differential adjusters. Two achromatic lenses with a diameter of 2.54 cm (Thorlabs AC254-100-AB-ML and AC254-030-AB-ML) couple the light into an imaging Schmidh-Czerny-Turner spectrograph (Teledyne Princeton Instruments IsoPlane 160). The spectrograph features a  $150\ \text{mm}^{-1}$  grating with a 500 nm blaze and silver coated mirrors. The ICCD is attached to the spectrograph and is responsible for measuring the outgoing image of the photon spectrum.

The most important and defining property of an ICCD is its intensifier. Its working principle is illustrated in Fig. 3.11a. A photon that arrives at the ICCD, situated at the output window of the spectrograph, first hits the photocathode. The photocathode converts the photon into an electron, which is subsequently accelerated by an electric field towards a microchannel plate (MCP). The MCP is a two dimensional matrix of channel electron multipliers that are slightly tilted. Once an electron hits the wall of a channel of the MCP, secondary electrons are emitted successively amplifying the initial electron. Finally, the electrons are accelerated towards a phosphor screen, where they are converted back into photons that are detectable by the CCD. By this series of processes, the intensifier can amplify a two-dimensional image, but even more importantly, it can be switched on and off within fractions of a nanosecond for time-gating the detection. In the on-state, the intensifier amplifies the image, whereas in the off-state, the electric fields are reversed such that no electrons can pass through the amplifier. All measurements that were conducted within this work use an amplification of 1, which means that 1 photoelectron is detected on the CCD per photon arriving at the intensifier. Consequently, it is predominantly the ability to turn the intensifier on and off that is used within the conducted experiments.

The intensifier basically works like a shutter and its fast switching capability allows to time-gate the spectral detection down to a gate width  $t_{gw} \geq 3\ \text{ns}$  at frequencies up to 1 MHz. The switching of the gate terminal of the MOSFET is operated by a trigger signal. For time-gating the spectral detection of the photons emitted from the MOSFET, the same trigger signal is used to operate the ICCD camera. This is illustrated in Fig. 3.11b. The  $V_{GS}$  of the MOSFET follows the trigger signal with a constant delay of  $t_{tr} = 50\ \text{ns}$ . The ICCD camera can trigger either on the rising (as illustrated in Fig. 3.11b) or falling transition of the trigger signal. After a minimum necessary delay  $t_{gd} \geq 25\ \text{ns}$ , the ICCD camera then switches the intensifier in the on-state for a time  $t_{gw}$ . As the intensifier works similar to a shutter, the CCD can continuously integrate until a defined number of trigger events  $N_{tr}$  has been detected. This avoids unnecessary readout noise. Furthermore, thermal noise in the ICCD is minimized by cooling it down to  $-20\ ^\circ\text{C}$ .

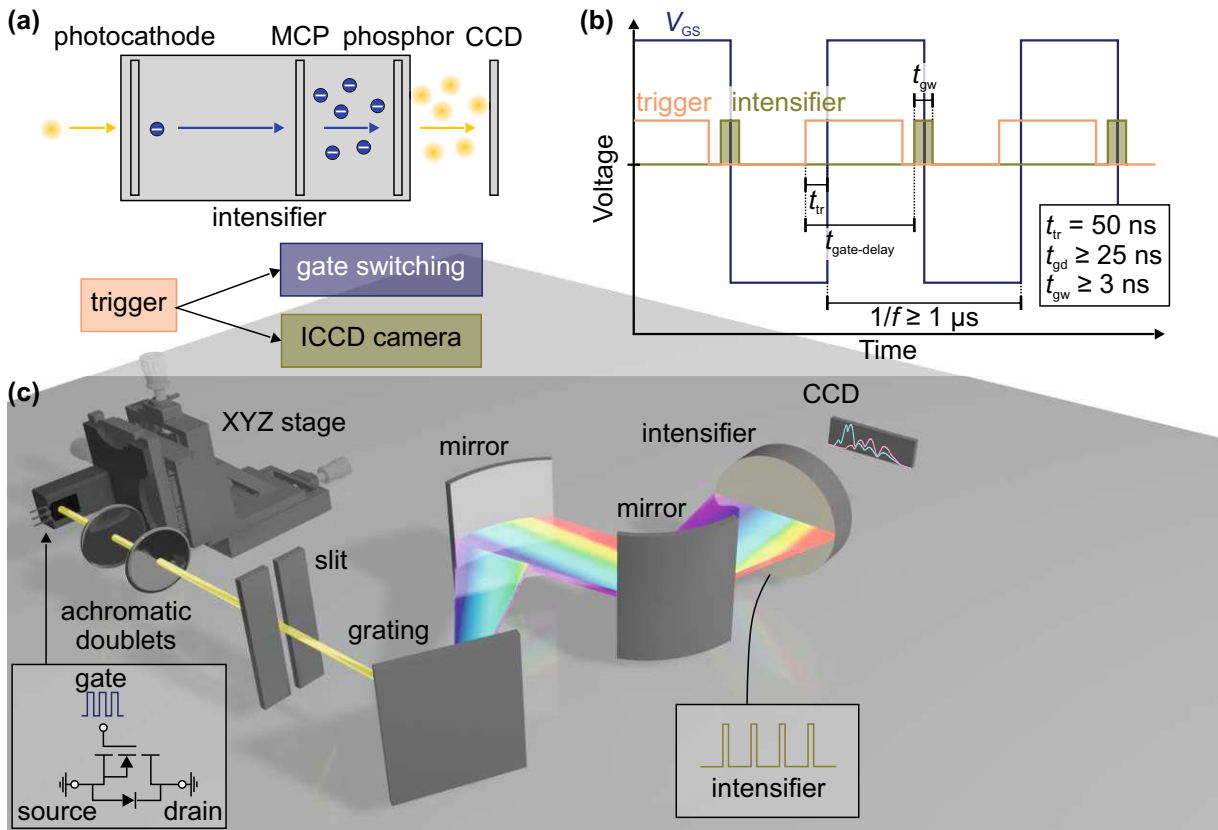


**Figure 3.11.** (a) Schematic illustration of an ICCD. This includes the CCD and the intensifier, which consists of a photocathode, a MCP, and a phosphor screen. The intensifier of the ICCD is operated by the same trigger signal as the gate switching. (b) Illustration of the timing between trigger signal,  $V_{GS}$ , and the state of the intensifier. (c) Illustration of the measurement setup used for time-gated optical spectroscopy, including the spectrograph and the ICCD camera. Adapted from [MFJ2], © 2024 American Physical Society.

The ICCD camera features a CCD array of  $1024 \times 256$  pixels. Each pixel has an area of  $26 \mu\text{m} \times 26 \mu\text{m}$ . However, due to the size of the intensifier, the number of active pixels being exposed to the incident photons is decreased to  $692 \times 253$  pixels. In all performed measurements, the emission spectrum was obtained by vertical binning of pixels of a stripe of pixels centered on the CCD. This improved spectral resolution and signal to noise ratio.

Compared to the previously presented measurement setups, the ICCD-based setup for time-gated spectroscopy has advantages and disadvantages. Compared to the setup based on the compact CCD spectrometer described in Section 3.6, its major advantage is the higher sensitivity and the possibility to time-gate the spectral detection. However, it has a more limited spectral range. Compared to the SiPM-based setup described in Section 3.5, it features spectral resolution and time-gating. However, the SiPM-based setup is the only available setup that can measure light emission from a single  $V_{GS}$ -transition. The advantages and disadvantages of the used setups are summarized in Table 3.1.

### 3.7.1 Wavelength and Intensity Calibration

As this measurement setup is used for quantitative modeling of the emission spectrum, it is important to have precise wavelength and intensity calibration over the entire range of

|  | SiPM setup   | CCD-spectrometer setup | ICCD/spectrograph setup                 |
|--|--------------|------------------------|---|
| <b>spectral resolution</b>   | no           | 200 – 1000 nm          | 412 – 884 nm (trusted wavelength range) |
| <b>time resolution</b>   | yes          | no                     | yes (time-gating $\geq 3$ ns)           |
| <b>capability to measure light emission of single <math>V_{GS}</math>-transition</b> | yes          | no                     | no                                      |
| <b>typical integration times</b>   | not required | $\approx 40$ s         | $\approx 1$ s                           |
| <b>intensity &amp; wavelength calibration</b>  | not possible | yes (by manufacturer)  | yes                                     |

**Table 3.1.** Comparison between different experimental setups used in the course of this work for the analysis of light emitted from SiC MOSFETs.

measured photon energies. This calibration is performed using the IntelliCal system from Teledyne Princeton Instruments.

The wavelength calibration is illustrated in Fig. 3.12a. For the wavelength range of 585–966 nm, the system of spectrograph and ICCD is calibrated with a neon-argon light source, which results in a root-mean-square of 0.2 nm. For the wavelength range of 254–579 nm, the calibration is confirmed with a mercury lamp.

For intensity calibration, a temperature-controlled array of light-emitting diodes (LEDs) is used that creates a continuous light spectrum, measured at the National Institute of Standards and Technology (NIST). The involved spectra are illustrated in Fig. 3.12b. As the spectrum of the LED-array is known, it can be used to calibrate the intensity detected by the system via

$$I_{\text{cal}}(\lambda) = \text{CF}(\lambda) \times I_{\text{raw}}(\lambda), \quad (3.14)$$

which introduces a correction factor CF to relate the calibrated intensity  $I_{\text{cal}}$  with the measured raw intensity  $I_{\text{raw}}$ . CF is determined by smoothing the values obtained by IntelliCal via a local regression with a second degree polynomial and weighted linear least squares.

As illustrated in Fig. 3.12b, it is to note that the LED-array emits light above about 900 nm, but as the quantum efficiency of the intensifier significantly drops, the CF strongly increases in this region. On the other side of the spectrum below about 450 nm, the LED-array does not emit light, but the quantum efficiency of the intensifier is still significant, which ties CF to zero.

In order to avoid both accumulation of noise in the spectrum for longer wavelengths and discarding measured data for shorter wavelengths, a trusted wavelength range is defined, where the intensity calibration is particularly reliable. This trusted wavelength range is set to the range where the measured, normalized, non-calibrated intensity in each pixel is above  $10^{-2}$ . The trusted wavelength range for this setup is between 412–884 nm and is indicated in plots in this work by a grey background. A constant CF is assigned to all data measured outside the trusted wavelength range, whereby its value is the last CF value inside the trusted wavelength range. This assures that no data is discarded due to the intensity calibration.

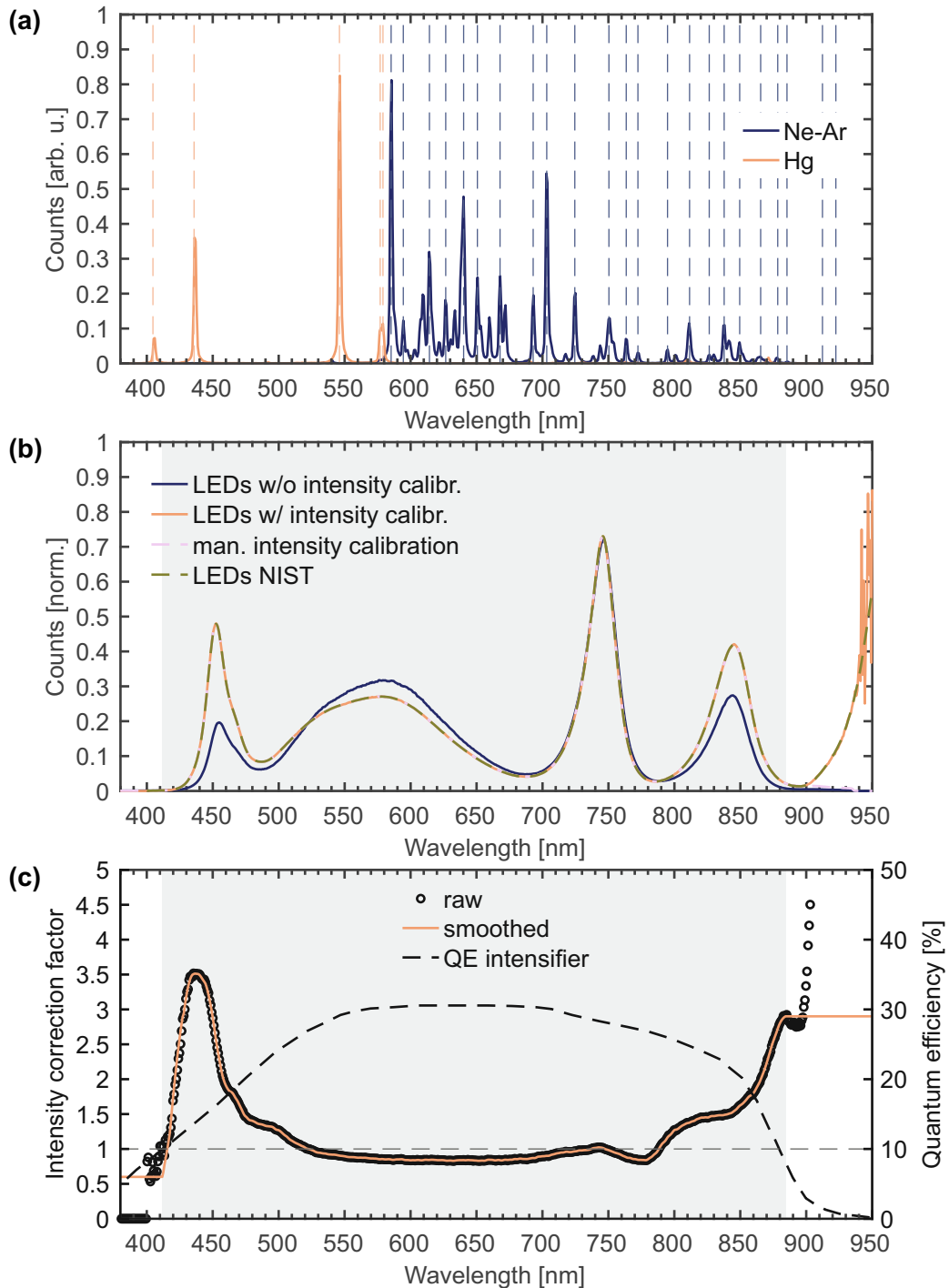


**Figure 3.12.** (a) The emission spectra of the neon-argon (Ne-Ar) and mercury (Hg) lamps, measured with the wavelength calibrated system. Vertical lines indicate the true positions of the emission lines. (b) All spectra of the NIST light-emitting diode (LED) array involved in the calibration of the intensity. Manual calibration uses a constant CF outside the trusted wavelength region. (c) The correction factor CF as delivered by IntelliCal (raw) and the CF used within the manual calibration. Additionally, the quantum efficiency (QE) of the intensifier is shown. Redrawn from [MFJ2].

### 3.8 Photon Emission Microscopy

Although its name is quite general, in the context of microelectronic devices emission microscopy usually refers to the detection of light emission from any type of semiconductor

chip [247]–[249]. The emission of photons from a semiconductor chip under operation can be caused by various effects, such as an avalanche breakdown [250], [251], hot carriers [252], [253], source-drain breakdown [254], gate oxide breakdown, or even Fowler-Nordheim tunneling [255]. Studying these photons with regard to their spatial origin or their spectral decomposition allows to localize and identify a potential failure or device behavior. Such setups are therefore used in failure analysis and reliability to study device failures and reliability related physical mechanisms. A typical setup consists of an ordinary microscope and an attached CCD or ICCD, which is cooled.

Die approbierte gedruckte Originalversion dieser Dissertation ist an der TU Wien Bibliothek verfügbar.  
The approved original version of this doctoral thesis is available in print at TU Wien Bibliothek.





# Chapter 4

## Measurements and Results

In this chapter, the measurements and results obtained in the course of this work are presented. Related scientific publications are pointed out at the beginning of each section.

First, Section 4.1 deals with the general behavior of trapping and detrapping processes at the semiconductor-insulator interface, including the silicon (Si)/silicon dioxide (SiO<sub>2</sub>) and silicon carbide (SiC)/SiO<sub>2</sub> interfaces. Essentially, it is shown that single-valued activation energies are not sufficient to model and understand bias temperature instability (BTI) and how the conventionally used apparent activation energies have to be interpreted in the context of widely distributed capture and emission activation energies. The peculiarities of the recoverable component of BTI at the SiC/SiO<sub>2</sub> interface are discussed.

It is this recoverable component of the SiC/SiO<sub>2</sub> interface in SiC metal-oxide-semiconductor field-effect transistors (MOSFETs), that is the central topic of Section 4.2. This component is characterized using different commercial power MOSFETs, including trench MOSFETs (UMOSFETs) and double-diffused MOSFETs (DMOSFETs). Besides the impact of the recoverable component on the threshold voltage ( $V_{th}$ ) and its recovery, the impact on gate-pulsed transfer characteristics is investigated. The gate-pulsed transfer characteristic represents the transfer curve with the worst-case impact of the recoverable component, but equally represents the more relevant characteristic measured under application conditions compared to characteristics measured during slow sweeps of the gate-source voltage ( $V_{GS}$ ). Finally, the use of conditioning with negative gate pulses within a  $V_{th}$  measurement is investigated and shown to be a successful strategy.

In contrast to the previous sections that dealt with BTI in SiC MOSFETs, Section 4.3 presents an extensive experimental analysis of a new degradation mechanism, meanwhile commonly referred to as gate switching instability (GSI). GSI is a degradation mechanism driven by the gate switching itself and highly relevant for power conversion applications and any other application that requires continuous switching between the on- and off-state of the MOSFET. This section describes the various experimental findings and properties of GSI and subsequently deduces the underlying physical mechanism leading to the conclusion that GSI is driven by defect-assisted electron-hole recombination and caused by recombination-enhanced defect reactions (REDRs). Finally, a comprehensive physics-based model is proposed that is able to describe the drift evolution and various effects encountered in experiments.

In Section 4.4, the previously used electrical characterization techniques are complemented by measurements of light emission from fully-processed SiC power MOSFETs that occurs exactly under the stress mode associated with GSI. As the light emission is effectively triggered by

the field-effect, this new discipline of characterization is referred to as field-effect stimulated optical spectroscopy. Using various experimental approaches, such as a pump-probe scheme of gate pulses, optical spectroscopy, and time-gated optical spectroscopy, the light emission is characterized covering emission from single  $V_{GS}$ -transitions up to light emission from continuous switching. The results obtained using this method are used to link the emitted photons to the recoverable component. Most importantly, the results allow to understand the microscopic trapping and detrapping processes occurring at the SiC/SiO<sub>2</sub> interface and even enable a detailed comparison with theoretical ab-initio calculations – revealing the nature of the involved defects.

## 4.1 Single-Value Apparent Activation Energies in Silicon and Silicon Carbide MOSFETs

*The contents of this section were previously published in [MF]3.*

As for any other degradation mechanism, one of the most important properties of bias temperature instability (BTI) is its temperature dependence. Increasing the temperature in an BTI experiment or stress test accelerates the degradation in time. Consequently, understanding the temperature dependence is important to calculate the degradation back to use conditions. As outlined in Section 2.1.2, the temperature dependence provides information on the underlying physical processes for instance the involved charge traps. Not only in industrial environments, but in the scientific literature this temperature dependence has often been modeled with a single Arrhenius law for either the threshold voltage shift ( $\Delta V_{th}$ ) that is reached after certain stress time following

$$\Delta V_{th} = \Delta V_{th,0} \exp\left(-\frac{E_{a,V}^{app}}{k_B T}\right) \quad (\text{vertical}) \quad (4.1)$$

or for the acceleration in stress time ( $t_s$ )

$$t_s = t_{s,0} \exp\left(\frac{E_{a,H}^{app}}{k_B T}\right) \quad (\text{horizontal}) \quad (4.2)$$

to reach a certain  $\Delta V_{th}$  [256]–[261]. Both variants contain only a single-value activation energy, which implies that the fact that the defect parameters are distributed is completely neglected [140], [141], [144], [262]–[264]. Most interestingly, the value of the activation energy has even been used to relate BTI to a certain physical mechanism, such as the diffusion of hydrogen [265], [266].

In a typical measure-stress-measure (MSM) experiment, these “apparent” activation energies are determined by evaluating  $\Delta V_{th}$  as a function of stress time for different temperatures (see Fig. 4.1a). For two temperatures  $T_1 < T_2$ , the apparent activation energies are determined via Equations 4.1 (“vertical” extraction) and 4.2 (“horizontal” extraction) as per

$$E_{a,V}^{app} = k_B \frac{T_1 T_2}{T_2 - T_1} \ln\left(\frac{\Delta V_{th}(T_2)}{\Delta V_{th}(T_1)}\right) \quad (4.3)$$

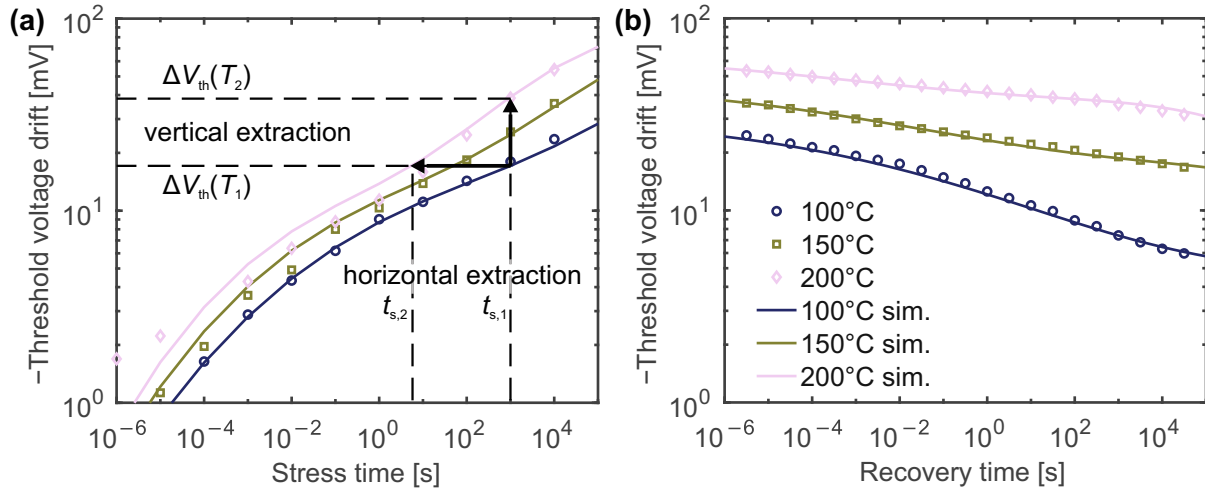


**Figure 4.1.** Measurement of  $\Delta V_{th}$  in a silicon (Si) technology upon negative gate stress of  $V_{GS} = -2$  V for three different temperatures. The solid lines represent the simulation from the analytic activation energy (AE) map in Fig. 4.2a. **(a)** Dependence on the stress time at a fixed recovery time of  $t_r = 1$   $\mu$ s. **(b)** Dependence on the recovery time after a stress time of  $t_s = 10^4$  s. Redrawn from [MFJ3].

and

$$E_{a,H}^{app} = k_B \frac{T_1 T_2}{T_2 - T_1} \ln \left( \frac{t_{s,1}}{t_{s,2}} \right). \quad (4.4)$$

Typically, these two activation energies differ considerably with  $E_{a,V}^{app} \approx 0.1$  eV [256], [257] and  $E_{a,H}^{app} \approx 1.0$  eV. As shown in Fig. 4.1b, the recovery curves of different temperatures show a notably different evolution that would lead to a variation of the apparent activation energy with the recovery time [257]. Indeed, as will be presented in this section, the apparent activation energies depend on many more parameters, such as bias and stress time.

### 4.1.1 The Analytic Activation Energy Map

In the following, the concept of analytic activation energy (AE) and capture-emission-time (CET) maps for modeling of BTI is used to investigate the dependencies of both the horizontal and the vertical apparent activation energies [140], [147]. In this framework, BTI is the collective response of an ensemble of defects with distributed capture activation energies  $E_c$  and emission activation energies  $E_e$ . The capture and emission time constants  $\tau_c$  and  $\tau_e$ , respectively, are linked to their activation energies by an Arrhenius law [144], [267], [268], as per

$$\tau_{c/e} = \tau_{0,c/e} \exp \left( \frac{E_{c/e}}{k_B T} \right). \quad (4.5)$$

For given stress and recovery voltages, an extended MSM scheme with long recovery phases can be used to extract a CET map for a certain temperature, which is the joint probability density function  $g(\tau_c, \tau_e)$  of the time constants, by calculating the second mixed partial derivative [140] as per

$$g(\tau_c, \tau_e) \approx - \frac{\partial^2 \Delta V_{th}(\tau_c, \tau_e)}{\partial \tau_c \partial \tau_e}. \quad (4.6)$$

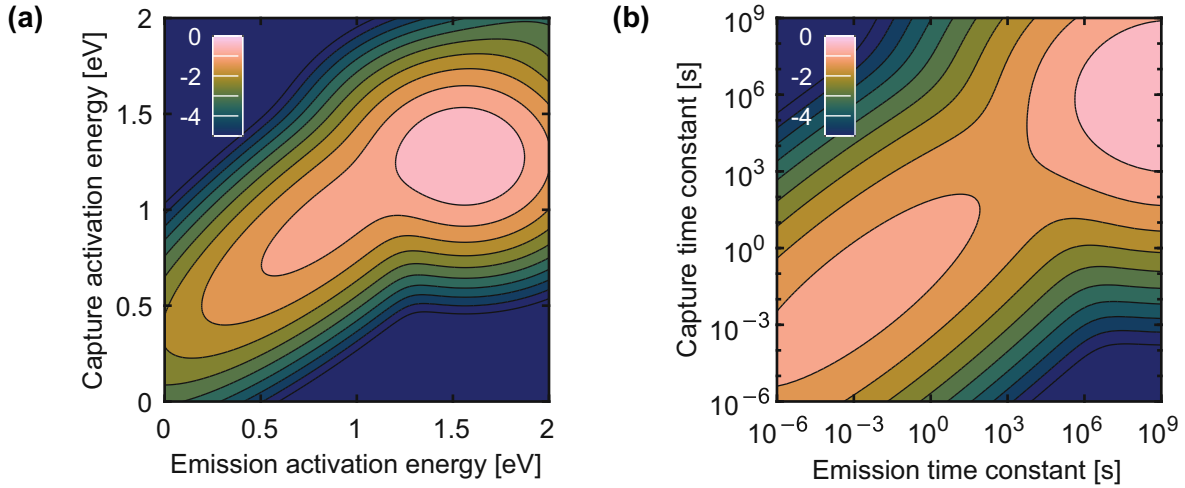


**Figure 4.2.** (a) AE map from a Si technology showing the recoverable and quasi-permanent component for  $V_{GS} = -2$  V. A density value of  $x$  corresponds to  $10^x \text{V eV}^{-2}$ . Based on data from [270]. (b) The CET map at  $T = 150$  °C calculated from a). Note that the shown density values are per squared decade in time. A density value of  $x$  corresponds to  $7 \times 10^x \text{mV}$ . Redrawn from [MFJ3].

| Component | $\tau_0$ [ns]         | $\mu_c$ [eV] | $\sigma_c$ [eV] | $\mu_{\Delta e}$ [eV] | $\sigma_{\Delta e}$ [eV] | $V_0$ [V] | $m$  | $r$ |
|-----------|-----------------------|--------------|-----------------|-----------------------|--------------------------|-----------|------|-----|
| R         | $5.55 \times 10^{-5}$ | 0.99         | 0.314           | -0.11                 | 0.216                    | -0.669    | 3.05 | 1   |
| P         | 0.573                 | 1.27         | 0.171           | 1.57                  | 0.211                    | -0.407    | 2.77 | 0   |

**Table 4.1.** Parameters of two bivariate Gaussian distributions from a Si technology. Redrawn from [MFJ3].

If several extended MSM schemes are conducted at different temperatures, Equation 4.5 allows to extract the parameters of an analytic AE map that is shown for a 130 nm silicon (Si) technology with a 2.2 nm nitrided gate oxide in Fig. 4.2a, whereas Fig. 4.2b shows a corresponding CET map. Hereby, the AE map is a superposition of two distributions. Based on their time scales, the two components are called recoverable component (R) and quasi-permanent component (P), respectively. Each component follows a distribution [269] that is given by

$$g(E_c, E_e) = \frac{A}{2\pi\sigma_c\sigma_{\Delta e}} \exp\left(-\frac{(E_c - \mu_c)^2}{2\sigma_c^2} - \frac{(E_e - (rE_c + \mu_{\Delta e}))^2}{2\sigma_{\Delta e}^2}\right). \quad (4.7)$$

Apparently, the parameter  $r \in [0, 1]$  represents a correlation between  $E_c$  and  $E_e$ . The parameters of both R and P of the map shown in Fig. 4.2a are listed in Table 4.1. In fact, the distribution in Equation 4.7 is a bivariate Gaussian distribution in  $E_c$  and  $E_e$ . The mean  $\mu_e$ , the standard deviation  $\sigma_e$  and the correlation coefficient  $\rho$  of the standard form of the bivariate Gaussian distribution are given by

$$\mu_e := r\mu_c + \mu_{\Delta e} \quad (4.8)$$

$$\sigma_e^2 := r^2\sigma_c^2 + \sigma_{\Delta e}^2 \quad (4.9)$$

$$\rho := r\frac{\sigma_c}{\sigma_e} \quad (4.10)$$

The analytic AE map allows to calculate  $\Delta V_{th}$  after a certain  $t_s$  and recovery time ( $t_r$ ). Hereby,  $\Delta V_{th}$  is calculated as the integral over the product of an occupation map and the CET map. Under the assumption that a defect with a certain  $\tau_c < t_s$  and a  $\tau_e > t_r$  is always occupied, the

occupation map is given by a product of Heaviside step functions

$$P(E_c, E_e, t_s, t_r) = \Theta(E_{cs} - E_c) \times \Theta(E_e - E_{er}) \quad (4.11)$$

with

$$E_{cs} = k_B T \ln\left(\frac{t_s}{\tau_{0,c}}\right), \quad E_{er} = k_B T \ln\left(\frac{t_r}{\tau_{0,e}}\right). \quad (4.12)$$

This leads to the result

$$\begin{aligned} \Delta V_{th}(t_s, t_r) &= \int_0^\infty \int_0^\infty P(\tau_c, \tau_e, t_s, t_r) g(\tau_c, \tau_e) d\tau_e d\tau_c \\ &= \int_0^\infty \int_0^\infty P(E_c, E_e, t_s, t_r) g(E_c, E_e) dE_e dE_c \\ &\approx \int_0^{E_{cs}} \int_{E_{er}}^\infty g(E_c, E_e) dE_e dE_c \\ &= \iint_S g(E_c, E_e) dS. \end{aligned} \quad (4.13)$$

Consequently,  $\Delta V_{th}$  can be obtained by simply integrating the AE map over an infinitely large rectangular area  $S$ . However, it has to be considered that  $\tau_0$  in Equation 4.5 might be different for R and P, which makes  $E_{cs}$  and  $E_{er}$  dependent on the considered component. Until stated differently, it is in the following assumed that the  $\tau_0$ 's are equal for both R and P.

#### 4.1.2 Basic Principle of Vertical Extraction

Based on two temperatures  $T_1 < T_2$ , the vertical extraction was defined in Equation 4.3, whereby  $\Delta V_{th}$  required for its calculation can be obtained using Equation 4.13. The principle of the vertical extraction is schematically illustrated in Fig. 4.3. For temperature  $T_1$ , the corresponding integration area  $S_1$  is defined by the parameters  $E_{c1} := E_{cs}(T_1)$  and  $E_{e1} := E_{er}(T_1)$ . Analogously for  $T_2$ ,  $S_2$  is determined by  $E_{c2} := E_{cs}(T_2)$  and  $E_{e2} := E_{er}(T_2)$ . These parameters contain the dependencies on  $t_s$  and  $t_r$ , whereas the AE map contains the dependencies on stress and recovery voltage.

First, Fig. 4.3 illustrates that there is an intersection between  $S_1$  and  $S_2$  that is called  $A$ . Subsequently, the area  $S$  can be expressed as  $S_1 = A \cup A_E$  and  $S_2 = A \cup A_C$ . Define  $I(S)$  as the integral of the AE map over the area  $S$ . Then, the apparent activation energy  $E_{a,V}^{app}$  is given by

$$E_{a,V}^{app} = k_B \frac{T_1 T_2}{T_2 - T_1} \ln \left( \frac{1 + \frac{I(A_C)}{I(A)}}{1 + \frac{I(A_E)}{I(A)}} \right). \quad (4.14)$$

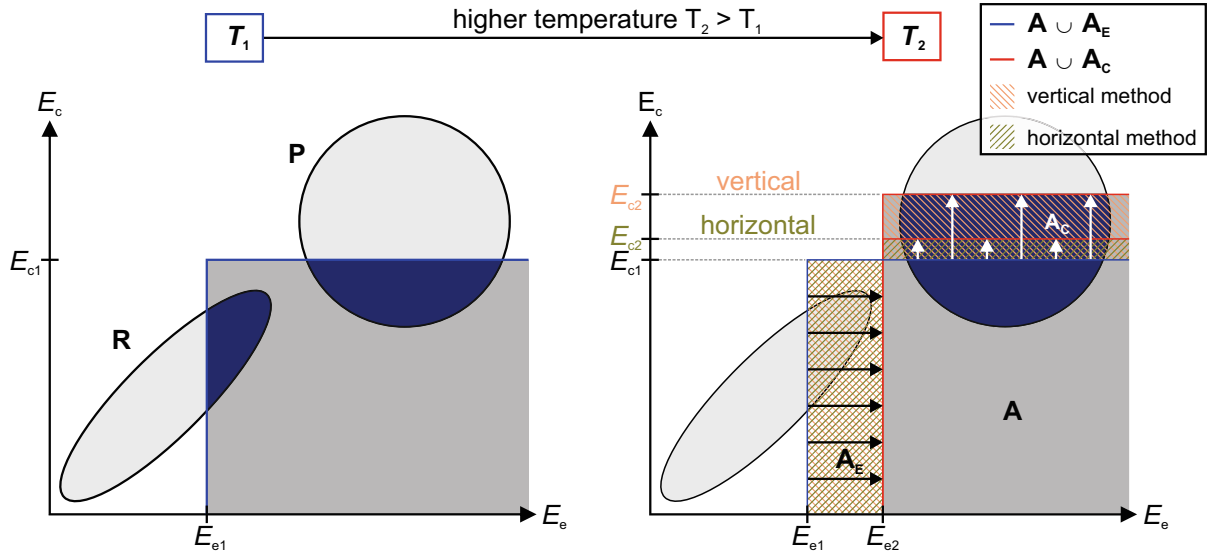


**Figure 4.3.** Schematic illustration of both horizontal and vertical energy extraction methods. For comparison, the stress times at temperature  $T_1$  are equal for both methods and the recovery time is set to be the same at both temperatures. This results in identical measurements at temperature  $T_1$ .  $\Delta V_{th}$  at  $T_1$  is obtained by integrating the AE map over the blue framed area, where the overlap of the distributions  $R$  and  $P$  with the integration area is marked in dark blue. The threshold voltage shift at the higher temperature  $T_2$  is obtained by integrating over the red framed area. For the vertical extraction, the quantities  $E_{c1}$ ,  $E_{e1}$ ,  $E_{c2}$ , and  $E_{e2}$  are determined by the freely chosen measurement conditions  $T_1$ ,  $T_2$ ,  $t_s$ , and  $t_r$ , which define the areas  $A_E$ ,  $A_C$  and  $A$ . The vertical activation energy is calculated by integrating the AE map over these areas using Equation 4.14. In contrast, the horizontal extraction differs from the vertical extraction even though both begin with the identical measurement at  $T_1$ . While the measurement conditions  $T_1$ ,  $T_2$ ,  $t_{s1}$ , and  $t_r$  are the same as for the vertical method,  $t_{s2}$  is determined by the condition that  $I(A_C) = I(A_E)$ . Under the condition of a comparably small contribution from  $A_E$  and a high amplitude of the distribution around  $E_{c1}$ ,  $E_{c2}$  will be close to  $E_{c1}$ . According to Equation 4.16, the horizontal activation energy will thus be close to  $E_{c1}$ . Redrawn from [MFJ3].

Apparently,  $E_{a,V}^{app}$  depends on ratios of integrals that are dependent on stress time, recovery time, and the considered temperatures. Thus, the horizontal apparent activation energy  $E_{a,V}^{app}$  depends on the same parameters.

### 4.1.3 Basic Principle of Horizontal Extraction

As given by Equation 4.4, the horizontal extraction is based on the ratio of the stress times to reach a certain  $\Delta V_{th}$ . Provided that at temperature  $T_1$  both stress and recovery times are chosen the same as for the vertical extraction,  $E_{c1}$  and  $E_{e1}$  have the same values. Furthermore, the values of  $E_{e2}$  are the same provided that the recovery times at temperature  $T_2$  are identical. Consequently, only the parameter  $E_{c2}$  differs from the vertical extraction, whereby its value is determined by the condition  $\Delta V_{th}(t_{s,1}, T_1) = \Delta V_{th}(t_{s,2}, T_2)$ . This condition translates into the equality of the integrals  $I(A_C) = I(A_E)$ . Using the definitions of  $E_{cs}$  and  $E_{er}$  in Equation 4.12, the ratio of stress times is given by

$$\frac{t_{s,1}}{t_{s,2}} = \exp\left(\frac{E_{c1}}{k_B T_1} - \frac{E_{c2}}{k_B T_2}\right) \quad (4.15)$$

Inserting this into Equation 4.4 yields

$$E_{a,H}^{\text{app}} = E_{c1} - \underbrace{\frac{T_1}{T_2 - T_1} (E_{c2} - E_{c1})}_{:=\Delta E}, \quad (4.16)$$

whereby the term  $\Delta E$  denotes the deviation from the energy  $E_{c1}$ . For a typical AE map of a Si technology (see Fig. 4.2a), the P component has a significantly larger amplitude  $A$  (see Equation 4.7) than the R component. As a result, the condition  $I(A_C) = I(A_E)$  leads to a relatively small height  $E_{c2} - E_{c1}$  of the area  $A_C$  compared to the width  $E_{e2} - E_{e1}$  of a given area  $A_E$  (see Fig. 4.3). Consequently,  $\Delta E$  is typically smaller than  $E_{c1}$ . Nevertheless, Equation 4.16 clearly demonstrates that also the horizontal activation energy  $E_{a,H}^{\text{app}}$  depends on stress time, recovery time, and temperature.

#### 4.1.4 Analytic Formulations of Apparent Activation Energies

Based on the basic principles of horizontal and vertical apparent activation energies, suitable approximations can be found to derive analytic formulations of these energies. Finding an analytic formulation for  $E_{a,V}^{\text{app}}$  is the more complex problem because it requires an analytic expression for  $\Delta V_{\text{th}}$ . As a first approximation, recovery is assumed to be negligible ( $t_r = 0$ s), which directly leads to  $E_{er} = -\infty$  and the integration over  $E_e$  in Equation 4.13 can therefore be eliminated. In a next step, the resulting one-dimensional Gaussian distribution is approximated by a logistic distribution of the same standard deviation [271]. Finally, it is assumed that  $(\mu_c \pi) / (\sqrt{3} \sigma_c) \gg 1$ , such that the lower limit of the integration can be extended from zero to negative infinity. These approximations lead to the result

$$\begin{aligned} \int_0^{E_{cs}} \int_{-\infty}^{\infty} g(E_c, E_e) dE_e dE_c &= A \int_0^{E_{cs}} \frac{1}{\sqrt{2\pi}} \exp\left(-\frac{(E_c - \mu_c)^2}{2\sigma_c^2}\right) dE_c \\ &\approx A \int_{-\infty}^{E_{cs}} \frac{\pi}{\sqrt{3}\sigma_c} \frac{\exp\left(\pi \frac{\mu_c - E_{cs}}{\sqrt{3}\sigma_c}\right)}{\left(1 + \exp\left(\pi \frac{\mu_c - E_{cs}}{\sqrt{3}\sigma_c}\right)\right)^2} dE_c \\ &\approx A \left(1 + \exp\left(\pi \frac{\mu_c - E_{cs}}{\sqrt{3}\sigma_c}\right)\right)^{-1}. \end{aligned} \quad (4.17)$$

As the AE map consists of the two components  $R$  and  $P$ , the corresponding integrals have to be evaluated and inserted into Equation 4.3, which finally leads to the analytic formulation for the vertical activation energy

$$E_{a,V}^{\text{app}} = k_B \frac{T_1 T_2}{T_2 - T_1} \times \ln \left( \frac{(1 + C_R(T_2) t_s^{-\gamma_R T_2})^{-1} + A' (1 + C_P(T_2) t_s^{-\gamma_P T_2})^{-1}}{(1 + C_R(T_1) t_s^{-\gamma_R T_1})^{-1} + A' (1 + C_P(T_1) t_s^{-\gamma_P T_1})^{-1}} \right). \quad (4.18)$$

$$\gamma_i := \frac{\pi k_B}{\sigma_{c,i} \sqrt{3}}, \quad C_i(T) := \exp\left(\frac{\pi \mu_{c,i}}{\sigma_{c,i} \sqrt{3}}\right) \tau_{0,i}^{\gamma_i T}, \quad i \in \{R, P\}$$

$$A' := A_P / A_R$$

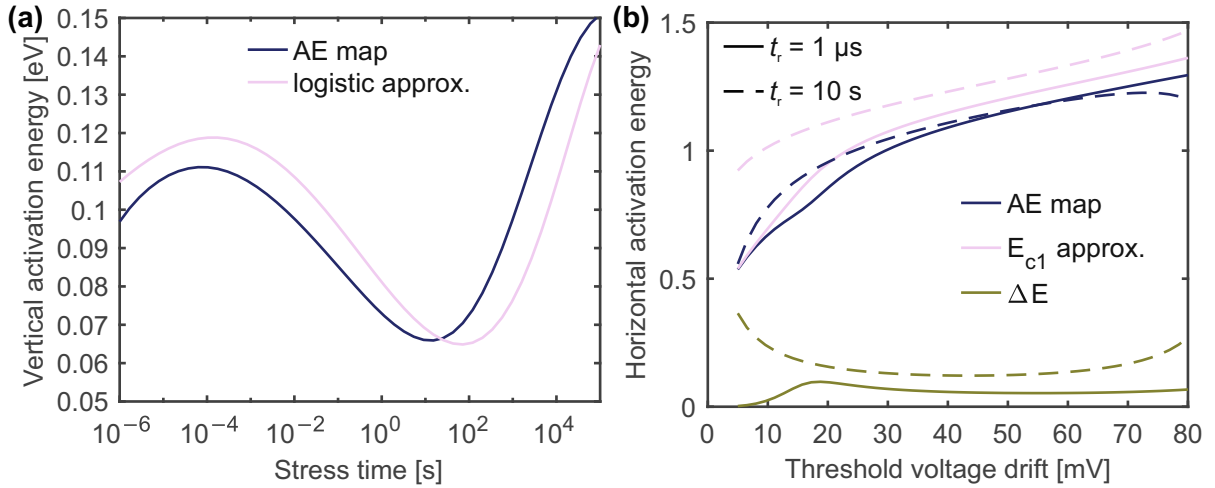


**Figure 4.4.** Analytic approximations for the apparent activation energies calculated based on the parameters in Table 4.1 and  $V_{GS} = -2$  V. **(a)** The dependence of the vertical activation energy on its extraction point (stress time). Both the direct result from the AE map with a recovery time of 1  $\mu$ s and the approximation from Equation 4.18 are shown. The temperatures were set to  $T_1 = 120$  °C and  $T_2 = 150$  °C. **(b)** The dependence of the horizontal activation energy on its extraction point ( $\Delta V_{th}$ ). As in (a), the results from the AE map and the analytic formulation from Equation 4.19 are compared. The temperatures are identical to the ones used in (a). The term  $\Delta E$  (see definition in Equation 4.16) is small compared to the apparent activation energy. Redrawn from [MFJ3].

A comparison of  $E_{a,V}^{app}$  directly obtained from the AE map and from the analytic formulation is presented in Fig. 4.4a. The two curves are in good agreement.

As already indicated by Equation 4.16, finding an analytic formulation for the horizontal activation energy  $E_{a,H}^{app}$  is more difficult because it requires to determine  $E_{c2}$  under the condition  $I(A_C) = I(A_E)$ . However, assuming sufficiently long stress times,  $\Delta E$  can approximately be neglected. Hence, the horizontal activation energy is given as

$$E_{a,H}^{app} \approx E_{c1} = k_B T_1 \ln \left( \frac{t_{s,1}}{\tau_{0,P}} \right). \quad (4.19)$$

Consequently, the horizontal activation energy is just the extraction point itself. It is proportional to the logarithm of the stress time that corresponds to  $\Delta V_{th}$  at  $T_1$  where the activation energy is extracted. As shown in Fig. 4.4b for two different recovery times, there is a good agreement between the direct result obtained from the AE map and Equation 4.19. Furthermore, the term  $\Delta E$  is significantly smaller than  $E_{a,H}^{app}$ , which also confirms the validity the approximation from Equation 4.19.

#### 4.1.5 Relation Between Horizontally and Vertically Extracted Energies

As the vertical extraction method is not motivated by physics, the resulting values of  $E_{a,V}^{app}$  differ strongly from the activation energies in the AE map, e.g. of the P component. However, under a certain condition, a relationship between the vertical and horizontal extraction methods can be derived. If  $\Delta V_{th}$  followed a power law dependence on the stress time with a power law exponent  $n$  and the temperature dependence was incorporated in the form of an exponential, as



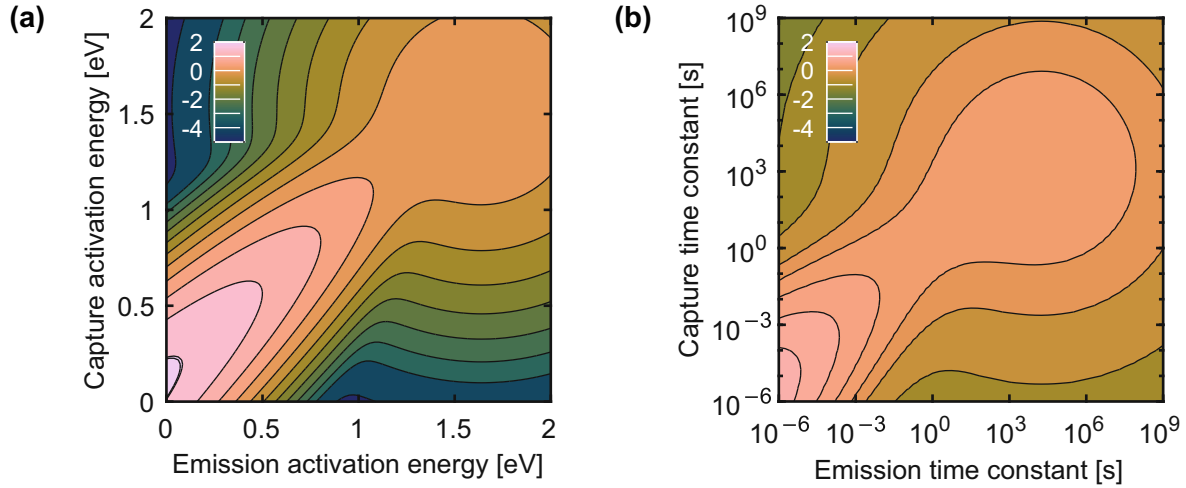


**Figure 4.5.** (a) AE map from a SiC trench MOSFET for  $V_{GS} = 25$  V. A density value of  $x$  corresponds to  $10^x \text{V eV}^{-2}$ . Based on data from [231]. (b) A CET map calculated from a) at  $T = 175$  °C. A density value of  $x$  corresponds to  $7 \times 10^x \text{mV}$ . Redrawn from [MF]3.

per

$$\Delta V_{th} \propto (t_s)^n \exp\left(-\frac{E_{a,V}^{app}}{k_B T}\right), \quad (4.20)$$

the two apparent activation energies can be converted via

$$E_{a,H}^{app} = \frac{E_{a,V}^{app}}{n}. \quad (4.21)$$

However, note that this relation is based on fitting the measurement data with a power law of which the exponent  $n$  has no specific physical meaning.

#### 4.1.6 Examples for the Dependencies of Apparent Activation Energies

This section presents the dependencies of both horizontal and vertical activation energies on measurement parameters using two examples. First, these dependencies are presented for a 130 nm Si metal-oxide-semiconductor field-effect transistor (MOSFET) followed by a silicon carbide (SiC) MOSFET with an asymmetric trench design (see Section 1.5.2). In contrast to the previous considerations on the basic extraction methodology and the analytic formulation, the apparent activation energies are extracted using an Arrhenius plot.

The Si technology belongs to the AE map from Fig 4.2a, where the P component has a significantly higher amplitude than the R component. In contrast to that, a SiC MOSFET typically has a more dominant R component compared to the P component. Its AE map is illustrated in Fig. 4.5 together with a CET map.

##### 130 nm Silicon MOSFET

First, the two extraction methods are analyzed regarding their dependence on the respective extraction point. Afterwards, the dependencies on recovery time and stress voltage are presented.

Fig. 4.6 shows the dependence of the vertical activation energy on the stress time (extraction point). Hereby, Fig 4.6a shows the extraction in an Arrhenius plot for three selected stress times.

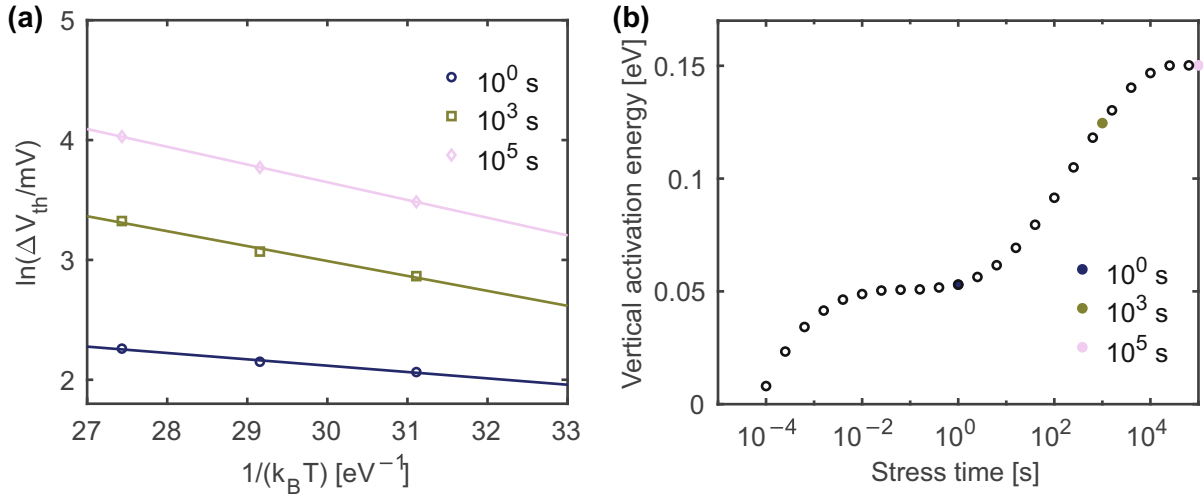


**Figure 4.6.** (a) Arrhenius plot for the vertical activation energy of a Si technology at three different stress times (extraction points) with three different temperatures (100 °C, 150 °C, and 200 °C). The stress voltage was set to  $V_{GS} = -2$  V. (b) Vertical activation energy of a Si technology versus the stress time (extraction point) at a recovery time of  $t_r = 1$   $\mu$ s. The three stress times from (a) are indicated by color. Redrawn from [MFJ3].

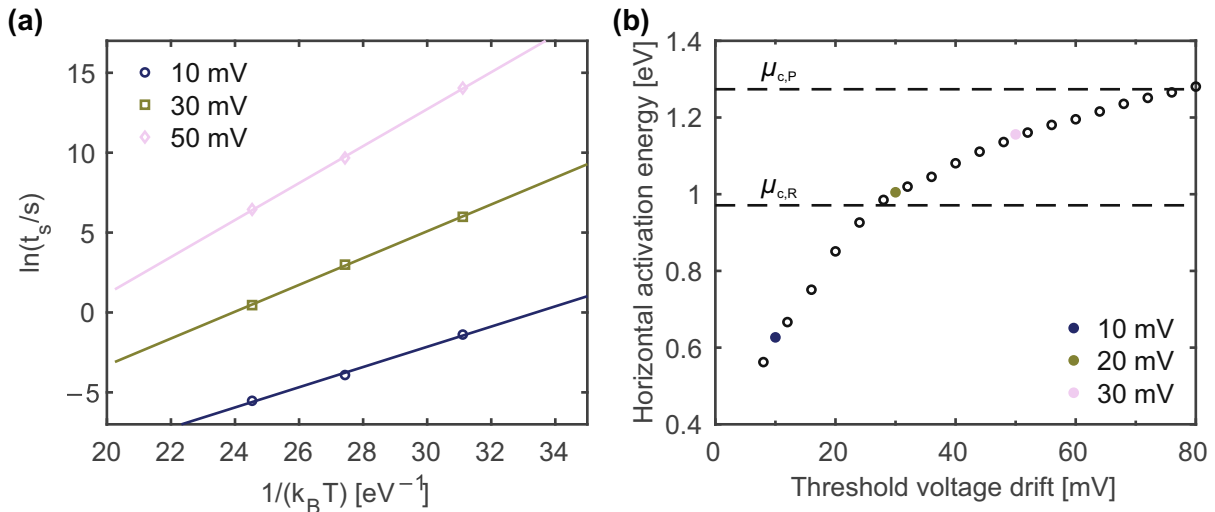


**Figure 4.7.** (a) Arrhenius plot for the horizontal activation energy of a Si technology at three different  $\Delta V_{th}$  values (extraction points) with three different temperatures (100 °C, 150 °C, and 200 °C). The stress voltage was set to  $V_{GS} = -2$  V. (b) Vertical activation energy of a Si technology versus  $\Delta V_{th}$  (extraction point) at a recovery time of  $t_r = 1$   $\mu$ s. The three  $\Delta V_{th}$  values from (a) are indicated by color. Redrawn from [MFJ3].

According to Equation 4.1, the vertical activation energy corresponds to the negative of the slope. The resulting values are shown in Fig. 4.6b. First, it is to note that the extracted values cover a broad range from 0.01 eV to 0.15 eV. Furthermore,  $E_{a,V}^{app}$  increases monotonously with increasing stress time, but there are two plateaus observed around  $10^{-1}$  s and  $10^5$  s. These plateaus stem from the two components R and P and can be understood by looking at the AE map in Fig. 4.2. For small stress times, the R component dominates  $\Delta V_{th}$  and the activation energy increases until the recoverable component is fully charged.  $\Delta V_{th}$  hardly changes in between of the components R and P, which leads to the plateau. Once the stress time is sufficiently long to reach the P

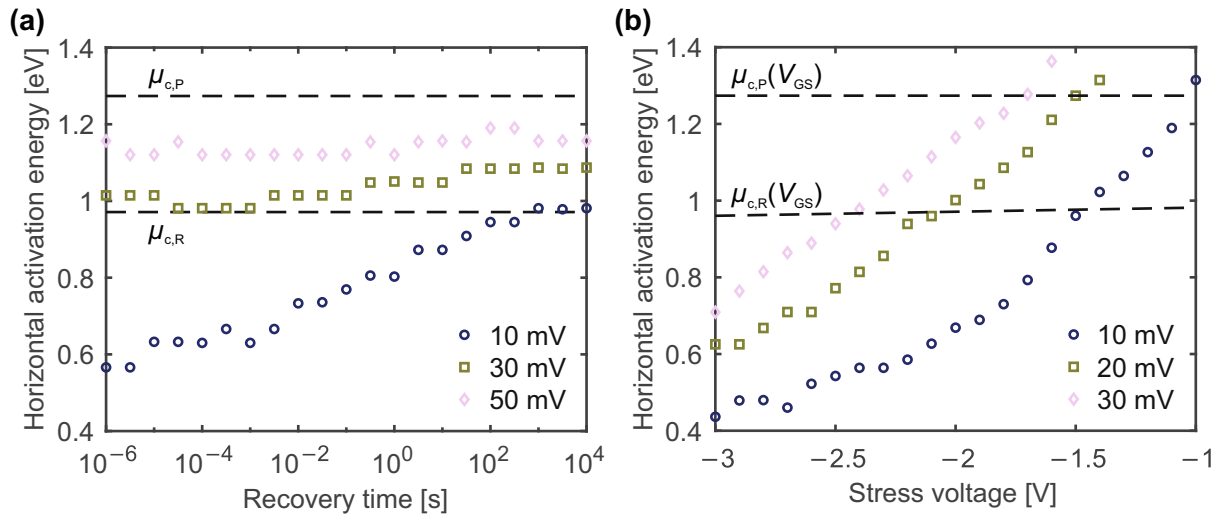


**Figure 4.8.** (a) The horizontal activation energy of a Si technology versus the recovery time at a stress voltage of  $V_{GS} = -2$  V for three different extraction points ( $\Delta V_{th}$ ). (b) The horizontal activation energy of a Si technology versus the stress voltage for three different extraction points. Redrawn from [MFJ3].

component, the activation energy increases again until the maximum of the P component is reached.

In analogy, Fig. 4.7 shows the dependence of the horizontal activation energy on  $\Delta V_{th}$  (extraction point). The Arrhenius plot in Fig. 4.7a exemplarily shows the extraction of the activation energy for three different values of  $\Delta V_{th}$ , whereby the value of the activation energy is given as the slope of each curve. The resulting values are shown in Fig. 4.7b and cover a range from 0.6 eV to 1.3 eV. As discussed in Section 4.1.3, the horizontal extraction measures the shortening of the stress time upon an increase in temperature around the extraction point. Consequently, the values are in the same range as the mean activation energies  $\mu_c$  of the R and P components in the AE map (indicated by dashed horizontal lines in Fig. 4.7b).

Apart from the extraction point, another parameter influencing the apparent activation energy is the recovery time. Its impact on the horizontally extracted activation energy is illustrated in Fig. 4.8a, which shows the horizontal activation energy as a function of the recovery time for three different extraction points. The dependence on the recovery time decreases with increasing  $\Delta V_{th}$ , which is a consequence of an increasing relative contribution from the P component. The higher the extraction point, the longer is the stress time needed to achieve the corresponding  $\Delta V_{th}$ , which increases the relative contribution of the P component. As its amplitude is significantly higher than the amplitude of the R component, the temperature dependence of the P component dominates the extraction of the apparent activation energy. Recovery on the time scale of the R component is therefore negligible. As indicated by the horizontal dashed lines in Fig. 4.8a, the extracted horizontal activation energy at  $\Delta V_{th} = 50$  mV is closer to  $\mu_{c,P}$  than at  $\Delta V_{th} = 10$  mV.

A conventional AE map is only valid for a certain stress and a certain recovery voltage. However, the stress voltage dependence can be included by introducing a stress voltage-dependent amplitude of both the R and P components [147], [272]. Hereby, the amplitude is given by a power law  $A = (V_{GS}/V_0)^m \text{ mV eV}^{-1}$ . Any other dependencies of model parameters, such as  $\mu_c$  of R and P components, were shown to be negligible. Fig. 4.8b presents the dependence of the horizontal activation energy on the stress voltage for three different extraction points. Apparently, there is an almost linear relation between these two quantities for all three extraction

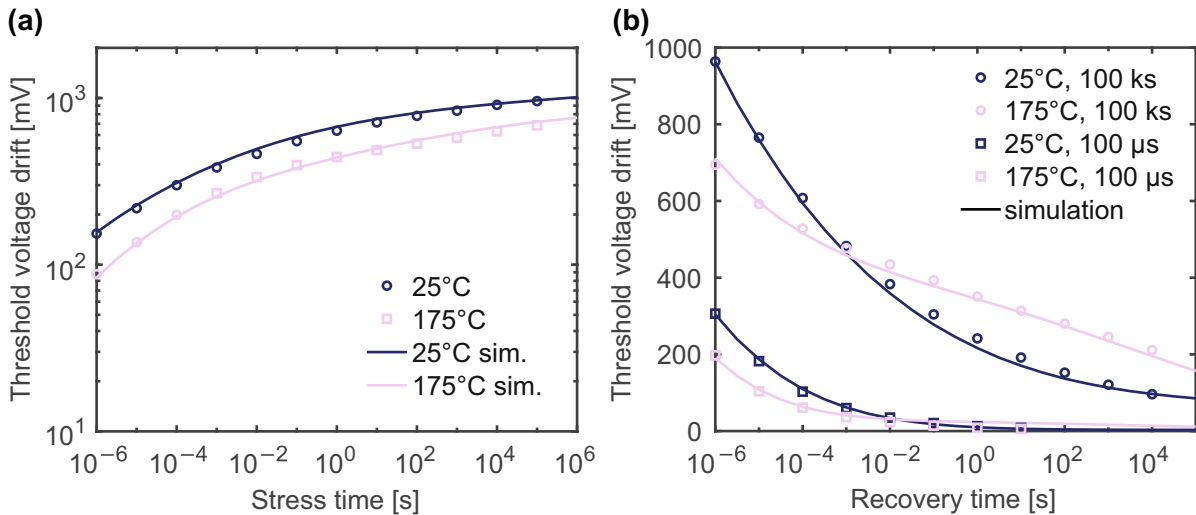


**Figure 4.9.** (a) The threshold voltage shift  $\Delta V_{th}$  of a SiC MOSFET versus the stress time for two temperatures at a recovery time of 1  $\mu$ s, a stress voltage of 25 V. Solid lines indicate the simulated result from the AE map in Fig. 4.5a. (b) The threshold voltage shift  $\Delta V_{th}$  of a SiC MOSFET versus the recovery time for two stress times and temperatures. Redrawn from [MF]3].

points, whereby the activation energy decreases with increasing absolute stress voltage. An increased absolute stress voltage decreases the stress time needed to achieve the same extraction point ( $\Delta V_{th}$ ). As shown by Equation 4.19, the horizontal activation energy decreases with decreasing stress time.

### Silicon Carbide MOSFET

As indicated by the AE map of a SiC trench MOSFET in Fig. 4.5, these devices typically feature a significantly stronger R component compared to the P component. Compared to a Si technology, where the R component is less dominant, the recovery time has a much stronger impact on any measurement. Furthermore, both negative bias temperature instability (NBTI) and positive bias temperature instability (PBTI) are significant and can lead to high shifts in  $\Delta V_{th}$  [149]. However, it has to be noted that the high values for  $\Delta V_{th}$  predominantly originate from the R component, which is fully recoverable. Consequently, the  $\Delta V_{th}$  associated with the R component cannot be considered as a degradation of the device.

Interestingly, this dominance of the R component can also lead to non-physical apparent activation energies [155]. This is illustrated in Fig. 4.9a, showing  $\Delta V_{th}$  as a function of the stress time, and in Fig. 4.9b, showing  $\Delta V_{th}$  as a function of the recovery time, for two temperatures. As shown by both plots for the shortest recovery time,  $\Delta V_{th}$  is higher at the lower temperature. In the context of phenomenological modeling, such a behavior is often associated with a negative apparent activation energy. Obviously, negative activation energies are completely non-physical. Finally, Fig. 4.9b shows that this behavior flips for recovery times above 1 ms and 1 s, respectively, depending on the stress time.

The impact of this phenomenon on the horizontal activation energy is illustrated in Fig. 4.10a, showing the horizontal activation energy versus its extraction point at a recovery time of 1  $\mu$ s and the corresponding simulated value, where the contribution of the R component was removed. The measurement data clearly show a negative horizontal activation energy over the entire range of  $\Delta V_{th}$ . In contrast, the simulated value is positive over the entire considered range. Of course,

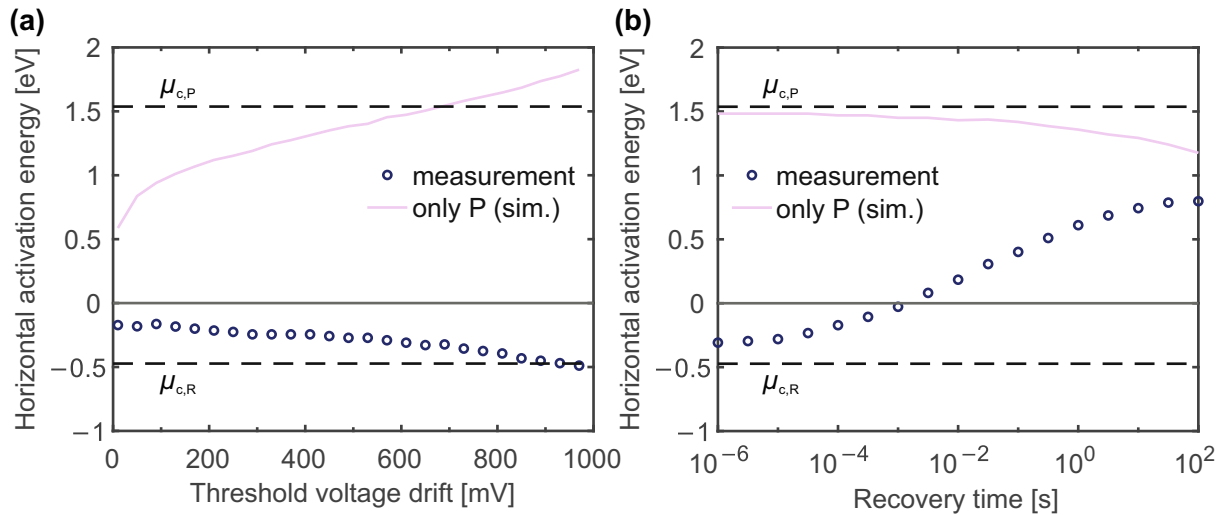


**Figure 4.10.** (a) The horizontal activation energy of a SiC MOSFET versus the extraction point ( $\Delta V_{th}$ ) at a stress voltage of  $V_{GS} = 25 \text{ V}$ . The solid line indicates the simulated dependence, where the R component was not considered. (b) The horizontal activation energy versus the recovery time. Redrawn from [MFJ3].

the explanation of this phenomenon lies in the distribution of activation energies. As already pointed out, SiC technology typically has a dominant R component, whereas Si technology has a dominant P component (see AE maps in Fig. 4.2a and Fig. 4.5a). For the distribution of SiC, it can occur that an increase of temperature leads to the situation where the contribution from defects with emission time constants lower than the used recovery time decreases more than the contribution from defects with decreased capture time constants increases. This leads to the observed behavior and thereby affects the horizontal activation energy. As illustrated in Fig. 4.10b, this behavior vanishes once the recovery time becomes sufficiently long, which subsequently leads to a change in sign of the horizontal activation energy. This is an important example that illustrates the non-physical character of apparent activation energies and why it is important to always consider the entire distribution of underlying activation energies. Furthermore, it clearly uncovers the challenges induced by the strong R component in SiC MOSFETs.

## 4.2 The Recoverable Component in SiC MOSFETs and its Impact on Measurements

*The contents of this section were previously published in [MFJ4].*

As discussed in the previous Section 4.1, the strong recoverable component in silicon carbide (SiC) metal-oxide-semiconductor field-effect transistors (MOSFETs) can lead to entirely non-physical, negative, apparent activation energies. Besides that, there are several other peculiarities that originate from the presence of the strong recoverable component. First, it leads to a subthreshold hysteresis in conventional transfer characteristics (see Section 3.1) [157], but also to a dynamically changing on-state resistance ( $R_{on}$ ) during gate switching [154]. Unlike in silicon (Si)-based devices, a reliable measurement of the threshold voltage ( $V_{th}$ ) in reliability testing is not trivial [273], [274]. Although different annealing techniques can significantly reduce the subthreshold hysteresis [275], it is an intrinsic property of all SiC MOSFETs, including commercially available devices. In this section, the impact of the recoverable component on device parameter measurements of different commercial devices is investigated.

For this purpose, four commercially available SiC MOSFETs were tested with regard to the presence and impact of the recoverable component on  $V_{th}$  measurements and measurements of the transfer characteristic. The used devices and their key figures are listed in Table 4.2. Two of them have a trench design (see Section 1.5.2), whereas the other two devices have a double-diffused MOS (DMOS) design (see Section 1.5.1). The tested devices originate from the same voltage class ( $V_{(BR)DSS}$ ) and have a comparable input capacitance  $C_{iss}$ . Also regarding the Baliga high-frequency figure of merit (BHFFOM) (see Equation 1.5) [13], three of these devices perform similarly well. All measurements were conducted at room temperature. The measurement of the threshold voltage was conducted with custom measurement equipment (see Section 3.3) by forcing a constant drain-source current ( $I_{DS}$ ) of 1 mA at a drain-source voltage ( $V_{DS}$ ) of 0.5 V.

| Label | $V_{(BR)DSS}$<br>[V] | $V_{th}$<br>[V] | $V_{GS,min}$<br>[V] | $V_{GS,max}$<br>[V] | $C_{iss}$<br>[pF] | Design | BHFFOM<br>[ns <sup>-1</sup> ] |
|-------|----------------------|-----------------|---------------------|---------------------|-------------------|--------|-------------------------------|
| A     | 1200                 | 3.5–5.7         | –7                  | 23                  | 182               | trench | 16                            |
| B     | 1200                 | 2.7–5.6         | –4                  | 22                  | 398               | trench | 16                            |
| C     | 1200                 | 1.8–N/A         | –10                 | 25                  | 290               | planar | 7                             |
| D     | 1200                 | 2.0–4.0         | –10                 | 25                  | 259               | planar | 14                            |

**Table 4.2.** Datasheet values and properties of the four tested devices including the maximum drain-source voltage  $V_{(BR)DSS}$ , the threshold voltage  $V_{th}$ , the minimum and maximum gate-source voltage ratings  $V_{GS,min}$  and  $V_{GS,max}$ , the input capacitance  $C_{iss}$ , the design type, and the BHFFOM. Redrawn from [MFJ4].

Due to the strong recoverable component in SiC MOSFETs, the measurement itself has already a considerable impact on the determination of a device parameter. Just continuously measuring  $V_{th}$  via the feedback loop of the used measurement equipment,  $V_{th}$  starts to shift significantly within fractions of a second. This is illustrated in Fig. 4.11 for the four tested commercial MOSFETs. With respect to the shortest recovery time used, the  $V_{th}$  of device C shows the strongest shift up to almost 0.7 V after about 100 s, whereas device D shows the lowest shift. Considering that both device C and D are double-diffused MOSFETs (DMOSFETs) and the other devices are trench MOSFETs (UMOSFETs), it appears that the device design does not ultimately determine the observed shift, although it is known that the difference in the used crystal face for the channel may have an impact on the hysteresis [157].

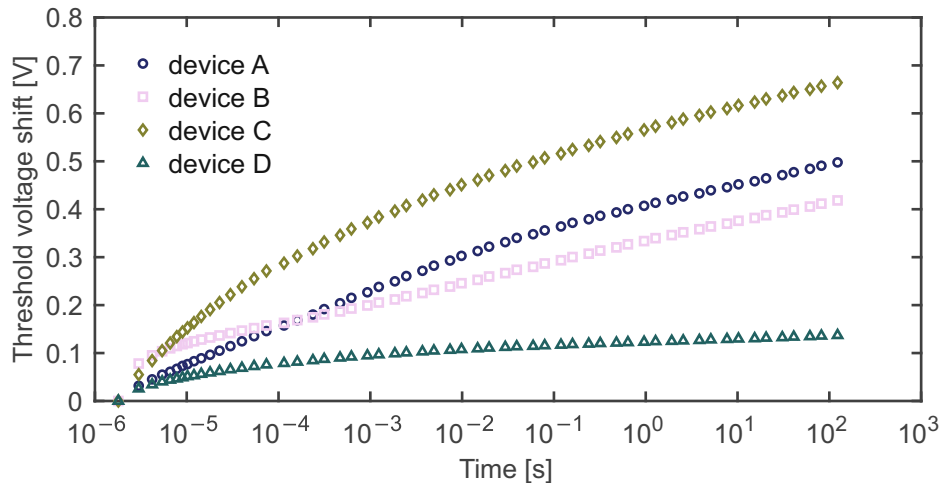


**Figure 4.11.** Evolution of threshold voltage shift ( $\Delta V_{th}$ ) while continuously measuring  $V_{th}$  of all tested devices A–D. During this  $V_{th}$  measurement,  $V_{th}$  is applied to the gate terminal which triggers electron trapping (constant  $I_{DS} = 1$  mA,  $V_{DS} = 0.5$  V, at room temperature). Redrawn from [MFJ4].

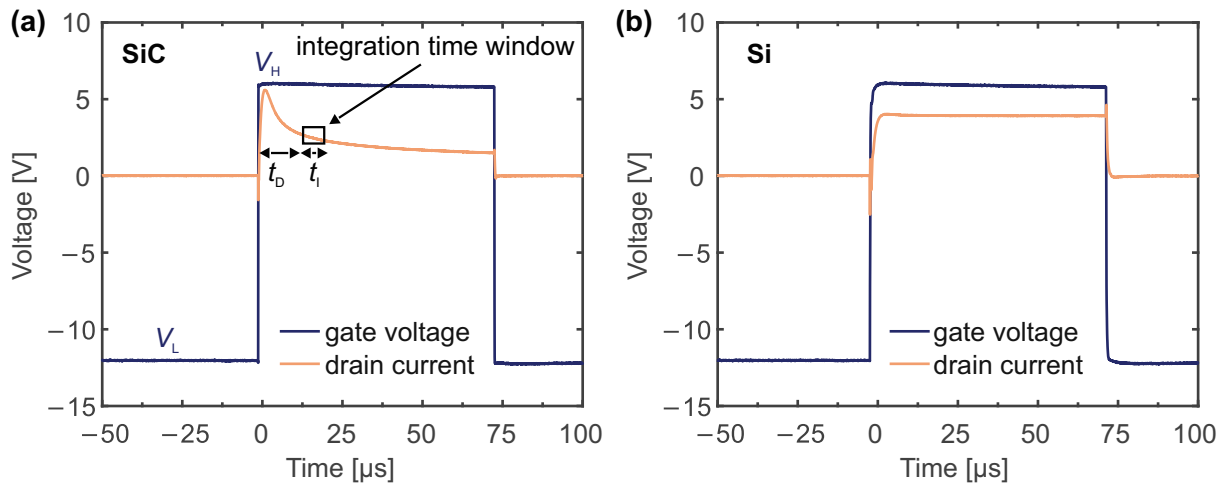


**Figure 4.12. (a)** Evolution of the gate voltage and a signal being proportional to the drain-source current over a  $70 \mu\text{s}$  gate pulse from  $V_L = -12$  V to  $V_H = 6$  V. The measurement delay time  $t_D$  and the integration time  $t_I$  are exemplarily indicated for a particular readout. After an initial overshoot of the current signal, it decreases monotonously during the gate-source voltage ( $V_{GS}$ ) pulse. **(b)** The same measurement conducted for comparison using a Si MOSFET. Here, neither an overshoot nor a significant decrease of the current signal is observed. Redrawn from [MFJ4].

As already pointed out in Section 1.4, SiC MOSFETs are predominantly used in applications where the gate terminal is switched between the on-state and the off-state with a high frequency up to hundreds of kilohertz. Due to its increased magnitude in SiC devices, the impact of the recoverable component on  $I_{DS}$  is more significant than in Si-based devices. Fig. 4.12 shows a gate pulse from a negative gate-source voltage ( $V_{GS}$ ) of  $-12$  V to a positive  $V_{GS}$  of  $6$  V for a SiC- and a Si-based MOSFET, respectively. The strong recoverable component in the SiC device leads to a significant overshoot of  $I_{DS}$ . In contrast to the application condition of fast switching between two voltage levels, a transfer curve is typically measured by slowly sweeping  $V_{GS}$  at a constant  $V_{DS}$  (see Section 3.1). During the sweep, previously trapped charges detrap and other charges get trapped, which dynamically influences the shape of the transfer curve [157]. In order to have a more application-relevant transfer curve, the measurement of the transfer curve must involve a pulsed  $V_{GS}$ , where the high level  $V_H$  is swept while keeping the low level  $V_L$  constant.

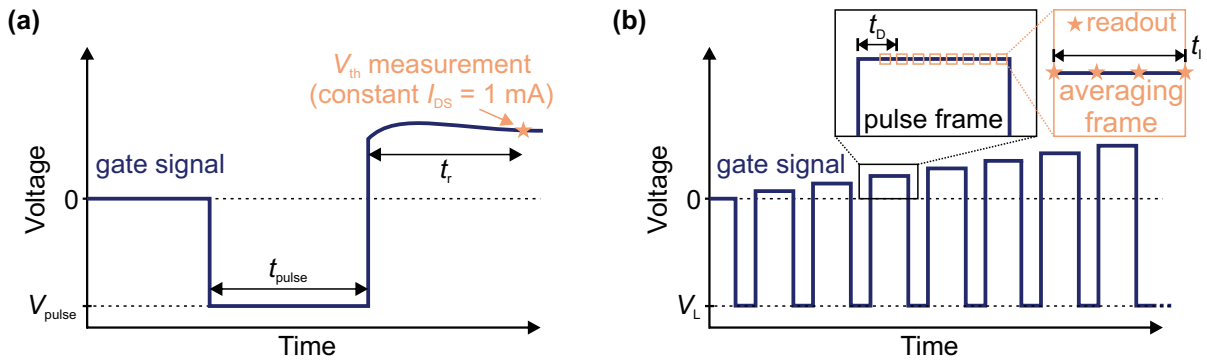


**Figure 4.13.** (a) The measurement sequence for short pulses. (b) The measurement sequence for gate-pulsed transfer characteristics. For each high level  $V_H$  (pulse frame),  $I_{\text{DS}}$  is measured within several averaging frames with a length of  $3.6 \mu\text{s}$ , each consisting of several  $I_{\text{DS}}$  readouts. Each averaging frame is triggered after a certain delay time  $t_D$  after the start of the pulse, ranging from  $7 \mu\text{s}$  to  $67 \mu\text{s}$ .

In the following Section 4.2.1, both the shift and the subsequent recovery of  $V_{\text{th}}$  of such short pulses are analyzed for the four commercial devices. Afterwards, Section 4.2.2 then contains an analysis of the mentioned gate-pulsed transfer characteristic and its parameter dependencies. Finally, device conditioning [276], [277] for reliability testing is analyzed by measuring the recovery of  $V_{\text{th}}$  after short double pulses.

#### 4.2.1 Threshold Voltage Shift after Short Gate Pulses

First, the four devices are analyzed with respect to their response in  $V_{\text{th}}$  to short gate pulses. The measurement principle is schematically illustrated in Fig. 4.13a. Each measurement consists of a pulse with a certain length  $t_s$  and with a voltage  $V_{\text{pulse}}$  that is applied to the gate terminal while both drain and source terminals are grounded. At the end of the pulse,  $V_{\text{DS}}$  is set to  $0.5 \text{ V}$  and the feedback loop at the gate terminal forces  $I_{\text{DS}} = 1 \text{ mA}$ . All the measurements are additionally separated by a period of  $2 \text{ min}$  during which all terminals are grounded to allow the device to return to its pristine state. In order to determine the threshold voltage shift ( $\Delta V_{\text{th}}$ ) of a particular pulse, the measured recovery curve is compared to a recovery curve without a preceding pulse at the gate terminal.

The resulting recovery curves of  $\Delta V_{\text{th}}$  of all four devices are shown in Fig. 4.14 for pulse voltages of both  $18 \text{ V}$  and  $-12 \text{ V}$ . Note that for such low recovery times down to  $1.8 \mu\text{s}$  and a pulse length of  $100 \text{ ms}$ ,  $\Delta V_{\text{th}}$  reaches up to around  $2.5 \text{ V}$  and down to  $-3 \text{ V}$ , depending on the device and the pulse voltage. For the negative pulse voltage, the UMOSFETs A and B exhibit a higher drift compared to the DMOSETs C and D.

For all the devices,  $\Delta V_{\text{th}}$  increases with increasing pulse length on a logarithmic time scale. Fig. 4.15 shows the corresponding  $\Delta V_{\text{th}}$  as a function of the pulse length for both pulse voltages of  $-12 \text{ V}$  and  $18 \text{ V}$ , respectively. For a pulse voltage of  $-12 \text{ V}$ , the two UMOSFETs show the strongest dependence of  $\Delta V_{\text{th}}$  on the pulse length up to about  $1 \text{ ms}$ , whereas  $\Delta V_{\text{th}}$  of the two DMOSETs has a linear relation to the logarithm of the pulse length. Regarding a pulse voltage of  $18 \text{ V}$ , all the devices show approximately a linear increase in  $\Delta V_{\text{th}}$  with the logarithm of the pulse length. In contrast to the  $-12 \text{ V}$  pulse, the  $18 \text{ V}$  pulse leads to a higher  $\Delta V_{\text{th}}$  in the DMOSETs than in the UMOSFETs.

Furthermore, increasing the absolute value of the pulse voltage significantly increases  $\Delta V_{\text{th}}$  as well, as illustrated in Fig. 4.16. Although the two shown pulse lengths of  $1 \mu\text{s}$  and  $100 \text{ ms}$  differ



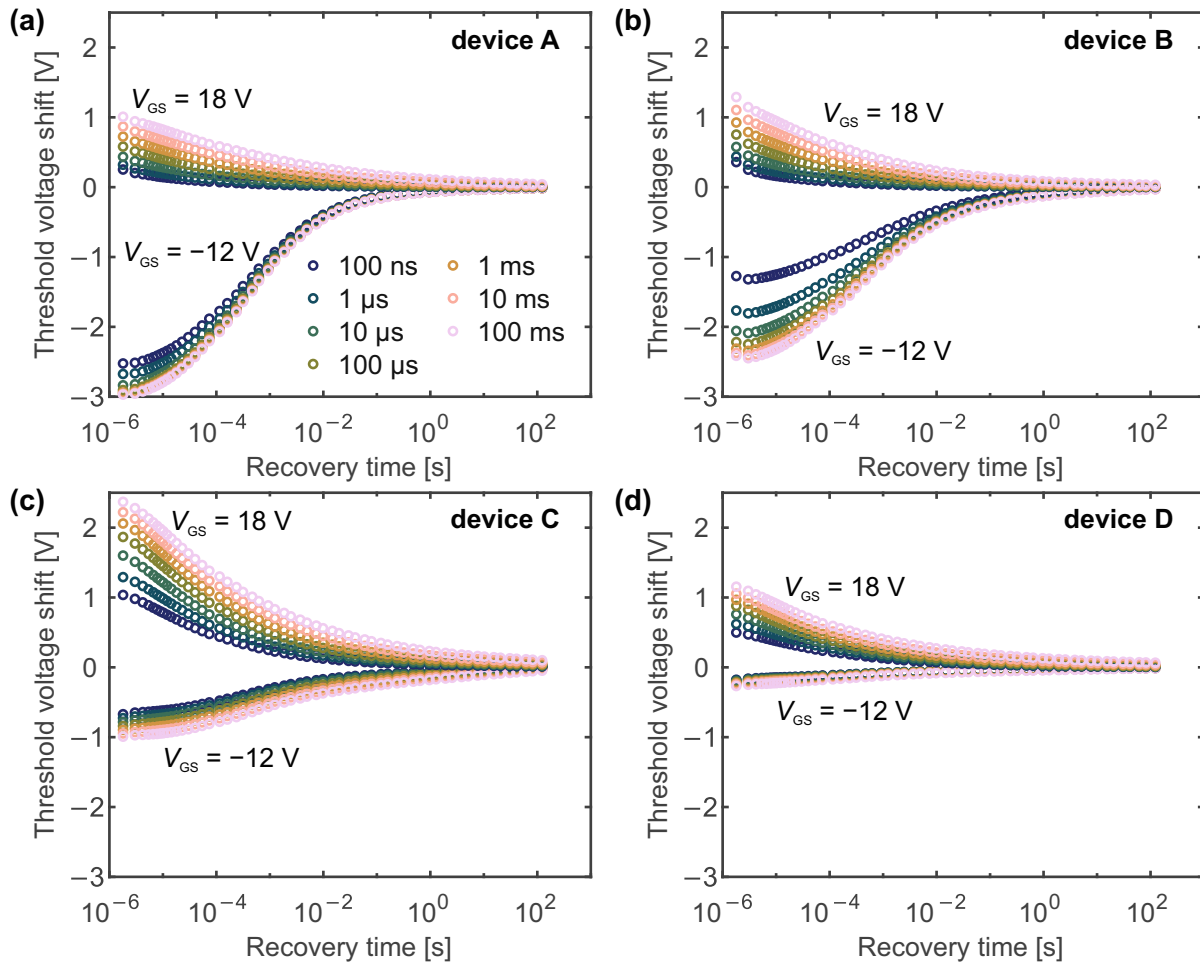


**Figure 4.14.** Recovery of  $\Delta V_{th}$  after positive gate pulses of 18 V ( $\Delta V_{th} > 0$ ) and negative pulses of -12 V ( $\Delta V_{th} < 0$ ) for various pulse lengths  $t_s$  between 100 ns and 100 ms. The plots (a)–(d) show these recovery curves of the tested devices A–D. Redrawn from [MFJ4].

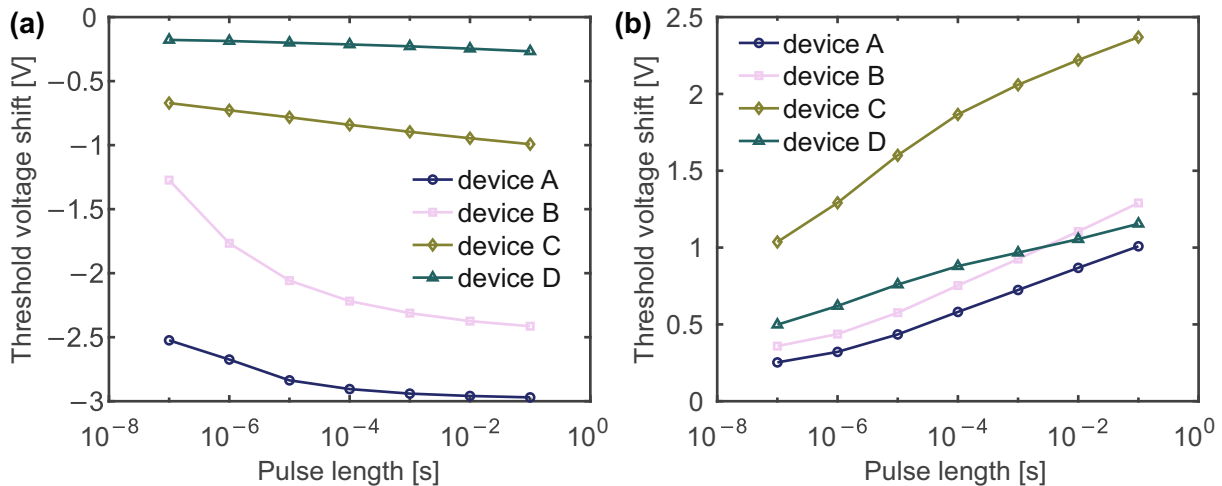


**Figure 4.15.** Dependence of  $\Delta V_{th}$  on the pulse length obtained using the shortest recovery time of 1.8  $\mu$ s. The plots compare the tested devices A–D using pulse voltages of (a) -12 V and (b) 18 V. Redrawn from [MFJ4].

by five orders of magnitude in time, the observed pulse voltage dependence is very similar for negative  $V_{pulse}$ , whereas for positive  $V_{pulse}$ , the observed  $\Delta V_{th}$  more than doubles its value. The

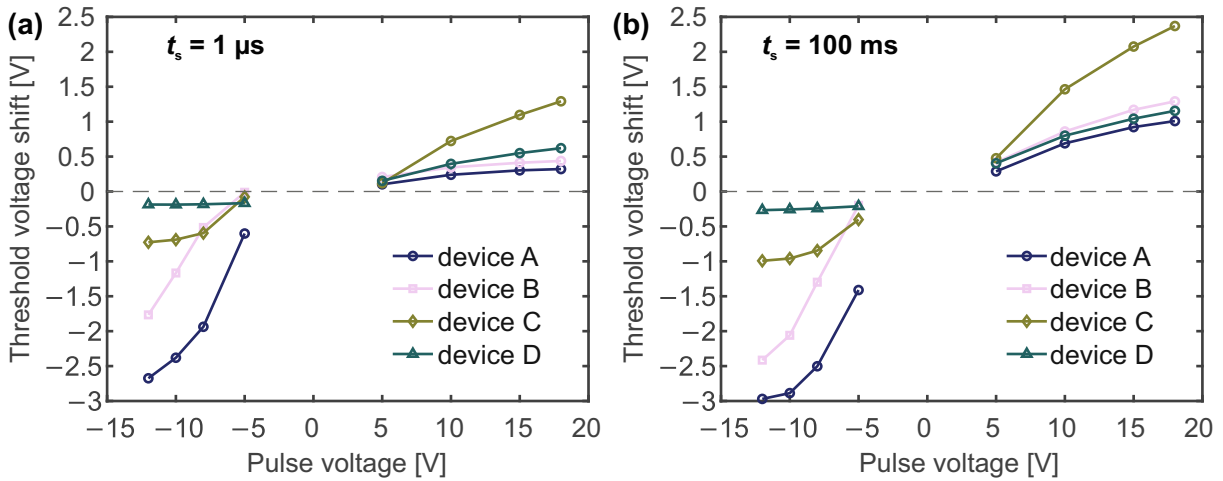


**Figure 4.16.** Dependence of  $\Delta V_{th}$  on the pulse voltage obtained using the shortest recovery time of  $1.8 \mu s$ . The plots compare the tested devices A–D using pulse lengths of (a)  $1 \mu s$  and (b)  $100 ms$ . Redrawn from [MFJ4].

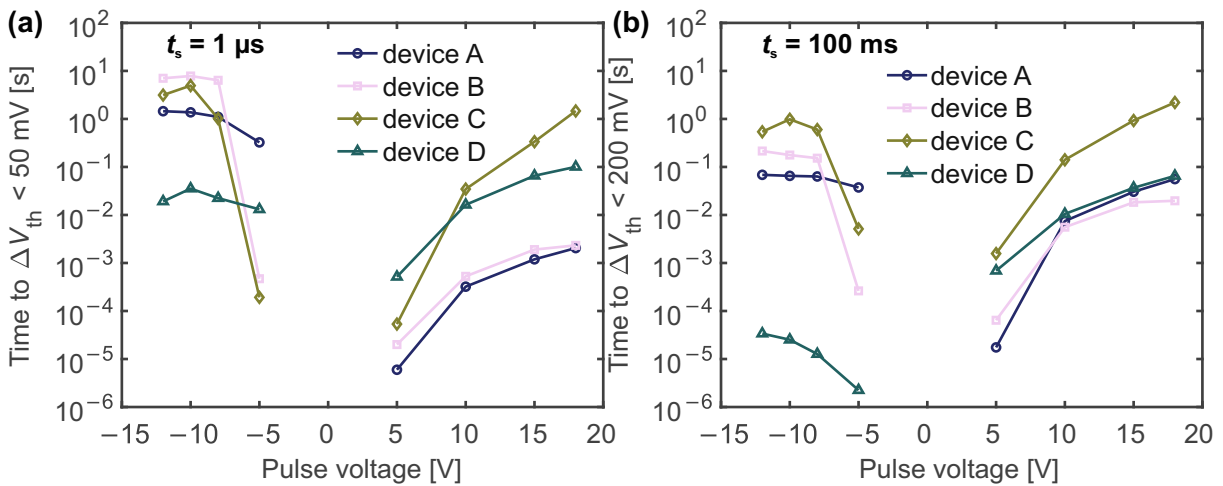


**Figure 4.17.** Dependence of the recovery time necessary to reach a  $\Delta V_{th}$  lower than a certain limit on the pulse voltage for a pulse length of (a)  $1 \mu s$ , a limit of  $50 mV$  and for a pulse length of (b)  $100 ms$  and a limit of  $200 mV$ . Redrawn from [MFJ4].

qualitative behavior of the two trench devices A and B is very similar. In particular for negative  $V_{pulse}$ , they exhibit a strong decrease of  $\Delta V_{th}$  with decreasing  $V_{pulse}$ . Apart from C, which is interestingly also the device with the worst BHFFOM, all devices show a similar behavior for positive  $V_{pulse}$ .

Overall, the recoverable component in SiC MOSFETs hence imposes challenges to device parameter measurements. A considerable charge corresponding to several volts of  $\Delta V_{th}$  is trapped at the SiC/silicon dioxide ( $SiO_2$ ) interface and can be built up within a microsecond gate pulse, however, it needs many more decades in time to fully recover back. Fig. 4.17 illustrates the time that devices need to recover to a certain limit in  $\Delta V_{th}$  after  $1 \mu s$  and  $100 ms$  long pulses, whereby the limits are set to  $50 mV$  and  $200 mV$ , respectively. For a negative  $V_{pulse}$ , the devices A, B, and C show similar values for this time in the range of  $1-10 s$  and  $0.1-1 s$  after the two different pulses, respectively. Device D shows much smaller values, because it exhibits in general a lower response in  $\Delta V_{th}$  to negative  $V_{pulse}$ . Concerning the dependence on negative  $V_{pulse}$ , the time to reach the limit is roughly a constant once a certain threshold in  $V_{pulse}$  has been

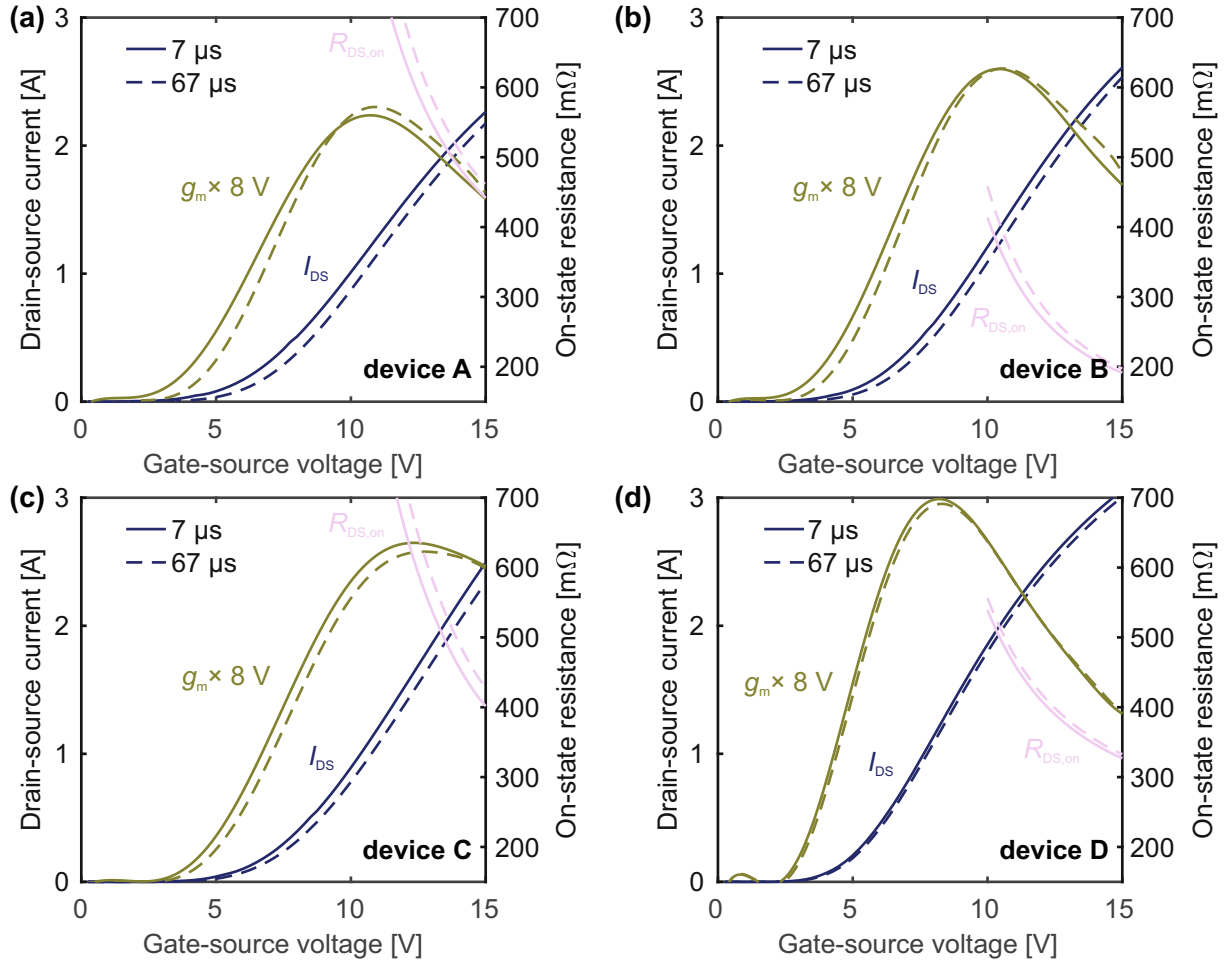


**Figure 4.18.** Impact of different delay times  $t_D$  on  $I_{DS}$ , transconductance  $g_m$ , and on-state resistance  $R_{DS,on}$  using a low level of  $-14$  V. While the off-state time was set to  $1$  ms,  $V_{DS}$  was set to  $1$  V (except for device B using  $V_{DS} = 0.5$  V). The plots (a)–(d) correspond to the tested devices A–D. The longer delay time leads to a reduced  $I_{DS}$  and increased  $R_{on}$ . Redrawn from [MF]4).

passed. In contrast to that, the time continuously increases for a positive  $V_{pulse}$  with increasing  $V_{pulse}$ . Furthermore, the trench devices seem to reach the limit faster for positive  $V_{pulse}$  than the DMOSETs. Overall, the recoverable component shows a strong asymmetry between the capture of the charge and its emission.

#### 4.2.2 Impact of the Recoverable Component on the Pulsed Transfer Characteristics

As already discussed in Section 3.1, a transfer characteristic that is measured by slowly sweeping  $V_{GS}$  at a constant  $V_{DS}$  is affected by the recoverable component of bias temperature instability (BTI) in SiC MOSFETs. In order to avoid self-heating, the applied  $V_{DS}$  is typically pulsed in order to minimize the dissipated power and keep the device at a constant temperature. In Si-based MOSFETs with their much weaker recoverable component, this measurement technique works flawlessly. However, in SiC MOSFETs, everything that is related to the timing of the measurement or the voltages applied before or during the measurement affect the shape of the measured transfer characteristic. This is caused by vivid trapping and detrapping dynamics during the measurement, which is caused by the applied  $V_{GS}$  and involves shifts in  $\Delta V_{th}$  on the order of several volts (see Fig. 4.14).

Consequently, there is a clear need for an alternative measurement of the transfer characteristic. Considering that most applications of SiC MOSFETs require continuous switching of  $V_{GS}$  at a frequency up to hundreds of kilohertz (see Section 1.4), pulsing  $V_{GS}$  instead of  $V_{DS}$  is a better approach. This is illustrated in Fig. 4.13b. Hereby,  $V_{GS}$  is pulsed between a constant low level  $V_L$ , that is applied for 1 ms and a successively increasing high level  $V_H$ .  $V_L$  can be chosen in such a way that it mimics the off-state voltage of a specific application. As shown in Fig. 4.12, the trapping of positive charge during the  $V_L$ -phase leads to an initially lower  $V_{th}$  and subsequently to an overshoot in  $I_{DS}$ , that is captured by this measurement scheme. Not enough that this scheme is more application-relevant than a slow  $V_{GS}$ -sweep, the  $V_L$ -phases reset the interface defects to a defined state before each pulse frame. This makes this measurement approach very reproducible and independent of potentially applied biases in the near past. However, the precise timing of the measurement during the  $V_H$ -phase is of particular importance. Each  $V_H$ -pulse (pulse frame) in Fig. 4.13b features eight averaging frames with a length of  $3.6 \mu\text{s}$ , during which the four  $I_{DS}$  measurements are conducted and averaged. Each transfer characteristic therefore provides eight  $I_{DS}$  values per  $V_H$ , measured with a reproducible and clearly defined timing with delay times between  $7 \mu\text{s}$  and  $67 \mu\text{s}$ .

From such a pulsed transfer characteristic, both the transconductance  $g_m$  and the on-state resistance  $R_{on}$  can be calculated (see Section 3.1). The most influential measurement parameters, affecting the outcome of  $I_{DS}$ ,  $g_m$ , and  $R_{on}$ , are the chosen delay time  $t_D$  and the low level  $V_L$ . In the following, their impact on the parameter measurements of the four different devices are examined.

Fig. 4.18 shows the parameter curves for the shortest delay time of  $7 \mu\text{s}$  and the longest delay time of  $67 \mu\text{s}$  for  $V_L = -14 \text{ V}$ . Apparently, the longer delay time leads to a lower  $I_{DS}$  and a subsequently increased  $R_{on}$  for all four devices. Also the transconductance shows a significant shift to higher  $V_{GS}$ , however, the fact that this shift is not constant hints towards changes in the channel mobility, because of changed Coulomb scattering [278]. Although the difference in the delay time is only  $60 \mu\text{s}$ , the increase in the measured  $R_{on}$  at  $V_{GS} = 15 \text{ V}$  reaches up to  $20 \text{ m}\Omega$  ( $\approx 5\%$ ) for device A and even  $30 \text{ m}\Omega$  ( $\approx 8\%$ ) for device C. As expected from the low shifts observed in  $V_{th}$  after short  $V_{GS}$ -pulses, device D shows the lowest impact of the chosen delay time on the transfer characteristic.

In contrast to that, Fig. 4.19 shows the parameter curves for the highest  $V_L$  of  $-0.25 \text{ V}$  and the lowest  $V_L$  of  $-14 \text{ V}$ . Here, the impact on the parameter curves is even worse than for the previously considered delay time. Generally, the lower  $V_L$  leads to an increase in  $I_{DS}$  and subsequently to a decreased  $R_{on}$ . Again, deviations from a constant horizontal shift in the transconductance hint towards changes in the channel mobility. In particular, devices A and B even show a significant reduction in their channel mobility with the lower  $V_L$ . This must be related to increased Coulomb scattering at trapped holes, captured during the  $V_L$ -phase. For device A,  $R_{on}$  is reduced by the lower  $V_L$  by  $20 \text{ m}\Omega$  ( $\approx 4\%$ ), whereas device C even shows a reduction of  $34 \text{ m}\Omega$  ( $\approx 8\%$ ).

The impact of  $V_L$  and the delay time is illustrated in Fig. 4.20 in greater detail. It shows the shift in  $I_{DS}$  as a function of  $V_L$  for different delay times. The quantities  $\Delta I_{DS}(t_D)$  and  $\Delta I_{DS}(V_L)$  are the maximum observed shift in  $I_{DS}$  caused by a change in delay time (relative to the lowest delay time) or by a change in the low level (relative to the highest  $V_L$ ), respectively. As observed for devices C and D,  $\Delta I_{DS}(V_L)$  covers a range between  $0.4\%$  and  $8.7\%$ . While devices A, B, and D show a monotonously increasing  $\Delta I_{DS}(V_L)$ , device C shows a local minimum around  $-2 \text{ V}$ .

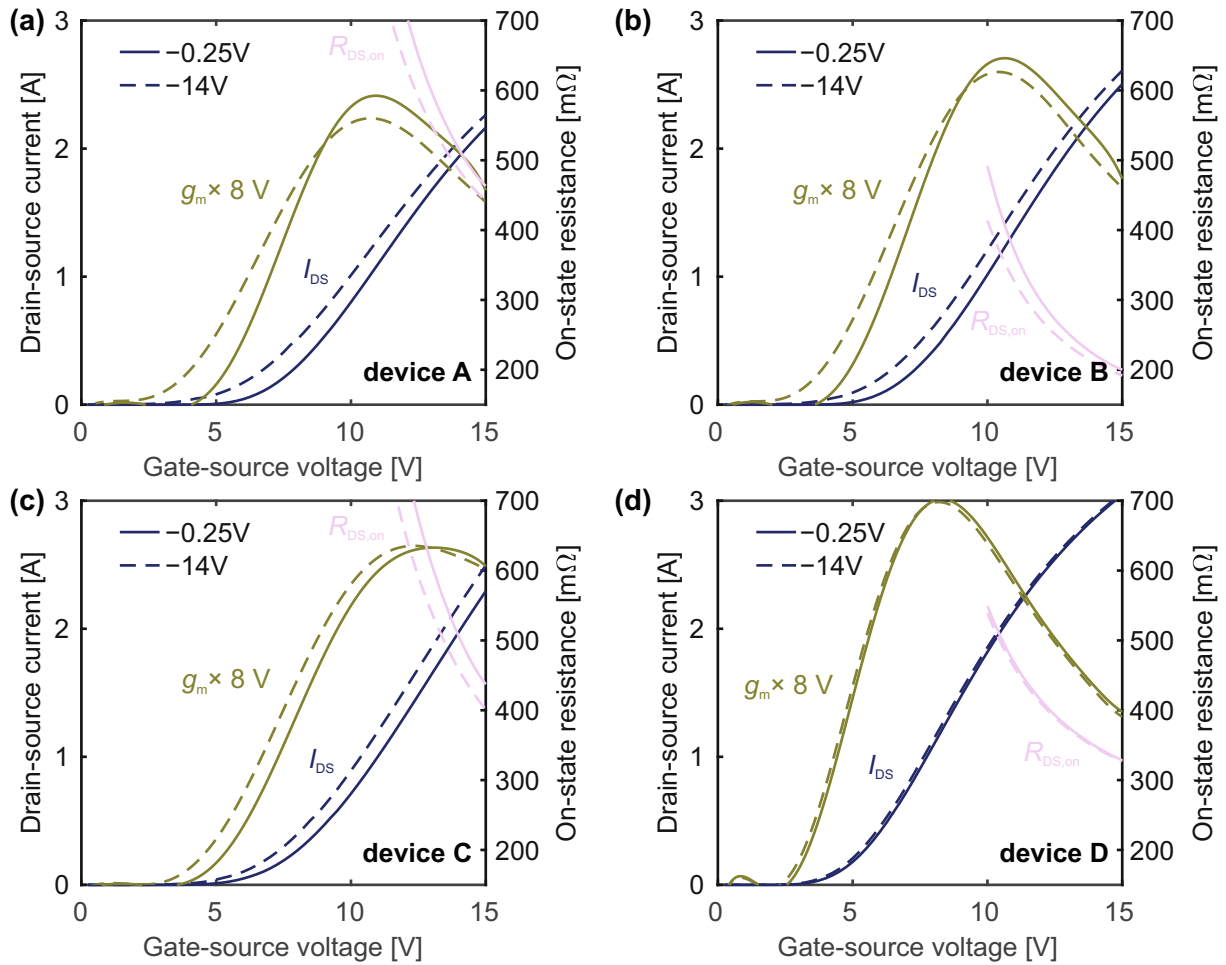


**Figure 4.19.** Impact of different low levels  $V_L$  on  $I_{DS}$ , transconductance  $g_m$ , and on-state resistance  $R_{DS,on}$  using a delay time of  $7 \mu\text{s}$ . While the off-state time was set to  $1 \text{ ms}$ ,  $V_{DS}$  was set to  $1 \text{ V}$  (except for device B using  $V_{DS} = 0.5 \text{ V}$ ). The plots (a)–(d) correspond to the tested devices A–D. The lower base voltage leads to an increased  $I_{DS}$  and decreased  $R_{on}$ . Redrawn from [MFJ4].

Consequently, from the minimum to the maximum, there are more than 10% variation in  $I_{DS}$ . The quantity  $\Delta I_{DS}(t_D)$  ranges from 0.2% (device D) up to 2.5% (device A).

Overall, the results show that the impact of the recoverable component on the parameter measurements is not a matter of the device design (compare devices A and C). It is inherently present in all SiC MOSFETs. It is important to note that this way to measure the transfer characteristic is not only relevant for small  $V_{DS}$ , the recoverable component is equally influential under more application-relevant high  $V_{DS}$ . This is illustrated in Fig. 4.21 that shows four transfer characteristics that are measured by quickly sweeping the gate bias from different starting voltages upwards within a time of  $5 \mu\text{s}$ .

### 4.2.3 Conditioning of Threshold Voltage Measurements

Reliability testing demands a clear understanding of what is actually required to be tested. Suppose there would be a way to measure the  $V_{th}$  of a SiC MOSFET without changing the occupancy of the defects at the SiC/SiO<sub>2</sub> interface. A stress test that exposes the MOSFET for a certain stress time to a positive  $V_{GS}$  which triggers the trapping of charges will lead to a  $\Delta V_{th}$  that includes a contribution from the recoverable component. The data would not reflect the

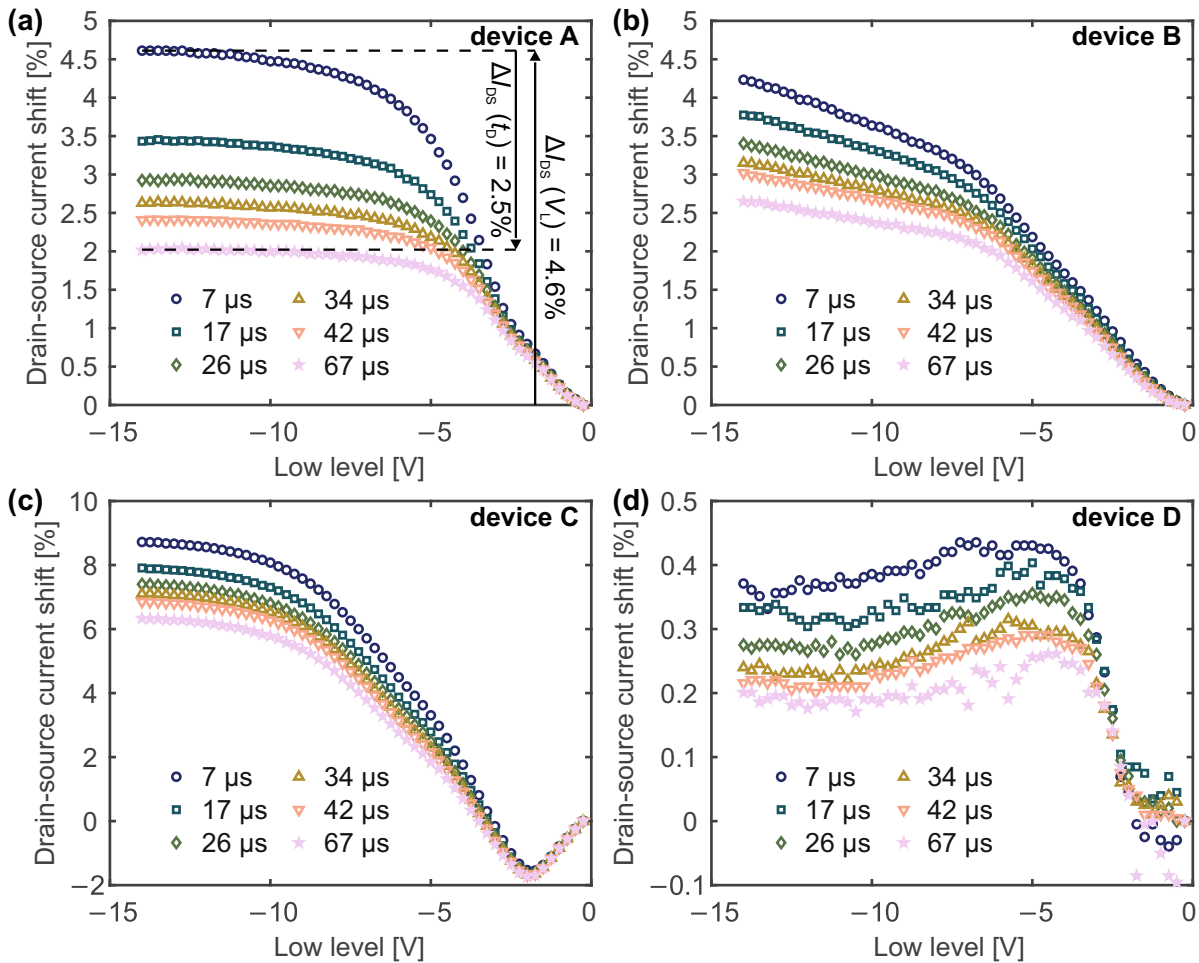


**Figure 4.20.** Normalized change in  $I_{DS}$  for different delay times  $t_D$ . The plots (a)–(b) correspond to the devices A–D. As indicated in (a), the quantities  $\Delta I_{DS}(t_D)$  and  $\Delta I_{DS}(V_L)$  are the maximum induced change in  $I_{DS}$  caused by a change of the delay time (relative to  $7 \mu\text{s}$ ) and by lowering the low level (relative to  $-0.25 \text{ V}$ ). Redrawn from [MFJ4].

fact that this component, which would be a major part of the observed drift in  $V_{th}$ , is completely recoverable and can be easily removed by applying a negative  $V_{GS}$  for a very short time. In an application-like operation mode, the recoverable component would anyway be charged and discharged each time the MOSFET is switched. The conclusion must be that the recoverable component should not be part of any considerations regarding long-term device instability. This is the reason why device conditioning was introduced [273], [276], [277], [279], [280]. The essence of device conditioning is that a pulse of a certain voltage and length brings the defects constituting the recoverable component into a defined state of occupancy. If each readout of the test is carried out in exactly the same way and if the degradation mechanism that occurs during the stress does not affect the recoverable component, the recoverable component cancels out. Device conditioning is consequently a valuable and suitable approach in reliability testing.

However, in cases where the timing of the readouts is not sufficiently reproducible, the defects need to be brought to a state that is close to thermal equilibrium at a defined voltage, e.g.  $V_{GS} = 0 \text{ V}$ . For this to be useful in a practical setting, the time to reach thermal equilibrium should be as short as possible. In the following, a  $20 \text{ V}$  and  $1 \text{ s}$  long  $V_{GS}$ -pulse is used to bring the interface defects of the recoverable component out of equilibrium. Such a pulse could easily arise during a readout procedure in a typical reliability test. This already leads to a  $\Delta V_{th}$  of about  $1 \text{ V}$

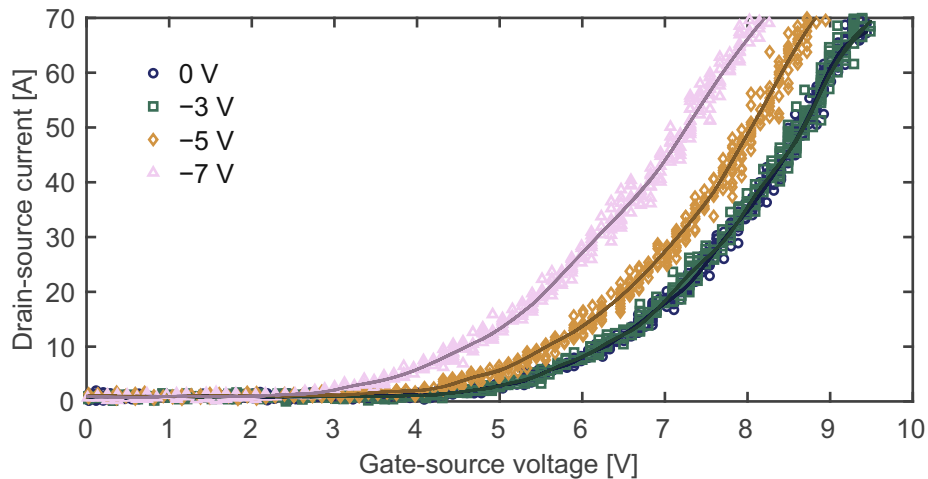


**Figure 4.21.** Fast transfer curves gate voltage sweeps starting from different gate voltages.  $V_{GS}$  is swept up to 15 V within 5  $\mu$ s at a drain-source voltage of 800 V and at 25  $^{\circ}$ C. Solid lines indicate the evolution of  $I_{DS}$  based on robust local regression smoothing. Although transfer curves with starting voltages of 0 V and  $-3$  V agree, the transfer curves using starting voltages of  $-5$  V and  $-7$  V are significantly shifted towards lower  $V_{GS}$ . This is caused by a transient  $\Delta V_{th}$ . Redrawn from [MFJ4].

that takes a long time of about 20–30 s to let the device return to thermal equilibrium. As it turns out, this time can be significantly shortened by applying a consecutive negative  $V_{GS}$ -pulse of a voltage  $V_L$  for a certain time  $t_L$ . Fig. 4.22 shows the recovery curves of  $\Delta V_{th}$  after such a scheme for various combinations of  $V_L$  and  $t_L$ . Here,  $t_L$  covers seven orders of magnitude from 1  $\mu$ s up to 10 s, while  $V_L$  was varied between  $-3$  V and  $-12$  V. Apparently, the impact of lowering  $V_L$  is much stronger than increasing  $t_L$ . Most importantly, the recovery curves gradually merge with decreasing  $V_L$ . At  $V_L = -12$  V, the recovery traces practically do not significantly depend on  $t_L$  anymore. Consequently, a  $-12$  V pulse brings the recoverable component in a state where the impact of the 1 V pulse vanished completely and the recoverable component is saturated. Fig. 4.23 shows the time of each recovery curve in Fig. 4.22 that is needed to reach a limit of  $\Delta V_{th} < 100$  mV. All times of recovery curves with  $V_L \leq -6$  V do not differ significantly and show time constants up to 440 ms. As already mentioned, without a negative pulse the device would require about 20–30 s to reach the same limit. Consequently, the use of the negative pulse significantly reduces the time to reach thermal equilibrium by about two orders of magnitude. This makes this approach a suitable technique for reliability testing where the reproducibility of the readout procedure that includes conditioning pulses cannot be guaranteed.

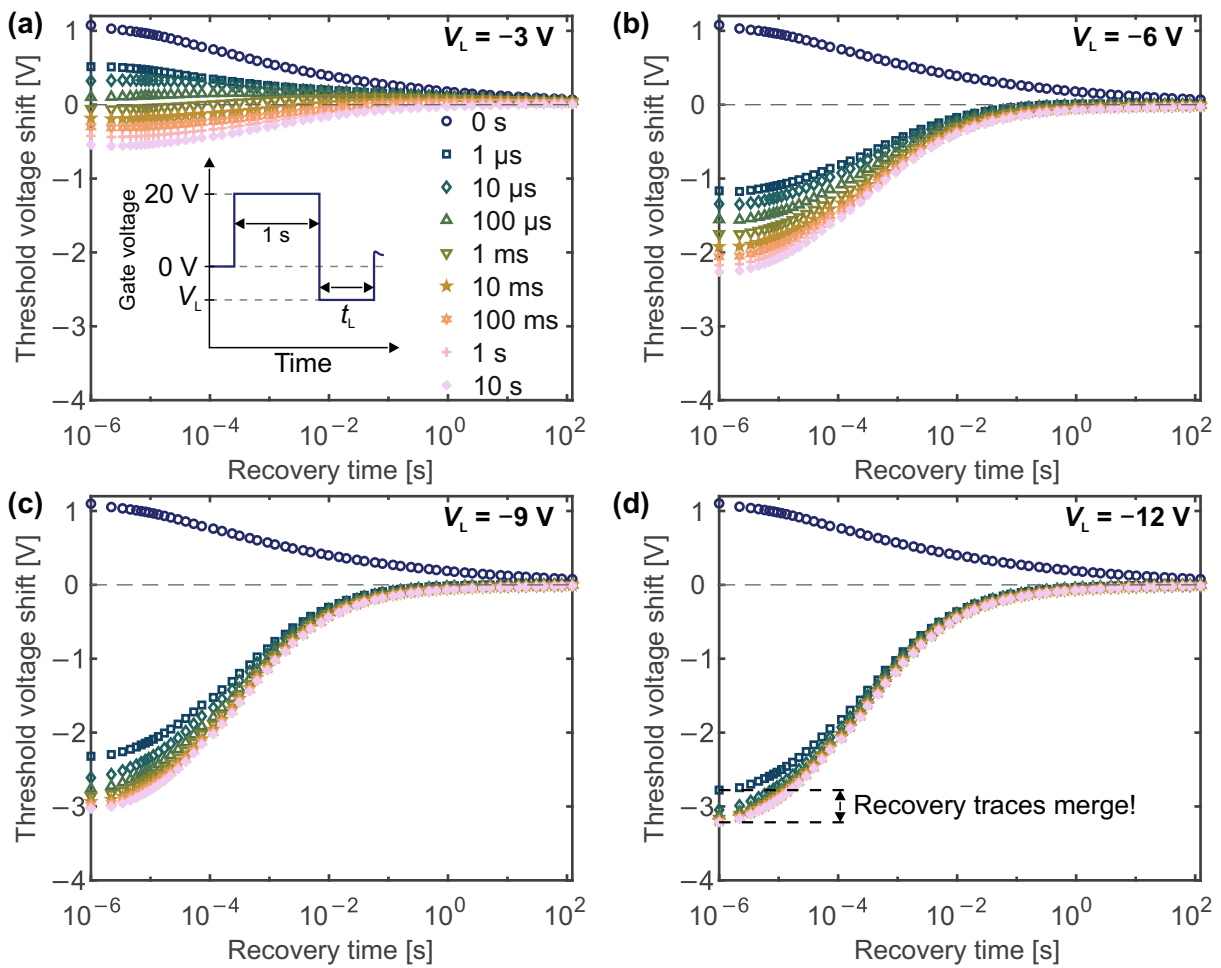


**Figure 4.22.** Recovery of  $\Delta V_{th}$  of device A without (0 s) and with conditioning pulses. The length of the conditioning pulse was varied between  $1 \mu\text{s}$  and 10 s. The plots (a)–(d) correspond to the voltage  $V_L$  of the conditioning pulse between  $-3 \text{ V}$  and  $-12 \text{ V}$ . As illustrated in the inset in (a), the measurement scheme consists of the stress pulse (20 V for 1 s) and the following conditioning pulse before the measurement. For a conditioning voltage of  $-3 \text{ V}$  and pulse lengths between  $1 \mu\text{s}$  and  $100 \mu\text{s}$ , the measured  $\Delta V_{th}$  is positive. For all other conditioning pulses, the sign of  $\Delta V_{th}$  changes. Redrawn from [MF]4).

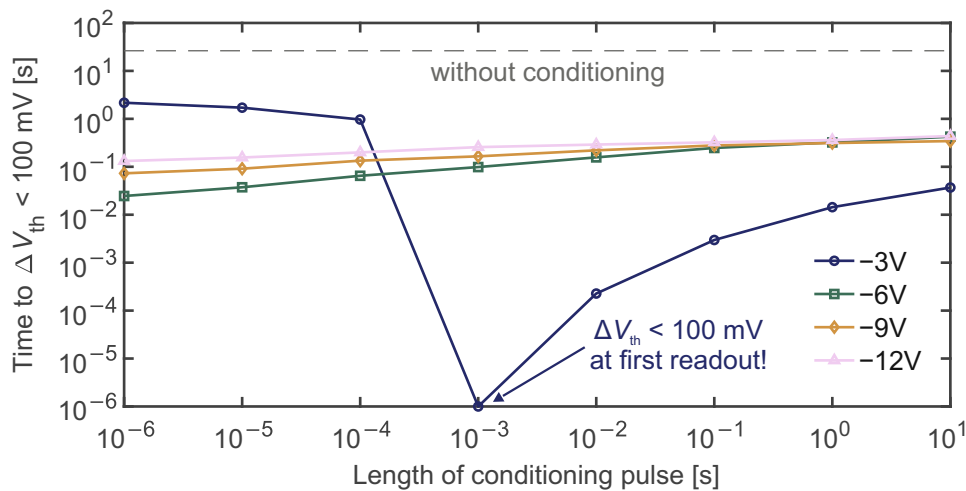


**Figure 4.23.** Recovery time to reach a  $\Delta V_{th}$  lower than 100 mV as a function of the length of the conditioning pulse for different voltages  $V_L$  of the conditioning pulse. Redrawn from [MF]4).



## 4.3 Gate Switching Instability

The contents of this section were previously published in [MFC2], [MFC4], [MFC5], [MFJ5], [MFJ6], [MFC6]. The paper “Towards Understanding the Physics of Gate Switching Instability in Silicon Carbide MOSFETs” [MFC2] received the Best Student Paper Award of the IEEE 2023 International Reliability Physics Symposium (IRPS) and the paper “Recent Developments in Understanding the Gate Switching Instability in Silicon Carbide MOSFETs” [MFC5] was an invited talk at the IEEE 2023 International Integrated Reliability Workshop (IIRW).

As presented in Section 1.4, the benefits of silicon carbide (SiC) metal-oxide-semiconductor field-effect transistors (MOSFETs) are particularly evident in energy conversion applications, which require continuous operation under high switching frequencies – up to hundreds of kilohertz. The devices are switched between an on-state voltage (typically 15–20 V) and an off-state voltage (typically  $-5-0$  V) [50], [281], [282]. In automotive applications, SiC MOSFETs are switched up to  $10^{11}$  times, whereas industrial applications range up to  $3 \times 10^{13}$  switching cycles [MFC7], [MFJ7]. Consequently, this mode of continuous switching is of major importance for any reliability and lifetime considerations.

It is exactly under the above mentioned switching operation where a recently discovered degradation mechanism appears that exclusively occurs in SiC MOSFETs. Compared to the previously discussed bias temperature instability (BTI) with its strong recoverable component, it has completely different properties. This degradation mechanism leads to a significant increase in the threshold voltage shift ( $\Delta V_{th}$ ) over time upon extensive switching of the gate-source voltage ( $V_{GS}$ ) [MFC7], [283]. In contrast to BTI, time and temperature are not any longer the driving forces of the degradation – it is the switching event itself that degrades the device [MFC4]. This is why this degradation mechanism was recently termed gate switching instability (GSI) [MFJ7]. The corresponding stress mode is referred to as gate switching stress (GSS). At the moment, the underlying physical mechanism is still under discussion [MFC5].

First, the history of GSI is outlined, followed by a description of the most important experimental characteristics, leading to a list of requirements that an underlying physical mechanism must fulfill. Next, these characteristics and requirements of an underlying physical mechanism are used to rule out a recently proposed mechanism based on locally-enhanced electric field and finally, to link GSI to recombination-enhanced defect reactions (REDRs) (see Section 2.1.3).

### 4.3.1 A Brief Historic Review of Gate Switching Instability

The history of GSI started in the year 2018, when Infineon Technologies AG published an application note [284] that described the existence and basic features of GSI, that is observed as an increased drift in threshold voltage ( $V_{th}$ ) upon switching a SiC MOSFET continuously between its on-state and off-state. As explained in Section 3.1, a drift in  $V_{th}$  leads to a drift of the channel resistance and thus of the total on-state resistance ( $R_{on}$ ) of the power MOSFET, which makes GSI highly relevant for the reliability of these devices. The motivation of this application note was to provide practical guidance for considering this new drift mechanism in applications. A few dependencies of GSI were already pointed out that are listed below.

- Dependence on the cumulative number of switching cycles
- Dependence on the high and low levels of  $V_{GS}$

- Impact of over- and undershoots of  $V_{GS}$
- Transition times of  $V_{GS}$

These and other dependencies will be discussed in detail later. Following this application note, Infineon published a whitepaper in 2020, that contained a more detailed description and model of this mechanism [285]. Also, a saturation of the drift in  $V_{th}$  was reported. A little later, Jiang *et al.* published the first scientific article [283] on GSI. The article described GSI as a mechanism that exclusively occurs if the MOSFET is turned off with a negative  $V_{GS}$  and that the drift increases for a fixed stress time with increasing switching frequency. Note that this is a fundamental difference to BTI, but this will be discussed later in greater detail. The authors also observed that the caused  $\Delta V_{th}$  seemed to be of a rather permanent character – it did not recover. In 2021, Salmen *et al.* published a more industrial perspective on GSI, in which the authors presented an approach to measure and evaluate GSI in reliability testing and determine the end-of-life drift [MFC7]. Besides that, the authors observed that GSI does not significantly affect the gate leakage current. In the years after, numerous ( $> 15$ ) scientific papers have been published on the topic of GSI. This strong resonance is for sure linked to the importance of understanding and finally mitigating GSI in commercial SiC MOSFETs. For the moment, this degradation mode can be observed in all commercially available devices [286] and therefore seems to be an intrinsically present phenomenon in SiC MOSFETs. The importance of GSI for all semiconductor manufacturers of SiC MOSFETs finally manifested itself in a new guideline recently launched by the Joint Electron Device Engineering Council (JEDEC) [287].

### 4.3.2 Measuring Gate Switching Instability

As discussed in Section 4.2.3, measuring long-term device parameter instabilities ideally excludes the recoverable component – as long as the recoverable component is not affected by the stress. In this context, device conditioning is a good option [273], [276], [277]. As demonstrated by Salmen *et al.*, this approach can equally be used for GSI stress tests because GSI does not affect the recoverable component [MFC7], [MFJ7].

In the course of this work, a different approach was used that is illustrated in Fig. 4.24a. In principle, this approach follows a conventional measure-stress-measure (MSM) scheme and is performed using the custom setup described in Section 3.3. The stress phase consists of continuous gate switching between a high level  $V_H$  and a low level  $V_L$  at a certain frequency with fixed rise and fall times of  $V_{GS}$  (typically 50 ns). The switching is controlled by a pulse-width modulation (PWM) signal that operates solid state switches alternately connecting the  $V_H$  and  $V_L$  sources to the gate terminal. As the time constant of charging the input capacitance  $C_{iss}$  of the MOSFET can be influenced by changing the output resistor of the respective voltage source (see Fig. 3.5), the rise and fall times of the stress signal can be varied separately.

It is important to note that  $C_{iss}$  of a particular device together with other circuit components of the measurement system limit the maximum switching frequency that can be used. Let  $\Delta V = |V_H - V_L|$  be the difference between the high and low levels, then  $C_{iss}$  stores an energy per pulse of  $E = (1/2)C_{iss}(\Delta V)^2$ . At a switching frequency  $f_{sw}$ , the measurement setup needs to supply an output power of  $P = Ef_{sw}$ . Even a rather small power MOSFET with  $C_{iss} = 1$  nF stressed with a typical  $\Delta V = 30$  V at a frequency of  $f_{sw} = 500$  kHz requires already an output power of  $P = 225$  mW. Furthermore, the involved solid state switches in this example would need to be able to withstand a peak current of  $I_{peak} = \Delta V/R = 3$  A and an average current of

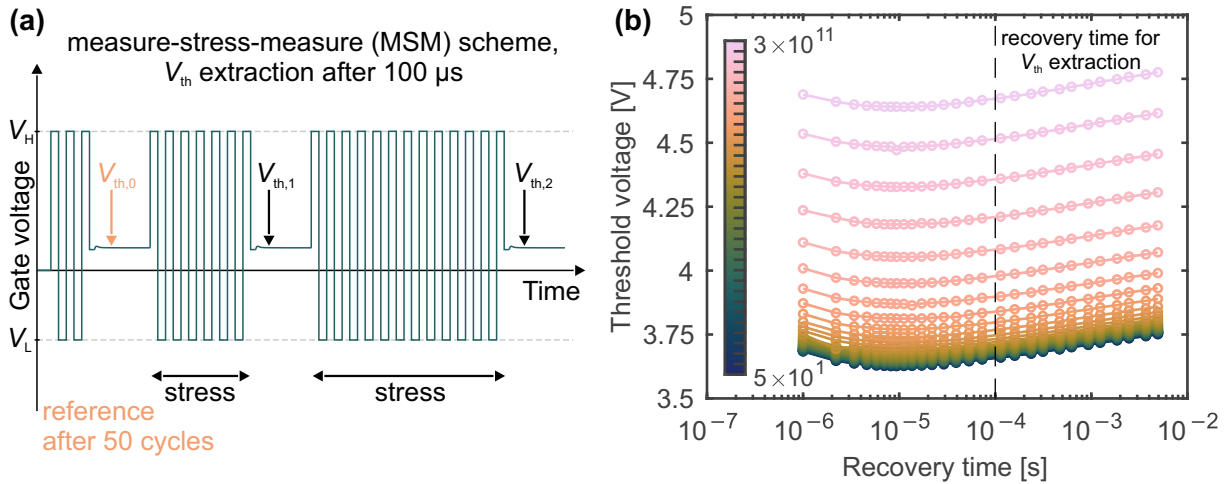


**Figure 4.24.** (a) Schematic illustration of the measure-stress-measure (MSM) scheme used to measure GSI. (b) Exemplary recovery curves from a measurement with  $V_H = 20\text{ V}/V_L = -10\text{ V}$  with a switching frequency of 500 kHz, a duty cycle of 50 %, and rise and fall times of 50 ns at a temperature of 175 °C. The reference  $V_{th}$  is extracted after  $10^{-4}\text{ s}$ . The readouts are logarithmically distributed between  $5 \times 10^1$  and  $3 \times 10^{11}$  switching cycles. Redrawn from [MFC4].

$I_{ave} = f_{sw} C_{iss} \Delta V = 15\text{ mA}$ .  $R$  denotes here the external gate resistor of the respective voltage source in the measurement setup (see Fig. 3.5). These considerations need to be taken into account when GSI experiments are conducted.

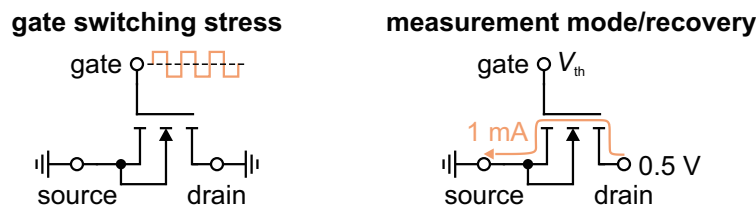


**Figure 4.25.** Stress and measurement modes of a GSI experiment. Redrawn from [MFJ5].

In the used setup, the stress can reproducibly be interrupted at any phase of the stress signal, which is intentionally chosen to be at the end of the  $V_H$ -phase. After the interruption, the gate terminal is charged up to a fixed pre-charge voltage  $V_{PreChrg} \approx V_{th}$ . During the following measurement phase, the feedback loop forces an  $I_{DS} = 1\text{ mA}$  at  $V_{DS} = 0.5\text{ V}$  and the gate terminal is measured as  $V_{GS} = V_{th}$ . The stress and measurement phases are also illustrated in Fig. 4.25.

The reference measurement of  $V_{th}$  is conducted after 50 cycles of switching and measured with a delay of  $1\text{ }\mu\text{s}$ . This removes the contribution of the recoverable component in the measurement of  $\Delta V_{th}$ . As the measurement delay is precisely controlled, there is no need for any further conditioning techniques. The obtained recovery curves of an exemplary measurement are shown in Fig. 4.24b. The curves of all readouts are just vertically shifted versions of the reference readout, which confirms the validity of the measurement approach and the reproducibility of the readout procedure. Furthermore, it is also a hint that hysteresis does not significantly change over stress time. Initially, up to  $10\text{ }\mu\text{s}$ ,  $V_{th}$  decreases due to emission of previously trapped negative charges during the  $V_H$ -phase. Afterwards,  $V_{th}$  increases again, likely due to trapping of negative charges in defects with longer time constants and detrapping of a fraction of positive charges that had been trapped during the previous  $V_L$ -phase. For each readout, the respective  $V_{th}$  is extracted at a recovery time of  $100\text{ }\mu\text{s}$ , and the resulting drift is calculated as  $\Delta V_{th} = V_{th} - V_{th,0}$ .

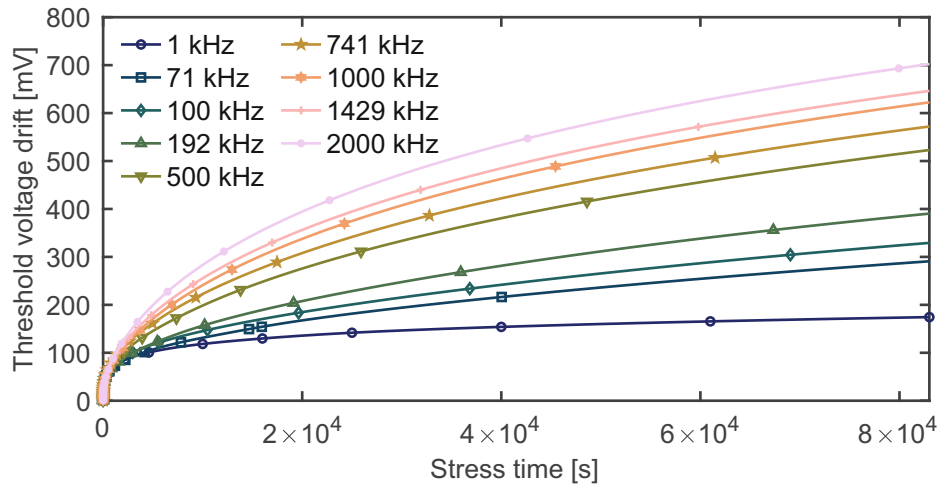


**Figure 4.26.**  $\Delta V_{th}$  versus the stress time from several devices, stressed with 20 V / -10 V, 175 °C, a duty cycle of 50 %, and transition times of 50 ns. The drift increases with increasing frequency. Redrawn from [MFC5].

Within this work, the measurements with regard to GSI are conducted on test structures of asymmetric trench SiC MOSFETs (see Section 1.5.2) that are placed in a TO-247 package with three pins. The devices feature a gate capacitance of 0.31 nF with a charging time constant of only 1.2 ns, which enables defined transients and a limited charging current during continuous switching. For an experiment involving several devices, the MOSFETs were selected from a larger population (on the order of  $10^2$  devices) according to similar values of  $V_{th}$  and  $R_{on}$ . This assures a better resolution of smaller differences in the degradation.

### 4.3.3 Switching Frequency

As already suggested by the name of the mechanism, the switching events themselves play a central role in the underlying physics. Therefore, by far the most important property of GSI is its dependence on the switching frequency  $f_{sw}$ . BTI has been extensively studied under gate switching in silicon (Si)-based MOSFETs [144], [146], [288], [289]. A  $\Delta V_{th}$  that is caused by BTI in a measurement as illustrated in Fig. 4.24a is expected to be independent of the switching frequency. However, this is not the case in SiC MOSFETs, which is illustrated in Fig. 4.26. For a fixed stress time,  $\Delta V_{th}$  increases significantly with increasing frequency – contrary to the behavior of BTI. This leads to the conclusion that BTI alone cannot be the only mechanism causing the observed  $\Delta V_{th}$ .

When analyzing BTI experiments, the drift  $\Delta V_{th}$  versus the stress time is typically plotted in a double logarithmic plot and very roughly follows a power law dependence as per

$$\Delta V_{th}(t_s) = A(t_s)^n \quad (4.22)$$

with a constant  $A$  and a power law exponent  $n$ , that usually ranges from 0.2 to 0.3 [137], [258], [290]. In double logarithmic plots, power laws appear as straight lines with slope  $n$ . Fig. 4.27a shows  $\Delta V_{th}$  versus the stress time in such a double logarithmic plot. Each drift curve appears to consist of two regimes with different slopes. While the slope at shorter stress times below  $10^3$  s is lower, it drastically increases at longer stress times above  $10^3$  s. The data becomes more

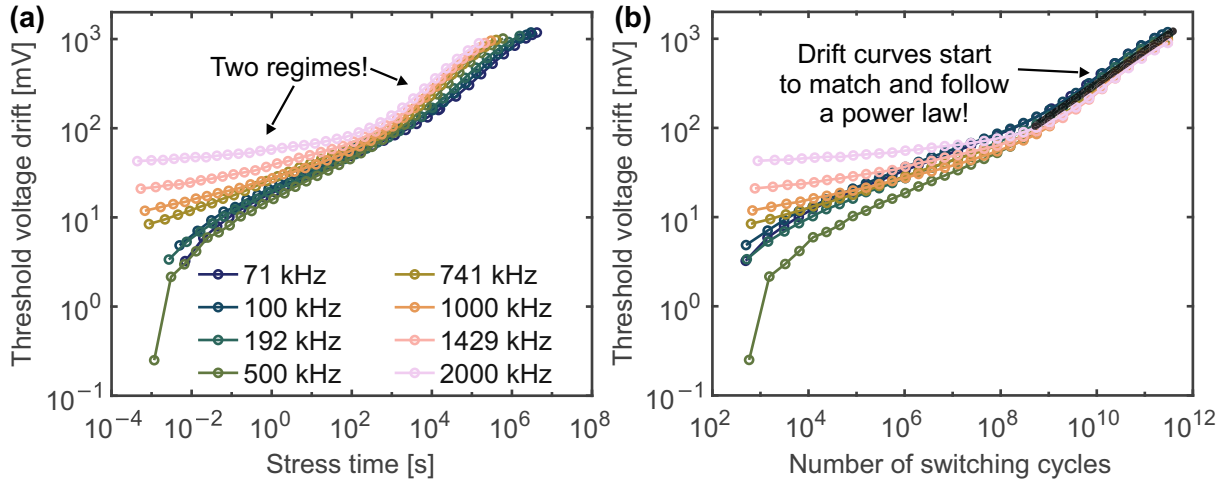


**Figure 4.27.** (a)  $\Delta V_{th}$  versus the stress time from several devices, stressed with 20 V/−10 V, 175 °C, a duty cycle of 50 %, and transition times of 50 ns. The switching frequency is varied between 71.4 kHz up to 2 MHz. (b) The data from (a) plotted versus the number of switching cycles  $N_{sw}$ . Redrawn from [MFC4].

conclusive once it is plotted versus the number of switching cycles

$$N_{sw} = t_s f_{sw}, \quad (4.23)$$

as shown in Fig. 4.27b. Apparently, the drift curves start to match for  $N_{sw} \geq 10^9$  and they seem to follow a power law. It is important to note that a power law in stress time would equal a power law in the number of switching cycles following

$$\Delta V_{th}(N) = \frac{A}{\underbrace{(f_{sw})^n}_{A'}} (N_{sw})^n \quad (4.24)$$

with a different factor  $A'$  but the same slope  $n$ . Fig. 4.27 clearly illustrates that the increasing drift with increasing frequency observed in Fig. 4.26 originates from another drift component besides BTI, that dominates at high numbers of switching cycles. This is the GSI component. Considering the wide range of used stress frequencies, the GSI component exclusively depends on the number of switching cycles and remains rather unaffected by the stress time. In summary, the observed  $\Delta V_{th}$  must be a superposition of two components, following

$$\Delta V_{th} = \Delta V_{th}^{BTI}(t_s) + \Delta V_{th}^{GSI}(N_{sw}). \quad (4.25)$$

Considering the strong increase in slope and the agreement of the curves in Fig. 4.27b for  $N_{sw} \geq 10^9$ , it can be assumed that  $\Delta V_{th}^{GSI}(N_{sw})$  is negligible for small stress times.

To obtain an estimate for  $\Delta V_{th}^{BTI}(t_s)$ ,  $V_{th}$  is not referenced anymore to the readout after 50 cycles, as illustrated in Fig. 4.24a, but to the  $V_{th}$  measured after 1 ms of switching. As the contribution from GSI at this point is negligible, the data is referenced to a point at which the recoverable component of BTI is charged independently of the used frequency. The result is shown in Fig. 4.28. Up to  $10^3$  s, the drift curves match quite well. This is fully consistent with the understanding of the frequency-independence of BTI. Hence, this drift can be identified with  $\Delta V_{th}^{BTI}(t_s)$ . Fitting a power law to the data in the range of 1– $10^2$  s yields a power law exponent

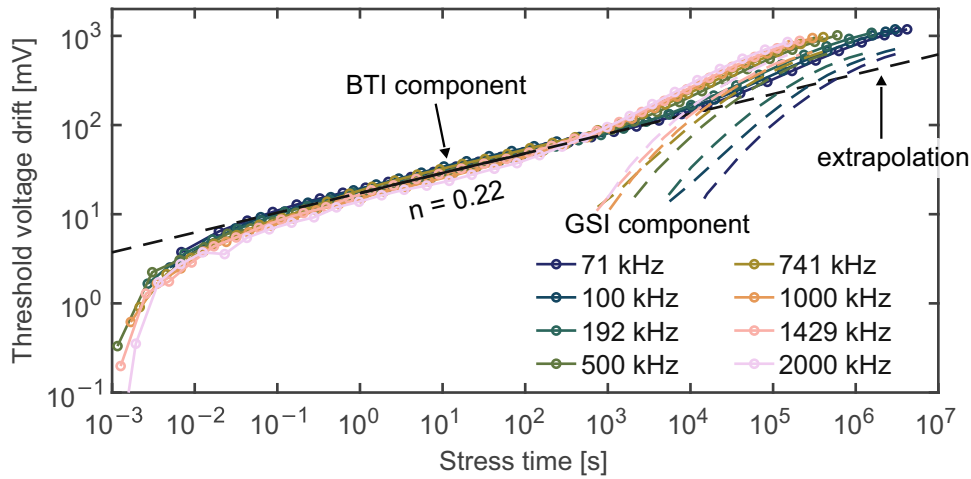


**Figure 4.28.** The data from Fig. 4.27a, referenced to 1 ms of gate switching. The frequency-independent BTI component and the frequency-dependent GSI component are indicated. Redrawn from [MFC4].

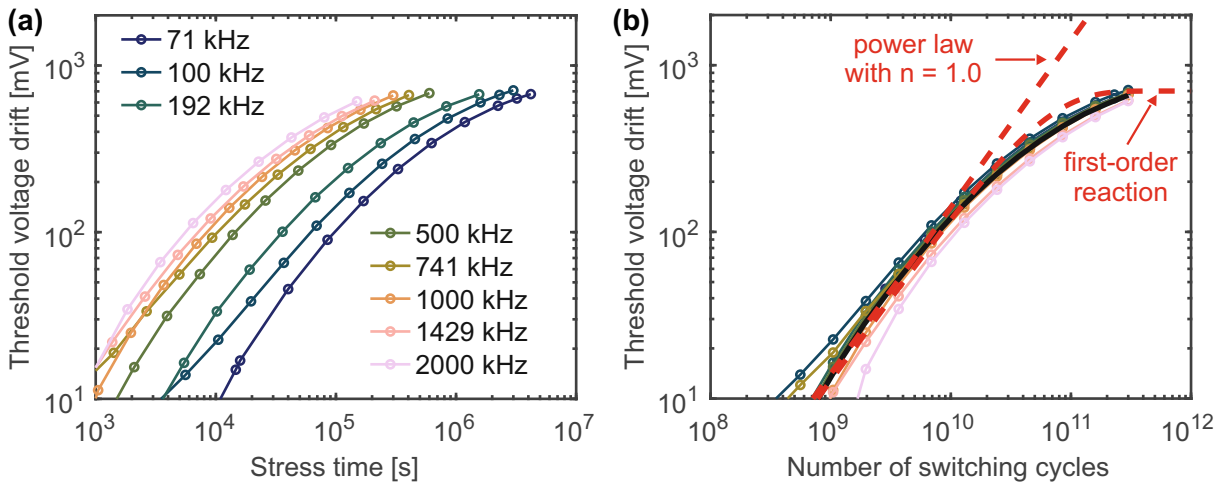


**Figure 4.29.** (a) The GSI component  $\Delta V_{th}^{GSI}$  as extracted in Fig. 4.28 versus the stress time. (b) The data from (a) plotted versus the number of switching cycles  $N_{sw}$ . The average drift initially roughly follows a power law with slope  $n = 1.0$ . As a first-order reaction would initially lead to the same slope, deviations from the power law might be explained by a first-order reaction. Redrawn from [MFC2].

of  $n = 0.22$ , which is perfectly in the range that is typical for BTI [137], [258], [290]. In a crude approximation, the BTI component is extrapolated towards longer stress times. Subsequently subtracting the BTI component from the total  $\Delta V_{th}$  yields the GSI component  $\Delta V_{th}^{GSI}(t_s)$ .

Fig. 4.29a shows  $\Delta V_{th}^{GSI}(t_s)$  versus the stress time for the different switching frequencies. As expected, increasing the frequency shifts the drift curve horizontally towards lower stress time. Plotting then the same data versus the number of switching cycles  $f_{sw}$  leads to an excellent agreement between all drift curves, confirming that  $\Delta V_{th}^{GSI}(N_{sw})$  is a function of  $N_{sw}$  only. Forming the average  $\Delta V_{th}$  over the drift curves of different frequencies provides a good estimate of  $\Delta V_{th}^{GSI}(N_{sw})$ . In addition to a saturation towards higher numbers of switching cycles,  $\Delta V_{th}^{GSI}(N_{sw})$  roughly follows a power law exponent of  $n \approx 1.0$ , which is about five times the exponent of conventional BTI. Most importantly,  $n = 1.0$  means that the power law breaks down into an ordinary proportionality relation as per

$$\Delta V_{th}^{GSI}(N_{sw}) = A'N. \quad (4.26)$$

Consequently, each switching cycle increases  $\Delta V_{\text{th}}^{\text{GSI}}$  by the proportionality factor, which here equals  $A' = 1.4 \times 10^{-8}$  mV. If  $\Delta V_{\text{th}}^{\text{GSI}}$  would be due to trapped electrons, this would correspond to about  $(C_{\text{ox}}A')/q \approx 0.03$  electrons trapped on average per switching cycle at the SiC/silicon dioxide ( $\text{SiO}_2$ ) interface. As it is the case for BTI, GSI is certainly a statistical process [140] where at each switching cycle there is a probability of 3 % that an additional electron is trapped.

A deviation from this power law might be related to limited populations. Assuming a first-order reaction with a reaction rate  $k$  of a number of initially available reactants  $A_0$  yields

$$\Delta V_{\text{th}}^{\text{GSI}}(N_{\text{sw}}) = \frac{q}{C_{\text{ox}}} A_0 (1 - \exp(-kN_{\text{sw}})) \quad (4.27)$$

with the oxide capacitance  $C_{\text{ox}}$  and the electron charge  $q$ . This indeed shares the initial slope of 1.0 in a double-logarithmic plot. Although it does not entirely reproduce the observed drift curve (see Fig. 4.29b), it would certainly explain the saturation of the drift curve.

The observations presented above are in agreement with other works. The conclusion that the total  $\Delta V_{\text{th}}$  might be a function of the switching cycles was established early on in the application note from Infineon Technologies and others [283], [284]. Later, it has been recognized that the drift must be a superposition of two components [MFC7], [MFJ7], [291]. The observation that plotting the total  $\Delta V_{\text{th}}$  versus the number of switching cycles yields approximately matching drift curves has also been observed [286].

In addition to studying GSI as an increase in  $V_{\text{th}}$ , the entire device characteristics can be considered [MFC4]. This includes the transfer characteristic (see Section 3.1) but more importantly the impedance of the device in the form of capacitance-voltage (CV) and conductance-voltage (GV) curves (see Section 3.2). The advantage of impedance measurements is that they access the device characteristic, including depletion and accumulation, where no or almost no drain-source current could be measured in a transfer characteristic. For measuring the CV and GV curves, a Keysight E4990A impedance analyzer was used. The devices were measured at different small-signal frequencies by sweeping  $V_{\text{GS}}$  from  $-30$  V up to  $30$  V and back down, yielding both the upward and the downward characteristic. The sweep rate was  $1.92 \text{ V s}^{-1}$  with a pause of  $11.7$  ms at  $30$  V. To determine how GSI affects these curves, the impedance measurements were conducted before and after stress of different switching frequencies, but the same number of switching cycles  $N_{\text{sw}}$ . According to Equation 4.25,  $\Delta V_{\text{th}}^{\text{GSI}}(N_{\text{sw}})$  should be the same for the different frequencies, while differences might be caused by  $\Delta V_{\text{th}}^{\text{BTI}}(t_s)$ .

The results of such an impedance measurement obtained from a single device are exemplarily shown in Fig. 4.30 (the corresponding drift curve is presented in Fig. 4.28). In contrast to the more classical CV curve shown in Fig. 3.4 of Section 3.2, there is a plateau in the inversion regime, that starts to vanish for  $V_{\text{GS}} \geq 15$  V. The reason for this behavior is found in the device design of the asymmetric trench structure (see Section 1.5.2). As the strong p-type doping covers a significant part of the surface around the trench, the inversion regime of this part of the trench surface occurs later than in the lightly p-type doped channel region. To compare the impact of GSI on the CV and GV curves, the difference in capacitance and conductance at a certain  $V_{\text{GS}}$  is calculated according to

$$\Delta C_{\text{p}}(V_{\text{GS}}) = C_{\text{p}}^{\text{stressed}}(V_{\text{GS}}) - C_{\text{p}}^{\text{pristine}}(V_{\text{GS}}) \quad \text{and} \quad (4.28)$$

$$\Delta G_{\text{p}}(V_{\text{GS}}) = G_{\text{p}}^{\text{stressed}}(V_{\text{GS}}) - G_{\text{p}}^{\text{pristine}}(V_{\text{GS}}). \quad (4.29)$$

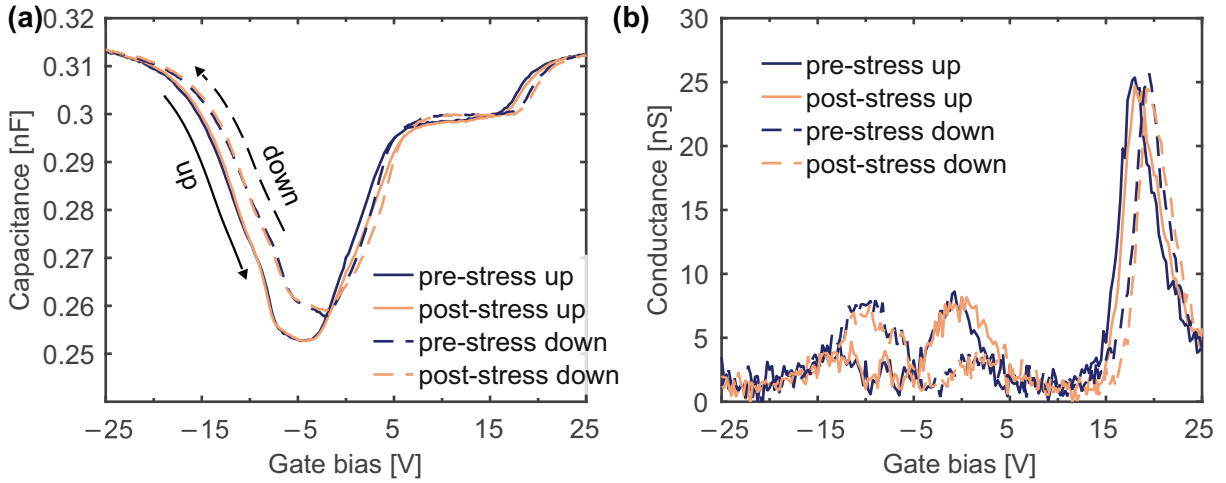


**Figure 4.30.** (a) The CV curves before (pre) and after (post) GSS (20 V / -10 V, 500 kHz, 175 °C,  $3 \times 10^{11}$  cycles), including both up and down sweeps. (b) The GV curves corresponding to (a). Redrawn from [MFC4].

These quantities do not bear physical meaning but serve well for comparison and are illustrated in Fig. 4.31 for both the up and down sweeps of experiments where different switching frequencies were used. Overall, the change in both the CV and GV curves is independent of the used switching frequency. In agreement with Fig. 4.28, no significant stress time dependent component  $\Delta V_{\text{th}}^{\text{BTI}}(t_s)$  was expected after  $N_{\text{sw}} = 3 \times 10^{11}$  cycles, because of the dominance of  $\Delta V_{\text{th}}^{\text{GSI}}(N_{\text{sw}})$ .

Next, to illustrate the impact of GSI on the hysteresis, the following quantities are defined.

$$H_C(V_{\text{GS}}) = C_p^{\text{up}}(V_{\text{GS}}) - C_p^{\text{down}}(V_{\text{GS}}) \quad (4.30)$$

$$H_G(V_{\text{GS}}) = G_p^{\text{up}}(V_{\text{GS}}) - G_p^{\text{down}}(V_{\text{GS}}) \quad (4.31)$$

$$\Delta H_C(V_{\text{GS}}) = H_C^{\text{stressed}}(V_{\text{GS}}) - H_C^{\text{pristine}}(V_{\text{GS}}) \quad (4.32)$$

$$\Delta H_G(V_{\text{GS}}) = H_G^{\text{stressed}}(V_{\text{GS}}) - H_G^{\text{pristine}}(V_{\text{GS}}) \quad (4.33)$$

$\Delta H_C$  and  $\Delta H_G$  are the stress-induced changes in  $H_C$  and  $H_G$ , respectively. These quantities are shown in Fig. 4.32. Apparently, all curves of different switching frequency match – the impact of GSI on the hysteresis is therefore frequency independent.

In addition to the switching frequency, the small-signal frequency of the impedance measurement can be varied. The shorter the capture and emission time constants of a defect at a certain  $V_{\text{GS}}$ , the better the occupancy of the defect can follow the small-signal modulation [223]. This allows to measure an interface defect capacitance

$$C_{\text{it}}(V_{\text{GS}}) = qAD_{\text{it}} = \frac{1}{C_{\text{LF}}(V_{\text{GS}})^{-1} - C_{\text{ox}}^{-1}} - \frac{1}{C_{\text{HF}}(V_{\text{GS}})^{-1} - C_{\text{ox}}^{-1}} \quad (4.34)$$

where  $q$  is the elementary charge,  $A$  is the gate area,  $D_{\text{it}}$  is the defect density,  $C_{\text{ox}}$  is the oxide capacitance, and  $C_{\text{LF}}$  and  $C_{\text{HF}}$  are the low and high frequency CV curves, respectively. Here,  $D_{\text{it}}$  refers to defects with time constants in between the time periods of the used small-signal frequencies. Here, the low and high frequencies were set to 1 kHz and 100 kHz, respectively. This means that only defects with time constants between 10  $\mu\text{s}$  and 1 ms contribute to the measured  $D_{\text{it}}$ . The results obtained from identical measurements before and after GSS are



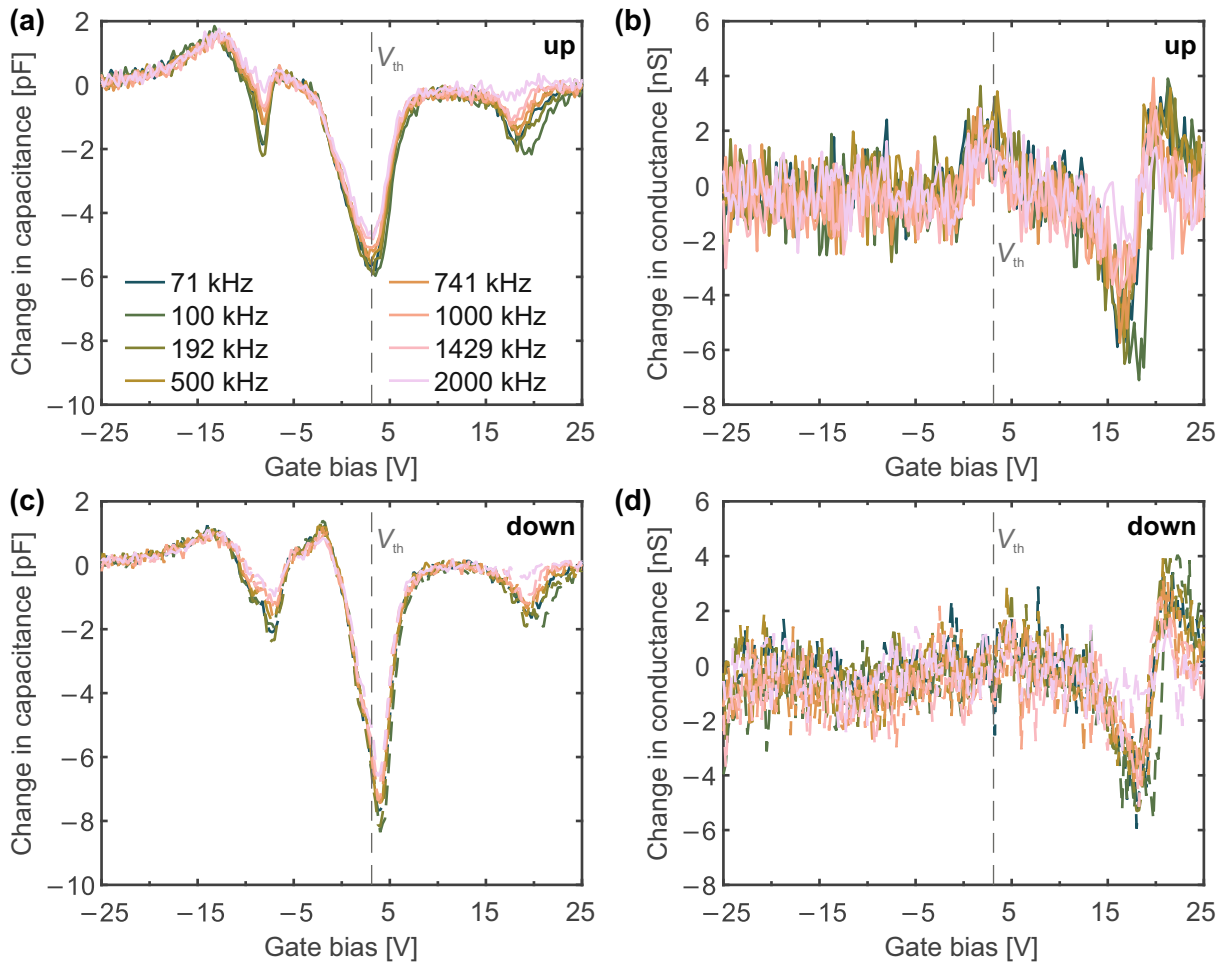


**Figure 4.31.** The change  $\Delta C_p(V_{GS})$  and  $\Delta G_p(V_{GS})$  in the CV and GV curves, respectively, upon GSI. (a)  $\Delta C_p(V_{GS})$  of the up sweeps. (b)  $\Delta G_p(V_{GS})$  of the up sweeps. (c)  $\Delta C_p(V_{GS})$  of the down sweeps. (d)  $\Delta G_p(V_{GS})$  of the down sweeps. Redrawn from [MFC4].

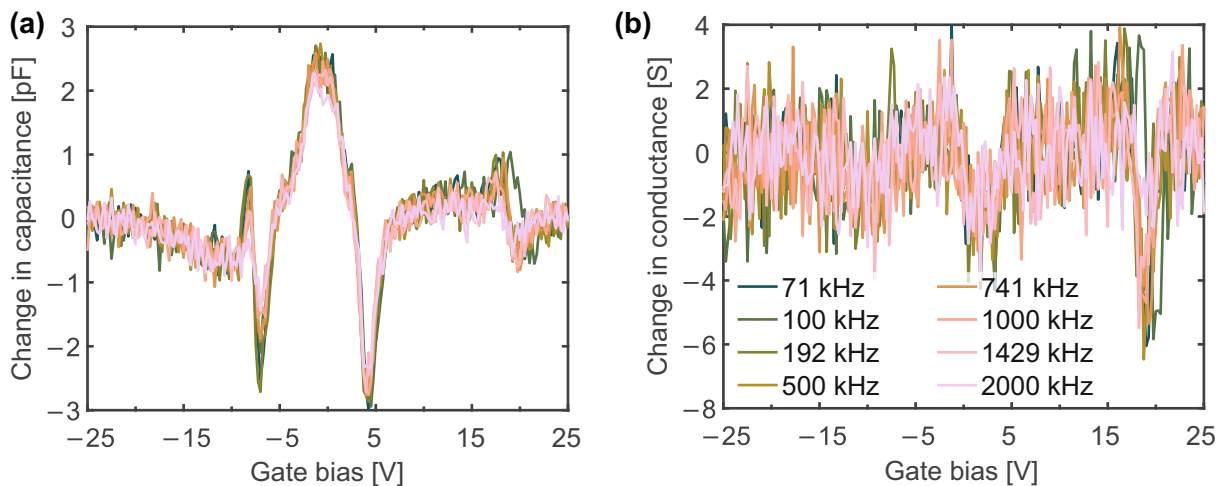


**Figure 4.32.** (a) The change in hysteresis of the capacitance  $\Delta H_C(V_{GS})$  upon GSI for different switching frequencies. (b) The change in hysteresis of the conductance  $\Delta H_G(V_{GS})$  upon GSI for different switching frequencies.

shown in Fig. 4.33, whereby Fig. 4.33a shows  $C_{it}$  before and after stress for a measurement with a switching frequency of 500 kHz and Fig. 4.33b shows the stress-induced change  $\Delta C_{it}$  for

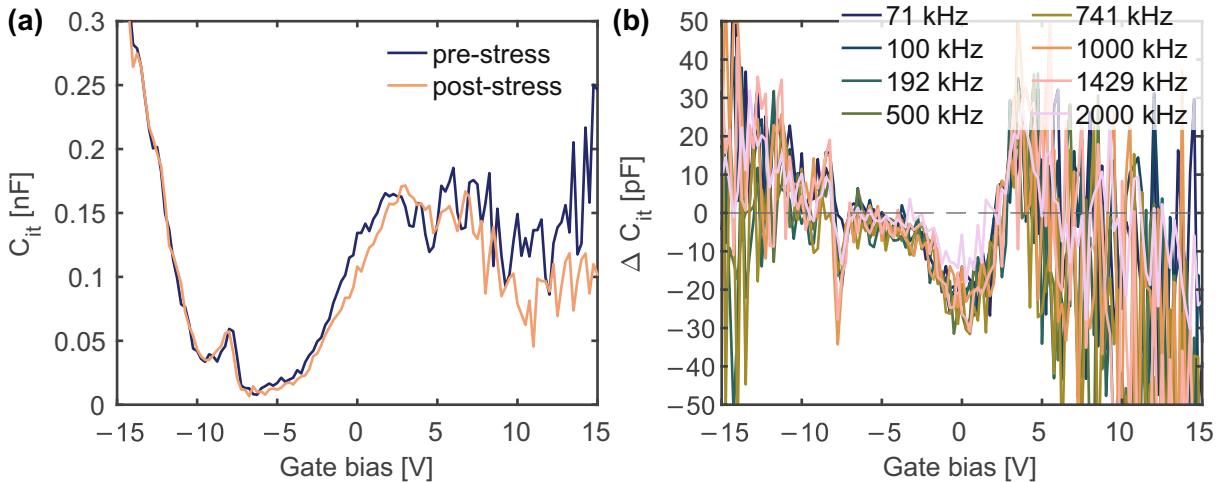


**Figure 4.33.** (a)  $C_{it}$  before (pre) and after (post) GSS (20 V / -10 V, 500 kHz, 175 °C,  $3 \times 10^{11}$  cycles) (b) The stress induced change (difference between curves in (a)) for various switching frequencies. Redrawn from [MFC4].

different switching frequencies. Besides a small horizontal stretch-out, there is no significant stress-induced change in  $C_{it}$  and thus, neither significant creation nor annealing of interface defects in the considered range of time constants is observed. Even more important, there is no dependence on the used switching frequency.

It can be concluded that only the number of switching cycles determines GSI – not only  $V_{th}$  but the entire device characteristic solely depends on  $N_{sw}$  [MFC4]. As the change in the entire device characteristic is identical, the caused degradation is most probably also identical. In the following section, the underlying cause of this change in the device characteristic is discussed.

#### 4.3.4 Origin of Gate Switching Instability: Acceptor-Like Interface Defects

The relevance of GSI for the reliability of SiC MOSFETs is the adverse influence of the associated  $\Delta V_{th}$  on the  $R_{on}$  [MFC7], [MFJ7]. The fact that GSI causes a positive  $\Delta V_{th}$  suggests that electrons are somehow trapped at the SiC/SiO<sub>2</sub> interface. If these electrons would be trapped quasi-permanently with a high emission activation energy, any transfer characteristic, including the CV curve, would shift exactly by the measured  $\Delta V_{th}$  towards higher voltages [225]. This should be the case in both the up sweep and the down sweep of the CV curve. As shown by Fig. 4.34, this is obviously not the case.

Besides the up sweep CV curves before and after stress, both Fig. 4.34a and Fig. 4.34b show the CV curve before stress shifted by the measured  $\Delta V_{th}$  (see Fig. 4.27) as a dashed line. As mentioned, if GSI was caused by quasi-permanently trapped electrons, the post-stress curve and the pre-stress curve shifted by  $\Delta V_{th}$  should agree over the entire range of voltages – both for the up (see Fig. 4.34a) and the down sweeps (see Fig. 4.34b). However, they only agree in the weak-to-strong inversion regime ( $V_{GS} \approx 0$  V). In the depletion and accumulation regimes, the curves clearly disagree. Consequently, GSI cannot be caused by quasi-permanently trapped charges. The drift measured in  $\Delta V_{th}$  is only visible in the weak-to-strong inversion regime. Importantly, the curves shown in Fig. 4.34 are the curves of several devices stressed with different switching frequencies between 71 kHz and 2000 kHz, consequently different stress times, but exactly same total number of switching cycles. As these curves agree very well (see Fig. 4.34c), the differences

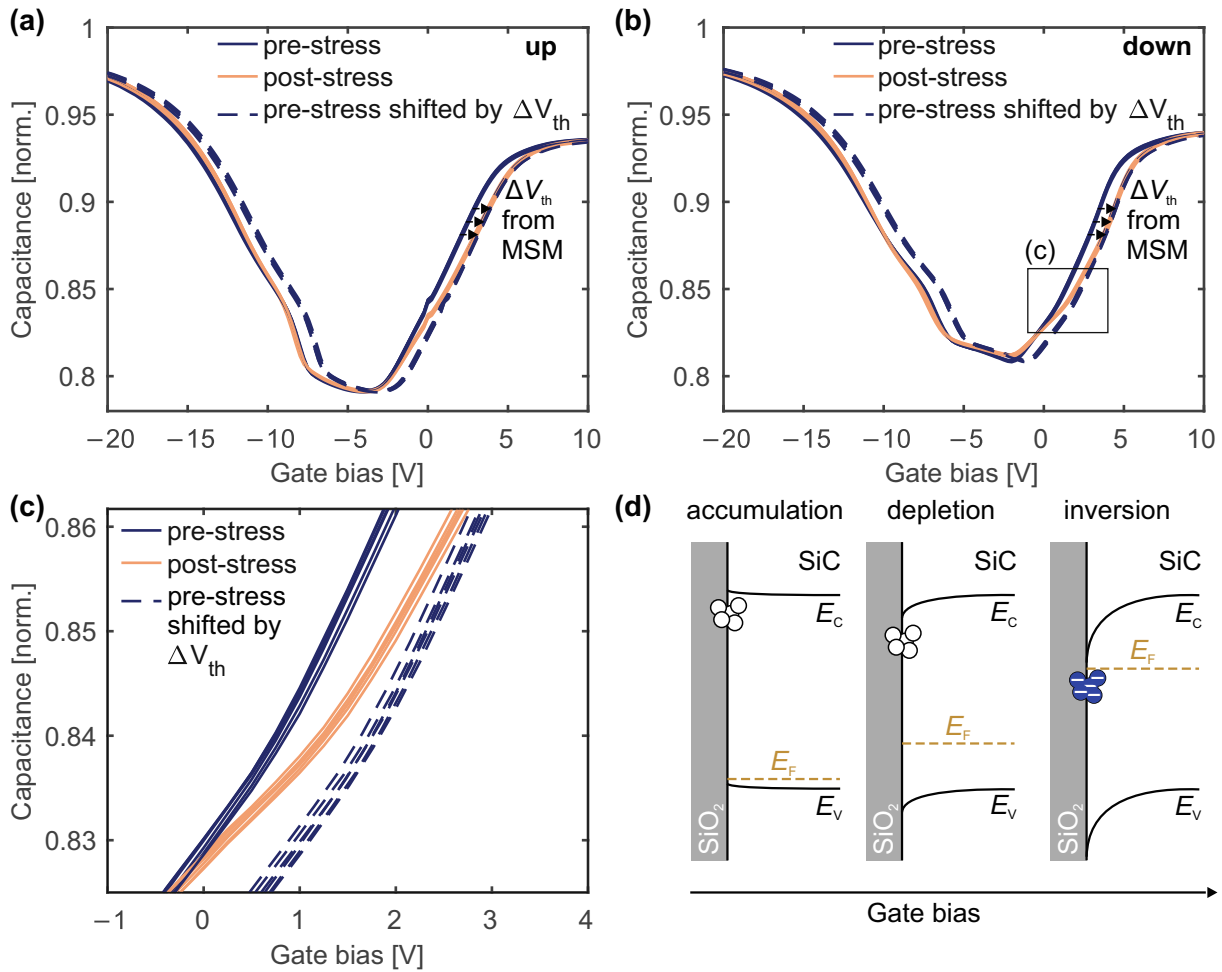


**Figure 4.34.** (a) Up sweep CV curves measured before and after GSS (20 V/−10 V, 175 °C,  $3 \times 10^{11}$  cycles) of various frequencies between 71 kHz and 2000 kHz. The corresponding drift curves are shown in Fig. 4.28. The insets illustrate the charge state of the acceptor-like interface defects created by GSS. (b) Down sweep CV curves corresponding to the up sweeps in (a). The box indicates the region shown by (c). (c) Zoomed region indicated in (b) by the box. Curves of same type and color originate from the different stress frequencies. (d) Illustration of the  $V_{GS}$  dependent occupancy of the acceptor-like defects created by GSS. Redrawn from [MFC2], [MFJ5].

are hard to recognize. As the stress times vary significantly, the observed behavior must clearly be assigned to GSI.

In summary, these observations lead to the conclusion that GSI must be related to the creation of acceptor-like interface defects [MFC2], [MFC5] that are created by the continuous switching stress. Certainly, this also requires some preexisting precursor states, however, those seem to be electrically inactive. As illustrated in Fig. 4.34d, depending on the applied  $V_{GS}$  and the corresponding Fermi level, these fast interface defects are either in their charged or discharged state. Starting in strong accumulation, the Fermi level is in close proximity to the valence band, leaving these acceptor-like defects in their uncharged state. By increasing  $V_{GS}$ , the Fermi level gradually shifts towards the conduction band and once it surpasses the trap level of these created defects, the defects start capturing electrons from the conduction band which gradually shifts the CV curve towards higher voltages. Once all of these acceptor-like defects are charged, the shift reaches its maximum. Note that in an MSM scheme as illustrated in Fig. 4.24a,  $V_{th}$  is measured while  $V_{GS} = V_{th} \approx 3.7 - 4.7$  V is applied to the gate terminal. The range of  $V_{th}$

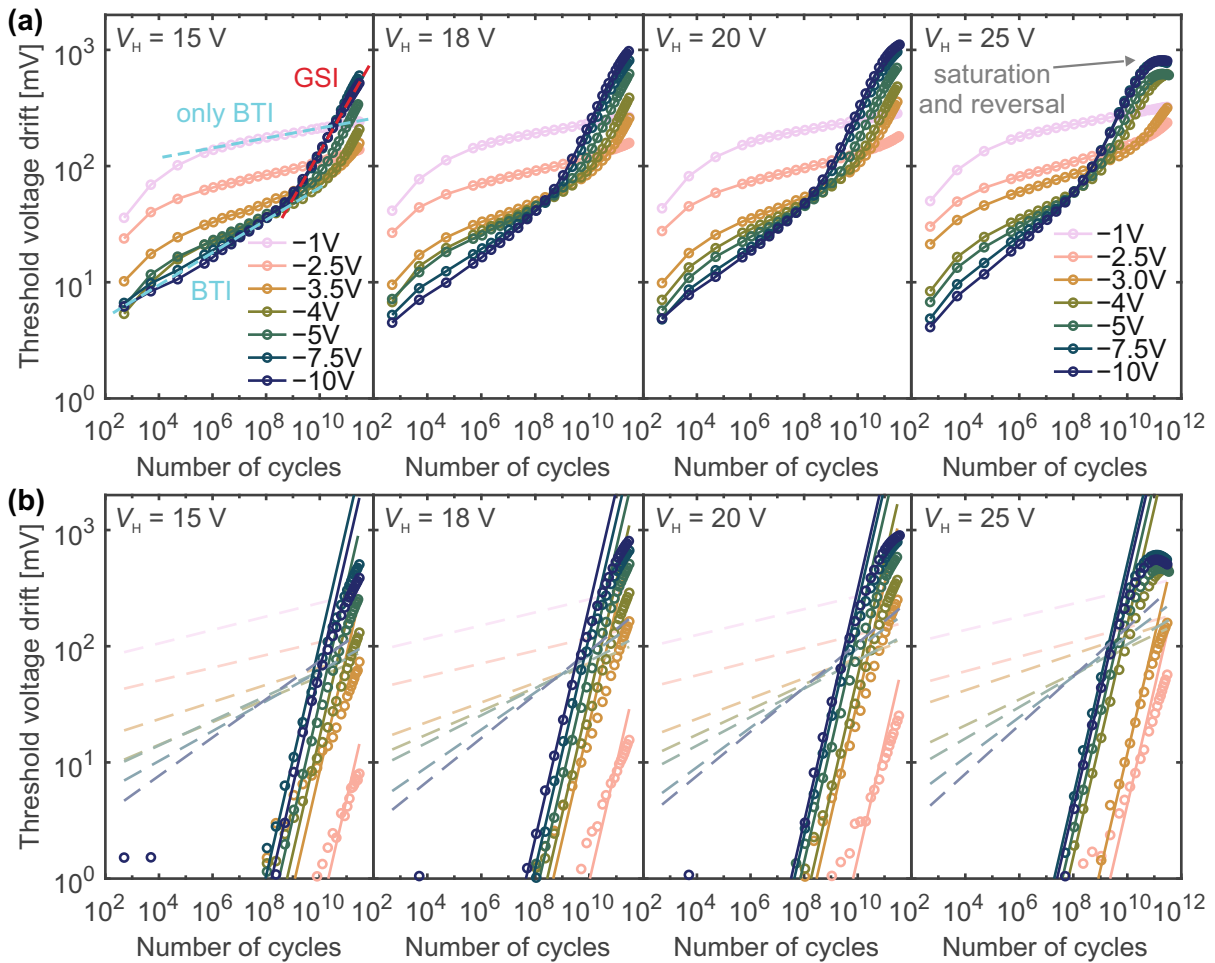


**Figure 4.35.** (a)  $\Delta V_{th}$  measured for different  $V_H$  (left to right) and  $V_L$  (within each plot). (b) The GSI component  $\Delta V_{th}^{GSI}$  measured for different  $V_H$  (left to right) and  $V_L$  (within each plot) based on the data from (a). Dashed lines indicate the BTI components  $\Delta V_{th}^{BTI}$ , whereas the solid lines indicate power laws with an exponent  $n = 1.0$ . Redrawn from [MFC2], [MFC5].

values lies exactly in the range of  $V_{GS}$ , where this shift is already at its maximum (see Fig. 4.24b). Consequently, during the measurement of  $V_{th}$  the created acceptor-like interface defects are in their fully charged state, which in turn confirms that  $\Delta V_{th}$  is a good measure for the GSI-related degradation. However, to see that the created degradation is due to fast interface defects, the measurement of a CV curve is required.

### 4.3.5 Voltage Levels

As outlined in the previous sections, the GSI component of the total  $\Delta V_{th}$  drift is solely dependent on the cumulative number of switching cycles  $N_{sw}$  to which the device is exposed during stress. This justifies to plot the measured drift of a GSI experiment versus  $N_{sw}$  instead of the stress time. Furthermore, GSS does not lead to quasi-permanently trapped charges at the interface, but to the creation of acceptor-like interface defects that are charged in the weak-to-strong inversion regime – which is why  $\Delta V_{th}$  is a good measure for the degradation. In the following, by measuring  $\Delta V_{th}$ , the creation of these interface defects is related to the used  $V_{GS}$ , meaning the high level  $V_H$  and low level  $V_L$  of the stress signal.

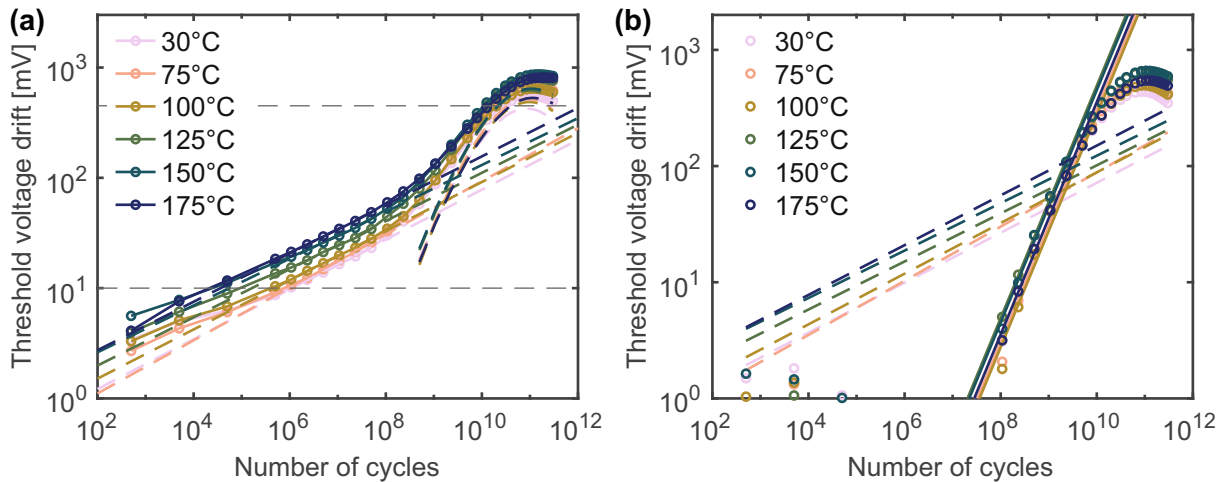


**Figure 4.36.** (a)  $\Delta V_{\text{th}}$  versus the number of switching cycles for different temperatures. The dashed lines indicate the BTI components and GSI components. (b) The GSI components from the data in (a). The dashed lines indicate the extracted BTI components, while the solid lines indicate power laws with exponent  $n = 1.0$ . Redrawn from [MFC2], [MFC5].

For this purpose, the drift was measured for different combinations of  $V_{\text{H}}$  and  $V_{\text{L}}$ , while keeping the frequency and temperature constant at 500 kHz and 175 °C, respectively. The resulting data set is shown in Fig. 4.35a. For moderate  $V_{\text{L}}$  down to  $-3$  V, the strong onset of the GSI component is virtually absent or weak. Only a typical BTI-like drift with a single slope is observed. Once  $V_{\text{L}}$  is lowered further, the strong onset in  $\Delta V_{\text{th}}$  of the GSI component starts to kick in at about  $10^9$  cycles. Up to  $V_{\text{H}} = 20$  V, the drift increases with increasing  $V_{\text{H}}$ , however, in particular at  $V_{\text{H}} = 25$  V, a saturation or reversal of the total  $\Delta V_{\text{th}}$  is observed. This saturation and reversal of the drift is most probably a result of limited populations of precursor states and/or a mechanism that neutralizes the electrical activity of the created interface defects again [MFJ6]. A proposal for a plausible mechanism will be presented in detail in Section 4.3.14.

Analogously to Fig. 4.28, the BTI component can be extracted by fitting a power law to the measured  $\Delta V_{\text{th}}$  in the range of  $1 \times 10^6 - 4 \times 10^7$  cycles. Subtracting the BTI component from the total  $\Delta V_{\text{th}}$  then yields an approximation of the GSI component, which is illustrated in Fig. 4.35b for all different combinations of  $V_{\text{H}}$  and  $V_{\text{L}}$ . Power laws with a fixed exponent  $n = 1.0$  were fitted to the GSI components. Independent of the  $V_{\text{H}}$  and  $V_{\text{L}}$  combination, this high power law exponent, which is about five times the one of the BTI component, is inherent to all drift curves and confirms the conclusion from Fig. 4.29b, that the GSI component is roughly proportional to the number of switching cycles – independent of the voltage levels. This suggests that the basic working principle of the underlying physical process is not affected by a change in the voltage levels – only its overall amplitude or probability per switching cycle to occur is affected.

It is very important to note that the dependence on the voltage levels suggests that GSI can only be triggered once the device is switched between inversion and accumulation [MFC2], [MFC5]. As a result, the setting in which GSI occurs comprises the alternating presence of channel electrons and accumulated holes at the interface. These findings agree with those from other studies, confirming this prerequisite of switching between inversion and accumulation to be able to trigger GSI [286], [291]–[293].

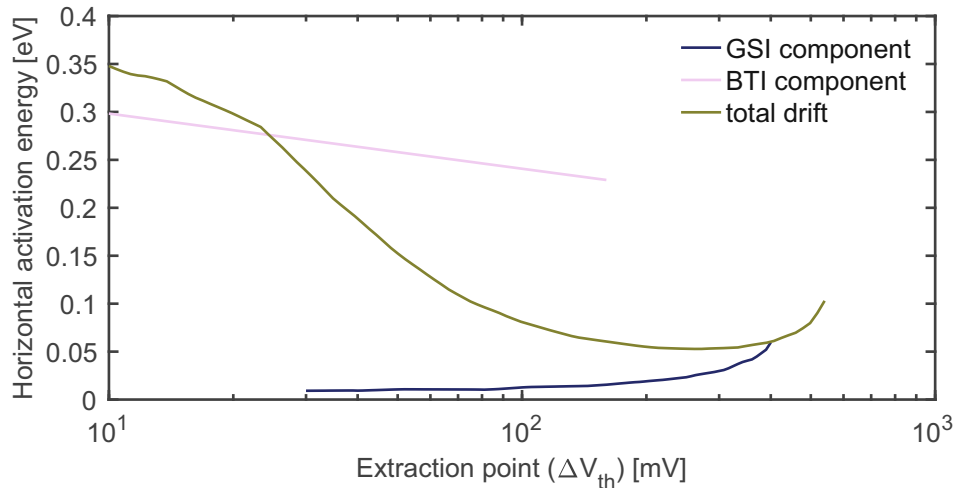


**Figure 4.37.** The horizontal activation energy of the total  $\Delta V_{th}$  and its BTI and GSI components, shown in Fig. 4.36. Redrawn from [MFC2].

### 4.3.6 Junction Temperature

Probably the most important aspect of a degradation mechanism in microelectronic devices is its temperature dependence. The temperature dependence is typically attributed to the underlying non-radiative multiphonon (NMP) processes [142] or to phonon scattering [294]–[296]. In order to understand the physical cause of the creation of these acceptor-like interface defects, it is important to understand the temperature dependence of GSI. This was investigated using six different temperatures in the range of 30–175 °C. Besides the temperature, the other stress parameters were kept constant (25 V/–10 V, 500 kHz). The results are shown in Fig. 4.36a. As expected from conventional BTI, the BTI component apparently increases with increasing temperature. Again, the GSI components were determined by extracting the BTI components and subtracting them from the total  $\Delta V_{th}$ . The striking result was: the GSI component is basically temperature independent, as shown in Fig. 4.36b. While the temperature-independent behavior again follows a power law with exponent  $n = 1.0$ , the saturation and reversal of the drift might show a slight temperature dependence. However, this might also be related to the rather crude extraction of the BTI component, as the BTI component will at some point rather follow a scaled complementary error function instead of a power law [147], [271].

This temperature independence is further illustrated in Fig. 4.37 that shows the horizontal activation energy (see Section 4.1) versus its point of extraction (the  $\Delta V_{th}$ ). The range of  $\Delta V_{th}$  values, where the activation energy is extracted, is indicated in Fig. 4.36a by horizontal dashed lines. The activation energy was calculated for the GSI component, the BTI component, and for the total  $\Delta V_{th}$ , respectively. While the GSI component shows a very small activation energy, well below 50 meV, the BTI component shows a typical value in the range of 0.25–0.30 eV. As the share of the GSI component increases with increasing number of switching cycles and  $\Delta V_{th}$ , the activation energy of the total  $\Delta V_{th}$  decreases with increasing extraction point.

The temperature independence of the GSI component represents a strong difference to conventional BTI, which is clearly temperature-activated [MFC2], [MFC5]. The mechanism behind GSI must therefore significantly differ from conventional NMP transitions. A review of other studies suggests that the temperature dependence of GSI could depend on the specific device under test – or rather on the differently processed SiC/SiO<sub>2</sub> interfaces. While some studies found an increasing total  $\Delta V_{th}$  with increasing temperature [285], others observed a

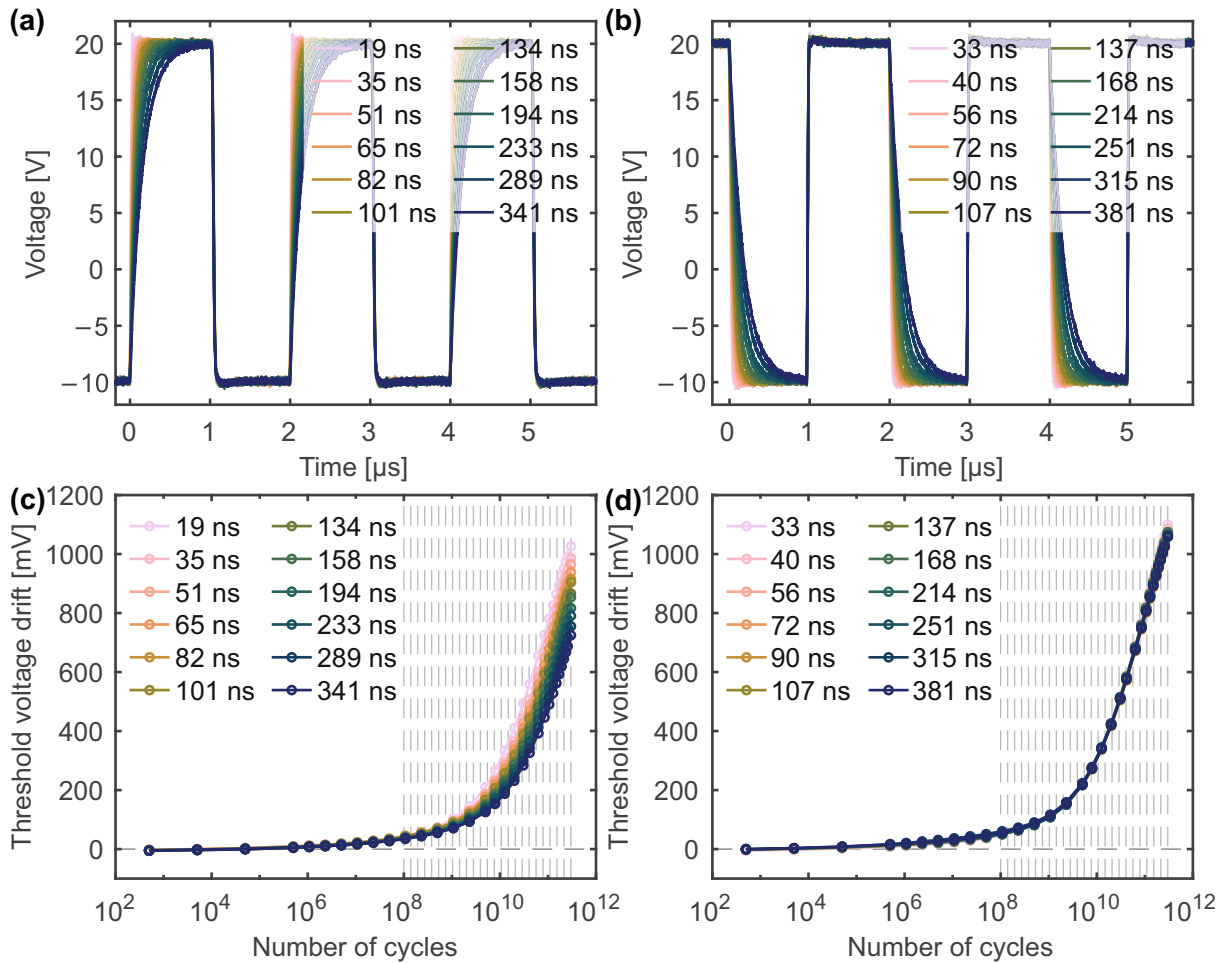


**Figure 4.38.** (a) The stress waveforms with different rise times. (b) The stress waveforms with different fall times. (c)  $\Delta V_{th}$  versus the number of switching cycles for the different rise times. (d)  $\Delta V_{th}$  versus the number of switching cycles for the different fall times. Redrawn from [MFC2].

decreasing total  $\Delta V_{th}$  with increasing temperature [286], [291], [297]. The underlying mechanism must therefore exhibit a certain degree of complexity, such that it allows for either temperature dependence.

### 4.3.7 Transition Times

As it was found that GSI is caused by the switching events themselves, it appears reasonable to assume that the shape of the transitions could have an impact on the degradation mechanism. As known from other experimental techniques, such as charge pumping (CP), the speed of switching between the voltage levels is of premier importance (see Section 3.4). The relevant quantity is the transition time of  $V_{GS}$  between the high level  $V_H$  and the low level  $V_L$ . The transition time associated with the transition from  $V_L$  to  $V_H$  is the rise time, whereas the transition time associated with the transition from  $V_H$  to  $V_L$  is the fall time. These times are defined according to an IEEE standard as the time between the 10% and 90% reference levels [298]. In order to investigate their impact on GSI, devices were stressed with 20 V/−10 V, 175 °C, a duty cycle of 50%, and a frequency of 500 kHz, while the rise and fall times were varied separately. The separate variation of rise and fall times was achieved by changing the respective external gate resistor (see Section 3.3). The resulting waveforms of the stress signal are shown in

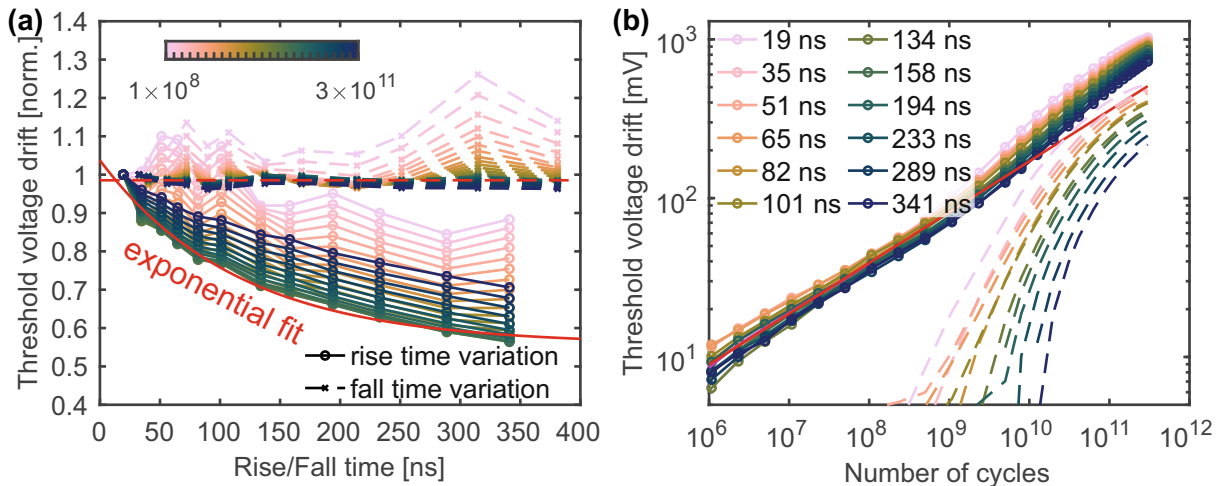


**Figure 4.39.** (a)  $\Delta V_{th}$  versus the transition time (rise/fall time) for different numbers of switching cycles.  $\Delta V_{th}$  follows an exponential dependence on the rise time, but is independent of the fall time. (b)  $\Delta V_{th}$  versus the number of switching cycles in a double logarithmic plot. In a crude approximation, a common BTI component (red line) is assumed, which yields the GSI component (dashed lines) that depends on the rise time. Redrawn from [MFC2].

Fig. 4.38a and Fig. 4.38b for the variation of the rise and fall times, respectively. The rise time was varied between 19 ns and 341 ns, whereas the fall time was varied between 33 ns and 381 ns. The corresponding drift plots are shown in Fig. 4.38c and Fig. 4.38d.

Apparently, the observed  $\Delta V_{th}$  does not depend on the fall time. Even on a linear scale of  $\Delta V_{th}$ , no differences could be recognized. In contrast to that, there is a clear dependence of  $\Delta V_{th}$  on the rise time of the stress waveform. With increasing rise time, the drift decreases significantly by up to 43 %. This is illustrated in more detail in Fig. 4.39a that shows  $\Delta V_{th}$ , normalized to the shortest transition time, as a function of the respective transition time. The color indicates different numbers of switching cycles between  $10^8$  and  $3 \times 10^{11}$ . A fit to the data at  $N_{sw} = 10^{10}$  shows an exponential dependence of  $\Delta V_{th}$  on the rise time. While the relative dependence on the rise time initially increases with increasing  $N_{sw}$ , it seems to decrease again above  $10^{10}$ . As shown in Fig. 4.39b, the dependence of the total  $\Delta V_{th}$  on the rise time is significant and increases at a higher number of switching cycles, where the GSI component dominates over the BTI component. This allows to clearly assign the rise time dependence to the GSI component.

This observed impact of the transition times on GSI has also been claimed in other studies [286], [297]. Similar to the temperature dependence, where others observed differing behavior for different types of devices, the impact of the transition time is not unique or identical for all types of devices. For some devices, the total  $\Delta V_{th}$  decreases only upon decreasing the rise time, whereas in other devices it decreases upon decreasing either the rise or the fall time [297]. Again, it must be concluded that a plausible model or mechanism for the degradation must cover the existence of both dependencies.

### 4.3.8 Similarity to Charge Pumping

As already discussed in the context of the dependence of GSI on the voltage levels, GSI seems to occur only once the MOSFET is switched between inversion and accumulation. In exactly this operation mode it is known that interface defect states assist electron-hole recombination – both in Si and SiC MOSFETs [299]–[302]. The number of recombining charges can be measured



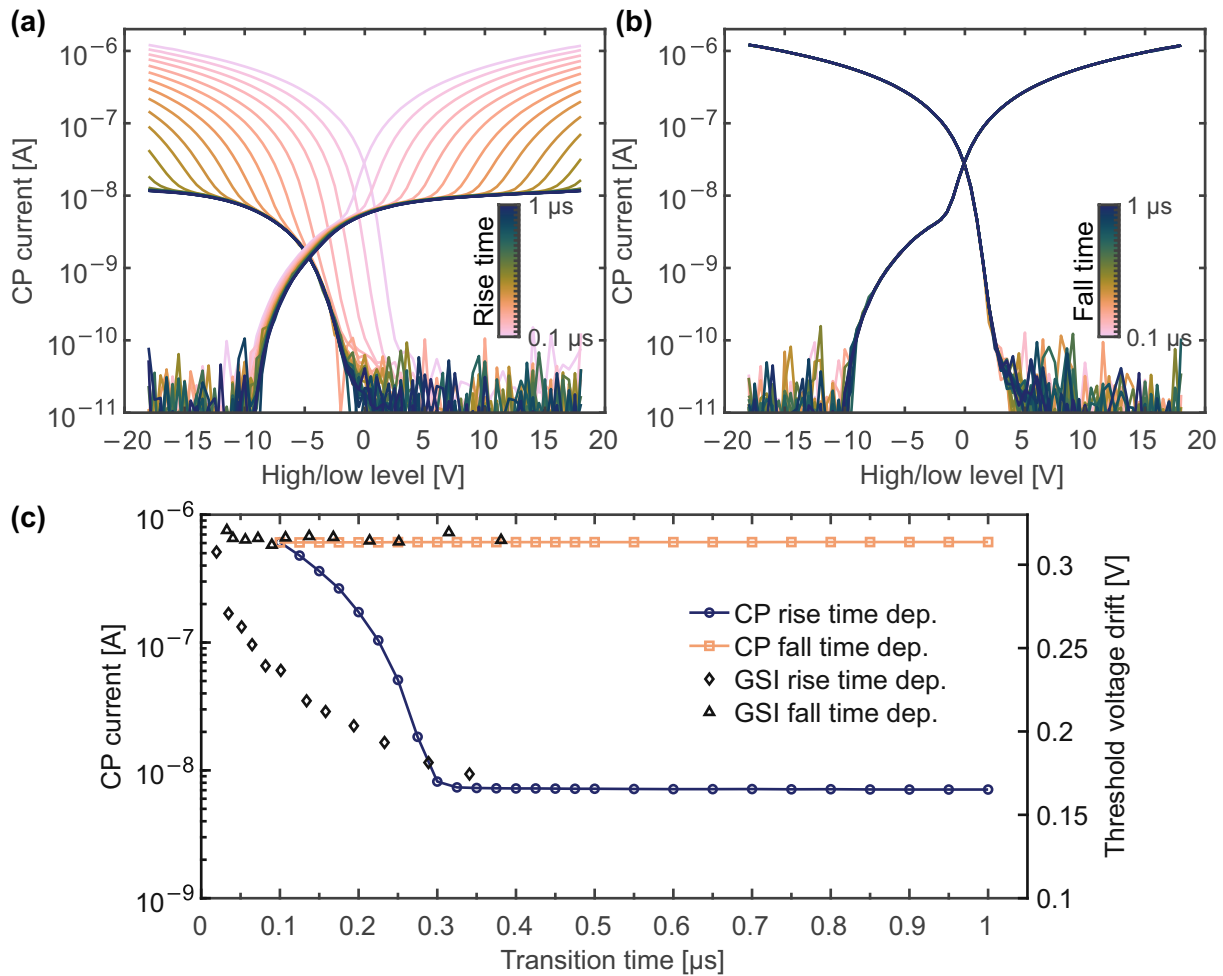


**Figure 4.40.** (a) The constant low level and constant high level curves of the CP current for different rise times. (b) The constant low level and constant high level curves of the CP current for different fall times. (c) The dependence of the CP current on the rise and fall time of an 18 V / -10 V, 100 kHz signal. Additionally,  $\Delta V_{th}$  as a function of the transition time obtained upon  $10^{10}$  switching cycles of 500 kHz, 20 V / -10 V, 175 °C, 50 % duty cycle GSS. Redrawn from [MFC5].

by the CP technique (see Section 3.4). Similar to the GSI-related drift, the CP current passing through the bulk terminal of the MOSFET decreases with increasing transition time.

In order to compare the transition time dependence of the CP current with the dependence of the GSI-related  $\Delta V_{th}$ , test-structures with a separate bulk terminal but identically processed interfaces were used. The low and high levels were kept constant at -18 V and 18 V, respectively, while the other level was varied. The switching frequency was fixed at 10 kHz and the experiments were conducted at room temperature. Fig. 4.40a shows the constant high level and constant low level curves of the CP current for various rise times between 100 ns and 1  $\mu$ s at a constant fall time of 100 ns. Analogously, Fig. 4.40b shows the same as Fig. 4.40a but for various fall times at a constant rise time of 100 ns. Interestingly, there is a significant component in the CP current that is only affected by the rise time, which resembles the behavior of the GSI-related drift in  $\Delta V_{th}$ . A comparison between the transition time dependence of the CP current and the GSI-related drift is shown in Fig. 4.40c. It reveals that the decrease of the CP current with increasing transition time occurs on the same time scale as the decrease of the GSI-related  $\Delta V_{th}$ .

This conspicuous similarity between the CP current and the GSI-related drift suggests that GSI could indeed be related to defect-assisted recombination at the SiC/SiO<sub>2</sub> interface [MFC5].

As both the CP current and the GSI-related  $\Delta V_{th}$  decrease with increasing transition time, the recombination effectively seems to create the suggested acceptor-like interface defects, that cause GSI. Note that a one-to-one correlation between the CP current and the drift would not be a straight-forward assumption or guess because the CP current represents all recombination paths that potentially exist, while the GSI-related drift is probably caused by only a single recombination path over which the detected acceptor-like interface defects are created.

### 4.3.9 Overshoots and Undershoots

Particularly for applications, over- and/or undershoots in  $V_{GS}$  are very common and can often not be avoided. Among other things, they could be created by a parasitic inductance connected to the gate terminal. It is therefore of major importance to understand their potential impact on GSI. For this purpose, a third voltage level of the setup for ultra-fast threshold voltage measurements (see Section 3.3), the pre-charge voltage source, is used to create a three-level stress signal. This allowed to create defined undershoots in the gate voltage with a length of only 200 ns. For the purpose of this investigation,  $-10$  V undershoots of equal length located at different positions during the  $V_L$ -phase were used to alter a  $20$  V /  $-3$  V,  $500$  kHz GSS stress waveform. The location of the undershoots were  $0$  ns,  $250$  ns,  $500$  ns, and  $800$  ns away from the start of the  $V_L$ -phase. These four stress signals are illustrated in Fig. 4.41a. The corresponding  $\Delta V_{th}$  versus the number of switching cycles together with the  $\Delta V_{th}$  drift without any undershoot ( $V_L = -3$  V) and with a complete  $V_L$ -phase at  $-10$  V are shown in Fig. 4.41b.

At low numbers of cycles, the stress waveform without undershoot and  $V_L = -10$  V has the lowest drift, followed by the waveforms with the different undershoots. The waveform without undershoot and  $V_L = -3$  V exhibits the highest drift. This order can be explained by an increasing BTI component, which is caused by the decreasing contribution from negative bias temperature instability (NBTI) to the BTI component. At higher numbers of switching cycles, where GSI dominates, the drift of the stress waveforms featuring the various undershoots equal the drift of the stress waveform without undershoot with  $V_L = -10$  V. Among the drift curves of the waveforms with the four different undershoots, there is no difference, neither in the regime where BTI dominates nor in the regime where GSI dominates – they cause an identical drift. Considering the significant difference to the drift of the waveform without undershoot and  $V_L = -3$  V, it can be concluded that the used undershoots create the same GSI component as a conventional waveform with  $V_L = -10$  V. The different positions of the undershoots during the  $V_L$ -phase do not cause any difference in the observed  $\Delta V_{th}$ .

The fact that the different undershoots cause exactly the same degradation is again verified by considering the impact of the degradation on the CV curves. They are illustrated for the up and down sweeps in Fig. 4.41c and Fig. 4.41d, respectively. No significant difference is observed. Furthermore, the change in the CV curve is identical to the behavior discussed in the context of Fig. 4.34, which resulted in the conclusion that GSI is related to the creation of acceptor-like interface defect states.

As already discussed in the previous sections, GSI is caused by the switching events themselves. Consequently, the absence of any difference between the stress waveforms with the differently positioned undershoots suggests that there is basically no recovery at any point of the  $V_L$ -phase of the charges trapped at the undershoot that is significant or relevant for the degradation. Once a certain  $V_L$  is reached during the low phase, independent of the time at which it is reached, the degradation corresponds to the degradation that would also be

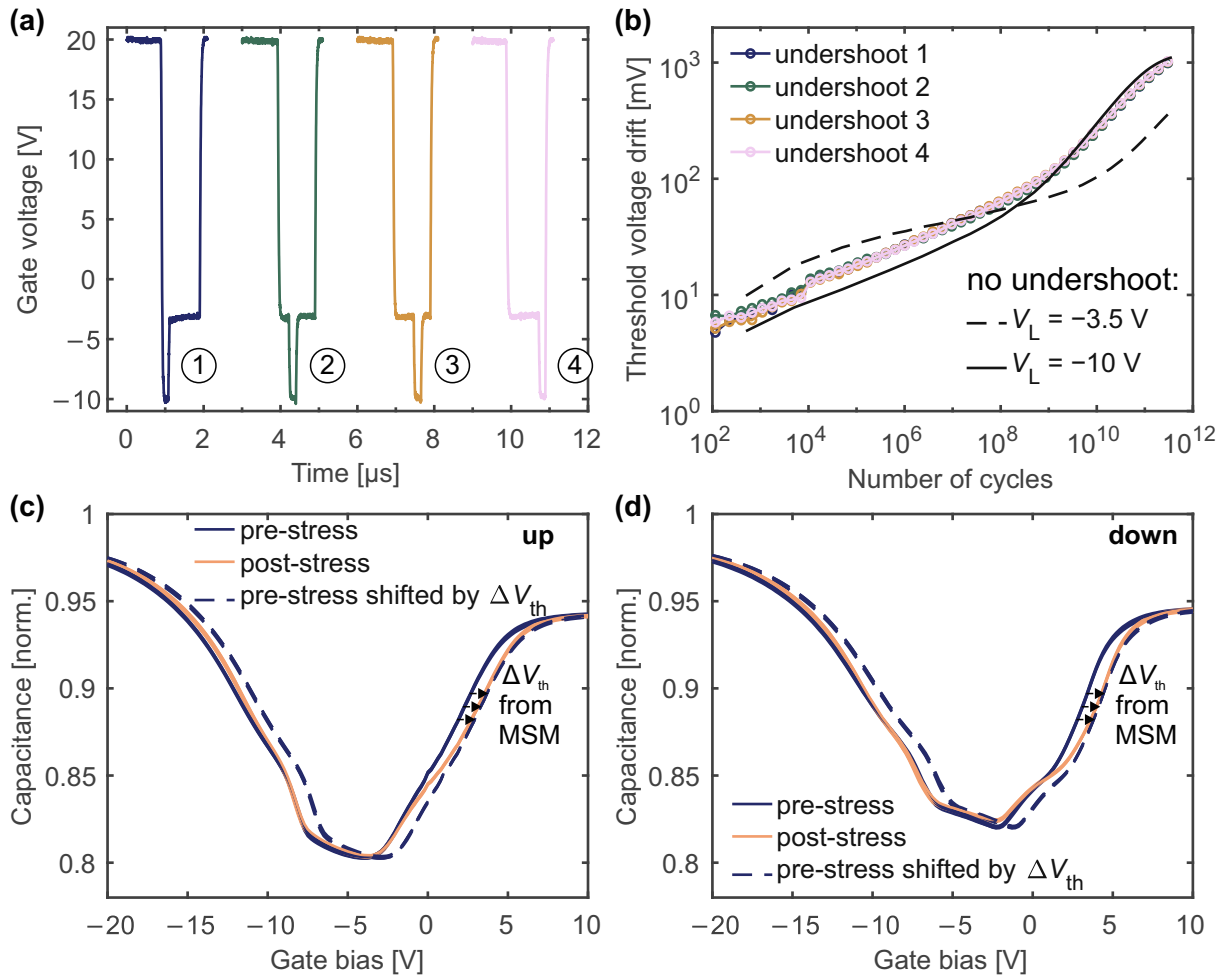


**Figure 4.41.** (a) Four different  $-10$  V undershoots used to alter a  $20$  V /  $-3$  V,  $500$  kHz GSS signal. (b) The corresponding drift curves obtained by stressing with the four waveforms shown in (a). The black dashed line represents the drift obtained by stressing with a regular two-level stress signal with  $V_L = -3$  V, while the black solid line indicates the drift with  $V_L = -10$  V. (c) Up sweep CV curves measured before and after GSS of the four undershoots in (a). (d) Down sweep CV curves measured before and after GSS of the four undershoots in (a). Redrawn from [MFJ5].

achieved by switching for the full low phase to this  $V_L$ . Considering the previously discussed dependence on the rise time allows to further conclude that the impact on GSI of the rise time is predominantly caused in a range of  $V_{GS} > -3$  V. Otherwise, an increasing GSI component would be expected going from undershoot 1 to 4.

Overall, the results agree with findings from another study [291], that found an impact of both over- and undershoots on GSI. However, the authors did not distinguish between the two, nor did they consider the entire drift curves or different positions of undershoots. Nevertheless, it is to assume that also overshoots have a similar effect as undershoots.

#### 4.3.10 Impact on the Hysteresis

As discussed, GSI is effectively the creation of acceptor-like interface defect states that capture electrons from the conduction band in the weak-to-strong inversion regime. It is therefore of interest how these newly created interface defects actually react to short gate pulses and

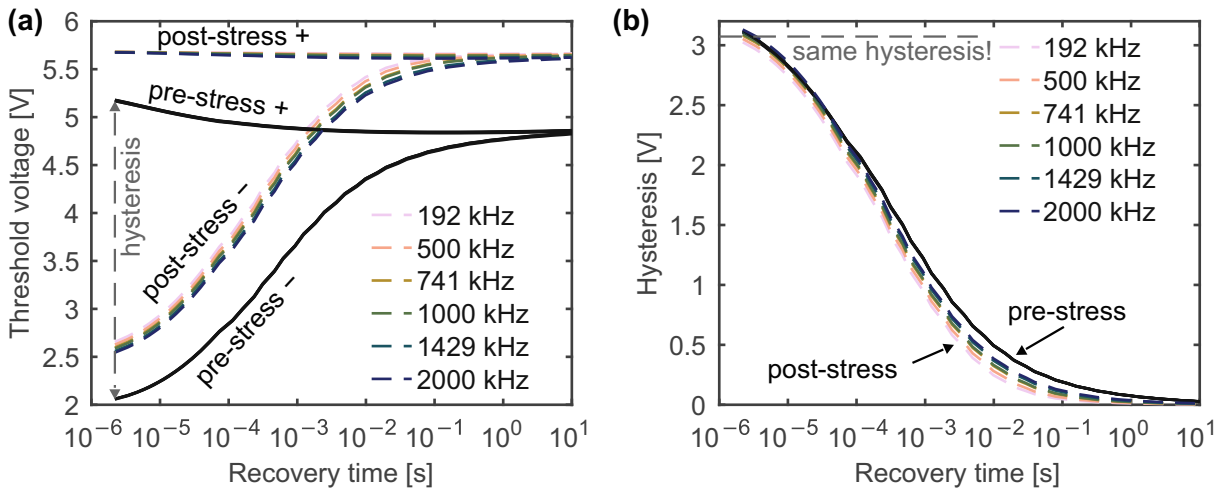


**Figure 4.42.** (a) The recovery curves after a 20 V (+) and a -10 V (-) pulse before and after GSS of 20 V/-10 V, 175 °C, a duty cycle of 50 %, transition times of 50 ns, and  $3 \times 10^{11}$  cycles. (b) The hysteresis, as the indicated difference between the recovery curves in (a) before and after GSS. Redrawn from [MFC2].

whether these defects appear or disappear as a part of the recoverable component (also referred to as hysteresis).

For this purpose, the devices were exposed to a 100  $\mu$ s long 20 V gate pulse and the following recovery curve was measured. Afterwards, the same procedure was repeated with a -10 V pulse. This measurement sequence was conducted before and after GSS of 20 V/-10 V, 175 °C, a duty cycle of 50 %, transition times of 50 ns and different stress frequencies. The resulting recovery curves are shown in Fig. 4.42a. The 20 V and -10 V pulses are indicated by a plus (+) and minus (-) sign, respectively. The difference between the recovery curves of these two pulses is defined as the hysteresis, which is plotted in Fig. 4.42b.

First, it is to note that the post-stress recovery curves are shifted by the GSI-induced  $\Delta V_{th}$  towards higher voltages. Slight variations between the different frequencies can be assigned to varying BTI components. As shown in Fig. 4.42b, the hysteresis at the shortest measured recovery time was not affected by GSS, however, a slightly faster recovery of the hysteresis is observed. This is predominantly caused by a faster recovery after the negative pulse after stress (see Fig. 4.42a). The stress caused an increase in  $V_{th}$ , which is applied to the gate terminal during recovery. This higher  $V_{GS}$  during recovery effectively accelerates the recovery in return. As discussed in the context of Fig. 4.34, the acceptor-like interface defects created by GSS are not charged in accumulation. In particular, this means that these defects are not charged during the application of the pulse voltage of -10 V. However, as the drift appears in the measurement of the recovery after this negative pulse, these acceptor-like interface defects must already be charged again, once the measurement is conducted. Consequently, this happens within less than 1.8  $\mu$ s. These defects must therefore be faster than the defects that contribute to the measured hysteresis.

Again, reviewing other studies shows that this might also – at least partly – depend on the respectively tested type of device. While most devices seem to show no change in the hysteresis [MFC7], [MFJ7], a few devices seem to show a significant increase [286], [293]. Differences with regard to the SiC/SiO<sub>2</sub> interface might significantly affect the time constants of

|                                    |  |
|------------------------------------|--|
| <b>number of switching cycles</b>  | Only the cumulative number of switching cycles determines the degradation. The corresponding stress time or frequency is not relevant. The degradation is roughly proportional to the cumulative number of switching cycles.         |
| <b>saturation/reversal</b>         | In particular at more extreme bias conditions, a saturation and reversal of the degradation is observed.   |
| <b>interface states</b>            | Impedance measurements reveal the creation of acceptor-like interface defects that are only charged in the weak-to-strong inversion regime.  |
| <b>voltage levels</b>              | The degradation only occurs upon switching between inversion and accumulation.   |
| <b>junction temperature</b>        | The mechanism must be temperature independent. Due to the results of other studies, it should allow the possibility to have any temperature dependence.  |
| <b>transition times</b>            | The degradation decreases in some devices with increasing rise time and is independent of the fall time. Due to the results of other studies, it should allow the possibility to have a similar dependence on the fall time as well. |
| <b>electron-hole recombination</b> | Due to the similarity to the charge pumping current, the degradation is likely related to defect-assisted recombination at the SiC/SiO <sub>2</sub> interface.   |
| <b>over- and undershoots</b>       | An undershoot creates the same degradation as fully switching down to the voltage level of the undershoot. This is probably similar for the overshoot.   |
| <b>hysteresis</b>                  | The hysteresis, as measured with an inherent measurement delay, should not change.   |
| <b>quasi-permanence</b>            | The degradation in terms of the measured $\Delta V_{th}$ is quasi-permanent.   |
| <b>annealing</b>                   | The reverse reaction (annealing) is linked to a considerable activation energy of about 2 eV.  |

**Table 4.3.** List of experimental findings with respect to GSI.

these acceptor-like interface defects, thus creating such contrary observations in the behavior of different devices.

#### 4.3.11 Recovery and Annealing

Already in the first scientific paper from Jiang *et al.* it was shown that GSI is a quasi-permanent degradation [283]. This means that once these acceptor-like interface defects are created, the reverse reaction back to the inactive precursor state is associated with a high activation energy. Indeed, it has been shown that this reverse reaction is in principle possible under high temperatures above 225 °C and significantly negative  $V_{GS}$  [286].

It can be estimated that this activation energy is about 2 eV at  $V_{GS} = 0$  V [MFC5]. At room temperature, the activation energy corresponds to a time constant of  $10^{22}$  s, whereas at 600 K it is reduced down to  $2 \times 10^5$  s.

#### 4.3.12 The Physics of Gate Switching Instability

The previous section provided a detailed analysis of various experimental characteristics of GSI. The intention of this section is to gather the experimental observations, draw conclusions on the underlying physics, and provide a physical understanding and model for this new

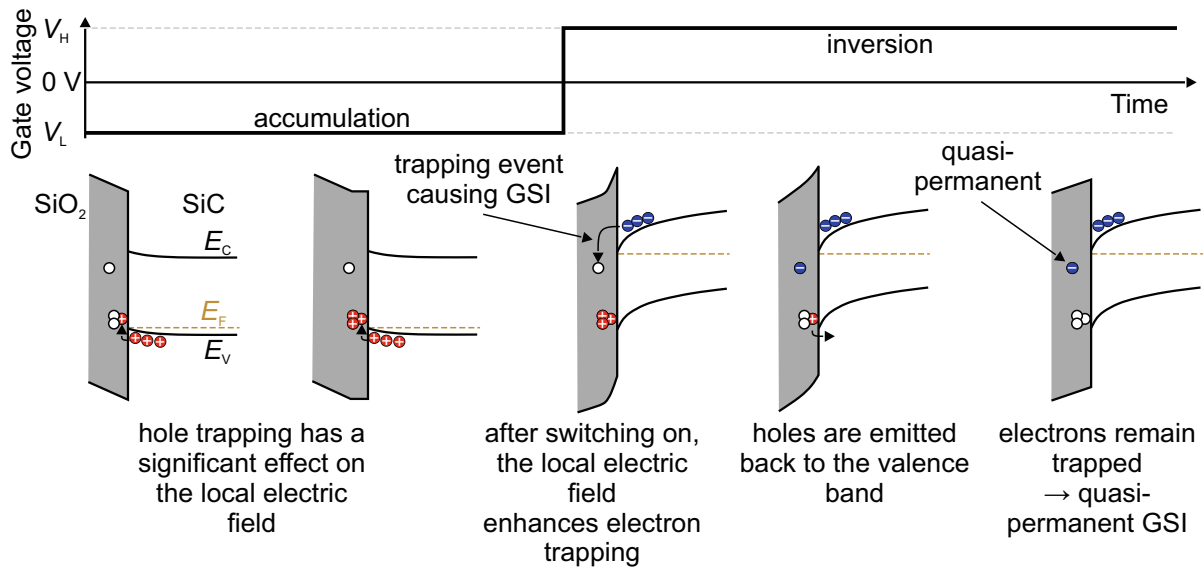


**Figure 4.43.** Illustration of locally-enhanced electric field as a possible cause of GSI. Trapping of holes in donor-like defects close to the valence band changes the electric field for a short time after the transition of  $V_{GS}$  in such a way that electron trapping is enhanced. Redrawn from [MFC5].

degradation mechanism. Table 4.3 summarizes the key findings from the previous sections. Any suggested mechanism must agree with all of these observations.

In literature, two models have been proposed to explain the physics of GSI. The first mechanism is related to a locally-enhanced electric field [297], [303], caused by the recoverable component of  $\Delta V_{th}$ , and the second mechanism is based on REDRs [MFC2], [MFC4], [MFC5], [MFC8]. In the following, these two mechanisms are discussed with respect to their agreement with experimental observations.

### Locally-Enhanced Electric Field

The idea that a locally-enhanced electric field might explain GSI was first proposed by Jiang *et al.* [297] and Scholten *et al.* [303]. The basic idea behind the proposed mechanism is based on the commonly known strength of the recoverable component (hysteresis) in SiC MOSFETs. As in detail discussed in Section 4.2, very short gate pulses down to 100 ns create a  $\Delta V_{th}$  in the regime of a few volts. This means that  $\Delta V_{th}$  can dynamically follow a switching frequency up to 10 MHz and probably even more, which was illustrated by Puschkarsky *et al.* [154], [155]. Consequently, a significant amount of charge is trapped and detrapped at the interface each time  $V_{GS}$  switches from the low level  $V_L$  to the high level  $V_H$ .

Jiang *et al.* argued that this charge alters the local electric field in such a way that the trapping of electrons into defects with higher activation energies is effectively enhanced within a short time after the  $V_{GS}$ -transition from  $V_L$  to  $V_H$ . This short time must be significantly shorter than half of the  $V_{GS}$  period. These trapped electrons then cause the positive  $\Delta V_{th}$  observed upon extensive GSS. This proposed mechanism is schematically illustrated in Fig. 4.43. During the time the MOSFET finds itself in accumulation, the negative  $V_{GS}$  causes a gradually increasing number of holes to get trapped in defects close to the SiC/SiO<sub>2</sub> interface. However, these trapped holes alter the local electric field or rather the potential. Once the MOSFET is then switched into inversion, this change in the local electric field around the trapped holes enhances the trapping of electrons into defects with higher capture activation energies. During the time the MOSFET is

in inversion, the previously trapped holes can detrapp again, which basically leaves the system with trapped electrons.

As GSI was found to be a quasi-permanent degradation, these electrons would have to be trapped quasi-permanently. This means the activation energy for detrapping of these electrons must be significant, such that these charge carriers do not detrapp within regular temperature and voltage conditions.

Jiang *et al.* motivated the proposal of this mechanism by the dependence of GSI on the number of switching events [297]. As the local field enhancement would occur only within a short time after each  $V_{GS}$ -transition from accumulation to inversion, the authors concluded that this agrees with the dependence of GSI on the number of switching cycles. However, this short time of field-enhancement conflicts with previous experimental observations [154], [155], that show that the decrease of  $\Delta V_{th}$  during the  $V_L$ -phase increases monotonously over time, which in turn would increase the field-enhancement per switching cycle and thus the GSI component for a fixed number of switching cycles. This is not supported by experimental observations (see Fig. 4.29b). Although it appears rather unlikely, the last resort would be to argue that even a short measurement delay time of 1  $\mu$ s (as used in [154], [155]) is not enough to capture the full extent of field enhancement.

The observed saturation and reversal of the drift might only partly agree with this model based on locally-enhanced electric field. While the saturation could be assigned to a limited population of precursor states, it remains unclear how a reversal of the drift would be explained. Possibly, this could be incorporated as increased hole trapping that is caused by locally-enhanced electric field at the falling transition caused by trapped electrons captured during the  $V_H$ -phase. This would lead to a negative  $\Delta V_{th}$  component and superimpose with the increased electron trapping at the rising transition.

With respect to the observation that the GSI component requires switching between inversion and accumulation, the model appears to show plausible agreement. The required strong hole trapping of the recoverable component is linked to the accumulation regime and the trapping of electrons from the conduction band similarly requires the device to switch into inversion.

Unfortunately, the temperature dependence does not allow any conclusions to be drawn about the correctness of the mechanism of local field enhancement. Depending on the ratio between increase in trapping and increase in detrapping of the involved holes, the GSI-related drift could go in either direction upon an increase in temperature.

Another argument of Jiang *et al.* was that decreasing the transition time would allow a higher fraction of the previously trapped holes to detrapp again [297]. Indeed, particularly for the data presented in this work with their GSI component that only depends on the rise time, this observation seems to fully agree with the proposed model. However, within the same paper, Jiang *et al.* presented data suggesting that double-diffused MOSFETs (DMOSFETs) could also exhibit a decreasing GSI-related drift with decreasing fall time. However, as the observed  $\Delta V_{th}$  would require enhanced capture of negative charge, this would contradict the proposed model of local field enhancement.

Scholten *et al.* argued in a very similar way [303]. Their central argument for the correctness of understanding GSI as the result of a local field enhancement caused by trapped holes was the observation that an equal drift in terms of  $\Delta V_{th}$  could be created by increasing  $V_{GS}$ . However, the used pulse scheme and successive increase of  $V_{GS}$  can equally be explained by voltage

acceleration of the BTI component. This becomes clearer considering that the authors use in their investigations still quite low numbers of switching cycles down to  $3.6 \times 10^8$ , where the BTI component might dominate over the GSI component (see Fig. 4.27).

The observation that different types of undershoots create an identical degradation could be explained by the fast trapping of holes and absence of their detrapping at negative  $V_{GS}$ . Also this property might therefore fit to the proposed model.

Overall, a few characteristics of GSI could indeed be explained by enhanced electron trapping due to a locally enhanced electric field. Even the fact that the hysteresis (see Fig. 4.42) is not affected by GSS agrees with the model. In this context, the similarity between the charge pumping current and GSI (see Fig. 4.40) would be handled as a coincidence. The permanence of the degradation is also not contradictory to this mechanism.

However, there is a central and very strong disagreement with the observed impact of GSI on the CV curves (see Fig. 4.34). The change in the CV curve clearly related GSI to the creation of acceptor-like interface defects. As already pointed out, enhanced trapping of electrons due to a locally enhanced electric field would lead to quasi-permanently trapped electrons that would lead to a horizontal shift of the CV curve – which is clearly not observed. In the devices used here, the BTI component is rather small compared to the GSI component, which supports the clear assignment of the observed acceptor-like interface defects to GSI. Even if there were devices with a stronger BTI component that introduces quasi-permanently trapped charges leading to an additional parallel shift of the CV curve, this would not be in immediate disagreement with the assignment of GSI to the creation of acceptor-like interface defects.

In summary, although the idea of increased electron trapping due to locally-enhanced electric field agrees with a lot of the experimental observations, it clearly fails to explain the change in the CV curve showing that GSI creates acceptor-like interface defects that are only charged in the weak-to-strong inversion regime. As it is understood at the moment, this model is not sufficient.

### Recombination-Enhanced Defect Reactions as the Cause of the Gate Switching Instability

As established in the preceding section, increased electron trapping due to a locally enhanced electric field cannot be the cause of GSI, as it clearly conflicts with experimental observations. The other proposed mechanism is based on REDRs (see Section 2.1.3) [MFC2], [MFC4], [MFC5], [MFC8]. In the following, based on the experimental findings summarized in Table 4.3, it will be deduced why a mechanism based on REDRs is fully consistent with all observations – also those from other researchers.

GSI is caused by the creation of acceptor-like interface defects, as discussed in Section 4.3.4. As the  $\Delta V_{th}$  observed in GSI experiments by far exceeds the observed  $\Delta V_{th}$  under direct current (DC) or unipolar alternating current (AC) stress conditions (see Section 4.3.5) [283], [286], a reaction creating the observed interface defects must feature a considerable activation energy on the order of a few electronvolts. This reaction is the transformation of an electrically inactive precursor state to an electrically active acceptor-like state. However, as it cannot be a conventional NMP process that would also occur under DC conditions at high temperature, this activation energy barrier must be overcome by another mechanism supplying the required energy. As suggested in Section 4.3.8, the similarity between the transition time dependence of GSI and the one of the CP current suggests that this reaction is driven by defect-assisted recombination.



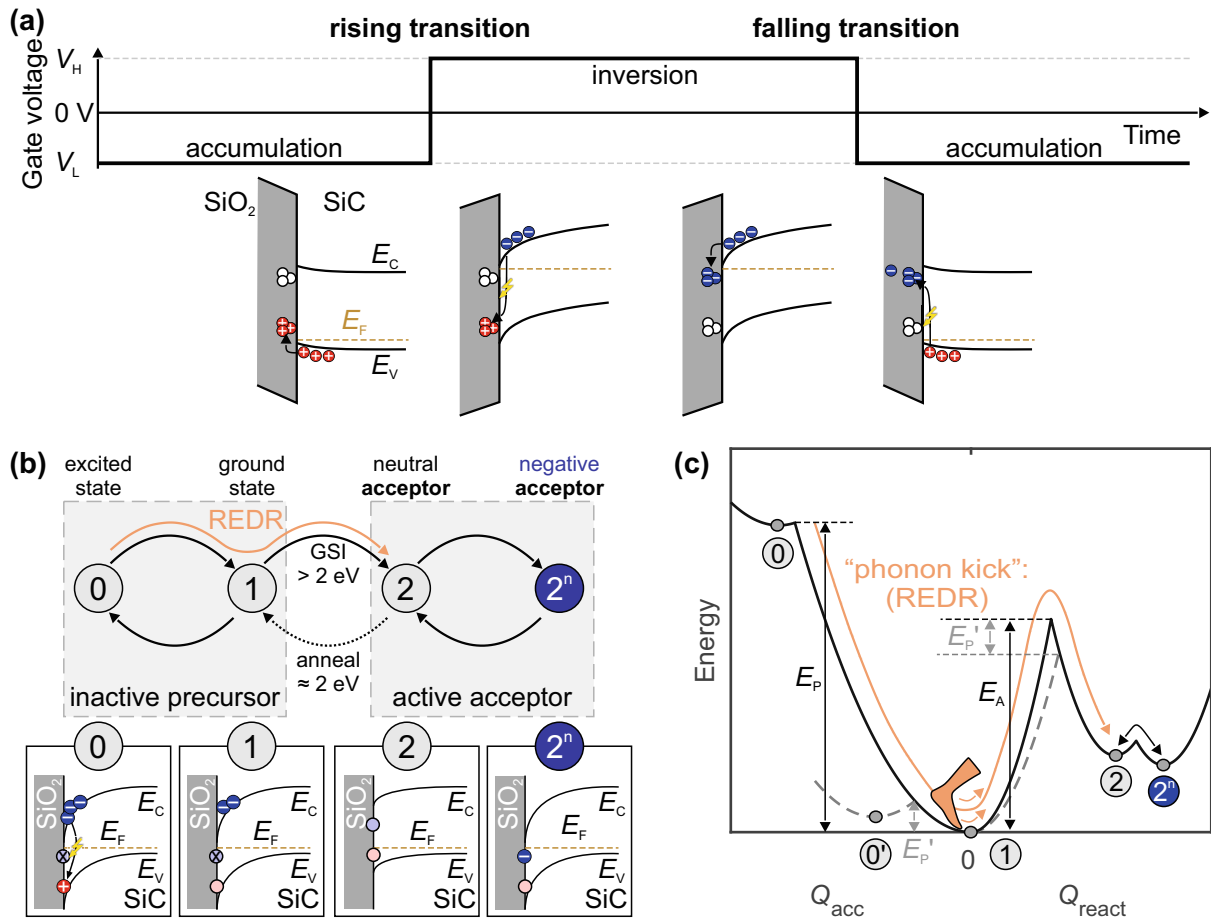


**Figure 4.44.** (a) Defect-assisted recombination at the rising and falling transition of  $V_{GS}$ . The released energy leads to the creation of acceptor-like defect states. (b) Illustration of the different states involved in GSI for a recombination event at the rising transition. (c) Configuration coordinate diagram corresponding to the states illustrated in (b). Potential energy curves (PECs) indicated by grey dashed lines illustrate a case where the energy barrier for the transition  $1 \rightarrow 2$  is only reduced by the phonon kick energy. Redrawn from [MFC5].

As outlined in Chapter 2, this recombination could either involve radiative or non-radiative transitions at the rising and/or the falling transition of  $V_{GS}$  (see Fig. 4.44a).

If it was a radiative transition, the energy of the recombination event would be released in the form of a photon. Theoretically, this photon could be reabsorbed by the inactive precursor state and thereby trigger its transformation into an active acceptor state. Essentially, the photon would transport the energy from the site of recombination to the site of the defect reaction. Alternatively, the creation of the acceptor-like interface defect could be related to non-radiative recombination. Since the conventional NMP process cannot overcome such large activation energy barriers within reasonable times, REDRs are the only option to transfer the energy from the recombination event into a defect reaction. This directly leads to the existence of several states that are illustrated in Fig. 4.44b. For simplicity, the processes prior to the recombination event are not depicted. Based on the observation that the GSI component depends exclusively on the rise time, recombination of a trapped hole in a state close to the valence band with a conduction band electron is a very likely choice for the recombination process supplying the needed energy. However, this can be generalized in a straight forward manner to include recombination of holes from the valence band with trapped electrons as well. The involved states

are labeled 0, 1, 2, and  $2^n$ . The acceptor-like interface defects created during GSS are described by states 2 and  $2^n$  being the neutral and negative acceptor state, respectively. Depending on the applied  $V_{GS}$ , the acceptor-like defect is in one of those two states. As discussed, NMP transitions between them occur rapidly within less than a microsecond. Before GSS, this defect is in its inactive precursor state, including the excited state 0 and the ground state 1.

The transition from state 0 to state 1 is the recombination event, which is triggered by switching the MOSFET from accumulation to inversion. During the  $V_L$ -phase, the hole trap captures a hole from the valence band. Once the MOSFET is switched into inversion, the hole is either emitted back to the valence band or it stays in the hole trap sufficiently long enough, such that it can subsequently recombine with an inversion electron from the channel. Their recombination ( $0 \rightarrow 1$ ) releases a phonon kick energy that is cast into the reaction thereby transforming the inactive precursor state into the active acceptor state ( $1 \rightarrow 2$ ). If the MOSFET is then situated in inversion, the transition  $2 \rightarrow 2^n$  can immediately occur and the system ends up in state  $2^n$ . In this state, the  $\Delta V_{th}$  created by the negatively charged acceptor state can be measured. But, once the MOSFET is switched back into accumulation, the active acceptor becomes neutral and could even be annealed out ( $2 \rightarrow 1$ ) at high temperature by overcoming the mentioned energy barrier of about 2 eV (see Section 4.3.11).

The corresponding configuration coordinate diagram including all transitions is illustrated in Fig. 4.44c. As discussed in Section 2.1.3, for the case of a sufficiently large phonon kick energy  $E_P > E_A$ , the transition  $1 \rightarrow 2$  would be temperature independent. The only temperature dependence would originate from the emission of the trapped hole in the hole trap close to the valence band at the transition from accumulation to inversion. With increasing temperature, the hole is more likely to be emitted back to the valence band and hence the observed GSI would decrease. However, for the other case of  $E_P < E_A$  (grey dashed lines in Fig. 4.44c), the activation energy barrier of the transition  $1 \rightarrow 2$  would be reduced by the phonon kick energy  $E_P$ . Consequently, there might even occur a case where GSI-related drift increases upon increasing the temperature – of course this would also depend on the detrapping kinetics of the previously trapped hole. However, such a behavior has not been observed yet. It can therefore be concluded that the energy barrier for the transition  $1 \rightarrow 2$  is smaller than the phonon kick energy. Theoretically, the phonon kick energy can be almost as high as the bandgap of 3.26 eV.

Furthermore, note that the postulated states could all be assigned to the same defect. In this case, the hole trap state close to the valence band might disappear upon creation of the active acceptor state. Alternatively, the trap level of the hole trap state might only slightly change its energy level upon the transformation of the defect into the active acceptor state. In addition to that, the recombination could trigger the release of a mediating species that subsequently reacts at another defect to create the active acceptor state [MFJ6], [MFC6]. In this case, the hole trap state would work as a catalyst for the reaction.

Indeed, the above presented mechanism fully agrees with all experimental observations summarized in Table 4.3. A point-by-point discussion is presented in the following.

First, the exclusive dependence of GSI on the number of switching cycles results from the fact that only a switching event between accumulation and inversion could provide the defect-assisted electron-hole recombination needed to drive an REDR. Each time the MOSFET is switched, there is a certain probability of an REDR to occur. Neglecting limited populations of defects, this leads to the observed proportionality to the number of switching cycles  $N_{sw}$ , that is

observed in experiment. The GSI component must roughly follow a relation of

$$\Delta V_{\text{th}}^{\text{GSI}}(N_{\text{sw}}) = \frac{q}{C_{\text{ox}}} \Delta N_{\text{it}}(N_{\text{sw}}) = \frac{q}{C_{\text{ox}}} k(V_{\text{H}}, V_{\text{L}}, \dots) N_{\text{sw}}, \quad (4.35)$$

where  $k(V_{\text{H}}, V_{\text{L}}, \dots)$  incorporates any dependence on other parameters, such as the voltage levels, that affect the probability for an REDR to occur. The saturation of the GSI component might originate from the fact that the reactants deplete: the more involved defects end up in states 2 and  $2^n$ , the less reactants are available. This leads to the saturation. A reversal of the GSI component might be caused by another reaction, which deactivates the acceptor state again [MFJ6], [MFC6].

The active acceptor states have been observed as a stretch-out in CV measurements and the voltage level dependence originates from the factor  $k(V_{\text{H}}, V_{\text{L}}, \dots)$ : the higher the electron and hole density at the interface during inversion and accumulation, the higher the probability of an REDR to occur. The trapping process for the charge carrier that will subsequently recombine must be a regular NMP process, which is of course sensitive to the electric field. Only switching between inversion and accumulation allows defect-assisted recombination and REDRs and thus causes GSI. If the emission of the trapped holes back to the valence band at negative  $V_{\text{GS}}$  is negligible, undershoots create an equal GSI-related drift as fully switching down to the voltage of the undershoot. Hence, this is in agreement with the experiments on the impact of undershoots.

The temperature independence or the decrease of GSI with increasing temperature fully agrees with the presented model. A sufficiently large phonon kick energy makes the REDR temperature independent. If some of the holes required for the recombination detrapp at higher temperature, the GSI component is reduced. This certainly depends on the exact distribution of the involved hole trap and might vary with the respective type of interface, the interface processing and consequently among different device designs. The dependence on the transition time equally results from enhanced detrapping of the required holes at longer transition times. If a device shows also a dependence on the fall time, this might be caused by the presence of another mechanism based on recombination of trapped electrons with accumulated holes in the valence band.

The quasi-permanence of GSI and its annealing are a consequence of the high activation energy of about 2 eV for the transition from  $2 \rightarrow 1$ . The observation that the hysteresis measured with a measurement delay after positive and negative pulses is not affected by GSS is the result of the fast trapping kinetics of the created acceptor state. Once the device is switched into the weak-to-strong inversion regime, the acceptors are always charged once  $V_{\text{th}}$  is measured.

All these explanations and the mechanism invoked for GSI are analogous to the processes involved in CP experiments, addressing any type of defect-assisted recombination at the semiconductor-insulator interface. Thus, the similarity between the transition time dependence of the CP current and the GSI-related drift is in full agreement with the presented model. A part of the CP current probably represents the recombination triggering the REDRs.

The correctness of the model is further supported by the  $V_{\text{L}}$ -dependence of the CP current, the absolute of  $\Delta V_{\text{th}}$  at the end of the  $V_{\text{L}}$ -phase (called hysteresis), and the GSI-related drift, that are shown in Fig. 4.45. Apparently, these quantities share a similar onset around  $-3$  V. The hysteresis represents the trapping of the holes required for the recombination and the CP current represents the recombination itself. As both their onsets agree with the onset of GSI, the model based on REDRs agrees with the observed behavior.

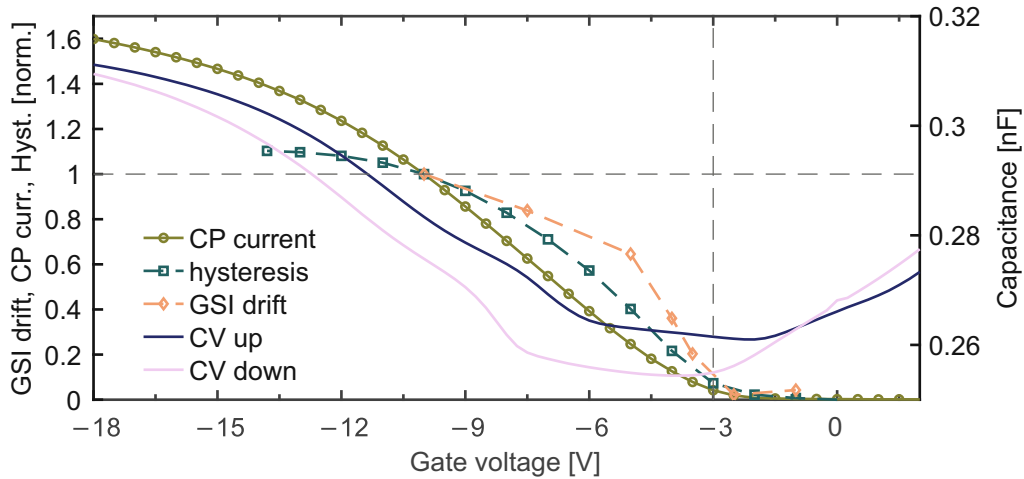


**Figure 4.45.** Comparison of low-level dependence between charge pumping current, recoverable threshold voltage shift and drift upon gate switching stress. Redrawn from [MFC5].

Finally, it needs to be said that REDRs are nothing unusual in wide-bandgap semiconductors or SiC-based systems. Indeed, REDRs were clearly demonstrated to exist in bulk 4H-SiC involving several defect reactions [304], [305]. For instance, a so-called HS2 hole trap that serves as a recombination center shows significant laser light and current induced REDRs. As measured by deep-level transient spectroscopy (DLTS), this state is located about 0.44 eV above the valence band. Overall, this supports the understanding of GSI as an REDR-based mechanism.

#### 4.3.13 Gate Switching Instability in Silicon MOSFETs?

GSI has always been discussed as a mechanism that exclusively arises in SiC MOSFETs. This section discusses observations in Si-based devices that have similar characteristics as GSI and compares them to the experimental properties and characteristics shown in the the previous sections of this work.

It was recognized early on that apart from pure hole trapping in the SiO<sub>2</sub> insulator of Si-based MOSFETs, the recombination of electrons and holes can give rise to a higher interface state generation [306]. This was referred to as “recombination-induced structural change” and could also explain the interface state generation upon high energy irradiation. Essentially, this must be REDRs as described in Section 2.1.3. However, in these devices, the created interface defects were rather slow, which is why they could be directly detected by using CV measurements of different small-signal frequency.

Similar results were obtained in time-dependent dielectric breakdown (TDDB) experiments [307], [308]. Devices were subjected to three different stress waveforms: a positive unipolar stress, a negative unipolar stress and a bipolar stress. While trapping in defects deeper in the oxide was higher at unipolar stress, interface state generation was significantly enhanced under bipolar stress. These interface states destructively affected the effective channel mobility of the devices and caused an increase in the subthreshold slope, but there was no correlation with the breakdown of the oxide. Only an increased  $\Delta V_{th}$  was observed. Interestingly, the interface state generation increased with decreasing frequency. Certainly, these experiments cannot be easily compared to the GSI experiments presented in the course of this work, however, the striking similarity is that in both cases, electron-hole recombination is suggested to be the cause of an enhanced degradation under bipolar switching. Although the frequency dependence is

the opposite of the dependence of GSI, it cannot be excluded that a similar mechanism is also responsible for the enhanced interface state generation upon bipolar switching at high electric fields. The differences might originate from the different charge injection/trapping processes that occur prior to the recombination events.

There was even another study that found an increasing interface state generation with increasing switching frequency using the CP technique [309]. This increased generation was also present if  $V_L$  was situated in depletion, which is different from GSI. However, the authors also observed a strong onset in generation once they entered accumulation and assigned this to increased electron-hole recombination. Although this would be a promising similarity to GSI, the authors also observed a strongly asymmetric dependence on the duty cycle, whereby the interface state generation decreased with increasing duty cycle.

In the context of a comparison to GSI in SiC MOSFETs, a particularly remarkable study showed a clearly switching frequency driven interface state generation in Si p-channel MOSFETs upon bipolar switching [310]. The fact that this interface state generation was temperature activated does not necessarily contradict the temperature independence observed in SiC devices – the temperature independence in SiC devices might be caused by the wider bandgap supplying more recombination energy. Furthermore, the authors found a strongly increasing power law exponent at higher frequency, which might match the observations of the GSI component in SiC devices, that causes this typical strong onset in  $\Delta V_{th}$ .

A more recent study investigated bipolar switching in Si fin field-effect transistors (FinFETs) [311]. The authors observed a higher contribution from generated interface defect states to the total  $\Delta V_{th}$  upon bipolar stress compared to unipolar or DC stress. These defects were detected by the CP technique. However, the total  $\Delta V_{th}$  was lower in the case of bipolar stress and it decreased with decreasing duty cycle.

Finally, the most recent study on bipolar switching of Si devices linked an increased interface state generation to the gate-sided hydrogen release model [312], which successfully describes many characteristics of BTI [313]–[316]. The authors observed an increased interface defect generation upon bipolar switching compared to unipolar switching, however, the degradation did not significantly increase with increasing switching frequency – at least as far as GSI is concerned. The authors also compared devices with a  $\text{SiO}_2$  insulator to  $\text{SiO}_2/\text{HfO}_2$  devices, whereby the latter exhibited lower interface state generation upon bipolar switching.

Overall, it is difficult to determine from the available literature on bipolar switching in Si-based devices whether GSI with similar characteristics as in SiC devices equally exists. As indicated by the presented studies, it can certainly be concluded that bipolar switching indeed leads to enhanced interface state generation, which would be a similarity to GSI, however, the exact characteristics are unclear. At least, it seems that significantly higher electric fields are required to trigger comparable effects. More studies on Si-based devices are needed to have concrete characterization and understanding of this effect. Such work should include measurements from very short to very long stress times, variations of the switching frequency, and an investigation of the temperature dependence. Attempts to separate off the BTI component, as it must also be present in Si devices, are desirable.

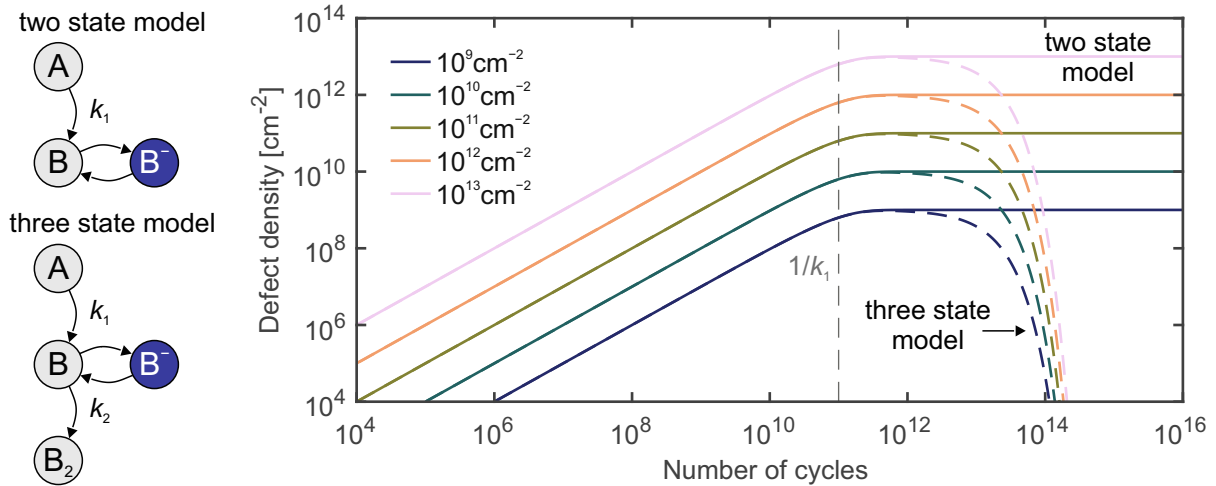


**Figure 4.46.** Schematic illustration of two and three state models and the corresponding drift curves for  $k_1 = 10^{-11}$ ,  $k_2 = 10^{-13}$ , and different  $A_t$ . Redrawn from [MFJ6].

#### 4.3.14 Mathematical Model based on Recombination-Enhanced Defect Reactions

*The contents of this section were previously published in [MFJ6], [MFC6].*

As outlined in Section 4.3.12, GSI is likely caused by REDRs. However, in order to achieve a good fit of the experimental data, some modifications of the linear relation between  $\Delta V_{th}$  and the number of switching cycles  $N_{sw}$  might be applied based on the following considerations.

First, it could be recognized that the observed drift as shown in Fig. 4.35 seems to change its shape for different high  $V_H$  and low level  $V_L$  combinations. Assume GSI would be caused by transforming a precursor state  $A$  into an active state  $B$  that can be negatively charged with an associated state  $B^-$ . This is illustrated in Fig. 4.46. The backward reaction is neglected, as GSI was found to be quasi-permanent. This would imply the following rate equations

$$\begin{aligned} \frac{dA}{dN_{sw}} &= -k_1 A \\ \frac{dB}{dN_{sw}} &= k_1 A \end{aligned}$$

which has the simple solution

$$B(N_{sw}) = A_t (1 - \exp(-k_1 N_{sw})) \quad (4.36)$$

where  $k_1$  is the reaction rate.  $A_t$  is the defect density of  $A$  initially available at  $N_{sw} = 0$ . Hereby,  $B(N)$  is the density of active acceptor-like defects. Transitions between  $B$  and  $B^-$  are fast on the time scale of a switching cycle, which means they can be neglected. According to the previously presented understanding, changing  $V_L$  and  $V_H$  just affects the number of defects  $A_t$  participating in the recombination. Apparently,  $B(N_{sw})$  scales with  $A_t$  and does hence not change its shape for different combinations of  $V_H$  and  $V_L$ . This is illustrated in the plot in Fig. 4.46. Furthermore, such a two state model would not be able to explain a drift reversal – it can only explain saturation around the point  $N_{sw} = 1/k_1$ . This means, GSI cannot be described by a simple two state model.

As a next step, a three state model, where the third state  $B_2$  would be an inactive state explaining the drift reversal, could be assumed. This is again illustrated in Fig. 4.46. The

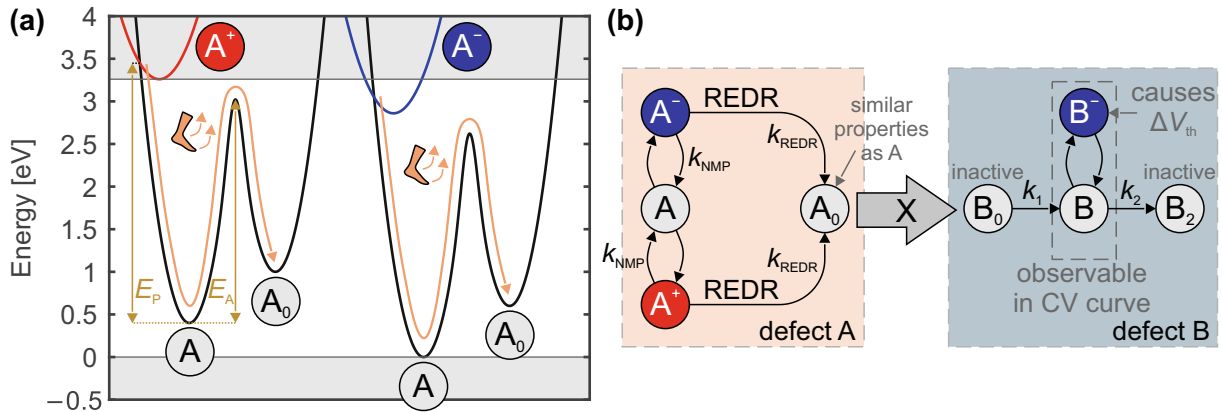


**Figure 4.47.** (a) Configuration coordinate diagrams illustrating the process of REDRs occurring at the rising and falling transitions, respectively. The phonon kick energy  $E_P$  and the activation energy  $E_A$  are indicated. (b) Schematic diagram illustrating the different states of the model describing GSI as an REDR-based mechanism. Redrawn from [MFJ6].

corresponding rate equations are

$$\frac{dA}{dN_{sw}} = -k_1 A \quad (4.37)$$

$$\frac{dB}{dN_{sw}} = k_1 A - k_2 B \quad (4.38)$$

$$\frac{dB_2}{dN_{sw}} = k_2 B \quad (4.39)$$

with the solution

$$B(N_{sw}) = A_t \frac{k_1}{k_2 - k_1} (\exp(-k_1 N_{sw}) - \exp(-k_2 N_{sw})) \quad (4.40)$$

where  $k_2$  is the rate for the deactivation of the active state  $B$ . Again,  $B(N_{sw})$  scales with  $A_t$ , which would not explain different shapes of drift curves for different combinations of  $V_H$  and  $V_L$ .

Consequently, another mechanism is suggested, which is based on the release and capture of a mediating species  $X$ . All the states are illustrated in Fig. 4.47. Assume to be at the end of the  $V_L$ -phase, meaning the defect  $A$  has captured a hole from the valence band. This state is referred to as  $A^+$ . Once the MOSFET is switched up to  $V_H$ , the trapped hole can either recombine with an electron from the conduction band and go back to state  $A$  via an ordinary NMP process or it can use the energy released by the recombination event to cast it into the reaction of releasing a species  $X$ . This way the defect goes over to state  $A_0$ , which must have similar properties as  $A$ , because it could not be observed in hysteresis or CV characterization. Analogously, at the end of the  $V_H$ -phase, the defect  $A$  has captured an electron from the conduction band and is thus in the state  $A^-$ . Once it is switched into accumulation, the trapped electron can recombine with a hole from the valence band by either going back to state  $A$  via an NMP process or by going into state  $A_0$  via an REDR.

Following the approach of Sumi [190], presented in Equations 2.27 and 2.28 of Section 2.1.3, for ideal coupling  $|g| = 1$ , this gives the activation energy of the REDR process following

$$E_H = \max(0, E_A - E_P). \quad (4.41)$$

The corresponding rate (quantum efficiency) of REDR is then given by

$$c = \text{QE}_{\text{REDR}} = \frac{k_{\text{REDR}}}{k_{\text{REDR}} + k_{\text{NMP}}} = f_c \gamma \exp\left(-\frac{E_H}{k_B T}\right) \quad (4.42)$$

with  $f_c \in [0, \dots, 2]$ . While  $f_c$  practically incorporates the fact that an REDR could occur at both the rising and falling transitions or at only one or none of the two transitions,  $\gamma$  describes the coupling between the energy accepting coordinate and the reaction coordinate. For simplicity, it is assumed that both the rising and the falling transitions have the same properties resulting in an identical  $c$ . However, this could be generalized at the cost of increased complexity in the following calculations.

The species  $X$  finally reacts at another defect  $B$ , transforming it from state  $B_0$  to  $B$  at a rate  $k_1$  in such a way that the observed acceptor-like interface defect close to the conduction band is created.  $B$  can get charged by an electron from the conduction band, which leads then to the state  $B^-$ .  $B^-$  is the cause of the observed  $\Delta V_{\text{th}}$  and the transitions between  $B^-$  and  $B$  were observed as a stretch-out of the measured CV characteristics. Finally, the observed drift reversal can be explained by another deactivating reaction with a species  $X$  from state  $B$  to state  $B_2$ , which must be an inactive state.

At a first glance, the idea with a mediating species  $X$  appears a bit far fetched, but there are indeed several known candidates for such a defect  $A$ , which are able to emit some sort of species  $X$ . This includes hydrogen bridges and hydroxyl  $E'$ -centers in  $\text{SiO}_2$ , which can emit a hydrogen atom [317], or even carbon clusters in  $\text{SiC}$  that can emit a carbon atom [318]. The deactivating reaction involves another species  $X$ , leading to saturation and drift reversal, which is e.g. a known behavior of hydroxyl  $E'$ -centers [313].

There are a few assumptions upon which this model is based. First, the capture of a charge carrier by  $A$  during the  $V_H$ - and  $V_L$ -phases, respectively, is fast enough such that it is completed at the end of each phase. The corresponding time constants must therefore be smaller than half of the period of  $V_{\text{GS}}$ . Second, the  $V_{\text{GS}}$  waveform is usually not ideal. During the  $V_{\text{GS}}$ -transition, some of the previously trapped charge carriers can be emitted back to the band from which they came from. This means that they cannot participate in the recombination. As already pointed out, this is described by the number of participating defects  $A_t$ , which depends on the rise time, the fall time, the temperature,  $V_H$ , and  $V_L$ . The corresponding dependencies can be understood in the framework of CP theory (see Section 3.4).



Overall, this model can be described by the following rate equations.

$$\frac{dA}{dN_{sw}} = -cA \quad (4.43)$$

$$\frac{dB_0}{dN_{sw}} = -k_1 B_0 X \quad (4.44)$$

$$\frac{dB}{dN_{sw}} = k_1 B_0 X - k_2 B X \quad (4.45)$$

$$\frac{dX}{dN_{sw}} = cA - k_1 B_0 X - k_2 B X \quad (4.46)$$

At cycle  $N_{sw} = 0$ , there are  $B_t$  defects available. While for  $A$  the solution is rather trivially obtained by

$$A(N_{sw}) = A_t \exp(-cN_{sw}) \quad (4.47)$$

there is no analytic solution for this system of differential equations. Empirically, it was found that

$$X(N_{sw}) \approx R \frac{c}{k_1} \exp(-cN_{sw}) \quad (4.48)$$

is a good approximation with  $R = A_t/B_t$ . Inserting this into Equation 4.44 gives

$$B_0(N_{sw}) = B_t \exp(-R(1 - \exp(-cN_{sw}))) = B_t f(R, N_{sw}, c) \quad (4.49)$$

Finally, inserting Equations 4.48 and 4.49 into Equation 4.45 yields the quantity  $B(N_{sw}, c)$  which is relevant for the degradation and follows

$$B(N_{sw}, c) = \frac{B_t}{r-1} (f(R, N_{sw}, c) - f(rR, N_{sw}, c)) \quad (4.50)$$

where  $r = k_2/k_1$ . The condition  $B_0 + B + B_2 = B_t$  results in

$$B_2(N_{sw}, c) = B_t - B_0(N_{sw}, c) - B(N_{sw}, c). \quad (4.51)$$

Finally, it is expected that at least the parameter  $c$  is distributed. This is analogous to the distribution of defect parameters in the NMP-based description of BTI (see Section 2.1.2) [140], [143], [319]–[321]. In this model, it is assumed that  $\log(c)$  is normally distributed, which translates into

$$B(N_{sw}) = \int B(N_{sw}, c) \frac{1}{\sigma_c \sqrt{2\pi}} \exp\left(-\frac{(\log(c) - \log(c_0))^2}{2\sigma_c^2}\right) d\log(c). \quad (4.52)$$

However, this is not analytically solvable. Based on previous approaches [140], [271], the function  $f(\rho, N_{sw})$  can be approximated by

$$f(\rho, N_{sw}) \approx H\left(\frac{1}{\rho c} - t\right) + H\left(t - \frac{1}{\rho c}\right) \exp(-\rho) \quad (4.53)$$

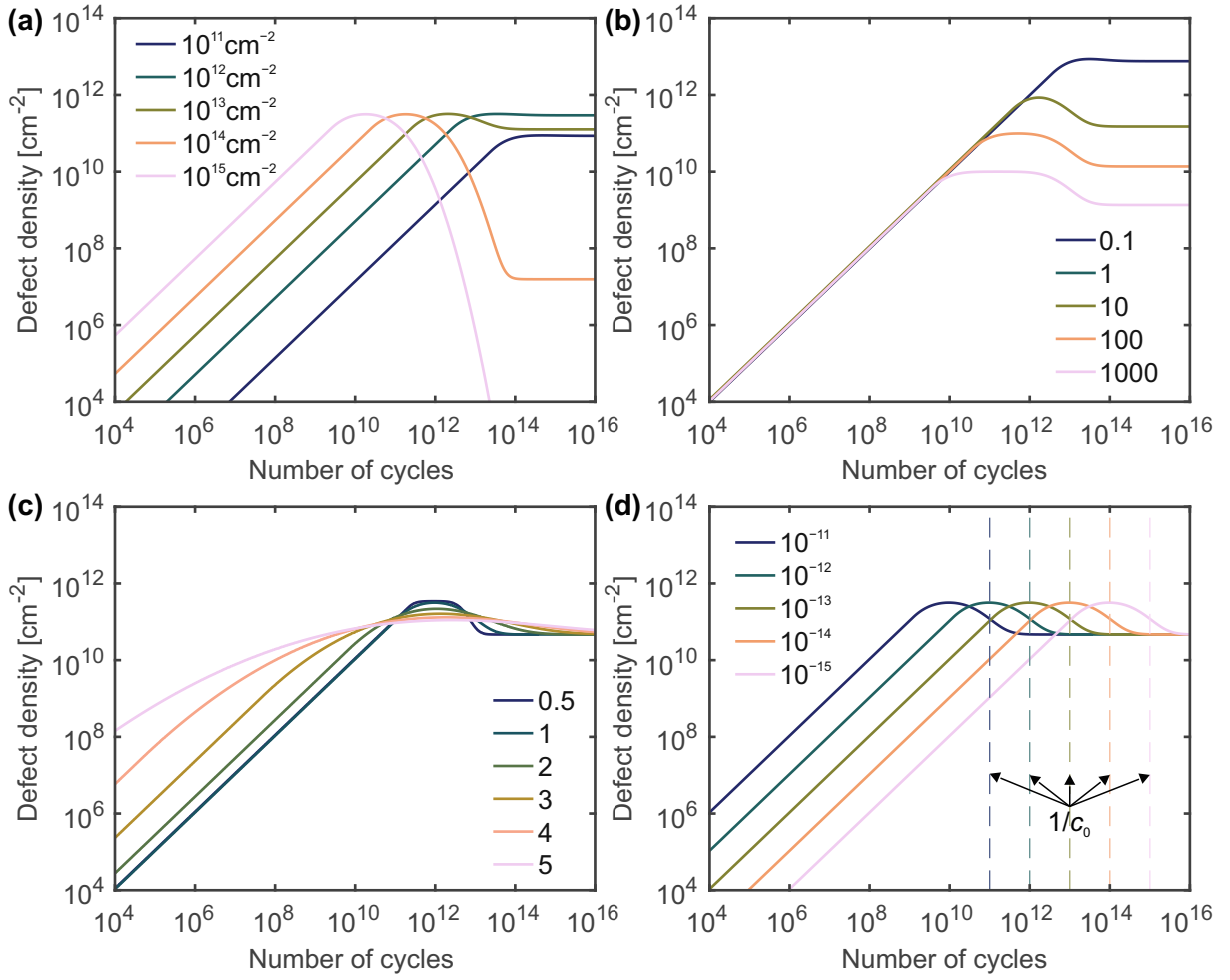


**Figure 4.48.** (a) Drift curves for different  $A_t$ . (b) Drift curves for different  $r$ . (c) Drift curves for different  $\sigma_c$ . (d) Drift curves for different  $c_0$ . Redrawn from [MFJ6].

with  $H$  being the Heaviside step function. Splitting up the cases for high and low  $N_{sw}$ , this gives an analytic approximation for the integral as per

$$B(N_{sw}) \approx \begin{cases} A_t \eta c_0 \exp\left(\frac{\sigma_c^2}{2}\right) N_{sw}, & N_{sw} \leq N_{th} \\ \frac{B_t}{r-1} (F(R, N_{sw}) - F(rR, N_{sw})), & N_{sw} > N_{th} \end{cases} \quad (4.54)$$

with

$$F(\rho, N_{sw}) = \Phi\left(-\frac{\log(c_0 \rho N_{sw})}{\sigma_c}\right) + \left(1 - \Phi\left(-\frac{\log(c_0 \rho N_{sw})}{\sigma_c}\right)\right) \exp(-\rho) \quad (4.55)$$

and the Gaussian integral

$$\Phi(x) = \frac{1}{2} \left(1 + \operatorname{erf}\left(\frac{x}{\sqrt{2}}\right)\right). \quad (4.56)$$

The values for  $\eta$  and  $N_{th}$  are related to approximating  $B(N_{sw})$  for small  $N_{sw}$  and large  $N_{sw}$ , separately. First,  $\eta$  is used to make the entire approximation function continuous, whereby  $\eta$  is

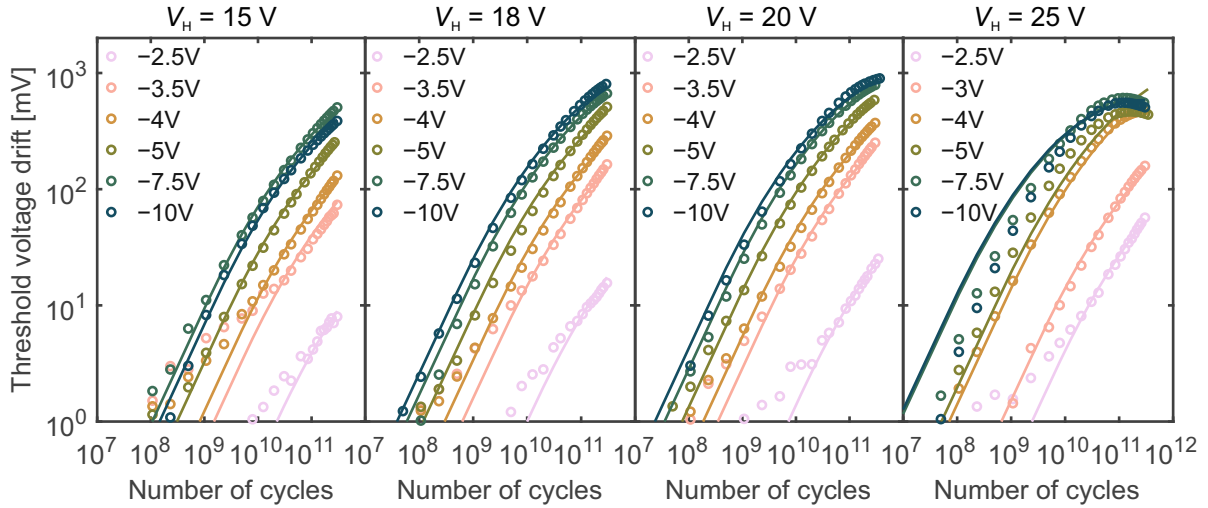


**Figure 4.49.** Comparison between the experimentally extracted GSI component for different  $V_H$  and  $V_L$  combinations, originally presented in Fig. 4.35, with the presented mathematical model. As the  $V_H/V_L$  combination should theoretically only affect  $A_t$ , each curve has its own free parameter  $A_t$ , but all other parameters are the same for the entire set of data.

then a function of  $N_{th}$  via

$$\eta(N_{th}) = \frac{B_t}{r-1} \frac{(F(R, N_{th}) - F(rR, N_{th}))}{A_t \eta c_0 \exp\left(\frac{\sigma_c^2}{2}\right) N_{th}}. \quad (4.57)$$

The values of  $\eta$  and  $N_{th}$  are related to the position of the maximum of  $\eta(N_{th})$ , which can be obtained by minimizing  $-\eta(N_{th})$ .

As a result, Equation 4.54 describes the GSI-related creation of active acceptor-like interface defects. The formula depends on the five parameters  $A_t$ ,  $B_t$ ,  $r$ ,  $c_0$ , and  $\sigma_c$ . The impact of the different parameters on the drift evolution is illustrated in Fig. 4.48.

As a last step, the model described by Equation 4.54 was used to fit the previously extracted GSI components for various  $V_H/V_L$  combinations. The resulting fit is shown in Fig. 4.49. As  $V_H$  and  $V_L$  should only affect  $A_t$ , the entire set of data were fitted by the same  $B_t$ ,  $r$ ,  $c_0$ , and  $\sigma_c$ , but each shown drift curve has its own  $A_t$ . For  $V_H \leq 20$  V, the fit is excellent, whereas for  $V_H = 25$  V, the fit is rather unsatisfactory. However, this might be related to the electrostatics of the used asymmetric trench devices. At 25 V, the other side of the trench, which is p+ doped, is clearly inverted (see Fig. 1.11). This is visible in the CV characteristic (see Fig. 4.30).

## 4.4 Field-Effect Stimulated Optical Spectroscopy of Interface Defects

The contents of this section were previously published [MFC3], [MFJ8] or were accepted for publication [MFJ2]. The paper “Electrically stimulated optical spectroscopy of interface defects in wide-bandgap field-effect transistors” [MFJ8] was selected as Editors’ Choice 2023 [322] of the journal *Communications Engineering*.

The gate switching instability (GSI) presented in the previous section is likely due to defect-assisted electron-hole recombination at the silicon carbide (SiC)/silicon dioxide (SiO<sub>2</sub>) interface. The released energy is hereby non-radiatively cast into the activation of an inactive precursor defect. Alternatively, the energy released by a defect-assisted recombination event could be released radiatively via the emission of a photon. Studying the properties of the photon emission could therefore allow to get deeper insights into the properties of the involved interface defects.

Indeed, in the years 2000–2001 it was already observed by Stahlbush *et al.* [240], [241] and Macfarlane *et al.* [239] that both 6H- and 4H-SiC metal-oxide-semiconductor field-effect transistors (MOSFETs) can emit light, once the gate-source voltage ( $V_{GS}$ ) is switched between inversion and accumulation, while keeping both drain and source terminals grounded. Note that this is exactly the operation mode where GSI occurs or where charge pumping (CP) experiments are conducted.

Macfarlane and Stahlbush investigated this effect on planar devices with a lateral current flow (see Section 1.5.1). The light was detected through the top of the device, meaning it first had to pass the SiO<sub>2</sub> and polycrystalline silicon gate before being detected. In their work, they observed two spectral contributions that they assigned to defect-assisted recombination at the interface and in the bulk, respectively. The interface recombination was located in the region of 500–800 nm (1.55–2.48 eV), whereas the bulk recombination was situated close to the bandgap of 6H-SiC around 425 nm (2.92 eV). Although the authors succeeded in time-gating the spectral detection, which allowed them to separately investigate the light emission from the rising and falling transition of  $V_{GS}$ , the emission spectra could not be related to known defect densities of the interface.

Indeed, their measurement technique was limited by absorption of the polycrystalline silicon layer, which the authors blamed for creating interference patterns in the observed spectra [240]. This hindered a deeper analysis of the emission spectra. Besides imaging the electron flow during turn-on, their method allowed the authors to provoke a dominance of the bulk recombination, which allowed to image 3C inclusions in the bulk crystal under unipolar switching. Finally, the authors did not find a significant impact of NO annealing on the emission spectrum [241]. Despite the fascinating character of the results shown by Stahlbush *et al.* [240], [241] and Macfarlane *et al.* [239], the topic of light emission from SiC MOSFETs under gate switching did not get further attention by the research community over two decades.

In the course of this work, the light emission from 4H-SiC MOSFETs is investigated and correlated to more conventional electrical measurements – including ultra-fast threshold voltage ( $V_{th}$ ) and capacitance-voltage (CV) measurements. In contrast to Stahlbush *et al.* and Macfarlane *et al.*, who used research-grade planar devices with a lateral current flow, fully-processed commercially-available 4H-SiC power double-diffused MOSFETs (DMOSFETs) were used here. Their light emission was measured through the backside of the chip. As any semiconductor is transparent below its bandgap and there are only weakly absorbing defect states within the bandgap of 4H-SiC [323], this approach avoids the mentioned limitations originating from absorption in the top layers above the gate oxide.

First, this measurement approach of detecting the light emission from the backside is outlined in greater detail, followed by presenting the measurements of the light emission with an emission microscope at different switching frequencies, which allows to spatially locate the light emission. Next, the measurement of light emission from single  $V_{GS}$ -transitions is presented and subsequently used to determine the voltage level dependence of the observed light emission and linking it to the well-known transient threshold voltage shift ( $\Delta V_{th}$ ). Afterwards, a pump-probe scheme is introduced which allowed to relate the light emission to the recovery of transient  $V_{th}$  shifts associated with the recoverable component of bias temperature instability (BTI). Also a link between  $\Delta V_{th}$  and light emission upon extended gate stress is presented.

In addition, the light emission is spectroscopically characterized and the thereby obtained energy distribution of the emitted photons is compared to density functional theory (DFT)-based ab-initio calculations from literature. Finally, time-gated optical spectroscopy is used to analyze the light emission throughout the entire switching period of  $V_{GS}$ .

#### 4.4.1 Light Emission from the Active Area of a Silicon Carbide Power MOSFET

In contrast to the previous investigations by Stahlbush and Macfarlane [239]–[241], the devices used throughout this work were n-channel 4H-SiC power DMOSETs that were commercially available. Consequently, all investigations were performed on fully-processed devices. In the used DMOSETs, the 4H-SiC/SiO<sub>2</sub> interface is at the (0001) plane of the 4H-SiC crystal. As the current flow in these devices is vertical, the drain contact is at the backside of the chip.

Initially, these devices had been fully-packaged in a transistor outline (TO) package featuring three pins for the three terminals of the MOSFET. The devices were subsequently opened from the backside by removing the copper lead frame in a wet-chemical process with nitric acid. Afterwards, the solder on the backside of the chip was etched away with aqua regia. In a final step, the backside metallization was polished off with diamond paste. This process can be performed either by completely removing the drain metallization or by processing the device in a way that the drain metallization remained functional along the lower edge of the chip. The latter case allows to have control over the potential of the highly-doped n-type region of the substrate. If not stated otherwise in this work, the drain metal was completely removed.

The advantage of the above outlined preparation of the device under tests (DUTs) is the flawless detection of the emitted light through the backside of the chip – directly through the 4H-SiC substrate and the epitaxial layer. This is illustrated in Fig. 4.50. As known from Stahlbush and Macfarlane [239]–[241], the emitted light is spectrally located below the bandgap of 4H-SiC of 3.26 eV. Besides minor absorption by n-type 4H-SiC around 464 nm (2.672 eV) [323], caused by a transition from the nitrogen donor to a higher conduction band state, the photon emitted at the interface can leave the device without being disturbed. For these photons, the 4H-SiC epitaxial layer and the substrate with a combined thickness of about 185  $\mu\text{m}$  are practically transparent. Interference effects from the 4H-SiC layer are not expected. Assuming a Fabry-Pérot cavity with a thickness  $d$  corresponding to the combined thickness of the epitaxial layer and the substrate, a constant refractive index  $n = 2.6305$  (at 300 K and a wavelength of 650 nm) [324], the energetic spacing between interference maxima would be  $(hc)/(2nd) = 1.3 \text{ meV}$ . As it turns out, this spacing is far less than any spectral feature observed in the later presented results.

Once such a prepared DMOSET is continuously switched between inversion and accumulation, the active area of the SiC DMOSET starts to emit light. At a high switching frequency above 500 kHz, the light emission is visible by bare eye. Pictures of the DMOSET with and without

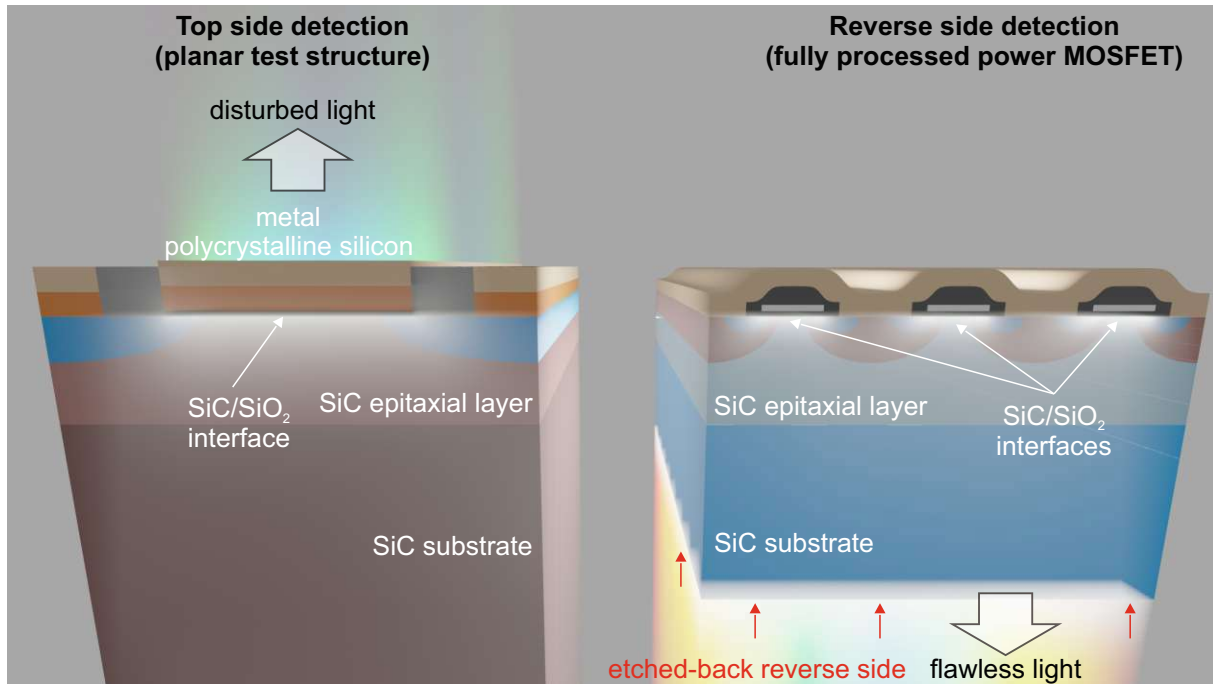


**Figure 4.50.** The left illustration shows the topside detection of light emission from the SiC/SiO<sub>2</sub> interface, using planar MOSFETs with lateral current flow, as used by Stahlbush and Macfarlane [239]–[241]. The emitted light can be disturbed by the topside metal/polycrystalline silicon. The right illustration shows the backside detection used throughout this work that allows flawless detection of light with energies below the bandgap of 4H-SiC and use of fully-processed power MOSFETs. Adapted from [MFJ8], © CC BY 4.0 DEED.

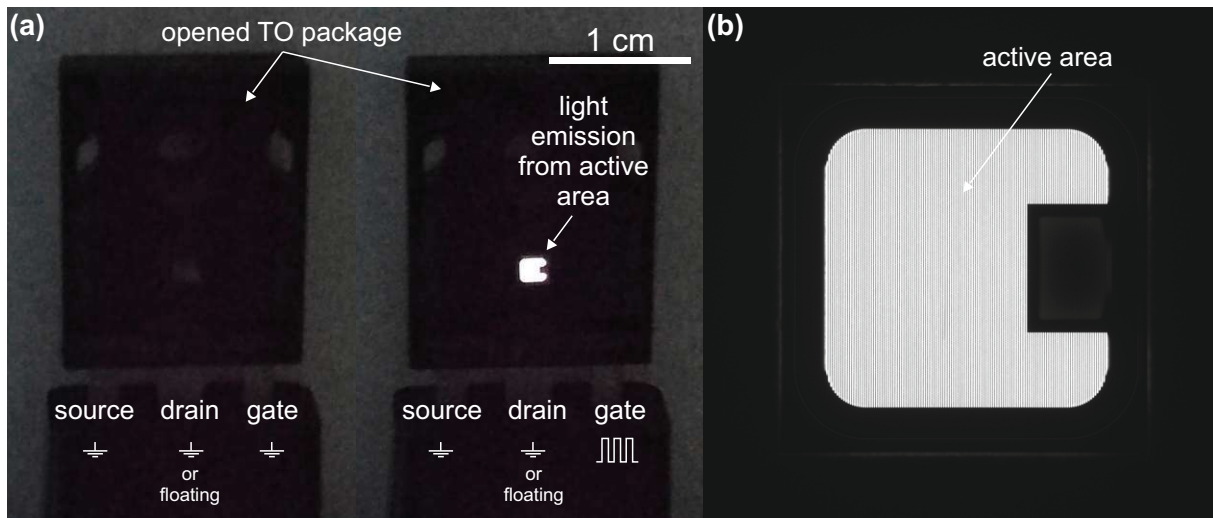


**Figure 4.51.** (a) Pictures of the DMOSET with and without being continuously switched between on-state and off-state. (b) Light emission originating from the active area imaged with an emission microscope. Adapted from [MFC3], © 2022 IEEE.

being continuously switched are shown in Fig. 4.51a. Humans perceive the light emission as a whitish glow of the active area. This light emission can be easily detected by an emission microscope (see Section 3.8). An image of the active area using an emission microscope is shown in Fig. 4.52b. The stripe-like structure of the light emission can be assigned to the structure of the DMOSET (see Section 1.5.1), where the channel regions are arranged in a parallel stripe-like manner (see Fig. 4.50).



**Figure 4.52.** (a) Illuminated and pseudo-color images created with an emission microscope with a five-time magnification objective showing the backside of a 4H-SiC power DMOSFET. The upper left image shows an illuminated image, while the others show the light emission under continuous switching between 10 V and  $-10$  V but different switching frequencies. (b) An illuminated and a pseudo-color image of the photon emission from a part of the active area using an emission microscope with a hundred-time magnification objective. (c) The total photon count rate of the entire images in (a), plotted versus the switching frequency. The dashed line indicates a linear fit. Adapted and redrawn from [MFJ8], © CC BY 4.0 DEED.

This is illustrated in greater detail in Fig. 4.52a. In the upper left, an illuminated image of the backside of the power MOSFET chip is presented. A  $5\times$  magnification objective was used. All images ( $1024 \times 1024$  pixels) of the active area of the MOSFET were created using an emission microscope, while continuously switching the gate terminal with a square waveform between 10 V and  $-10$  V at different switching frequencies between 50 kHz and 2 MHz. The integration time of the charge-coupled device (CCD) varied between 1 s and 24 s and was chosen in such a way that the CCD detector did not saturate. The background was corrected by averaging the measured photon counts over the non-emitting area in the upper left  $100 \times 500$  pixels and by subsequently subtracting it from the raw data. Furthermore, the counts were then normalized to the respective integration time. The images were ordered according to the used switching frequency, clearly revealing a continuous increase in the light emission with increasing switching frequency. The already mentioned stripe-like emission pattern is further illustrated in Fig. 4.52b, showing  $100\times$  magnified images of a part of the active area – both an illuminated image and an image of the emission under gate switching. It clearly shows the parallel channels and the light emission originating from the same regions.

Finally, the dependence of the total detected photon emission on the switching frequency can be calculated by summing up the contributions from all pixels. This total count rate is plotted versus the switching frequency and shown in Fig. 4.52c. As the gate switching is the

cause of the photon emission, it appears reasonable to assume that the measured photon flux is proportional to the frequency, as per

$$\frac{dN_{\text{total}}}{dt} = (N_{\text{rise}} + N_{\text{fall}}) \times f \quad (4.58)$$

where  $N_{\text{rise}}$  and  $N_{\text{fall}}$  are the number of emitted photons from the rising and falling transition, respectively. The slope of the linear relationship is therefore the number of emitted photons per switching period. As shown in Fig. 4.52c, the proportionality between the total count rate and the switching frequency is well approximated by a linear relationship. However, with increasing frequency, there is an increasingly significant deviation from the linear fit, indicating changes in the underlying mechanisms that lead to the emission of the photons. However, it is unclear whether only one or both types of  $V_{\text{GS}}$ -transitions are responsible for the deviation. It is therefore of particular importance to be able to study the light emission from the rising and falling transitions separately.

#### 4.4.2 Light Emission from Single Gate Voltage Transitions

Studying the light emission from the different  $V_{\text{GS}}$ -transitions separately is possible by using the setup based on a silicon-photomultiplier (SiPM) described in Section 3.5. Due to its high sensitivity even to single photons, it allows to detect the light originating from single  $V_{\text{GS}}$ -transitions. As the setups for optical spectroscopy and time-gated optical spectroscopy described in Sections 3.6 and 3.7, respectively, require integration over thousands to millions of switching cycles, they are not suitable for analyzing single  $V_{\text{GS}}$ -transitions. However, this ability to study single transitions is particularly important to compare the light emission to electrical measurements, such as the transient  $\Delta V_{\text{th}}$  of the recoverable component. Indeed, it turns out that the light emission is temporally located right at the transitions of  $V_{\text{GS}}$  where a significant change in the measured  $\Delta V_{\text{th}}$  indicates the occurrence of a lot of trapping/detrapping events. As discussed in Section 3.5, the response of a SiPM on an impinging photon is determined by the recovery characteristic of the involved single-photon avalanche diodes (SPADs). Using a Wiener deconvolution [325], it is possible to extract the temporal distribution of incident photons from the measured photo current.

As already shown by Puschkarsky *et al.*, it is exactly at the rising and falling transitions of  $V_{\text{GS}}$ , where the transient  $\Delta V_{\text{th}}$  exhibits significant jumps on the order of volts [155], [231]. Consequently, there is strong trapping and detrapping of charges occurring right at these transitions, which concurrently happens with the emission of the observed photons. This is illustrated in Fig. 4.53a, which shows  $V_{\text{GS}}$ ,  $\Delta V_{\text{th}}$  and the measured photo current during continuous switching between 25 V and  $-13$  V at a frequency of 100 kHz. The shown  $\Delta V_{\text{th}}$  was measured as by Puschkarsky *et al.* [155], [231] with a measurement delay of 1  $\mu\text{s}$ . During the  $V_{\text{H}}$ -phase,  $\Delta V_{\text{th}}$  is positive and gradually increases to higher values, indicating trapping of negative charges. During the  $V_{\text{L}}$ -phase,  $\Delta V_{\text{th}}$  behaves in the opposite way, indicating trapping of positive charges. Apparently, the SiPM detects photons both at the rising and falling transitions of  $V_{\text{GS}}$ , coinciding with significant and fast changes in  $\Delta V_{\text{th}}$ . These jumps in  $\Delta V_{\text{th}}$  indicate a high number of trapping and detrapping events within a very short time. This is illustrated in more detail in Fig. 4.53b and Fig. 4.53c, which show zoom-ins to the falling and rising transitions, respectively. They clearly show that the strong jumps in  $\Delta V_{\text{th}}$  and the photon emission temporally occur at



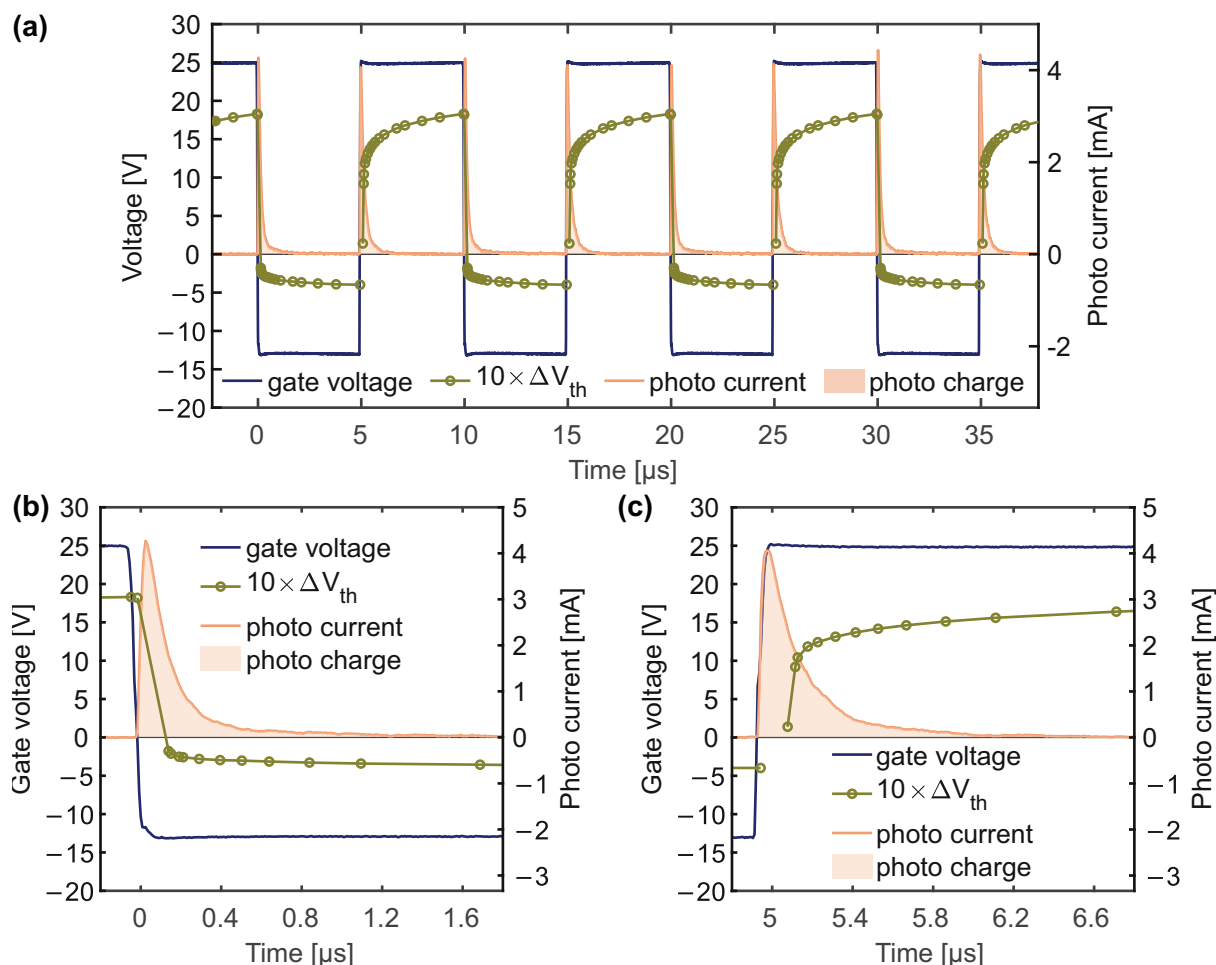


**Figure 4.53.** (a) The waveforms of  $V_{GS}$  and the photo current together with the transient  $\Delta V_{th}$ . (b) Zoom-in of the falling transition. (c) Zoom-in of the rising transition. Redrawn from [MFJ8].

around the same time, where the defects at SiC/SiO<sub>2</sub> interface change their overall charge state. The assumption that these two events have something to do with each other is thus obvious.

As discussed in Section 3.5, a SiPM consists of an array of SPADs, that are connected in parallel. Once a single photon hits a SPAD, this creates a characteristic single photon response  $r(t)$ . Once several cells are hit by photons within the same time frame, the photo current is a superposition of these single photon responses. Indeed, based on a previously reported methodology [326], it is possible to obtain the underlying temporal distribution of incident photons  $r(t)$ . The measured output current of the SiPM  $s(t)$  is a convolution of the single photon response and the photon distribution function added to the regular noise  $n(t)$ , as given by

$$s(t) = (p * r)(t) + n(t). \quad (4.59)$$

Consequently, the calculation of the photon distribution function requires the knowledge of the single photon response. As there is basically no difference in response due to a thermally activated electron-hole pair and the response to a photon, the single photon response can be measured as a single event of the random noise in the output signal. The measured single photon response is illustrated in Fig. 4.54a. In addition to the single photon response, Equation 4.59 requires an estimate for the regular noise  $n(t)$ . It can be obtained by sampling the first 100 ns of the single photon response of the entire time window. The problem can be solved

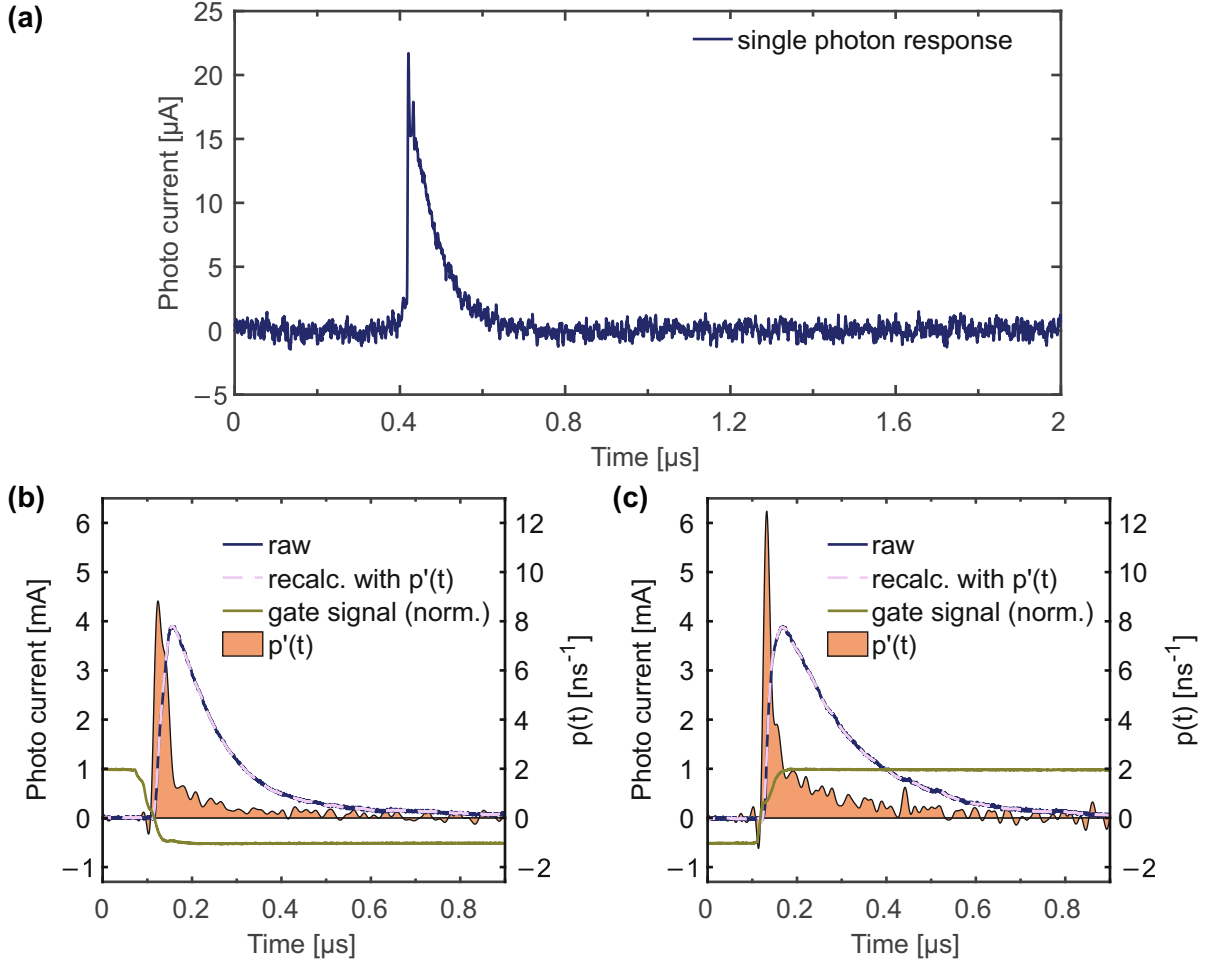


**Figure 4.54.** (a) Single photon response of the SiPM. (b) Deconvolution of the photo current signal of the falling transition, yielding the photon distribution  $p'(t)$ . (c) Deconvolution of the photo current signal of the rising transition. Redrawn from [MFC3].

in frequency space using fast Fourier transformation [327]. As outlined by Bretz *et al.* [326], a Wiener deconvolution [325] can be used, which yields a function

$$\hat{g}(f) = \frac{1}{\hat{r}(f)} \times \frac{\hat{r}(f)\hat{r}(f)^*}{\hat{r}(f)\hat{r}(f)^* + \frac{\hat{n}(f)\hat{n}(f)^*}{\hat{s}_{\text{sm}}(f)\hat{s}_{\text{sm}}(f)^*}} \quad (4.60)$$

that fulfills

$$\hat{p}'(f) = \hat{g}(f) \times \hat{s}(f). \quad (4.61)$$

Hereby,  $\hat{p}'(f)$  is an estimate for  $p(f)$ ,  $s_{\text{sm}}(t)$  is the SiPM output smoothed by locally estimated scatterplot smoothing. In a last step, an inverse Fourier transformation of  $\hat{p}'(f)$  yields an estimate  $p'(t)$  for  $p(t)$ . Using the result  $p'(t)$  together with Equation 4.59, the SiPM output can be recalculated and compared to the original signal – which should agree.

The results are shown in Fig. 4.54b and Fig. 4.54c. As the raw and recalculated waveforms match, the deconvolution was successful. The photon distributions show strongly localized peaks of about  $9 \text{ ns}^{-1}$  and  $12 \text{ ns}^{-1}$  at the falling and rising transitions, respectively, with widths

of less than 50 ns. It can be concluded that the photon emission consists of extremely short “light flashes” at the rising and falling  $V_{GS}$ -transitions. Due to its strong localization, most of the detected photo current waveform is determined by the slow recovery of the SiPM. Another contribution on the right hand side of the main peak might be related to correlated noise, such as afterpulsing or delayed crosstalk [244]. These are secondary breakdown events in the SiPM following the detection of a photon.

Note that integrating the peak of the photo current  $I_{\text{photo}}$  yields the photo charge  $Q_{\text{photo}}$ , which is proportional to the number of detected photons  $N_{\text{photo}}$  (see Section 3.5) via

$$Q_{\text{photo}} = \int I_{\text{photo}}(t) dt \propto N_{\text{photo}}. \quad (4.62)$$

This can also be recognized by looking at Equation 4.59, which yields

$$Q_{\text{photo}} = \int s(t) dt = \int (p * r)(t) dt + \underbrace{\int n(t) dt}_{=0} \quad (4.63)$$

$$= \underbrace{\left( \int p(t) dt \right)}_{=N_{\text{photo}}} \times \underbrace{\left( \int r(t) dt \right)}_{=Q_r}, \quad (4.64)$$

meaning that the proportionality factor  $Q_r$  relating  $Q_{\text{photo}}$  and  $N_{\text{photo}}$  is the integral of the single photon response. The area of a photo current peak at a  $V_{GS}$ -transition is therefore an excellent measure for the number of detected photons at the respective  $V_{GS}$ -transition.

#### 4.4.3 Voltage Level Dependence

The ability to assign a number of photons to a single  $V_{GS}$ -transition opens up the way to analyze the light emission from any switching waveform using the SiPM-based measurement setup (see Section 3.5).

As a first step, this is used with respect to the dependence on the high and low levels  $V_H$  and  $V_L$ , respectively. To minimize a possible effect of continuous switching onto the trapping/detrapping kinetics of the involved interface defects, short double pulses were used for these experiments, which are shown in Fig. 4.55a and Fig. 4.55b for the rising and falling transitions, respectively. The double pulse for the investigation of the rising transition consists of a negative  $V_{GS}$ -pulse followed by a positive  $V_{GS}$ -pulse. Two emission peaks are observed, whereby the first one is caused in interaction with the previous double pulse. Effectively, the previous positive probe pulse serves as a positive pump pulse and the thereby trapped charges subsequently recombine at the now negative pump pulse. Consequently, this peak can therefore be ignored. The emission peak at the rising transition, covering the entire voltage range from  $V_L$  to  $V_H$  is the emission peak of interest. The reason is outlined in a schematic illustration of the evolution of the trapped charges and the free charges in the semiconductor. During the  $V_L$ -phase, where the MOSFET is in accumulation, the free holes in the valence band of 4H-SiC get rapidly trapped in interface defects, leading to an increase in the trapped positive charge at the interface. Once the MOSFET is switched to  $V_H$ , thereby entering inversion, the channel is formed and the free charge in 4H-SiC turns negative. In consequence, a lot of those channel electrons get trapped in interface defects, building up negative trapped charge. Concurrently to

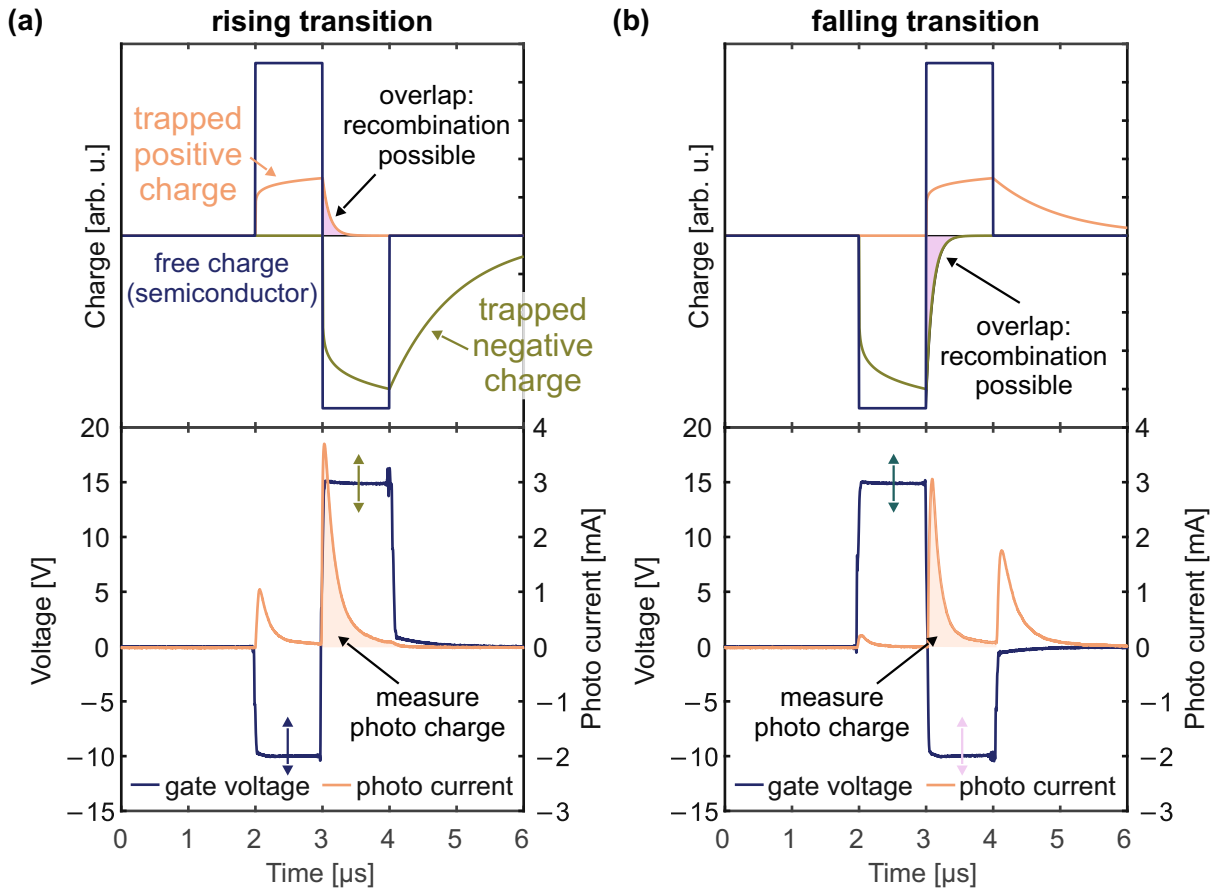


**Figure 4.55.** (a) The double pulse used to measure the dependence of the light emission of the rising transition on the voltage levels. The upper plot schematically illustrates the evolution of the positive trapped charge, the negative trapped charge, and the free charge in the semiconductor. (b) The double pulse used to measure the dependence of the light emission of the falling transition on the voltage levels. The additional peak at the rising transition of the  $V_L$ -pulse is assumed to be related to the highly doped source contacts and the gate oxide, where free electrons are available at 0 V. Redrawn from [MFJ8].

the very fast trapping of negative charges, the previously trapped holes can detrapp. However, they could also recombine with the present electrons, thereby releasing the measured photons. The double pulse for the investigation of the falling transitions works analogously, however, the role of electrons and holes are inverted.

For a fixed pair of  $V_H$  and  $V_L$ , the emission peak at the respective transition was averaged over ten double pulses, that were separated by 1 s long periods at  $V_{GS} = 0$  V to guarantee almost full recovery and return to thermal equilibrium (see Fig 4.17). After another pause of 2 s, the measurement could then be repeated with another pair of voltage levels. Analogously to the constant low level and constant high level technique in CP experiments (see Section 3.4), while keeping either  $V_H$  or  $V_L$  fixed at 25 V and  $-13$  V, respectively, the other voltage level is swept in steps of 0.1 V.

Overall, this creates four curves of the measured photo charge that are illustrated in Fig. 4.56a. These curves are very similar to typical curves of the CP current (compare to Fig. 3.7). The two constant high level curves show a strong increase around  $-8$  V, while the two constant low level curves show a strong increase around 2 V. Analogously to CP experiments, these onsets of increase can be associated with the flatband voltage ( $V_{fb}$ ) and  $V_{th}$ , respectively. This can

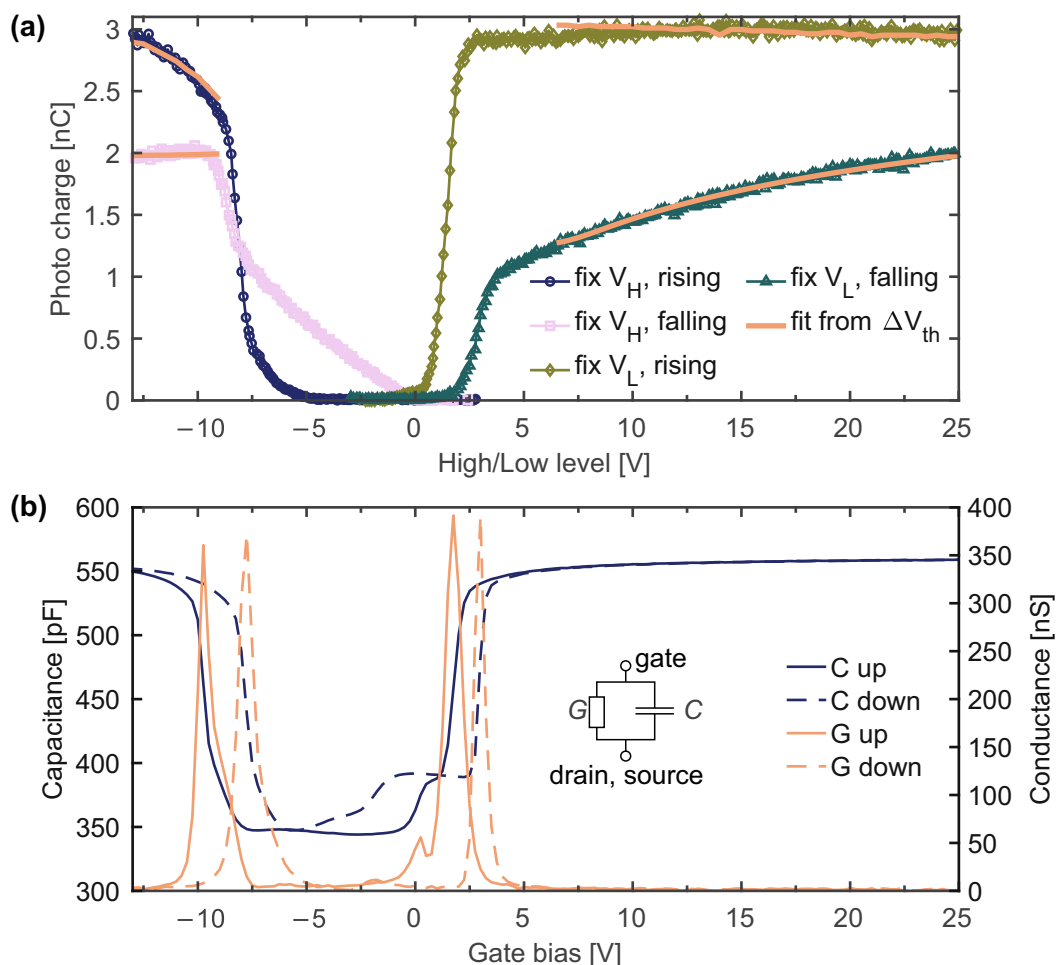


**Figure 4.56.** (a) The dependence of the measured photo charge of the rising and falling transitions on the high and low level voltages. The fits following Equation 4.70 are indicated. (b) Impedance measurement consisting of up and down CV and GV sweeps. The  $V_{th}$  and  $V_{fb}$  agree with the strong onsets in photo charge in (a). Redrawn from [MFJ8].

be confirmed by comparing these curves to an impedance measurement, shown in Fig. 4.56b, in the form of CV and conductance-voltage (GV) curves of an up sweep (corresponds to the rising transition) and a down sweep (corresponds to the falling transition). The hysteresis observed in the CV curve also explains the shift between the onsets of the rising and falling transitions in Fig. 4.56a: the difference in the onsets of strong increase are due to the electrostatic impact of the trapped charges at the interface.

In order to confirm the understanding that the trapped charge related to the recoverable component is involved in the defect-assisted recombination creating the photon emission, the transient  $\Delta V_{th}$  right after the first of the two pulses was measured with a delay of 1  $\mu$ s using pristine devices that had not been opened from the backside. Assuming all the trapped charges at the interface, the pulse-induced change in the trapped charge is proportional to  $\Delta V_{th}$  and of course also to the number of trapped charges  $\Delta N$  via

$$\Delta V_{th}(V_{GS}) = -\frac{\Delta Q}{C_{ox}} \propto \Delta N \quad (4.65)$$

where  $C_{ox}$  is the oxide capacitance. However, as the measurement of  $\Delta V_{th}$  is limited by the measurement delay of 1  $\mu$ s, a significant amount of charge might have already recovered once  $\Delta V_{th}$

is measured. To compare  $\Delta V_{\text{th}}$  with the photon emission therefore requires a few considerations, which are presented in the following.

The  $V_{\text{th}}$  of the DUT is measured with the setup described in Section 3.3, which measures  $V_{\text{th}}$  via a feedback loop. The applied  $V_{\text{GS}}$  during the time  $V_{\text{th}}$  is measured leads to a parasitic threshold voltage shift  $\Delta V_{\text{par}} > 0$ . This is illustrated in Fig. 4.57. As a result, the measured value  $V_{\text{th},0}^s$  exceeds the real pristine value of the device via

$$V_{\text{th},0}^s = V_{\text{th},0}^{\text{real}} + \Delta V_{\text{par}}. \quad (4.66)$$

During the measurement delay time, it needs to be assumed that accelerated recovery after the negative pulse is absent and that additional trapping after a positive pulse is negligible [328]. In particular the latter can be easily justified, because  $\Delta V_{\text{th}}$  increases with the logarithm of the stress time and the voltage of the pulse is usually higher than  $V_{\text{th}}$ , which decreases the time constants of the involved defects. This makes additional trapping during the measurement delay time negligible, as the involved defects are already occupied. Using these approximations, it can be concluded that the threshold voltage after positive ( $V_{\text{th}}^+$ ) and negative pulses ( $V_{\text{th}}^-$ ) relate to the true threshold voltage shifts  $\Delta V_{\text{th}}^+$  and  $\Delta V_{\text{th}}^-$  via

$$V_{\text{th}}^+ = V_{\text{th},0}^{\text{real}} + \Delta V_{\text{th}}^+ \quad \text{and} \quad (4.67)$$

$$V_{\text{th}}^- = V_{\text{th},0}^{\text{real}} + \Delta V_{\text{par}} + \Delta V_{\text{th}}^-. \quad (4.68)$$

Consequently, the  $V_{\text{th}}$  measurement after negative pulses contains an additional contribution  $\Delta V_{\text{par}}$ , which is the same as the one arising in the measurement of the pristine value  $V_{\text{th},0}^s$  in Equation 4.66. As  $\Delta V_{\text{th}}$  is proportional to the change in trapped charge (see Equation 4.65) and as the photon emission should be proportional to the change in trapped charge, it is assumed that the true threshold voltage shift relates to the photo charge via

$$|\Delta V_{\text{th}}(V_{\text{GS}})| \propto Q_{\text{photo}}(V_{\text{GS}}). \quad (4.69)$$

This can be expressed in a generalized way as per

$$Q_{\text{photo}}(V_{\text{GS}}) = C_s |V_{\text{th}}(V_{\text{GS}}) - V_{0,s}|, \quad s \in \{+, -\}, \quad (4.70)$$

where  $s$  indicates whether the measurement was conducted after a negative or positive pulse, corresponding to the rising and falling transition, respectively. Furthermore,  $C_s$  is the proportionality factor and  $V_{0,s}$  incorporates the impact of the parasitic contribution  $\Delta V_{\text{par}}$  in  $V_{\text{th}}$  after a negative pulse. Relating Equations 4.70, 4.67, and 4.68 leads to the following relations for  $V_{0,s}$ .

$$V_{0,+} = V_{\text{th},0}^{\text{real}} \quad (4.71)$$

$$V_{0,-} = V_{\text{th},0}^{\text{real}} + \Delta V_{\text{par}} \quad (4.72)$$

| Parameter                   | Positive pulse (+) | Negative pulse (-) |
|-----------------------------|--------------------|--------------------|
| $C_s$ [nC V <sup>-1</sup> ] | 0.428              | 9.499              |
| $V_{0,s}$ [V]               | 1.973              | 4.953              |

**Table 4.4.** Parameters of Equation 4.70 yielding the fit shown in Fig. 4.56a. Redrawn from [MFJ8].

Fitting Equation 4.70 to the four curves in Fig. 4.56a yields excellent agreement with the use of only four parameters, listed in Table 4.4. According to these four parameters, the real threshold voltage is  $V_{\text{th},0}^{\text{real}} = 1.973 \text{ V}$  and the parasitic contribution is given by  $\Delta V_{\text{par}} = 2.98 \text{ V}$ . As stated by Equation 4.66, a measurement of the pristine value should correspond to the fitting parameter  $V_{0,-}$ . A separate measurement yields  $V_{\text{th},0}^{\text{s}} = 4.996 \text{ V}$ , meaning that the fitting parameter deviates  $< 1\%$  from the measured value. Besides that,  $V_{\text{th},0}^{\text{real}}$  agrees well with the threshold voltage observed in the CV curve of Fig. 4.56b. These two observations and, above all, the fit in Fig. 4.56a suggest that the above outlined considerations regarding the relation between threshold voltage measurement and photon emission are valid and that the transient  $\Delta V_{\text{th}}$  is indeed related to the observed photon emission. The observed radiative defect-assisted recombination is related to the recoverable component, which is the transient  $\Delta V_{\text{th}}$ .

#### 4.4.4 Field-Effect-Based Pump-Probe Scheme

As presented in the previous section, there seems to be a clear relation between the photon emission and the measured  $\Delta V_{\text{th}}$ , whereby the relation is mediated by the trapped charge. During the positive pulse, electrons are trapped in interface defects and subsequently recombine with holes from the valence band, once the MOSFET is switched down into accumulation. The opposite occurs upon a negative pulse, during which holes are trapped in interface defects that subsequently recombine with electrons from the channel, once the MOSFET is switched into inversion.

This relation was confirmed by varying the voltages of the used double pulses. In a next step, an additional period of time at  $V_{\text{GS}} = 0 \text{ V}$  is introduced, that separates the two pulses from each other. The associated transitions and potential energy curves (PECs) are presented in Fig. 4.58. During the recovery period  $t_r$ , the previously trapped charge carriers have now the opportunity to recover during the time at  $V_{\text{GS}} = 0 \text{ V}$ , which means they can be emitted back via a non-radiative multiphonon (NMP) transition to the band from which they were originally captured. This recovery path opens up because the electric field shifts the PEC of the state of the electron/hole being in the conduction/valence band to lower energies, thereby lowering the emission activation energy (see Section 2.1.2). Consequently, during the recovery, the occupancy of the charged defect state gradually decreases. Once the second pulse is then applied to the MOSFET switching it with opposite polarity of the first pulse, the radiative path of recombination opens up only for those charge carriers being trapped in the defect state. Finally, once the charge carriers have recombined, vibrational relaxation of the involved defects is expected, but cannot be measured directly.

The corresponding measurement scheme is shown in Fig. 4.59a and Fig. 4.59b for the falling and rising transition, respectively. Indeed, the principle of this measurement scheme is similar to pump-probe spectroscopy as frequently used in photonics and solid state physics to detect the response of optical observables after an out-of-equilibrium excitation with a second excitation [329]. In pump-probe spectroscopy, these are the pump and probe laser pulses. In contrast to that, the corresponding pulses here are a  $1 \mu\text{s}$ -long pump and a  $1.6 \mu\text{s}$ -long probe  $V_{\text{GS}}$ -pulse. Depending on its polarity, the pump pulse triggers capture of either holes or electrons from the valence and conduction band, respectively, and after a defined recovery time  $t_r$ , the probe pulse provides the opposite type of charge carrier at the interface to trigger their recombination.

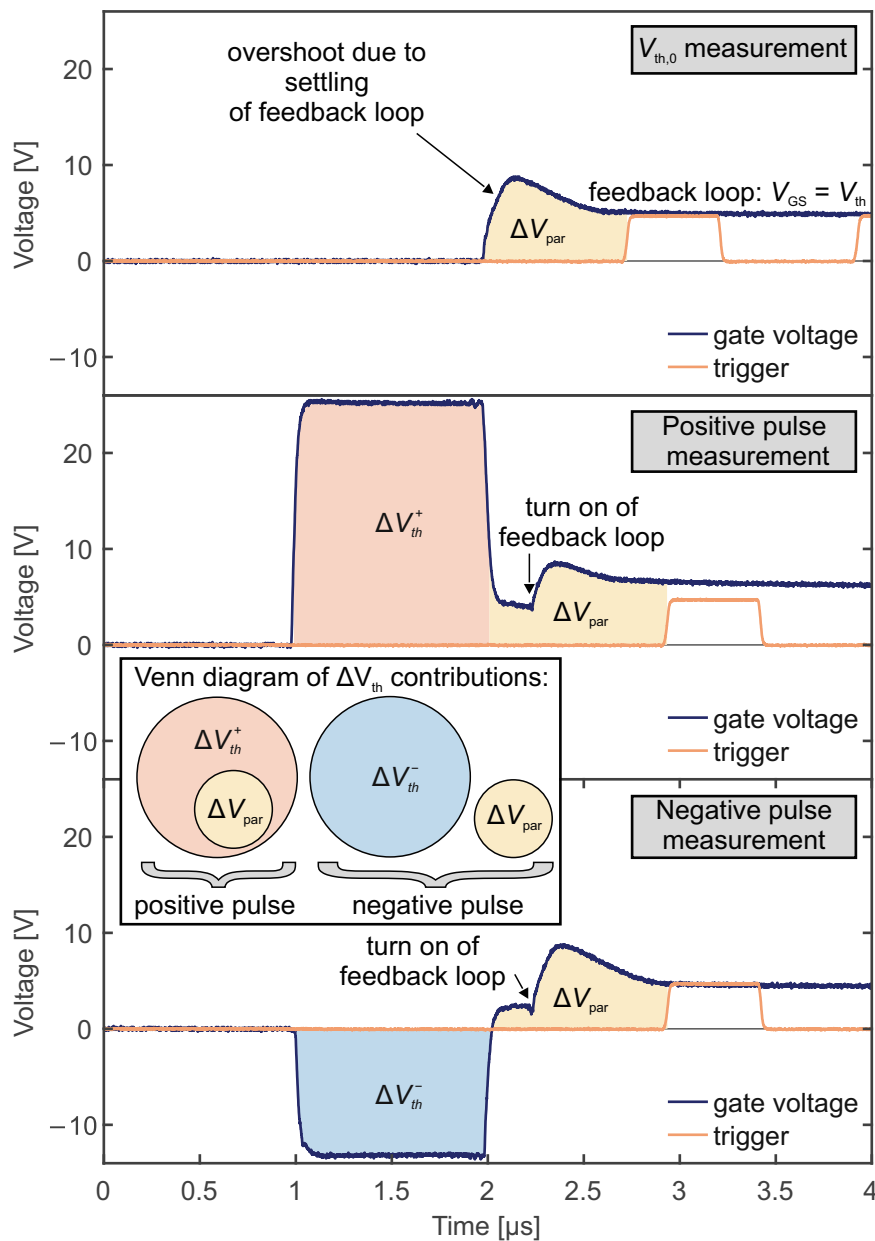


**Figure 4.57.** Illustration of the different contributions to  $\Delta V_{th}$  depending on the type of measurement. The upper plot shows a typical measurement of  $V_{th,0}^s$ . The yellow marked area indicates the region where the parasitic contribution  $\Delta V_{par}$  is caused. The measurement of  $V_{th}$  occurs at the rising edge of the trigger signal. The central plot shows a measurement of  $V_{th}^+$ , which is after a positive  $V_{GS}$  pulse. Here, the yellow marked area associated with  $\Delta V_{par}$  does not contribute to the measured  $V_{th}$ , because the addressed defects are already charged. The lower plot shows the measurement of  $V_{th}^-$ , which is after a negative  $V_{GS}$  pulse. In contrast to the measurement of  $V_{th}^+$ ,  $\Delta V_{par}$  creates another contribution, because the addressed defects are charged additionally to the ones charged by the negative pulse. The difference between the measurements of  $V_{th}^+$  and  $V_{th}^-$  is illustrated in the shown Venn diagram. Redrawn from [MFJ8].

The change in trapped charge should therefore correlate to the photo charge as per

$$Q_{photo}(t_r) \propto |\Delta Q(t_r)|. \quad (4.73)$$



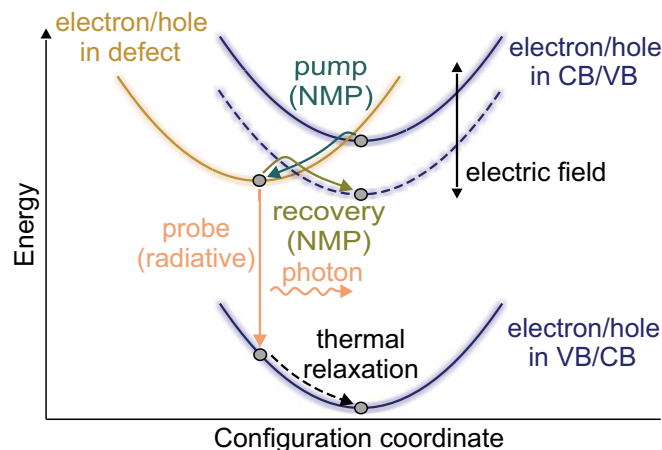


**Figure 4.58.** Transitions and potential energy curves (PECs) of processes involved in pump-probe measurement scheme. During the pump pulse, charge carriers from the conduction or valence band get trapped via an non-radiative multiphonon (NMP) process in a defect state. Subsequently, the charged defect state leads to a measurable  $\Delta V_{th}$ . During the recovery time between the pump and the probe pulse, the trapped charges can be emitted back to conduction or valence band via an non-radiative multiphonon (NMP) process. This decreases  $\Delta V_{th}$  with increasing recovery time. Once the probe pulse is applied, the remaining trapped charge carriers can recombine radiatively (vertical process) by the emission of a photon. Redrawn from [MFC3].

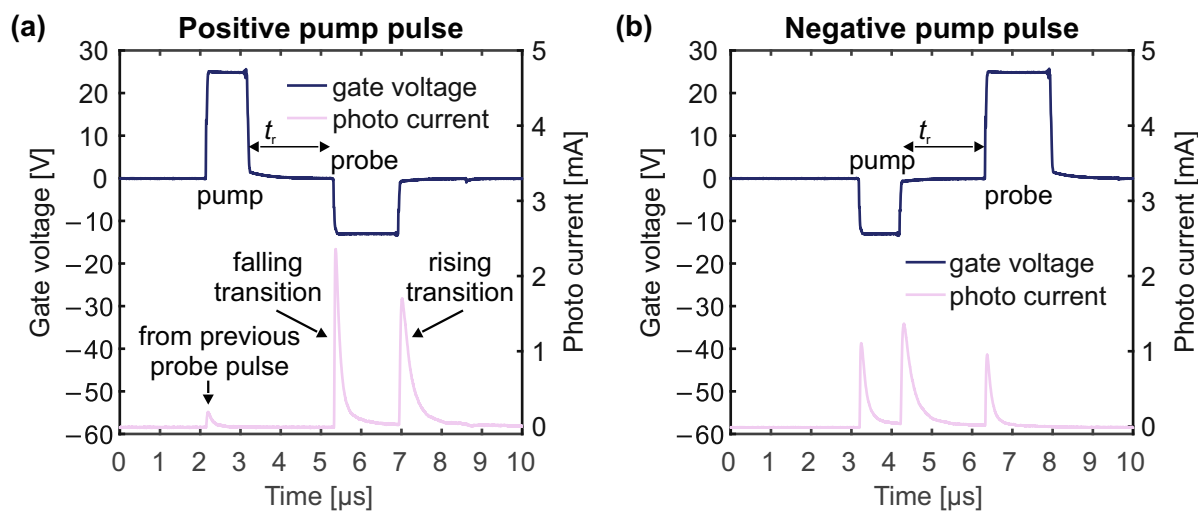


**Figure 4.59.** (a) Pump-probe measurement scheme using a positive (inversion) pump pulse and a negative (accumulation) probe pulse, separated by a recovery time  $t_r$ . This investigates the light emission of the falling transitions. (b) Pump-probe measurement scheme using a negative (accumulation) pump pulse and a positive (inversion) probe pulse, separated by a recovery time  $t_r$ . This scheme investigates the light emission of the rising transitions. Redrawn from [MFC3].

As extensively discussed in Section 4.2, the charge trapped during the pump pulse leads to a transient  $\Delta V_{th}$  that recovers during the recovery time, which is also related to the change in the trapped charge via

$$\Delta V_{th}(t_r) = -\frac{\Delta Q(t_r)}{C_{ox}}. \quad (4.74)$$

If the understanding of the light emission, its relation to the trapped charge and thus also to  $\Delta V_{th}$  are correct, apparently, the measured number of photons after a certain recovery time

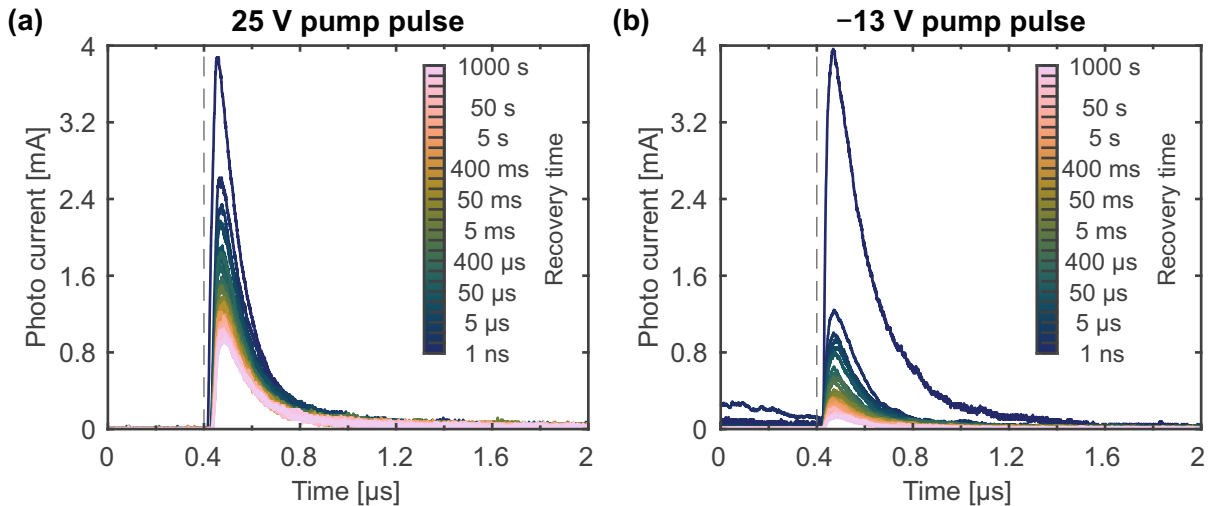


**Figure 4.60.** (a) Photo current peaks after a 25 V pump pulse for different recovery times. (b) Photo current peaks after a  $-13$  V pump pulse for different recovery times.

between the two pulses should then correlate to the transient  $\Delta V_{\text{th}}$  after the same recovery time. As shown in Fig. 4.59a, there are three emission peaks in an experiment with a positive pump pulse. The first one originates from the previous probe pulse, the second peak is the peak of interest within the pump-probe scheme, and the third peak is equally monitored as the second one. Although the origin of the third peak is unclear, it might originate from the overlap region of the gate oxide and the highly doped source regions, where electrons are probably already available for recombination at  $V_{\text{GS}} = 0$  V. Analogously, Fig. 4.59b shows the three emission peaks in an experiment with a negative pump pulse. Here, the negative pump pulse has now the two peaks at its falling and rising transition and the probe pulse has the peak of interest for the pump-probe measurement.

For each pump pulse polarity, three pump pulse voltages were used. The probe pulse always had the opposite polarity of the pump pulse and had either a voltage of 25 V or  $-13$  V to assure full inversion or accumulation during probing, respectively. The recovery time was varied on a logarithmic time scale between 1 ns and 1000 s. Hereby, 1 ns refers to a direct transition. This finite time is assumed because also a direct transition must exhibit some kind of recovery during the transition. As the transition time is 50 ns, a small fraction of it appears to be a reasonable choice. Each pump-probe measurement of a certain recovery time is separated to the next measurement by a recovery time of 120 s at zero bias to allow the device to return to the thermal equilibrium close to its pristine state. As outlined in Section 4.2.1, the choice of this time is indeed appropriate.

The photo current measurements of the various recovery times are shown in Fig. 4.60a and Fig. 4.60b for positive and negative pump pulses, respectively. For both pulse polarities, the photo current peaks evidently show a significant decrease of the light emission with increasing recovery time. As outlined in Section 4.4.2, integrating the photo current peak of each transition yields the photo charge associated with the respective recovery time, which yields the number of emitted photons upon division by the integrated single photon response. The resulting number of emitted photons is shown for all positive pump pulses in Fig. 4.61a and for all negative pump pulses in Fig. 4.61b. As already pointed out, for the positive pump pulses in Fig. 4.61a, it needs to be distinguished between the photo current peaks at the rising and falling transition of the probe pulse, whereby the latter is of greater interest for the discussed physics. Indeed, the rising

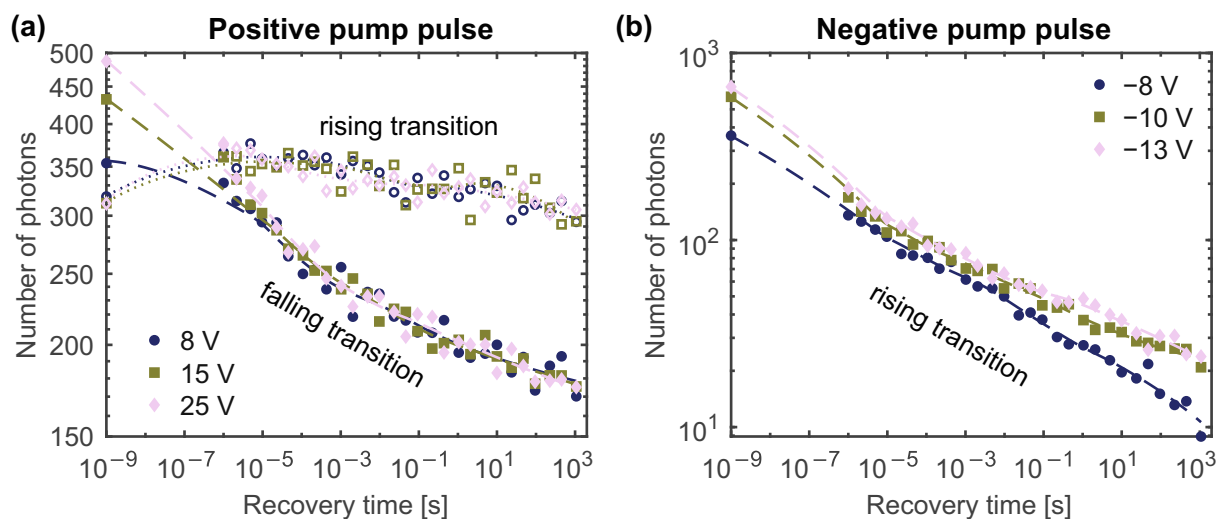


**Figure 4.61.** (a) Number of photons emitted at the probe pulse using three different positive pump pulse voltages. The photons emitted at the rising transition of the probe pulse is independent of the recovery time, whereas the number of photons emitted at the falling transition of the probe pulse decreases with the recovery time. (b) Number of photons emitted at the probe pulse using three different negative pump pulse voltages. Redrawn from [MFC3].

transition of the negative pump pulse shows only a minor or even negligible dependence on the recovery time – this would agree with its interpretation as recombination at the overlap regions underneath the gate oxide. In contrast to that, the falling transition shows a clear decrease in the number of emitted photons over time and roughly follows a straight line in a double logarithmic plot. Apparently, the differences between the different pulse voltages is mainly located between the direct transition and a recovery time of 1  $\mu$ s. Within the noise of the measured number of photons, these curves otherwise agree reasonably well. As there is only a single photo current peak at the probe pulse for a negative pump pulse (see Fig. 4.59b), Fig. 4.61b shows only the number of photons emitted at the rising transition of the probe pulse. Again, the decreasing number of photons with increasing recovery time follows roughly a power law in a double logarithmic plot.

In order to relate the number of emitted photons to the transiently trapped charge at the SiC/SiO<sub>2</sub> interface, the recovery of  $\Delta V_{th}$  is measured after the application of the same pump pulses as used for the optical pump-probe measurements. The minimum possible measurement delay is the lowest recovery time. As long measurements of  $V_{th}$  can cause more quasi-permanently trapped charge, the maximum measured recovery time is 120 s. Additionally, to let the device return to its pristine state in thermal equilibrium, the measurement of the recovery curves were separated by 10<sup>3</sup> s. Fig. 4.62a shows the measured recovery curves for the three positive pump pulse voltages. As usually expected, the higher the pump pulse voltage, the higher the observed  $\Delta V_{th}$ . Dashed lines indicate that the measured recovery curves roughly follow a power law dependence. Analogously, Fig. 4.62b shows the recovery curves measured with negative pump pulse voltages. In contrast to the positive pump pulses, here, the pump pulse voltage has a minor impact on the observed  $\Delta V_{th}$ .

As a last step, the number of emitted photons is plotted versus  $\Delta V_{th}$  for the different recovery times of a certain pump pulse. Fig. 4.63a and Fig. 4.63b show these plots for positive and negative pump pulses, respectively. For positive pump pulses, the number of emitted photons increases with increasing  $\Delta V_{th}$  and dashed lines indicate a linear relation between the

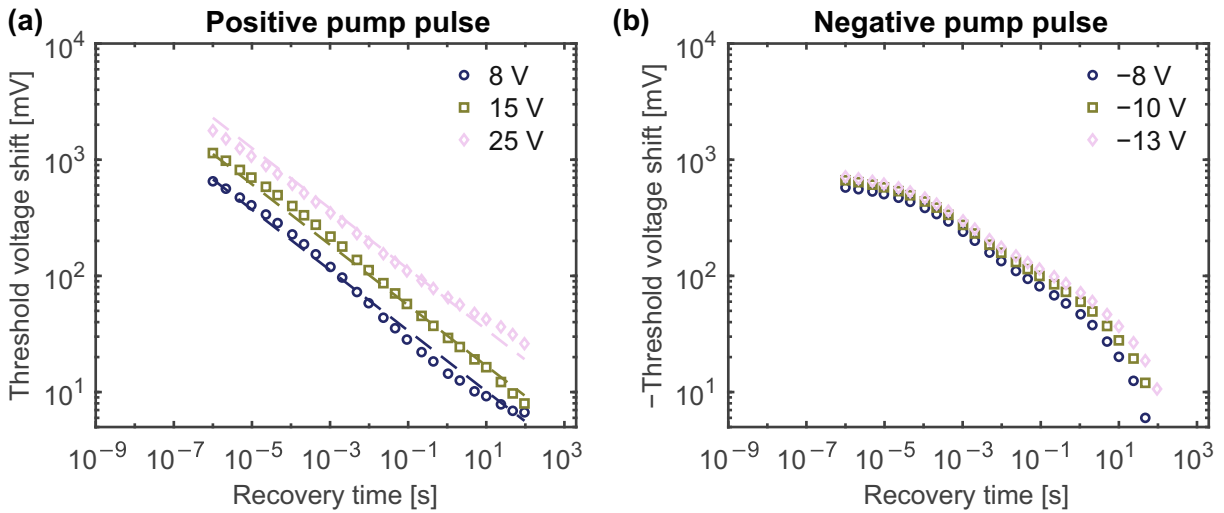


**Figure 4.62.** (a) Recovery of the threshold voltage shift following the three used positive pump pulses in a double logarithmic plot. Dashed lines indicate power law fits. (b) Recovery of the threshold voltage shift following the three used negative pump pulses in a double logarithmic plot. Redrawn from [MFC3].

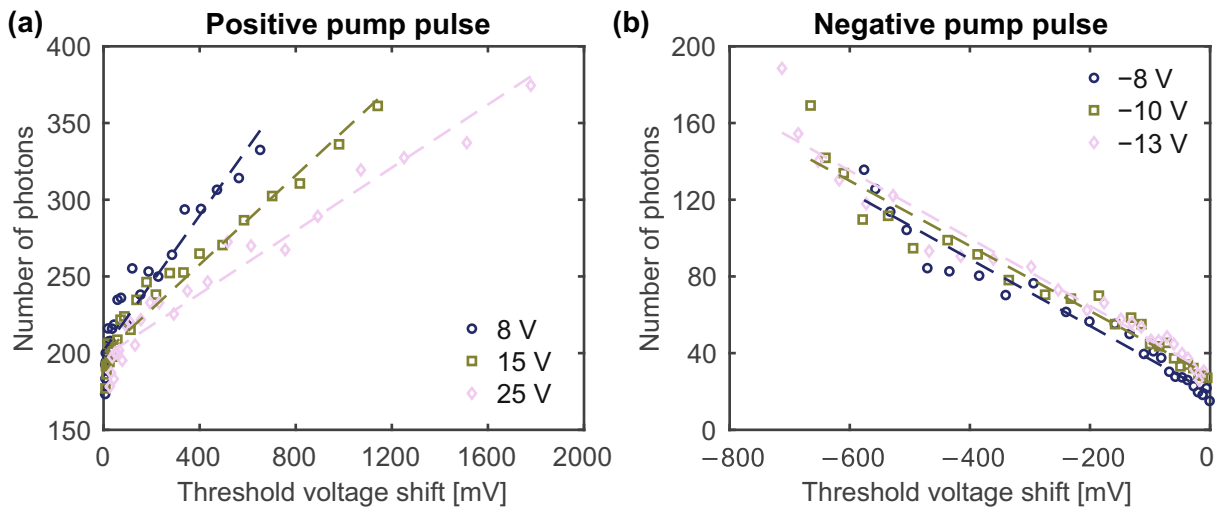


**Figure 4.63.** (a) Number of emitted photons versus  $\Delta V_{th}$  for different recovery times in a pump-probe experiment with positive pump pulses. Dashed lines indicate a linear correlation. (b) Number of emitted photons versus  $\Delta V_{th}$  for different recovery times in a pump-probe experiment with negative pump pulses. Dashed lines indicate a linear correlation. Redrawn from [MFC3].

two quantities. Interestingly, for a fixed  $\Delta V_{th}$ , the number of emitted photons increases with decreasing pump pulse voltage. This indicates that not all defects that get charged during the pump pulse can contribute to the light emission. However, similar considerations as for the measurement of the voltage level dependence in Section 4.4.3 regarding a parasitic contribution  $\Delta V_{par}$  apply. Compared to the voltage level dependence, this is more complicated because  $\Delta V_{par}$  now depends on the recovery time. Due to the measurement of the  $V_{th}$  recovery at  $V_{GS} = V_{th}$ , the difference between the optical measurement and the  $V_{th}$  measurement becomes more significant with increasing recovery time. For negative pump pulses, the number of emitted photons increases with  $|\Delta V_{th}|$  and equally shows a clear correlation between the two quantities. Overall, this clearly confirms the postulated mechanism and clearly relates the emitted photons to the transient  $\Delta V_{th}$ , which is nothing else than the recoverable component of BTI.

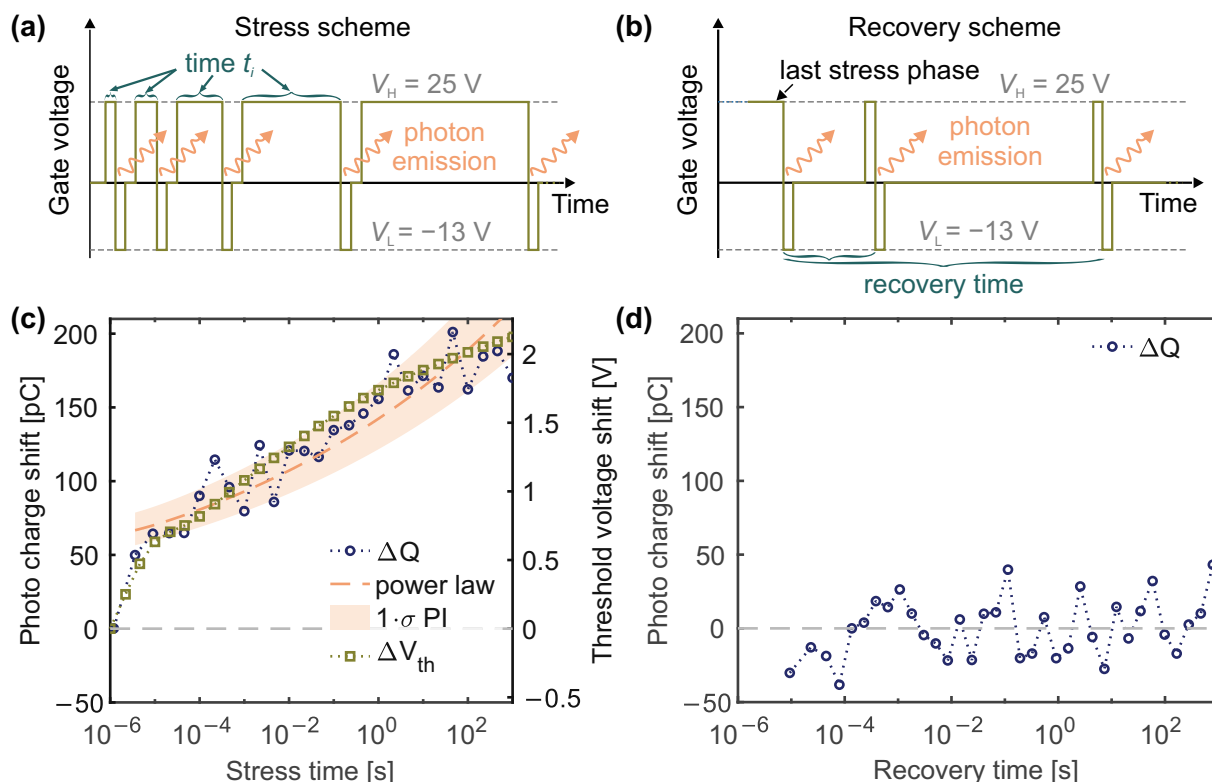


**Figure 4.64.** (a) Stress scheme with increasing length of a positive pump pulse. (b) Recovery scheme to measure the recovery of the light emission following the stress scheme in (a). (c) The photo charge shift versus the stress time, measured with the stress scheme in (a). A power law fit and the corresponding  $1\sigma$  prediction interval (PI) are indicated. (d) The photo charge shift versus the recovery time, measured with the recovery scheme of (b). Redrawn from [MF]8].

#### 4.4.5 Impact of Extended Gate Stress onto the Photon Emission

It remains to be tested whether not only the recovery behavior of the transient  $\Delta V_{\text{th}}$  is correlated to the light emission, but also its stress dependence. The longer the pump pulse, the more charges should get trapped and be available for recombination. The corresponding measurement or stress scheme is illustrated in Fig. 4.64a. In this experiment, the pump pulse voltage is 25 V and the probe pulse voltage is  $-13$  V. While investigating the impact of the pump pulse length, only direct transitions are used, meaning no recovery periods are in between the pump and the probe pulse. The probe pulses have a constant length of  $1 \mu\text{s}$ , while the length of the pump pulse increases from  $1 \mu\text{s}$  up to  $10^3$  s. After the last probe pulse, the recovery behavior is investigated by introducing recovery phases at  $V_{\text{GS}} = 0$  V in between several double pulse measurements consisting of  $1 \mu\text{s}$  pump and probe pulses with direct transitions. This recovery scheme is illustrated in Fig. 4.64b. The recovery time ranges from  $9 \mu\text{s}$  up to 787 s.

In this context, a stress time  $t_s = t_i - t_0$  is defined, which is the length of the time periods of positive bias  $t_i$  with respect to the very first double pulse of length  $t_0 = 1 \mu\text{s}$ . The photo charge shift  $\Delta Q = Q_i - Q_0$  ( $Q_0 = 1.14$  nC) versus the stress and recovery time is shown in Fig. 4.64c and Fig. 4.64d, respectively. Apparently, the photo charge shift increases with increasing stress time and very roughly follows a power law with a power law exponent  $n = 0.062$ , as per

$$\Delta Q_i \propto (t_i - t_0)^n. \quad (4.75)$$

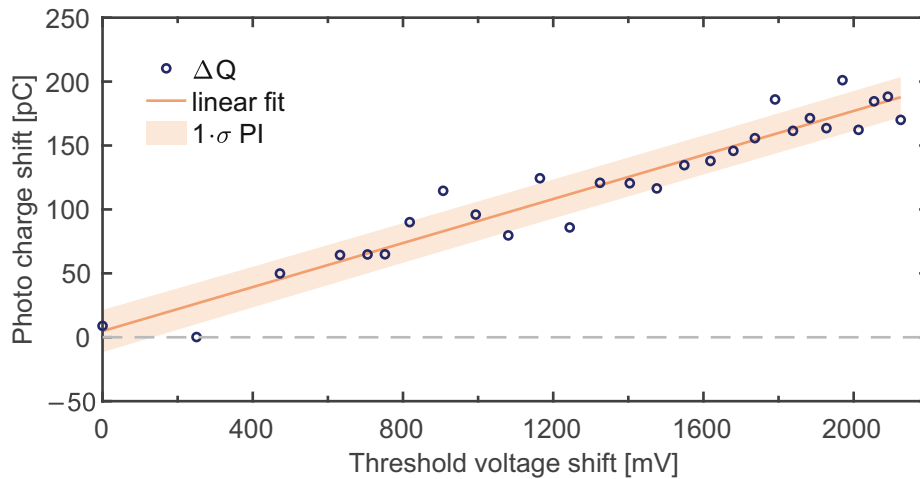


**Figure 4.65.** The photo charge shift versus the measured  $\Delta V_{\text{th}}$ . A linear fit together with the  $1\sigma$  prediction interval (PI). Redrawn from [MFJ8].

This approximate power law dependence is a typical signature of BTI, as the trapped charge increases with increasing stress time. However, there is no notable dependence on the recovery time. This indicates that those defects that are involved in the radiative recombination recover completely, once a probe pulse is applied. There is simply no charge left, which is why the photo charge shift returns to zero and stays independent of the recovery time.

In order to correlate the photo charge shift to the transient  $\Delta V_{\text{th}}$ , the same measurement as illustrated in Fig. 4.64a is conducted, however, with the feature of a measurement of  $\Delta V_{\text{th}}$  in between the pump and probe pulses with a measurement delay time of  $1\ \mu\text{s}$ . Nonetheless, there was a period of time of  $10\ \mu\text{s}$  at  $0\ \text{V}$  following the  $V_{\text{th}}$  measurement. This period of time created unintentionally could not be avoided, but its influence on the transient  $\Delta V_{\text{th}}$  is negligible. Strikingly, there is a clear correlation between the measured  $\Delta V_{\text{th}}$  and the measured photo charge shift, including features such as a strong increase up to  $10^{-3}\ \text{s}$  and a saturation above  $1\ \text{s}$ . The correlation between the two quantities is further illustrated in Fig. 4.65. Indeed, this correlation features a Pearson correlation coefficient of 0.96.

#### 4.4.6 Optical Spectroscopy

So far, the light emission has been characterized using the measurement setup described in Section 3.5, which is based on a SiPM. However, this setup did not provide any information on the spectral distribution in terms of wavelength or energy of the emitted photons. Initially, this distribution was measured with the setup described in Section 3.6.

As this work deals with the kinetics of defects at the SiC/SiO<sub>2</sub> interface, the spectrum of the emitted photons is more important in the form of a distribution in energy  $E$  – not in wavelength  $\lambda$ . As a spectrometer provides a distribution in wavelength, this spectrum  $I(\lambda)$  needs to be converted into energy space using a Jacobian transformation

$$I(E) = I(\lambda) \left| \frac{d\lambda}{dE} \right| = I(\lambda) \frac{hc}{E^2}, \quad (4.76)$$

where  $h$  is the Planck constant and  $c$  is the speed of light [330]. The raw emission spectrum is shown in Fig. 4.66a. Due to the rather low light intensity, the spectrum had to be measured over an integration time of 40 s during continuous switching of the gate terminal between 20 V

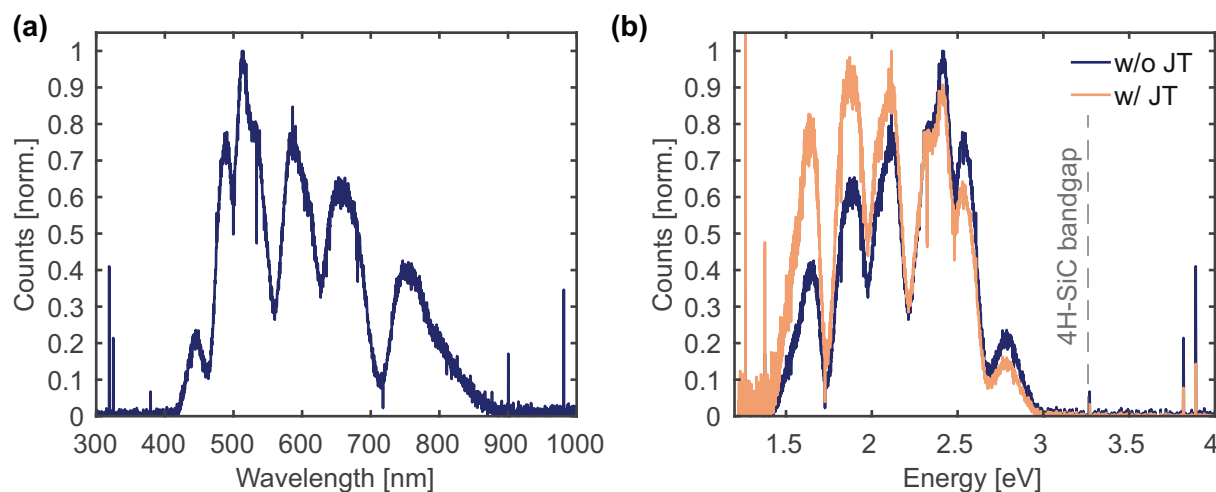


**Figure 4.66.** (a) Emission spectrum of a DMOSET obtained by integrating over 40 s of 1 MHz, 20 V/−10 V continuous switching. (b) Spectral data from (a) converted to energy space with (w/ JT) and without (w/o JT) using a Jacobian transformation.

and −10 V at 1 MHz. The impact of the Jacobian transformation on the shape of the emission spectrum is illustrated in Fig. 4.66b. One of the shown spectra is just plotted versus energy instead of wavelength and the other spectrum was obtained using a Jacobian transformation. Although the impact onto the peak positions is rather small, the peak shape and in particular the peak intensities are affected. Consequently, the Jacobian transformation is particularly important for the relative peak intensities distributed in this case over a wide range of photon energies.

Furthermore, the emission spectrum contains energies between 1.4 eV and 3.0 eV. It is to note that the considered range of photon energies is located below the bandgap of 4H-SiC (3.26 eV, see Section 1.2). No significant band-to-band luminescence could be observed. Consequently, all the observed emission peaks must be related to point defects that assist electron-hole recombination.

Most interestingly, the emission spectrum exhibits several peak-like features. Indeed, it turned out that the total emission spectrum can be fitted by a set of emission peaks. A few types of lineshape functions were tried, including Lorentzian [205], Voigt [331], [332], and Gaussian functions [333]. Both Voigt and Gaussian functions can fit the observed spectrum well, whereby it needs to be noted that the Voigt profile is a convolution of a Gaussian and a Lorentzian. As the Lorentzian being the natural lineshape [205] does not fit the transitions in the observed emission spectrum, the emission peaks seem to involve significant broadening, probably both thermal broadening and broadening induced by distributed trap levels at the SiC/SiO<sub>2</sub> interface. At temperatures where  $k_B T$  is significantly higher than the energy of involved phonons the lineshape of a transition is typically a Gaussian profile [334]. In addition to that, trap levels are typically assumed to be Gaussian distributed. A fit of the emission spectrum with ten Gaussian profiles following

$$I(E) = \sum_{i=1}^{10} A_i \exp\left(-\frac{(E - p_i)^2}{2\sigma_i^2}\right) \quad (4.77)$$

is presented in Fig. 4.67a. The obtained parameters from Equation 4.77 are listed in Table 4.5.

Apparently, the energetic positions of the emission peaks provide valuable information on the underlying defects, involved in the recombination process. Theoretical studies employing DFT with a hybrid exchange functional yielded charge transition levels (CTLs) of various

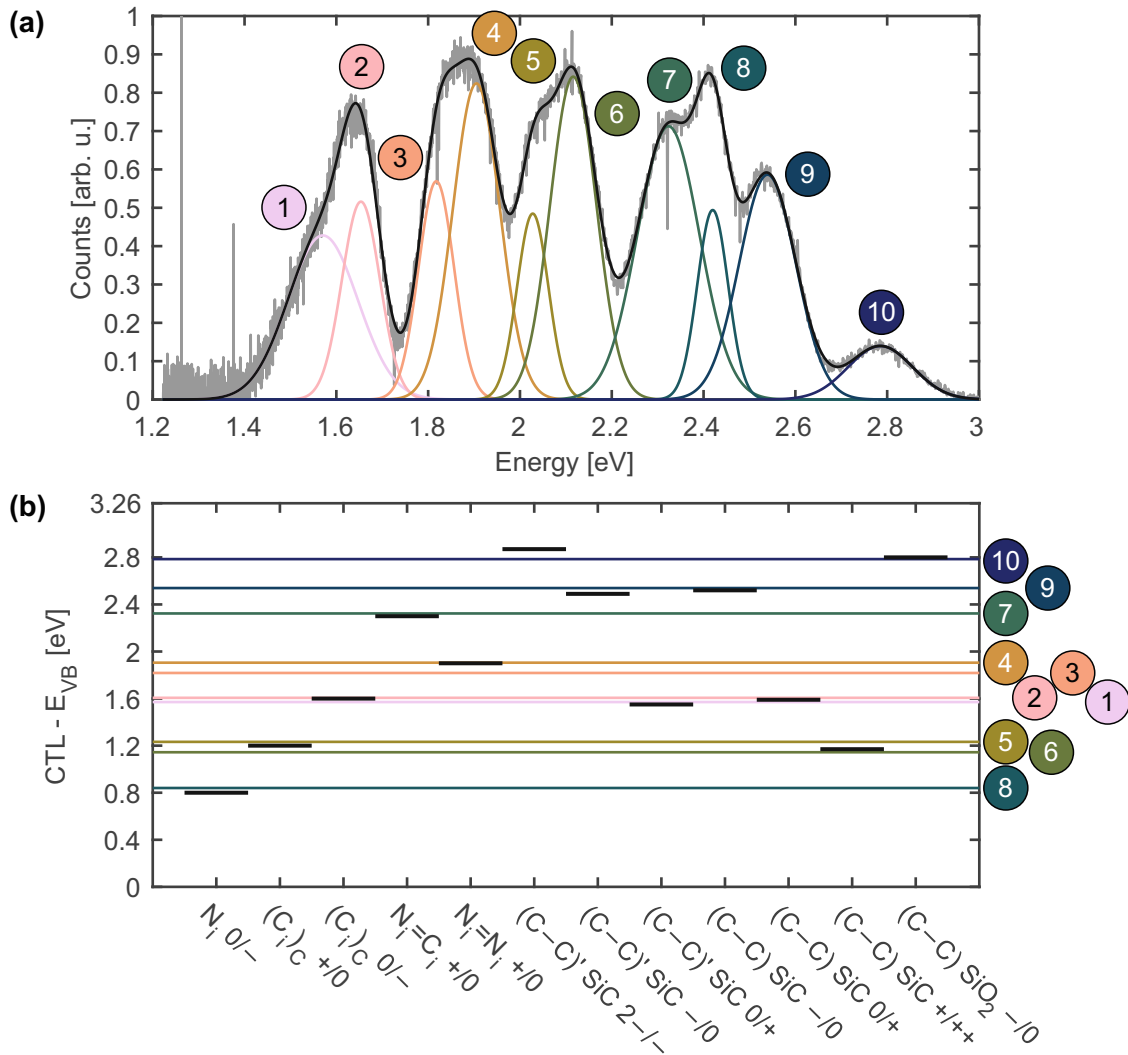


**Figure 4.67.** (a) Fit of emission spectrum with ten Gaussian lineshape functions. (b) Assignment of charge transition levels (CTLs) from literature studies based on DFT calculations [335], [336] to the experimentally obtained peak energies from (a). Redrawn from [MFJ8].

| Index $i$ | $p_i$ (eV; nm) | FWHM (meV) | $A_i$ | Defect candidate                                  |
|-----------|----------------|------------|-------|---|
| 1         | 1.57; 789      | 180        | 0.51  | (C-C)', (C <sub>i</sub> ) <sub>C</sub> , (C-C) VB |
| 2         | 1.65; 750      | 97         | 0.61  | (C-C)', (C <sub>i</sub> ) <sub>C</sub> , (C-C) CB |
| 3         | 1.82; 682      | 91         | 0.68  | N <sub>i</sub> =N <sub>i</sub> VB                 |
| 4         | 1.91; 651      | 120        | 0.98  | N <sub>i</sub> =N <sub>i</sub> VB                 |
| 5         | 2.03; 611      | 80         | 0.58  | (C <sub>i</sub> ) <sub>C</sub> , (C-C) CB         |
| 6         | 2.12; 586      | 119        | 1.00  | (C <sub>i</sub> ) <sub>C</sub> , (C-C) CB         |
| 7         | 2.32; 534      | 159        | 0.85  | N <sub>i</sub> =C <sub>i</sub> VB                 |
| 8         | 2.42; 512      | 79         | 0.59  | N <sub>i</sub> CB                                 |
| 9         | 2.54; 488      | 145        | 0.70  | (C-C)', (C-C) VB                                  |
| 10        | 2.79; 445      | 166        | 0.17  | (C-C)', (C-C) VB                                  |

**Table 4.5.** Parameters of spectral fit according to Equation 4.77. VB indicates recombination in interaction with the valence band, whereas CB indicates interaction with the conduction band. The listed defect candidates were taken from Deák *et al.* [335] and Devynck *et al.* [336]. Redrawn from [MFJ8].

defect candidates [335], [336]. Each experimentally obtained emission peak gives rise to two CTLs depending on whether the recombination process occurs in interaction with the valence or conduction band. A comparison between some of the theoretically calculated CTLs from



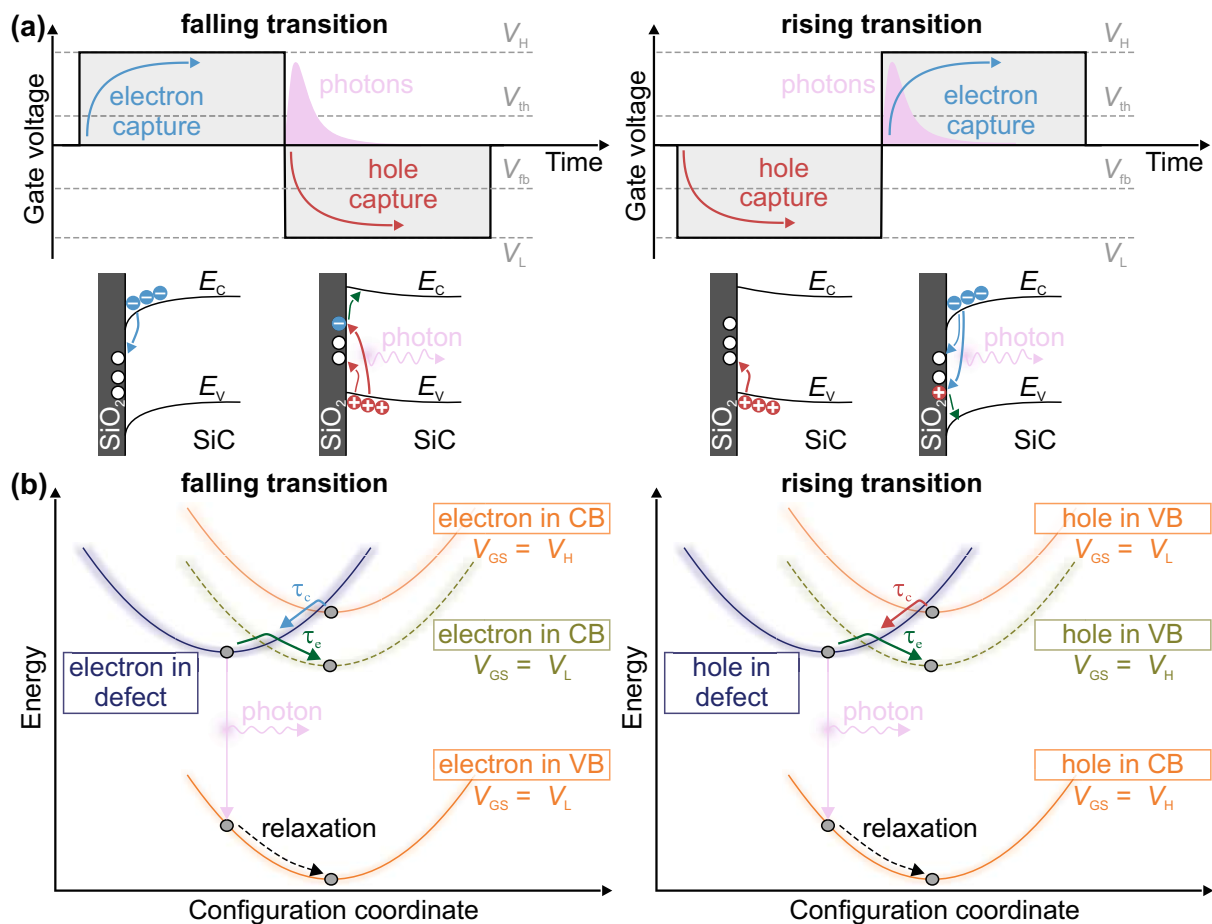


**Figure 4.68.** (a) Schematic illustration of recombination occurring at the falling (left schematic) and rising (right schematic) transitions, respectively. At the falling transition, during the  $V_H$ -phase, electrons get captured in defects. While most charges get emitted back to the conduction band (CB), a fraction of these trapped electrons recombine with accumulated holes from the valence band (VB) once  $V_{GS}$  changes to  $V_L$ . At the rising transition, the roles of electrons and holes are inverted. (b) Configuration coordinate diagrams corresponding to (a). Redrawn from [MFJ]8.

literature and the experimentally obtained CTLs is presented in Fig. 4.67b, which are in excellent agreement. First, it is to note that the assignment is not unique but rather leads to the conclusion that there are indeed defects that fit the experimentally observed properties. Second, it needs to be considered that the theoretical CTLs are obtained by single-particle excitations within the Kohn-Sham picture [337]. Taking into account lattice vibrations or collective electronic excitations could lead to significant deviations from those values and hence also explain partial disagreements. Such studies would have to include electron-phonon coupling or solving the Bethe-Salpeter equation [338]. However, such investigations have not yet been performed for the SiC/SiO<sub>2</sub> interface.

Based on the results presented so far, the understanding of the light emission caused by electron-hole recombination via interfacial point defects is summarized in Fig. 4.68a and agrees with the understanding previously established by Macfarlane and Stahlbush [239]. Essentially, at the falling  $V_{GS}$ -transition, electrons trapped during the time in inversion recombine with accumulated holes from the valence band, whereas at the rising  $V_{GS}$ -transition, holes trapped during the time in accumulation recombine with inversion electrons from the conduction band. These recombination events lead to the emission of a photon. The corresponding configuration

coordinate diagrams are illustrated in Fig. 4.68b. Note that the trapping processes that precede the recombination event are ordinary NMP transitions and there is also the possibility that the trapped charge can be emitted back to the band from which it originally came from – which was investigated by the presented pump-probe-scheme. The trapped charges give rise to a transient  $\Delta V_{th}$  that could be correlated to the light emission while the energies in the emission spectrum provide information on the CTLs of the involved defects.

However, it is to note that this spectral analysis is only based on an emission spectrum that was measured over a long integration time, which means that this spectrum is a superposition of both the emission spectra from the rising and the falling transitions – there was no way to distinguish between these two contributions using the setup for ordinary optical spectroscopy described in Section 3.6. This was tackled by employing time-gated optical spectroscopy which is presented in the next section.

#### 4.4.7 Time-Gated Optical Spectroscopy

*The contents of this section were accepted for publication in Physical Review Applied [MFJ2].*

As pointed out in the previous section, the setup for optical spectroscopy described in Section 3.6 cannot distinguish between the light emission occurring at the rising and falling transitions, respectively. Up to here, this distinction between light emission caused at rising and falling transitions was only possible by measuring the light emission with the highly sensitive SiPM-based setup described in Section 3.5. However, the SiPM-based setup does not have spectral resolution.

In order to detect enough photon counts for good statistics and consequently a good signal-to-noise ratio, optical spectroscopy requires integrating over a certain number of  $V_{GS}$ -transitions. The only possibility to introduce time resolution and be able to only detect the light emission from a certain time window within a  $V_{GS}$  switching period, is to introduce time-gating of the spectral detection. The setup used here, which is based on an intensified charge-coupled device (ICCD), was described in detail in Section 3.7.

Again, fully-processed n-channel 4H-SiC power MOSFETs were used – exactly the same type as in the previous sections. However, for time-gated spectroscopy, the backside metallization of the drain terminal was removed in such a way that some contact to the highly n-doped substrate remained functional. The CV characteristics of devices with and without a residual drain contact are compared with the characteristic of a pristine device, which was not opened, in Fig. 4.69. The difference between the pristine device and the opened device with remaining drain contact is minor, making this preparation method an excellent choice for studying fully-processed devices. All experiments were performed at room temperature. The trusted energy region obtained by the calibration procedure described in Section 3.7.1 is marked in spectral plots with a grey background. As described in Section 4.4.6, the spectral data was transformed from wavelength space to energy space using a Jacobian transformation [330].

#### Rising Versus Falling Transition

As already pointed out and illustrated in Fig. 4.68, the mechanisms of defect-assisted electron-hole recombination occurring at the rising and falling transitions are expected to differ significantly – which is why there is substantial interest to use time-gated spectroscopy to separate these two spectra. They superimpose to the total light emission spectrum presented

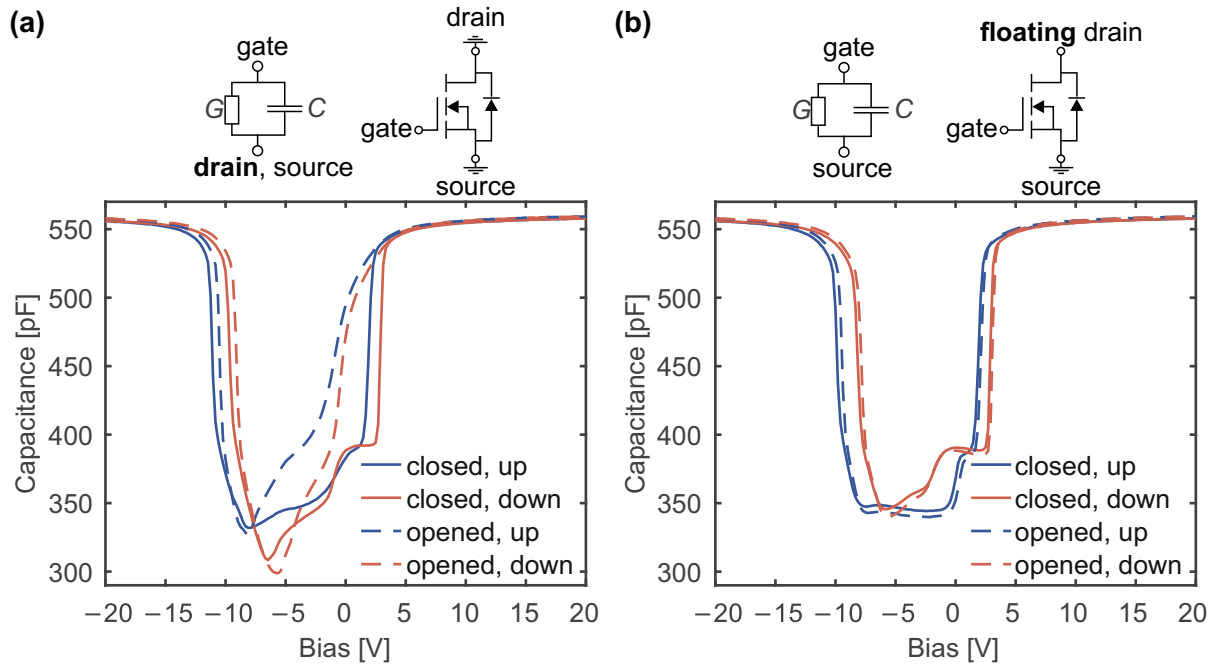


**Figure 4.69.** (a) CV curves of a pristine device (fully-packaged, not opened) and a opened device without residual drain contact measured using a small-signal frequency of 1 kHz. (b) CV curves of a pristine device (fully-packaged, not opened) and a opened device with residual drain contact. Redrawn from [MFJ2].

in Section 4.4.6. Fig. 4.70a shows the  $V_{GS}$  signal used to continuously switch the gate terminal between 15 V and  $-15$  V at a frequency of 500 kHz with a duty cycle of 50 % using transition times of 50 ns. As explained in Section 3.7, there is a trigger signal that operates the gate switching, whereby  $V_{GS}$  has a delay of 50 ns with respect to the trigger signal. The gate delay was set to 25 ns, which means that the intensifier of the ICCD is turned on 25 ns before  $V_{GS}$  is switched. Subsequently, the light is detected over a gate time window of 1  $\mu$ s, which covers half of the period of the  $V_{GS}$  signal. The ICCD returns a feedback, indicating at which time the intensifier is turned on and allows the light to pass to the CCD. As illustrated in Fig. 4.70a, the gate time window can be set in such a way that it starts either 25 ns after the rising or the falling transition of the trigger signal.

This allows to separate the light emission during the rising and falling transitions, which is illustrated in Fig. 4.70b. It shows the emission spectra obtained by either detecting the light from the rising or the falling transition using the 500 kHz switching waveform between 15 V and  $-15$  V presented in Fig. 4.70a. The spectrum of the rising transition covers a significantly broader range of energies up to 3.0 eV, whereas the spectrum of the falling transition only reaches up to around 2.65 eV. Besides these two spectra, another measurement was conducted using a gate time window of 2  $\mu$ s covering the full  $V_{GS}$  period. As a consistency check, summing up the contributions from the rising and the falling transitions and comparing the result with the light emission measured over the full period yields good agreement. The two emission spectra of the rising and the falling transitions indeed constitute the total light emission observed from the SiC MOSFET.

Besides the light emission caused at the SiC/SiO<sub>2</sub> interface, which is illustrated in Fig. 4.71a, applying a positive bias to the source terminal ( $V_{DS} < 0$ ) with respect to the drain terminal, while keeping the channel closed, leads to electron-hole-recombination at the forward biased

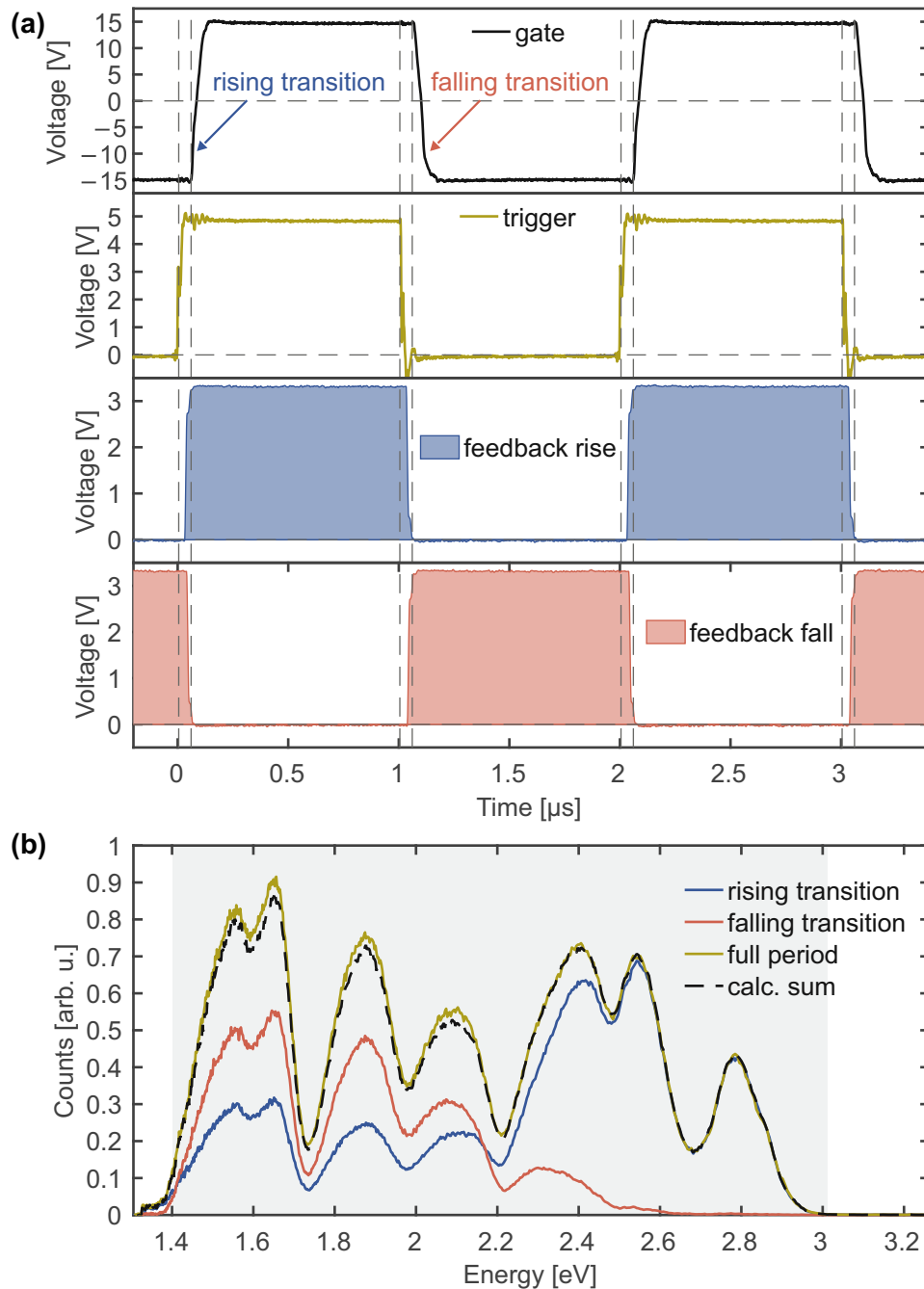


**Figure 4.70.** (a)  $V_{\text{GS}}$  signal, trigger signal, and the feedback from the ICCD of an experiment that allows to separately detect the light from the rising and falling transitions. (b) The corresponding spectra from (a) and from a measurement with a gate time window covering the full  $V_{\text{GS}}$  period. The calculated sum of the spectra of the rising and falling transitions is also indicated. Redrawn from [MFJ2].

body diode [339]–[343]. This is illustrated in Fig. 4.71b. The associated recombination occurs predominantly in the bulk 4H-SiC crystal of the MOSFET. Depending on  $V_{\text{GS}}$ , the channel can conduct a certain share of the current. If it is open,  $V_{\text{DS}}$  decreases and the entire current is conducted via the channel and not via the body diode. Here,  $V_{\text{DS}}$  is set in such a way that a constant current of 40 mA is forced and the emission spectrum was measured for several values of  $V_{\text{GS}}$  in the range of  $-12$ – $7$  V. The resulting spectra are shown in Fig. 4.71c. Except for the overall intensity, the spectrum does not depend on  $V_{\text{GS}}$ . The intensity in the form of the

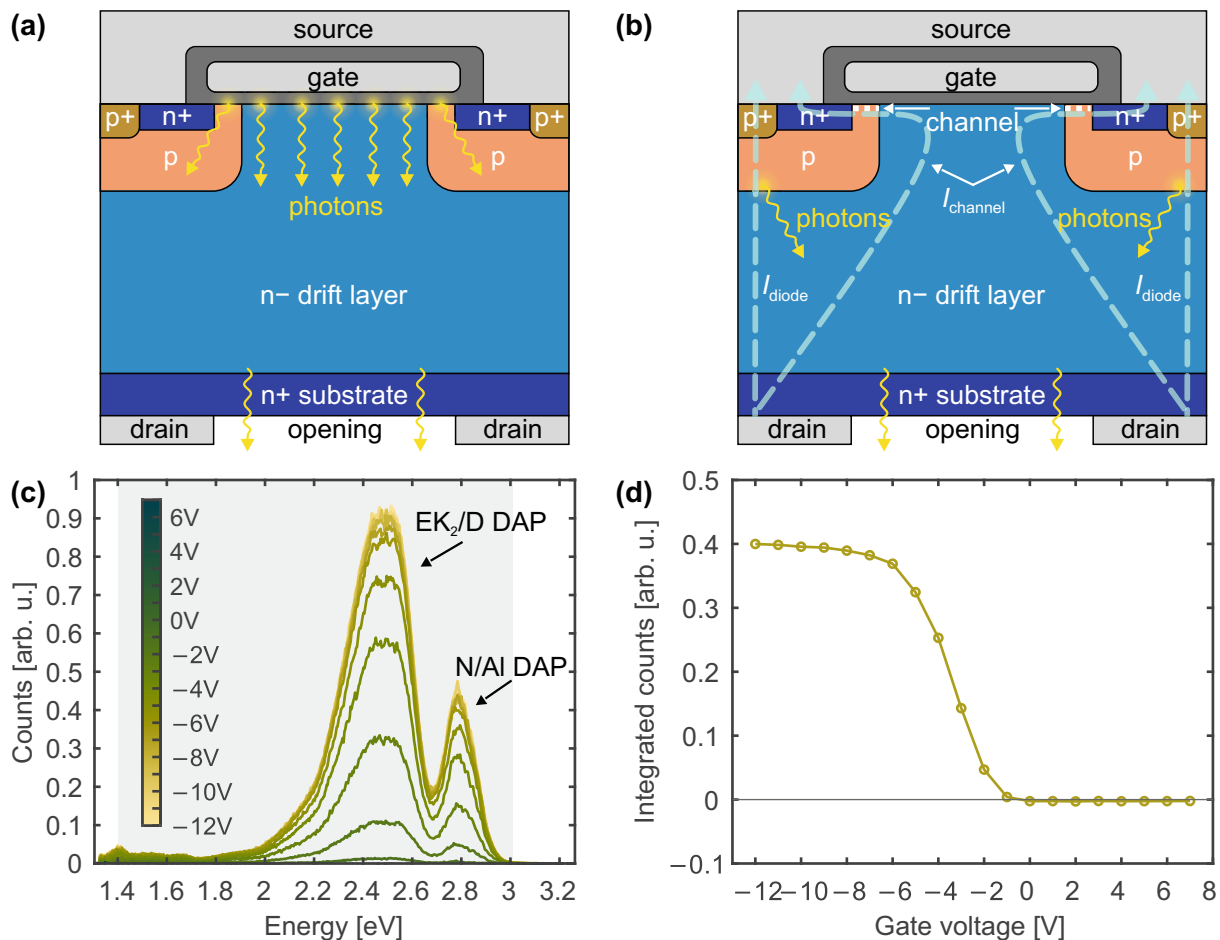


**Figure 4.71.** (a) Schematic illustration of the DMOSFET and its light emission upon gate switching. (b) Schematic illustration of the DMOSFET and its light emission and internal current paths upon a forward biased body diode at a constant current of 40 mA. The share of current through the body diode depends on the conductance of the channel, and therefore on  $V_{GS}$ . (c) The emission spectra obtained by forward biasing the body diode of the DMOSFET in (a) for different  $V_{GS}$ . The labels indicate the assignment of the two emission peaks to two types of donor-acceptor-pair (DAP) recombination, that is discussed in Section 4.4.7. (d) Integrated counts of the emission spectra from (c). Redrawn from [MFJ2].

integrated emission spectrum is shown in Fig. 4.71d as a function of  $V_{GS}$ . Only if the channel is closed completely, corresponding to  $V_{GS} < -1$  V, the body diode is forward biased and thus exhibits electron-hole recombination that leads to the observed light emission. The spectrum covers predominantly higher energies in the range of 2.0–3.0 eV, which appears as a blueish glow of the active area. As the characteristic in Fig. 4.71d depends also on  $V_{th}$ , detecting the light emission can be used for temperature and current sensing or condition monitoring [339]–[343]. Here, this emission spectrum serves for comparison to the emission spectra obtained from the SiC/SiO<sub>2</sub> interface via gate switching. Note that the body diode is shortened during the gate switching experiments, which is why light emission from the body diode should be absent.

This comparison between the emission spectrum of the body diode and the spectra from the rising and falling transitions is shown in Fig. 4.72. Furthermore, this figure illustrates the extraction of two spectral components, which will play an important role in the following considerations. Scaling down the emission spectrum of the falling transition reveals that this emission seems to equally exist in the emission spectrum of the rising transition. This scaled emission

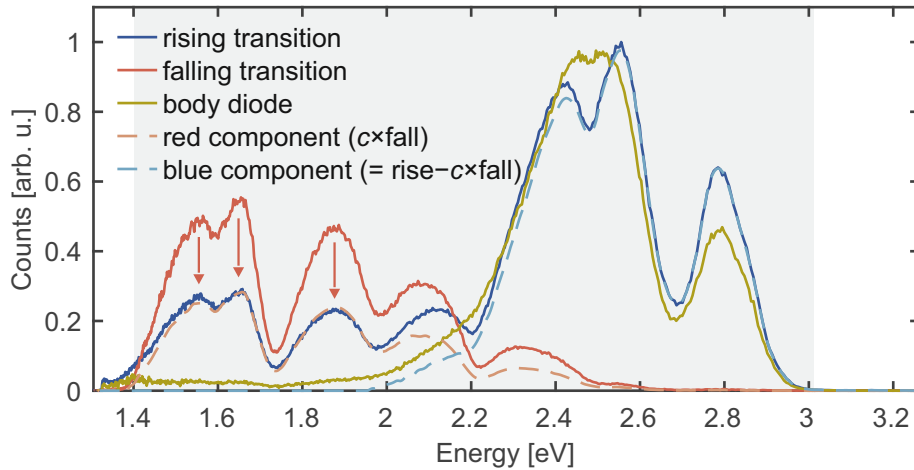


**Figure 4.72.** Emission spectra of the rising and falling transitions and the forward biased body diode. The red (spectrum of the falling transition scaled by a factor  $c = 0.52$ ) and the blue components (difference between the spectra of the rising transition and the scaled falling transition) are also indicated. Importantly, the blue component agrees with the emission of the forward biased body diode. Redrawn from [MFJ2].

spectrum of the falling transition is now defined as the “red component”, whereby its name is based on its spectral location and the associated human-perceived color (red: 1.6–2.0 eV). Subsequently, this scaled emission spectrum from the falling transition can be subtracted from spectrum of the rising transition, which yields the “blue component” (blue: 2.5–2.8 eV). Interestingly, the blue component agrees well with the emission spectrum of the body diode.

In summary, the emission spectra of the rising and falling transitions are basically composed of two fractions: the red and blue components. The red component occurs at both the rising and falling transitions, whereas the blue component occurs solely at the rising transition and is comparable to the emission spectrum of the body diode. Consequently, the last step of the total mechanism leading to recombination associated with the red component seems to be the same for the rising and the falling transitions, whereas the mechanism associated with the blue component is suppressed at the falling transition. In the following, the behavior of these two spectral components is studied separately under different switching conditions to investigate the origin and underlying mechanisms.

### The Red Component

The red component exhibits a very interesting conspicuousness: almost all its emission peaks seem to be equally spaced in energy. Equal spacing in energy hints towards an underlying harmonic PEC (see Section 2.2). This originates from transitions from a vibrational ground state of an excited electronic state to the different vibrational eigenstates of an electronic ground state.

As explained in detail in Section 2.2, the emission spectrum of such a configuration is given by

$$I(E_{\text{ph}}) \propto \sum_{m,n} \omega_{\text{ph}}^3 |\langle \phi_m^2 | \phi_n^1 \rangle|^2 L(E_{\text{ph}}, E_{mn}, \sigma_{mn}). \quad (4.78)$$

This equation basically depends on eight parameters, whereby four of them describe the two harmonic potentials of the two electronic states ( $\Delta E_{21}$ ,  $\hbar\omega_1$ ,  $\hbar\omega_2$ ,  $\Delta q$ ) and another four describe

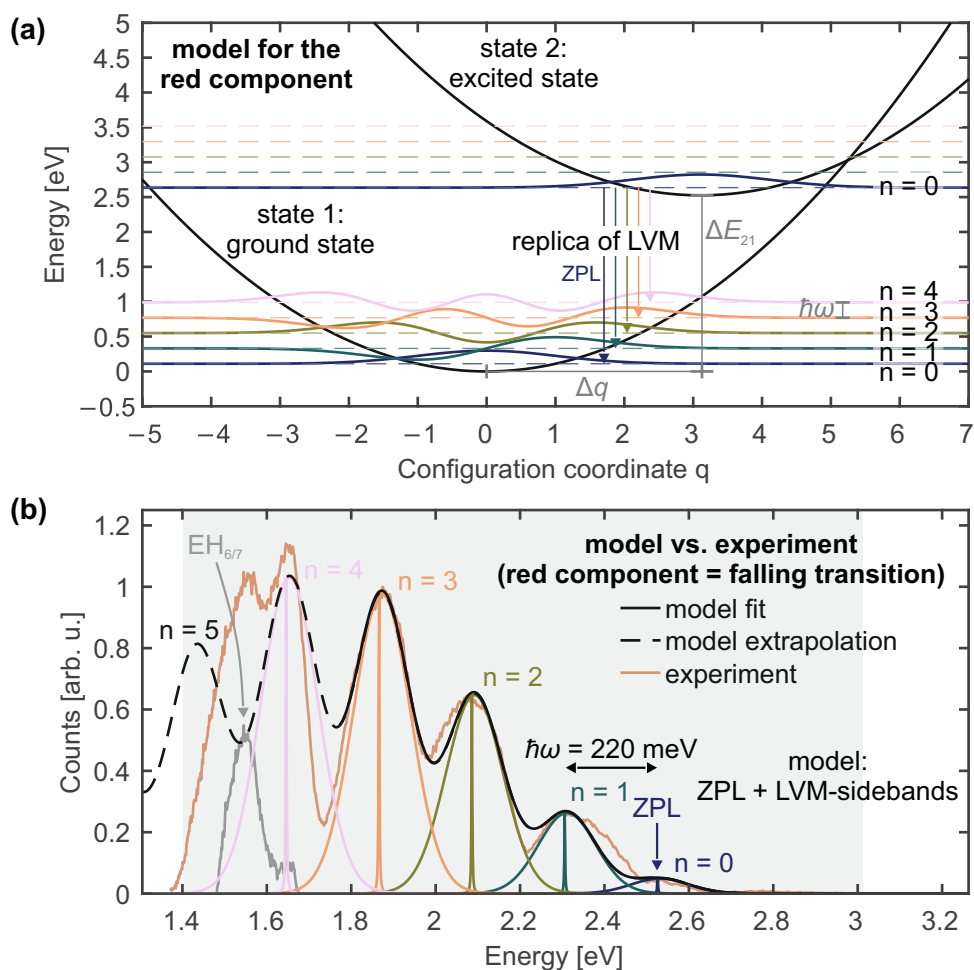


**Figure 4.73.** (a) The model of the red component based on transitions from the vibrational ground state of an excited electronic state 2 to the vibrational eigenstates of the electronic ground state 1, leading to equally spaced emission peaks in energy. (b) The spectrum of the red component fitted with Equation 4.78, which results from the model illustrated in (a). Redrawn from [MFJ2].

the broadening effects ( $\sigma_1$ ,  $\sigma_2$ ,  $\sigma_{\Delta E}$ ,  $\Delta E_L$ ). Typically, this can be reduced down to six parameters by assuming that  $\omega := \omega_1 = \omega_2$  and  $\sigma := \sigma_1 = \sigma_2$  [197], [344]–[346]. The absolute position of the comb of emission peaks is determined by  $\Delta E_{21}$ , whereas their spacing is determined by  $\hbar\omega$ . The peak intensities are determined by  $\Delta q$ , which is directly linked to the Huang-Rhys factor (HR-factor)  $S = (1/2)(\Delta q)^2$ . Independently from that, the three parameters  $\sigma$ ,  $\sigma_{\Delta E}$ , and  $\Delta E_L$  are only related to the broadening of the transition peaks. The model is illustrated in Fig. 4.73a. For the excited electronic state (state 2), only the vibrational ground state is considered. As the spacing between the peaks is about twice as large as the energy of the highest phonon mode in 4H-SiC, the occupation probability of any excited vibrational state is negligible (see Section 1.3.4). In contrast to that, for the electronic ground state, the lowest five vibrational states are taken into account.

Based on Equation 4.78, this model was fitted to the red component in the energy range above 1.77 eV. The resulting fit is illustrated in Fig. 4.73b and the obtained parameters of the fit are listed in Table 4.6. The fit comprises the lowest four transitions  $n = 0$ –3. By extrapolating it to lower energies, it can even predict the fifth transition  $n = 4$  with good agreement. However, it does not predict the peak around 1.55 eV. This additional peak is indicated in Fig. 4.73b and can potentially be assigned to the  $\text{EH}_{6/7}$  center [MFJ9]. The fit yields a zero-phonon line (ZPL)

| Parameter           | Value     | 95 % confidence interval |
|---------------------|-----------|--------------------------|
| $\Delta E_{21}$     | 2.526 eV  | 2.525 – 2.527 eV         |
| $\hbar\omega$       | 220.0 meV | 219.6 – 220.4 meV        |
| $\Delta q$          | 3.109     | 3.089 – 3.129            |
| $\sigma$            | 0 meV     | –                        |
| $\sigma_{\Delta E}$ | 67.43 meV | 67.18 – 67.67 meV        |
| $\Delta E_L$        | 2.095 meV | 1.175 – 3.016 meV        |

**Table 4.6.** Defect parameters of the red component based on the model shown in Fig. 4.73a. Redrawn from [MFJ2].

of 2.53 eV and the spacing of the emission peaks is  $\hbar\omega = 220$  meV. Both the standard deviation  $\sigma$  of  $\hbar\omega$  and the full width at half maximum (FWHM) of the Lorentzian lineshape  $\Delta E_L$  are negligibly small. The broadening of the radiative transitions is therefore dominated by  $\sigma_{\Delta E}$ , which corresponds to a FWHM =  $2\sqrt{2 \ln(2)}\sigma_{\Delta E} = 158$  meV. This broadening of  $\Delta E_{21}$  originates from broadening of the two involved CTLs. Assuming equal standard deviations for both of the involved CTLs, each FWHM would be 112 meV. Apparently, the model does only contain relative information regarding the two electronic states 1 and 2. Under the assumption that the two CTLs were centered within the bandgap of 4H-SiC, the CTLs would be  $(E_G - \Delta E_{21})/2 = 0.36$  eV away from the conduction and valence bands, respectively.

A very important experimental observation is that the red component occurs at both the rising and the falling transitions. It suggests that the underlying recombination processes are identical. This seems to conflict with the previous understanding that the recombination at the rising transition occurs in interaction with electrons from the conduction band and at the falling transition with holes from the valence band (see Fig. 4.68). Assume the red component would be caused by the recombination of a trapped hole with an electron from the conduction band, this would mean that the recombination could not occur at the falling transition. The reason would be that the electron in the conduction band would have already disappeared once the MOSFET is switched into accumulation and a hole gets trapped with which the electron in the conduction band could subsequently recombine. The same argumentation would hold for a trapped electron that would recombine with a hole in the valence band. The red component could occur only at one of the two transitions – not at both of them. Consequently, the red component must be caused by a sort of donor-acceptor-pair (DAP) recombination, which means that the red component is caused by recombination between two trapped charge carriers. This is illustrated in Fig. 4.74a. For both the rising and falling transition, the recombination occurs from an overall neutral state ( $A^-/D^+$ ) to a state ( $A^0/D^0$ ). The difference between the rising and the falling transitions is the order of charging either the donor  $D^+$  or the acceptor  $A^-$  state first. It is important to note that this does not conflict with all the previous observations from Section 4.4. For instance, the relation to the transient  $\Delta V_{th}$  caused either by the charge stored in the acceptor state or in the donor state would still hold. The only difference is that two NMP transitions for charging both the acceptor and the donor state are required prior to the recombination of the involved charges.

### The Blue Component

As shown in Fig. 4.72, the blue component agrees well with the emission spectrum of the forward biased body diode. As the light emission of the body diode is predominantly created in the bulk 4H-SiC crystal, it is reasonable to conclude that the blue component must be assigned



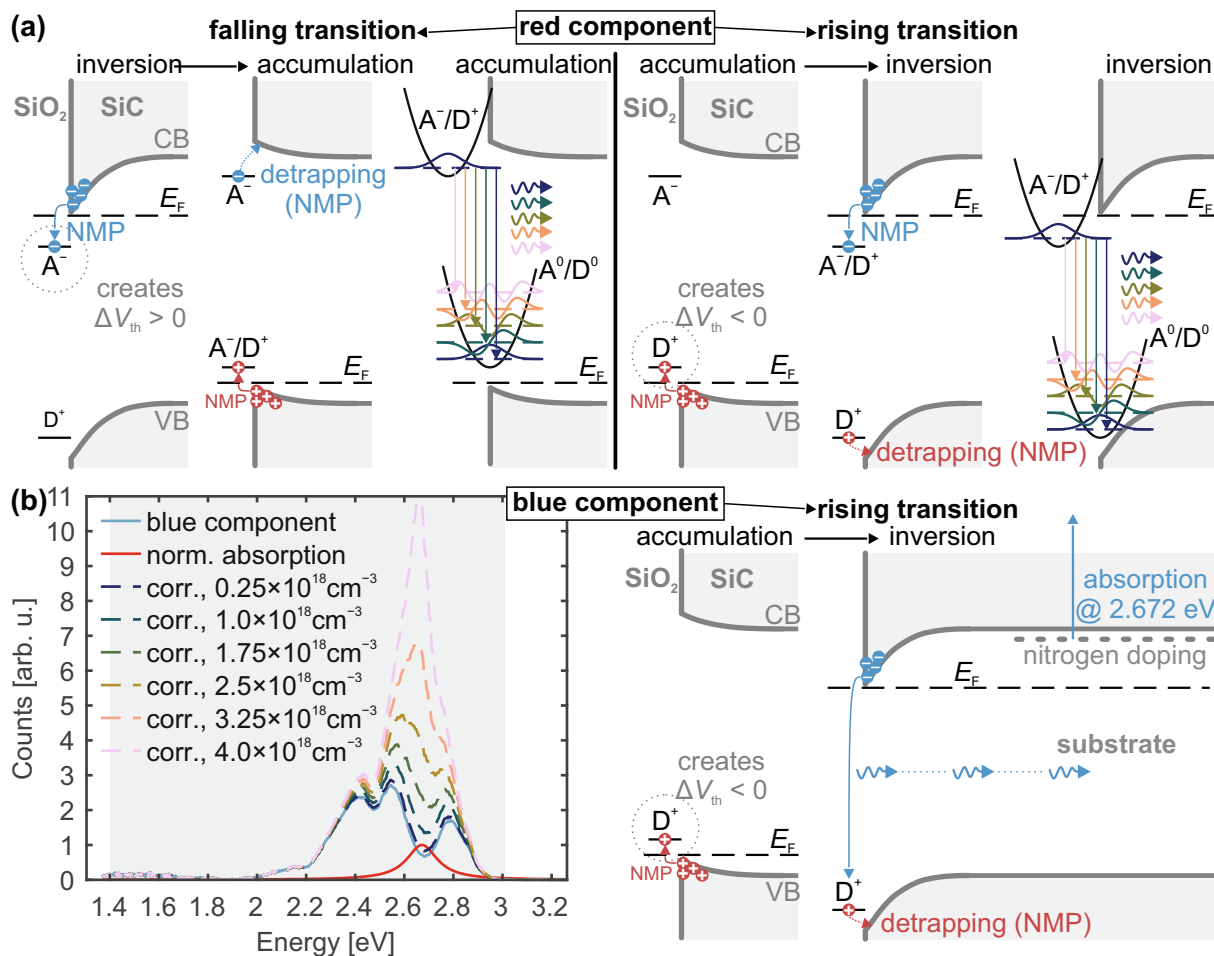


**Figure 4.74.** (a) Schematic illustration of the processes involved in the mechanism creating the red component. (b) The impact of absorption in bulk n-doped 4H-SiC on the blue component and a schematic illustration of the processes involved in the mechanism creating the blue component. Redrawn from [MFJ2].

to defects that exist both at the 4H-SiC/SiO<sub>2</sub> interface and in the bulk crystal. Bulk defects in 4H-SiC have been thoroughly studied in the past, which tentatively allows to assign the light emission of the blue component to DAP transitions. As illustrated in Fig. 4.71c, the emission peak around 2.5 eV is assigned to DAP recombination between the D-center as an acceptor and a donor-defect EK<sub>2</sub>, that were identified by deep-level transient spectroscopy (DLTS) in the past [347], [348]. Besides that, this peak could contain contributions from Z<sub>1/2</sub> centers [349]. Furthermore, the emission peak around 2.8 eV could be assigned to DAP recombination between nitrogen and aluminum dopants [347], [350], but might also contain contributions of D<sub>1</sub>-center related recombination [MFJ9], [351]. However, it is to note that the blue component in the presented experiments behaves more like a donor-like defect close to the valence band. This is illustrated in Fig. 4.74b and is predominantly based on the observations that the blue component solely occurs at the rising transition and the presented dependence on the transition times (see Section 4.4.7). However, this behavior might also be caused by very short trapping/detrapping time constants of the acceptor state close to the conduction band.

Independent of the discussion on its origin, the blue component might be prone to absorption in the n-doped 4H-SiC bulk crystal, which is created by a transition from the nitrogen dopants to a higher state in the conduction band, which was investigated by Weingärtner *et*

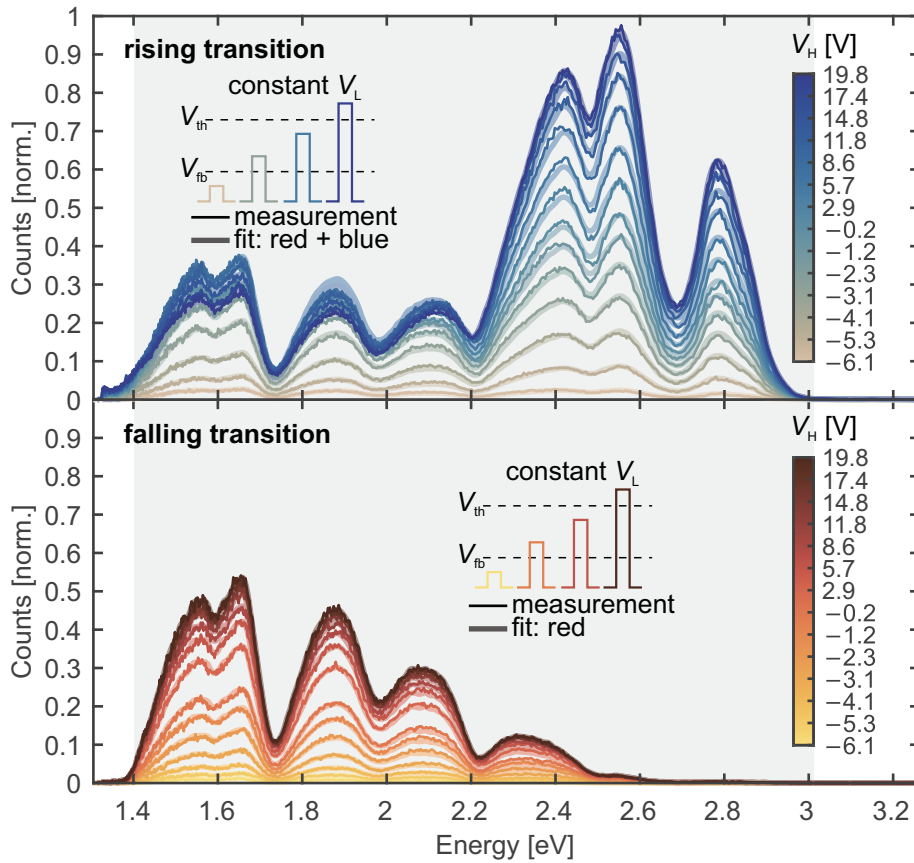


**Figure 4.75.** Emission spectra of the rising and falling transition obtained by the constant low level ( $V_L$ ) technique. The spectra of the rising transition were separately fitted by a superposition of the red and blue components, whereas the spectra of the falling transition were fitted with the red component only. Redrawn from [MFJ2].

*al.* [323]. Based on fitting the absorption peak presented by Weingärtner *et al.* with a Lorentzian-shaped absorption peak, the impact on the blue component can be estimated for different n-doping concentrations. According to Weingärtner *et al.*, the peak absorption coefficient  $\alpha$  is given by  $\alpha(c_n) = \alpha_0 + (\kappa \times c_n)$ , with  $\kappa = 3.6 \times 10^{-17} \text{ cm}^2$ ,  $\alpha_0 = 2.4 \text{ cm}^{-1}$ , and  $c_n$  as the n-type nitrogen doping concentration. The light intensity is related to the thickness  $d$  of the 4H-SiC layer by the Bouguer-Lambert-Beer law [352]–[354] following

$$I(E_{\text{ph}}, d) = I_0 \exp(-\alpha(E_{\text{ph}})d), \quad (4.79)$$

where  $I_0$  is the light intensity before being exposed to the absorption of the layer. As the approximate thickness  $d = 185 \text{ }\mu\text{m}$  of the 4H-SiC layer is known, the impact of this absorption profile can be estimated for different effective doping concentrations. This is illustrated in Fig. 4.74b. Although the impact is probably rather minor, it is to note that the absorption peak coincides with a valley in the emission spectrum of the blue component.

### Voltage Levels

As already discussed in Section 4.4.3, the dependence of the light emission on the voltage levels is essential to deepen the understanding of the underlying mechanisms. Analogously to these measurements with the SiPM-based setup, here, the setup for time-gated spectroscopy

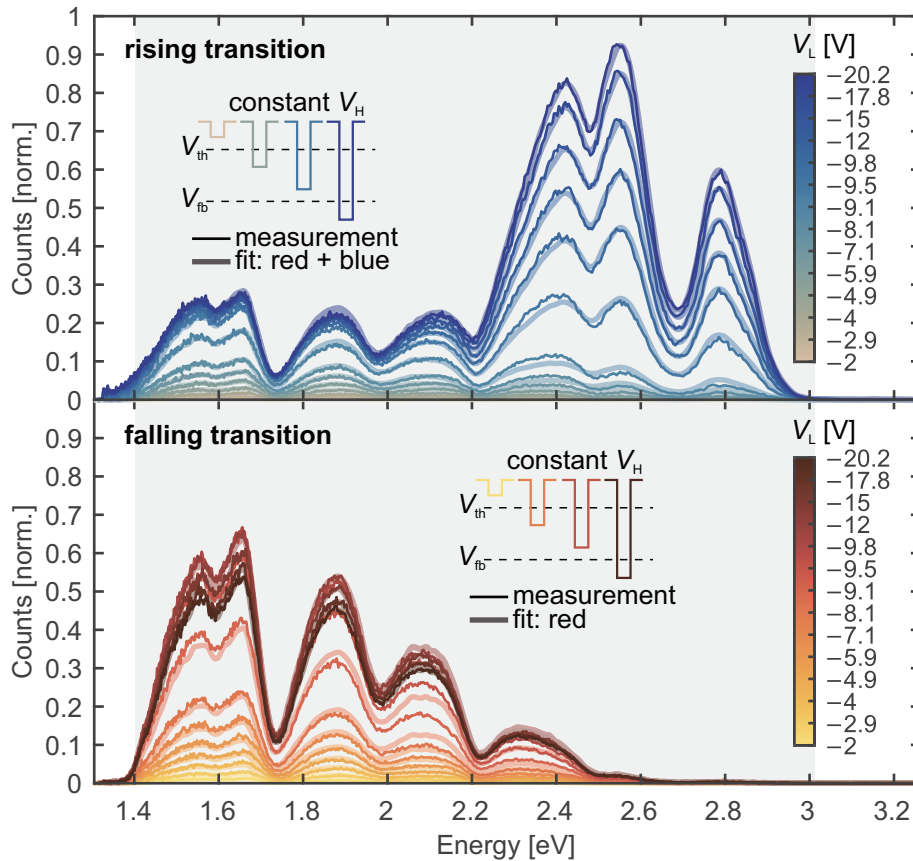


**Figure 4.76.** Emission spectra of the rising and falling transition obtained by the constant high level ( $V_H$ ) technique. The spectra of the rising transition were separately fitted by a superposition of the red and blue components, whereas the spectra of the falling transition were fitted with the red component only. Redrawn from [MFJ2].

is used to investigate the light emission from the rising and falling transitions separately. The essential advantage over the previous measurements is the spectral resolution. However, the disadvantage is the necessity of continuous switching to gain enough statistics for the emission spectrum. In contrast to the SiPM-based measurement, the device can therefore not recover back to its pristine state at  $V_{GS} = 0$  V. Another difference is the partial removal of the drain metallization at the backside of the chip, such that the drain potential remained grounded.

Analogously to the previous measurements with the SiPM based setup, the dependence on the low level  $V_L$  and the high level  $V_H$  is investigated similarly to the constant low level and constant high level techniques known from CP (see Section 3.4). While keeping either  $V_L$  or  $V_H$  constant, the other level is swept and the light emission is measured from the rising and falling transitions separately. In contrast to the CP current (bulk current) in a CP experiment or the photo charge from the SiPM-based setup, a full light emission spectrum is recorded for each combination of  $V_L$  and  $V_H$  levels. Consequently, this results in four sets of spectra.

The spectra obtained from the constant low level technique are shown in Fig. 4.75 for both the rising and falling transitions. Considering the understanding of the recombination mechanisms presented in Fig. 4.74, it will be shown that be assumed that the red and blue components do not depend on the used voltage levels. This was particularly expected for the red component because the ratios of the emission peaks depend only on the matrix elements in Equation 4.78. Indeed, all the spectra of the rising transition of the different voltage level

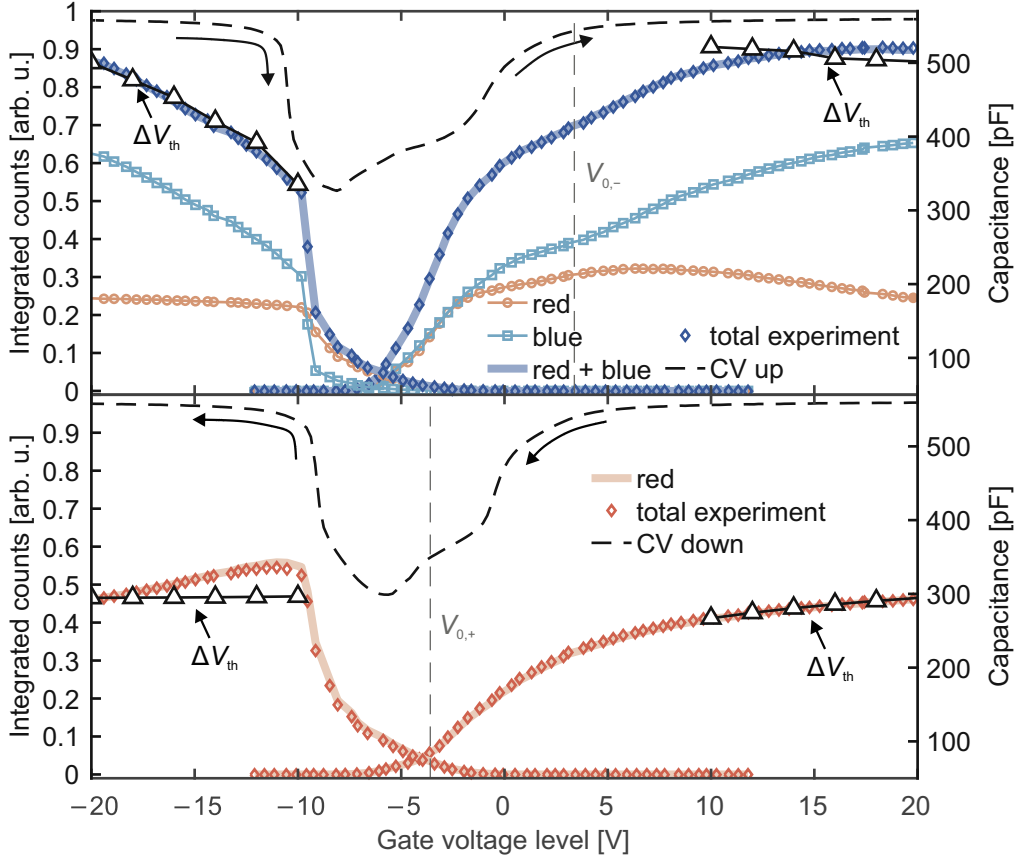


**Figure 4.77.** Constant low and constant high level curves of the red and blue components of the rising (upper plot) and falling transitions (lower plot). The integrated photon counts are given by the amplitudes from Equations 4.80 and 4.81. As a consistency check, the total integrated counts of the experimental data are also shown and agree well with the value of the fit function. CV curves of an up and a down sweep for the rising and falling transitions, respectively, are also shown. The integrated photon emission can be fitted with Equation 4.82, relating it to the transient  $\Delta V_{th}$ . Redrawn from [MFJ2].

combinations can be fitted well with a superposition of the red ( $I_{red}(E_{ph})$ ) and blue ( $I_{blue}(E_{ph})$ ) components as per

$$I_{rising}(E_{ph}) = A_{red}^{rise} \times I_{red}(E_{ph}) + A_{blue}^{rise} \times I_{blue}(E_{ph}) \quad (4.80)$$

only by optimizing the amplitudes  $A_{red}$  and  $A_{blue}$  of the red and blue components, respectively. The fits are indicated in Fig. 4.75. Note that only the amplitudes of the red and blue components are varied – the spectra themselves remain untouched. In contrast to those spectra of the rising transition, the emission spectra of the falling transition were fitted with the red component only, following

$$I_{falling}(E_{ph}) = A_{red}^{fall} \times I_{red}(E_{ph}). \quad (4.81)$$

Again, these fits agree well with the measured spectra. In summary, the red and blue components themselves are not affected by the choice of  $V_L$  and  $V_H$ , only their respective overall amplitudes  $A_{red}$  and  $A_{blue}$  change. Consequently, the electric field does not affect the emission energies. Due to the linearity of integration, the amplitudes are proportional to the integrated counts

from the respective component. These amplitudes are plotted in Fig. 4.77 for both the rising and falling transitions. In order to illustrate the success of the spectral fits, the agreement of the total integrated counts of the superimposed components and the integrated experimental data is presented as well.

These characteristics of the rising and falling transitions can be well compared with CV up and a down sweeps. Both curves are indicated in Fig. 4.77. Both the red and blue components increase significantly once the MOSFET is switched between accumulation and inversion. The onsets are around  $V_{fb}$  and  $V_{th}$ , respectively.

As already pointed out, the mechanisms illustrated in Fig. 4.74 for the red and blue components should still yield a correlation between the transient  $\Delta V_{th}$  and the total integrated emission spectrum. Hereby, the transient  $\Delta V_{th}$  represents the amount of trapped charge prior to recombination. In contrast to the methodology introduced in Section 4.4.3, where double pulses were employed, a different approach is used because the detection of the light emission occurs during continuous switching. For this purpose, a pristine MOSFET with intact drain metallization is exposed to the same 500 kHz switching between  $V_H$  and  $V_L$  for a total time of 4.1 ms. The  $V_{th}$  was measured prior to the respective  $V_{GS}$ -transition with a measurement delay of 1  $\mu$ s.

Analogously to Equation 4.70, the integrated counts can be related to  $V_{th}$  via

$$IC_{photo}(V_{GS}) = C_s |V_{th}(V_{GS}) - V_{0,s}|, \quad s \in \{+, -\}. \quad (4.82)$$

Fitting this equation with the four parameters to the integrated counts in Fig. 4.77 yields good agreement and thus confirms the understanding of the red and blue components illustrated in Fig. 4.74.

### Frequency and Duty Cycle

Depending on the time constants of the involved NMP trapping processes prior to recombination, which are shown in Fig. 4.74, the used frequency or the duty cycle might influence the red and blue components in their intensity. This was investigated by the experiments presented in this section, in which the light emission upon different frequencies and duty cycles was measured.

To investigate the impact of the switching frequency, it was varied between 20 kHz and 1000 kHz at a fixed duty cycle of 50 %. The light emission of both the rising and the falling transitions were measured and are shown in Fig. 4.78a. Particularly in these experiments, it is important to recall that it is not the integration time of the CCD, which is kept constant, but it is the number of  $V_{GS}$ -transitions. Here, in total  $2 \times 10^6$  transitions between 15 V and  $-15$  V were integrated. For the same number of transitions, only minor if not negligible differences in the emission spectra were observed. Only around 1.6 eV in the emission spectrum of the falling transition, there might be a slight impact of the switching frequency.

Similarly, the duty cycle was varied between 5 % and 95 % at a fixed frequency of 100 kHz. The results in Fig. 4.78b do not show any impact of the duty cycle.

This suggests that the involved NMP transitions prior to the recombination are very fast, at least below 500 ns, which corresponds to half of the period of the 1000 kHz waveform (highest frequency) and to 5 % of the period of the 100 kHz waveform (lowest/highest duty cycle).

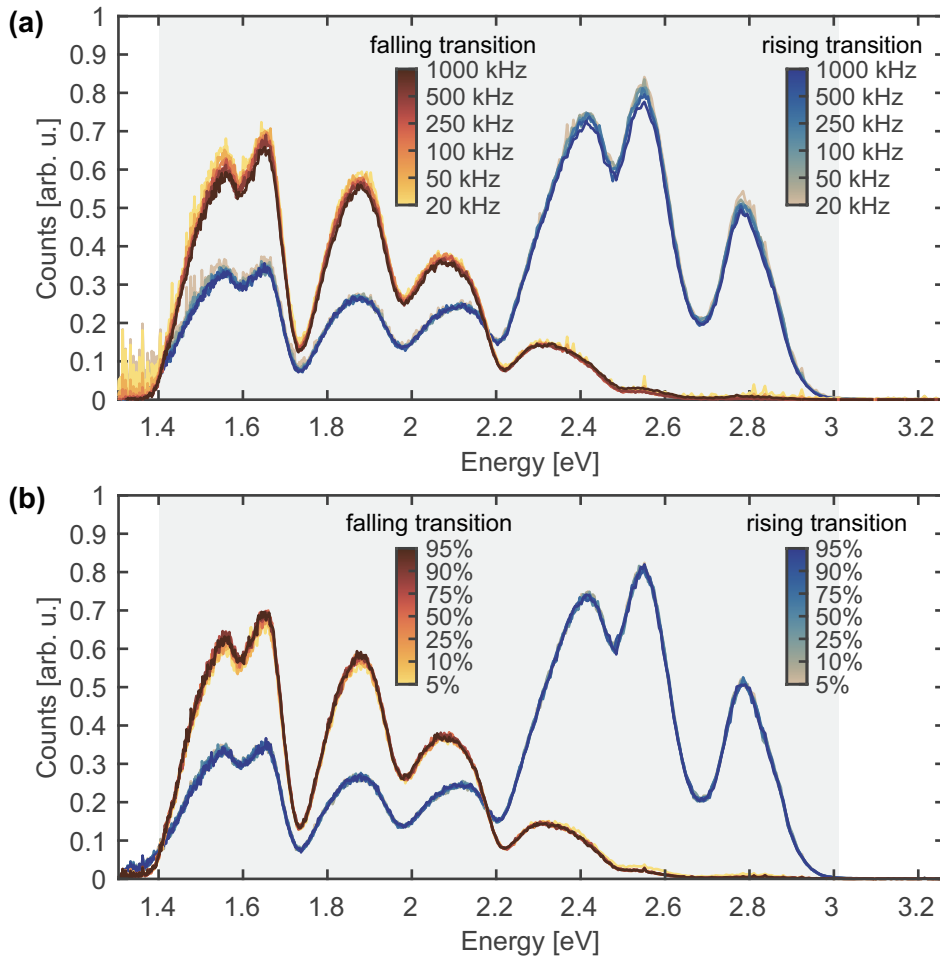


**Figure 4.78.** (a) Emission spectra of the rising and falling transitions for different frequencies, but a constant duty cycle of 50%. (b) Emission spectra of the rising and falling transitions for different duty cycles, but a constant frequency of 100 kHz. Redrawn from [MF]2].

### Transition Times

As commonly known from CP experiments, the transition time of  $V_{GS}$  has a significant impact on defect-assisted recombination at the semiconductor-insulator interface (see Section 3.4). In this section, the impact of both the rise and the fall times on the light emission at the rising and falling transitions are presented. In contrast to the previous investigations of time-gated spectroscopy, where the setup described in Section 3.3 was used, here, an Agilent 4156C precision semiconductor parameter analyzer with a 41501B pulse generation and expander unit were used to create a trapezoidal switching waveform. The pulse generator provided a 20 V / -20 V, 50 kHz signal of which the rise and fall times were separately varied between 0.5  $\mu$ s and 8.0  $\mu$ s while keeping the other transition time constant at 0.5  $\mu$ s. The results are shown in Fig. 4.79.

Fig. 4.79a shows the the emission spectra of both the rising and the falling transitions for different rise times. First, the emission spectrum of the falling transition is completely independent of the rise time. This fits to the short trapping time constants concluded from the independence of frequency and duty cycle. In contrast to that, the emission spectrum at the rising transition indeed depends on the rise time. Apparently, the impact of the rise time depends on the photon energy. While the intensity decreases with increasing rise time for energies above 2.4 eV, it increases with increasing rise time for energies below 2.2 eV. As previously,

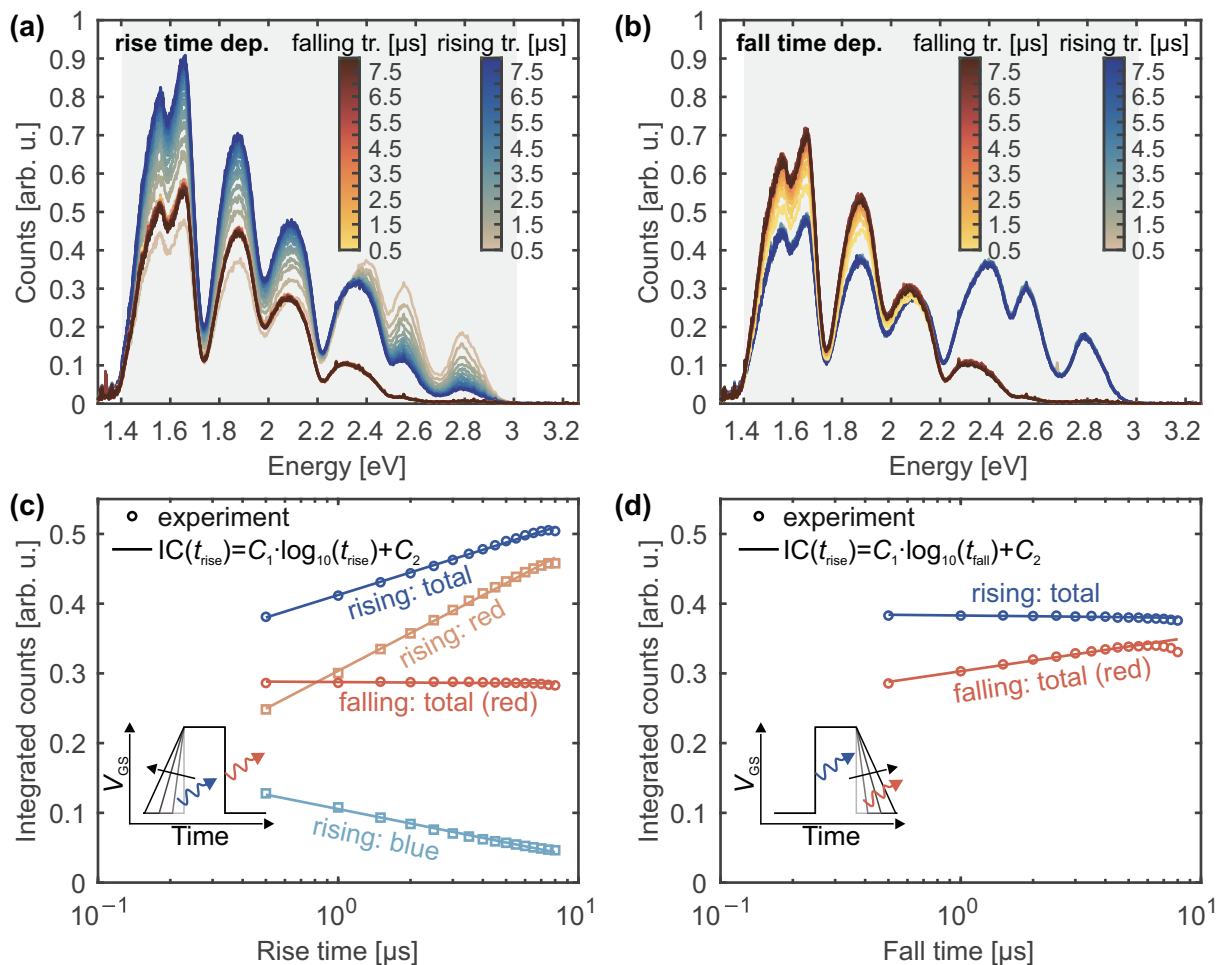


**Figure 4.79.** (a) Dependence of the emission spectra of the rising and falling transitions on the rise time at a constant fall time of  $0.5 \mu\text{s}$ . (b) Dependence of the emission spectra of the rising and falling transitions on the fall time at a constant rise time of  $0.5 \mu\text{s}$ . (c) Dependence of the different components on the rise time based on the data from (a). (d) Dependence of the different components on the fall time based on the data from (b). Redrawn from [MF]2].

the emission spectrum could be fitted by a superposition of the red and blue components, following Equation 4.80. This allowed to separately consider the rise time dependence of the two components, whereby the results are illustrated in Fig. 4.79c. Apart from the independence of the emission at the falling transition (red component), it clearly indicates an increase of the red component at the rising transition with increasing rise time. In contrast, the blue component at the rising transition decreases with increasing rise time. Besides that, both the red and blue components depend linearly on the logarithm of the rise time, which is a characteristic well-known from CP experiments (see Equation 3.12).

Fig. 4.79b shows the emission spectra of both the rising and the falling transitions for different fall times. Analogously to the emission at the falling transition upon a variation of the rise time, the emission spectrum of the rising transition is independent of the fall time. The emission spectrum of the falling transition increases its intensity upon increasing the fall time. The associated red component is illustrated in Fig. 4.79d. As before, the red component increases linearly with the logarithm of the fall time.

First, it can be summarized that the light emission is only affected by the transition time of the transition at which it occurs. Second, while the blue component decreases with increas-

ing transition time, the red component increases. However, in both cases, this occurs with a linear relation to the logarithm of the transition time. The behavior of the blue component resembles the known behavior of the CP current and is consequently in full agreement with the mechanism illustrated in Fig. 4.74. The longer the rise time, the more previously trapped holes can be emitted back to the valence band prior to the moment when recombination with conduction band electrons becomes possible. Most importantly, the observation of an increasing red component with increasing transition time confirms the red component to be caused by DAP recombination. Effectively, there must be two regimes. Initially, the recombination increases with increasing transition time and then decreases with increasing transition time again. The performed experiment apparently captured the regime of increasing recombination. For a more intuitive understanding, consider the rising transition as an example. As illustrated in Fig. 4.74, DAP recombination requires both an electron and a hole to get trapped before recombination becomes actually possible. The longer the rise time, the more previously trapped holes can be emitted back to the valence band again. On the other hand, the longer the transition time the more electrons get trapped and can subsequently recombine. This interplay between the capture time constant of the electron and the emission time constant of the hole determines the regime and dependence on the transition time and it strongly depends on the respective bias dependence of these time constants. Consequently, this emphasizes the difference between the underlying mechanisms of the red and blue components.

### Temporal Resolution

So far, the gate time window has been set to half of the period of the  $V_{GS}$  signal to separately investigate the emission of the rising and falling transitions. As discussed in Section 3.7, the measurement setup for time-gated spectroscopy allows gate widths as short as 3 ns. This was used within the experiment presented in this section investigating the time evolution of the emission spectrum over the entire  $V_{GS}$  period. In contrast to the approach based on the SiPM setup, presented in Section 4.4.2, that requires only a single  $V_{GS}$  period, the entire spectrum can be measured, however, at the cost of integrating over several switching periods during continuous switching.

For this purpose, a switching frequency of 78.1 kHz was used. This corresponds to a period of 1.28  $\mu$ s. The MOSFET is switched between 15 V and  $-15$  V with transition times of 50 ns. By sweeping through the gate delay  $t_{gd}$  over the entire period in steps of 3 ns, the evolution of the emission spectrum is captured completely.

The results are illustrated in Fig. 4.80a. As the ICCD is triggered on the rising transition of the trigger signal, the rising transition of  $V_{GS}$  is scanned first. The middle of the  $V_{GS}$  period is marked by a horizontal line, after which the falling transition is scanned. In contrast to the falling transition, the rising transition contains the prominent emission above 2.2 eV, that was associated with the blue component.

In fact, it was found that the use of the red and blue components is still valid for describing the time evolution. Exactly as done in the previous sections, each emission spectrum was fitted with the introduced red and blue components, which allowed to investigate their evolution separately. Fig. 4.80b shows the fitted evolution of the emission spectrum. It agrees well with the corresponding raw data in Fig. 4.80a. This is further illustrated in Fig. 4.81a, which exemplarily shows two emission spectra: one of the rising transition and one of the falling transition. Even though the gate width was reduced down to only 3 ns, both spectra can be well described



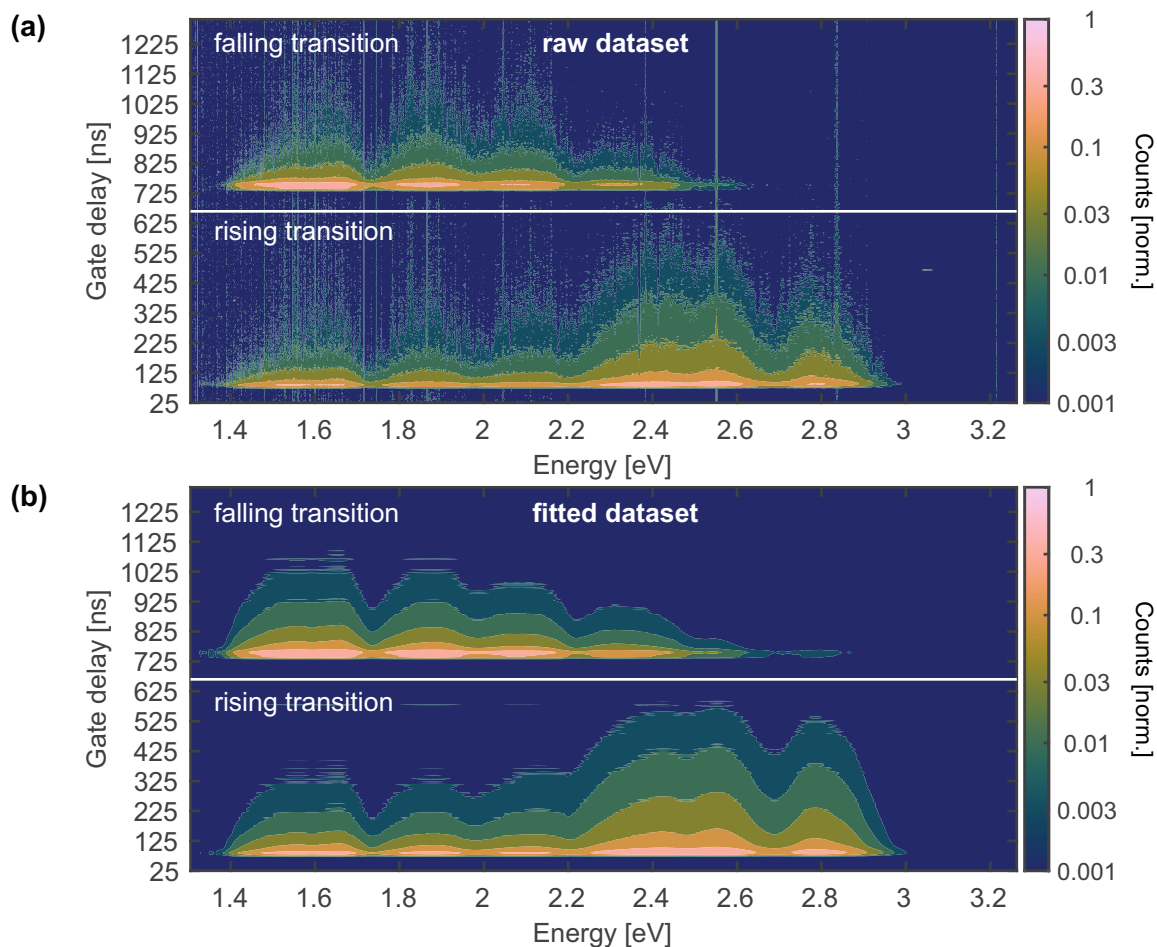


**Figure 4.80.** (a) Contour plot of raw dataset of the evolution of the emission spectrum over an entire  $V_{GS}$  period. A horizontal line indicates the middle of the period, whereby the lower emission spectra are associated with the rising transition and the upper spectra are associated with the falling transition. (b) Contour plot of fitted spectra from (a). Redrawn from [MFJ2].

by a superposition of the red and blue components. The associated amplitudes are plotted in Fig. 4.81b, showing the time evolution of the red components at both the rising and falling transitions and the evolution of the blue component at the rising transition.

The same data is shown in Fig. 4.81c with a logarithmic vertical axis. Both the red and blue components were normalized to their maximum at the rising transition. This reveals more details on their temporal evolution. Apparently, they exhibit a biexponential decay, which can be described by

$$I(t_{gd}) = C \times \exp\left(-\frac{t_{gd} - t_0}{\tau_1}\right) + (1 - C) \times \exp\left(-\frac{t_{gd} - t_0}{\tau_2}\right). \quad (4.83)$$

Hereby,  $t_{gd}$  is the gate delay,  $t_0$  is the point in time of maximum photon emission,  $\tau_1$  and  $\tau_2$  are the decay time constants, and the parameter  $C$  represents the share of the first exponential decay. Fitting this equation to the components at the rising and falling transitions yields the parameters listed in Table 4.7. Most interestingly, the red component has similar values for  $C$ ,  $\tau_1$ , and  $\tau_2$  at the rising and the falling transitions. This suggests that the red components of the rising and falling transitions originate from the same underlying recombination process, which is in full agreement with the DAP recombination suggested in Fig. 4.74. Besides that, the blue

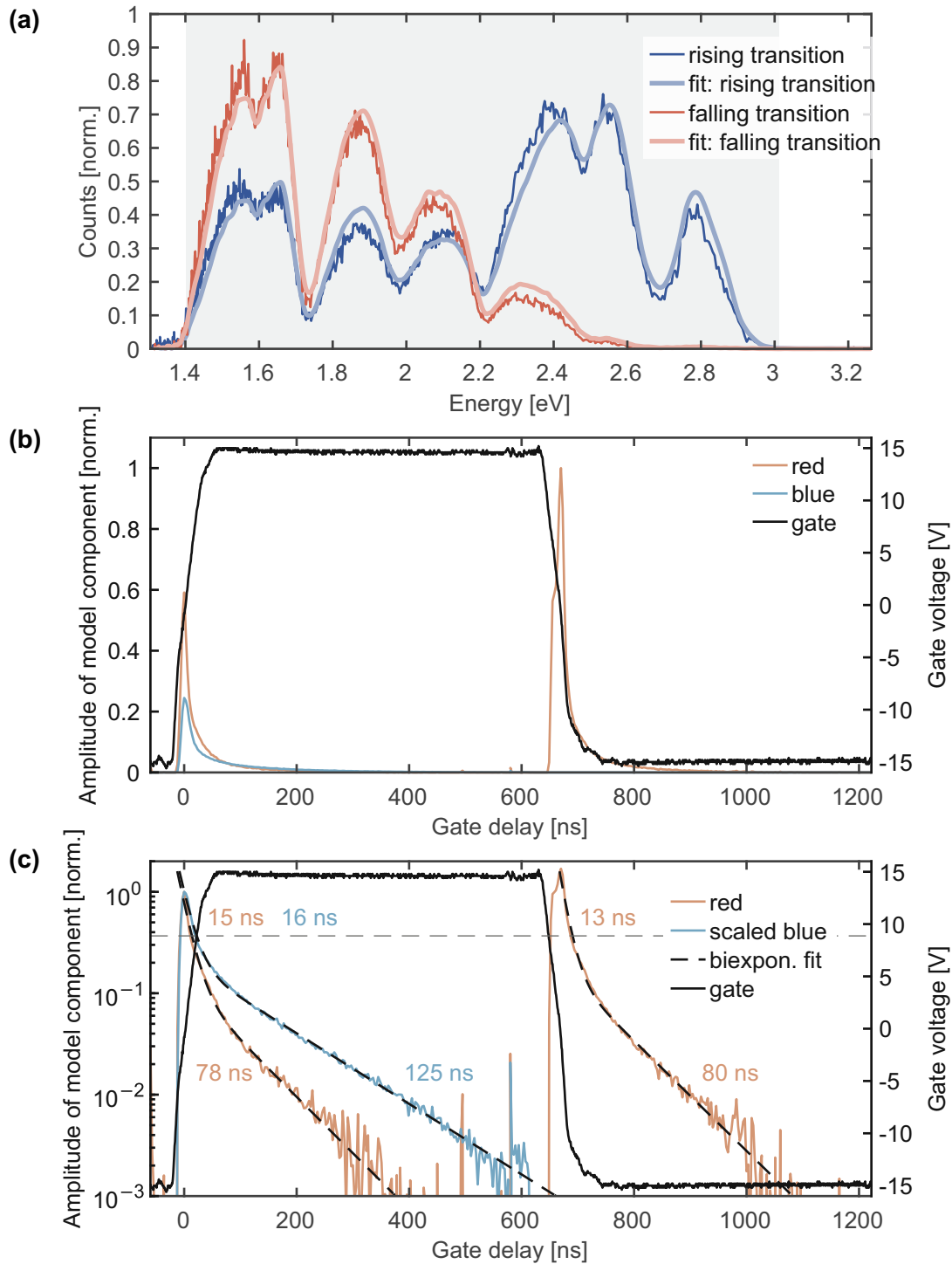


**Figure 4.81.** (a) The two emission spectra from Fig. 4.80a of the rising and falling transitions with maximum integrated counts. Their corresponding fits from Fig. 4.80b are also indicated. (b) Evolution of the red and blue components over the entire  $V_{GS}$  period. (c) Evolution of the red and blue components from (b) on a logarithmic vertical axis. The components were normalized to their maximum at the rising transition. The biexponential fits according to Equation 4.83 are indicated by dashed lines and the obtained decay time constants are indicated. Redrawn from [MFJ2].

component shares with the red component the same  $\tau_1$ , however, it has an almost 60% longer  $\tau_2$  with respect to the red component.

|         | red  |               |               | blue |               |               |
|---------|------|---------------|---------------|------|---------------|---------------|
|         | C    | $\tau_1$ [ns] | $\tau_2$ [ns] | C    | $\tau_1$ [ns] | $\tau_2$ [ns] |
| rising  | 0.87 | 15            | 78            | 0.80 | 16            | 125           |
| falling | 0.89 | 13            | 80            | –    | –             | –             |

**Table 4.7.** Parameters obtained by fitting Equation 4.83 to the data in Fig. 4.81c. Redrawn from [MFJ2].

Considering that  $\tau_1$  is smaller than the actual transition time of  $V_{GS}$ , its meaning is rather hard to interpret. Only if the  $V_{GS}$ -transition would be instantaneous, the real  $\tau_1$  could be measured. Nevertheless,  $\tau_2$  falls predominantly in the time regime of constant  $V_{GS}$ . The significant difference between the  $\tau_2$  of the red and the blue components and the agreement of all parameters of the red components at the rising and falling transitions suggest that the selection of the red and blue components is suitable and that the underlying mechanisms are indeed fundamentally different.

### Carbon Clusters as the Cause of the Red Component

The experimental results presented in the previous sections confirm the mechanisms illustrated in Fig. 4.74. The most interesting conclusion is that the emission spectrum of the red component is caused by transitions from a vibrational ground state of an electronic excited state to several vibrational eigenstates of an electronic ground state. Particularly remarkable are the experimentally extracted parameters obtained by fitting the quantum mechanical model to the spectrum of the red component. The parameters, listed in Table 4.6, suggest a transition with a vibrational mode that features an astonishingly high energy of  $\hbar\omega = 220$  meV. It is important to note that this is much higher than the highest optical phonon modes in 4H-SiC and SiO<sub>2</sub> of 120 meV and 137 meV, respectively (see Section 1.3.4) [86], [89], [355]. Consequently, it must be concluded that the observed vibrational mode cannot be an ordinary phonon mode, but it must be a local vibrational mode (LVM) of the defect that assists the recombination event (see Section 1.3.5).

| parameter           | exp. | (C <sub>3</sub> ) <sub>Si,k</sub> | (C <sub>3</sub> ) <sub>Si,h</sub> | (C <sub>BC</sub> ) <sub>4,kkkk</sub> | (C <sub>BC</sub> ) <sub>4,hhhh</sub> |
|---------------------|------|-----------------------------------|-----------------------------------|--------------------------------------|--------------------------------------|
| ZPL [eV]            | 2.53 | 2.56                              | 2.67                              | 2.36                                 | 2.49                                 |
| $\hbar\omega$ [meV] | 220  | 249                               | 247                               | 193                                  | 192                                  |
| S                   | 4.83 | 2.59                              | 2.35                              | 5.1                                  | 5.5                                  |

**Table 4.8.** Comparison of defect parameters obtained by experiment and theoretically calculated values from literature [100]. Redrawn from [MFJ2].

LVMs with such high energies are indeed known in SiC. They have been experimentally detected by low temperature photoluminescence measurements and were assigned to carbon clusters (see Table 1.4) [96], [101]. A lot of theoretical work based on DFT has been conducted on investigating the vibrational structure of these defects [99], [100], [102], which can even migrate through the crystal [356] and are affected by annealing temperature and doping concentration [96], [357].

Table 4.8 compares the experimentally obtained parameters of the red component, including ZPL,  $\hbar\omega$ , and the HR-factor  $S$ , to some selected values obtained by a recent theoretical study employing DFT [100]. The listed defects are the cubic/hexagonal tri-carbon antisite clusters and the cubic/hexagonal tetra-carbon interstitials. The values for the three parameters are clearly located in the range of the theoretically obtained values, suggesting that the red component

is probably caused by a carbon cluster-like defect. However, it is to note that the theoretical calculations consider only recombination of bound excitons involving a donor state and a free charge carrier. As argued previously, the red component must be caused by DAP recombination. Therefore, it appears likely that this DAP recombination involves a defect complex where the commonly studied carbon clusters serve as building blocks. This interpretation is supported by the fact that LVMs of such a high energy, as observed in experiment, are extremely rare. While di-interstitials and dicarbon antisites exhibit suitable CTLs [100], LVMs of sufficiently high energy are found in tri-carbon antisite complexes (see Table 1.4).

In addition to that, the theoretically studied carbon clusters are bulk defects. However, it has been found that the SiC/SiO<sub>2</sub> interface features a particularly high density of carbon clusters which have been linked to a lowering of the channel mobility [358], [359]. Oxidation or other processing steps might lead to the injection of carbon into SiC [360], whereby it needs to be mentioned that the interface is a transition layer rather than an atomically sharp interface [361]. This transition layer is also directly related to the channel mobility: the wider the transition layer the worse the channel mobility [362]. However, this heavily depends on the used interface processing [363].

In addition to knowing about the presence of carbon clusters at the SiC/SiO<sub>2</sub> interface, there are several experimental observations that agree with the proposed relation between carbon clusters and the red component. Characterizing the photoluminescence in the range of 1.55–2.48 eV leads to the observation of LVMs up to 220 meV and could even be linked to the interface-defect density extracted by capacitance-voltage measurements [364], [365]. Both the range of energy and the energy of the observed LVMs perfectly fit to the red component. Other studies showed that probably the same defects are single-photon-emitters [366]–[368]. In agreement with the above mentioned emission of carbon into SiC, their polarization hints towards defects at the SiC-side of the interface. In addition, these defects appear upon thermal oxidation and disappear again upon removing the oxide again. Finally, these defects have been successfully mapped in two dimensions using confocal photoluminescence and tunneling electroluminescence [369], [370] as well as capacitive methods [371]. These experiments share the observation that the involved defects predominantly appear at bumps of the (0001) crystal surface.

#### 4.4.8 Relation Between Gate Switching Instability and Field-Effect Stimulated Photon Emission

The results of Section 4.3 and 4.4 have clearly revealed numerous similarities between GSI and field-effect stimulated emission of photons. The intention of this section is to summarize these similarities and point out why these two effects might indeed be related.

Experimentally, the similarities are apparent: both effects occur in the same operation mode of gate switching. Also, in contrast to the permanent component of ordinary BTI, both effects occur at room temperature – GSI even seems to be athermal. Furthermore, GSI and light emission are caused by switching events between inversion and accumulation. Consequently, they have a similar dependence on the low and high levels  $V_L$  and  $V_H$ , respectively. In addition to that, these two effects share their inherent relation to the switching event itself. Independent of the switching frequency and the duty cycle, the same number of switching cycles leads for the two effects either to the same  $V_{th}$  drift or the same total number of emitted photons. Even the relation to the transition times is similar. In the presented experiments, GSI was only

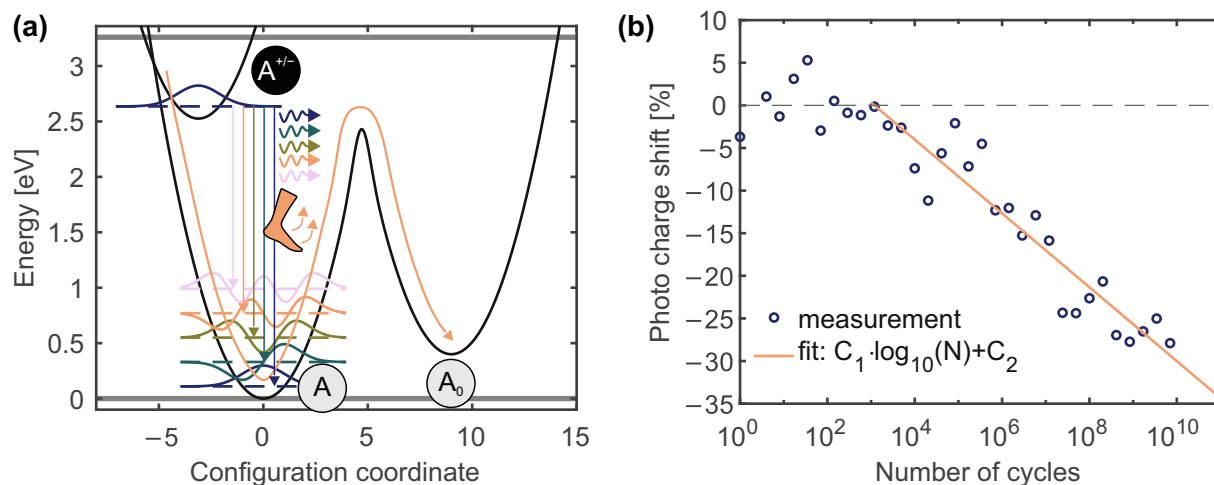


**Figure 4.82.** (a) Configuration coordinate diagram to explain both GSI and field-effect stimulated light emission upon gate switching. (b) Shift of the photo charge upon continuous switching of  $V_{GS}$  with 25 V / -13 V at 500 kHz. Redrawn from [MFJ5].

dependent on the rise time, but was independent of the fall time. Keeping this in mind, it appears particularly interesting that the blue component did only occur at the rising transition, while the red component occurred both at the rising and the falling transition.

As argued in the respective sections, both effects originate from defect-assisted electron hole recombination. While GSI was argued to be related to recombination-enhanced defect reactions (REDRs), where a significant amount of energy ( $> 2$  eV) of a non-radiative transition is channelled into the creation of a defect, light emission is caused by a radiative transition with a ZPL of 2.53 eV (red component) or even higher (blue component). Consequently, it appears natural to conclude that the two effects are basically two competing pathways for the same transition – a radiative and a non-radiative pathway. This is illustrated in Fig. 4.82a using the red component. Indeed, bringing the understanding of those two effects together is rather straight forward. It just requires to modify the understanding of GSI in the sense that recombination does not occur in direct interaction with the conduction or valence band, but that it occurs as well via DAP recombination. This does indeed not create any immediate conflict with the presented experimental findings. Consider for example the rising transition. At the end of the  $V_L$ -phase, the donor state has captured a hole from the valence band, once the MOSFET is switched up into inversion, an electron is captured in the acceptor state. Once both the donor and the acceptor states are charged, the system has three options to relax from this excited state. The first option is an ordinary NMP transition under the emission of multiple phonons, bringing the defect back into its pristine state. The second option is the REDR, which effectively transforms the defect from its state  $A$  to  $A_0$ . As argued previously, the states  $A$  and  $A_0$  must differ only slightly with respect to the used experimental characterization techniques. And the third option is the radiative transition, in which the energy is released via a photon. Also in this case, the defect returns to its pristine state.

This mechanism appears to be confirmed once the light emission is measured from the falling  $V_{GS}$ -transitions of continuous gate switching stress (GSS) with the setup based on a SiPM described in Section 3.5. The results are shown in Fig. 4.82b. Apparently, the light emission decreases with increasing number of switching cycles. As suggested above, the number of defects in state  $A$  would reduce over time, which would potentially allow less of those defects to participate in the radiative pathway, leading to the observed reduction of the light emission.

It needs to be noted that all experimental results related to GSI and presented in the course of this work were obtained using asymmetric trench SiC power MOSFETs, whereas the results related to field-effect simulated light emission were obtained using SiC DMOSETs. Considering the strong differences in device design, in particular the different crystal faces of the channel, it is clear that an ultimate relation between GSI and field-effect stimulated light emission cannot be proven based on the presented data. This would require studies on their relation on the exact same type of device, which is strongly suggested for future research.

# Chapter 5

## Summary and Outlook

This chapter summarizes the experiments and findings of this work and gives an outlook on possible future research directions.

### 5.1 Summary

Silicon carbide (SiC) metal-oxide-semiconductor field-effect transistors (MOSFETs) are of fundamental importance for power conversion in various green technologies. The wider bandgap of SiC compared to silicon (Si) enables higher power conversion efficiency at reduced weight and size of applications. However, the SiC/silicon dioxide (SiO<sub>2</sub>) interface has a hundred times higher density of interface defects that affect the device characteristic. These defects feature a broad distribution of capture and emission time constants reaching down to nanoseconds. The associated trapping and detrapping kinetics at the SiC/SiO<sub>2</sub> interface were the premier subject of research. Significant contributions to understanding the trapping kinetics at the SiC/SiO<sub>2</sub> interface were achieved in particular for processes occurring during gate switching, while keeping both drain and source terminals grounded. This comprised the recently revealed degradation mechanism gate switching instability (GSI) and the detection and analysis of light emission from fully-processed power MOSFETs.

The introduction of this work in Section 1 outlined the motivation for using SiC-based technology and summarized its history. This was complemented by reviewing the properties of its growth, its electronic structure and its vibrational properties. Furthermore, typical applications for SiC-based technology were presented and prevalent designs and reliability concerns were discussed.

Afterwards, the underlying physical concepts were presented in Section 2. It explored both non-radiative and radiative transitions involving defects at the SiC/SiO<sub>2</sub> interface. In addition to that, the discussion encompassed Shockley-Read-Hall (SRH) theory, non-radiative multiphonon (NMP) theory, recombination-enhanced defect reactions (REDRs) as well as the competition between radiative and non-radiative transitions.

Experimental techniques employed within this work were introduced in Section 3. In addition to more conventional characterization techniques, such as the transfer characteristic, impedance characterization, or charge pumping (CP), more advanced techniques were presented. Those techniques ranged from ultra-fast threshold voltage measurements over the measurement

of light emission from a single voltage transition to optical spectroscopy and time-gated optical spectroscopy using fully-processed SiC power MOSFETs.

The first part of the results obtained in the course of this work were presented in Section 4.1. Apparent single-value activation energies, that are commonly used both in industry and academia to model the temperature dependence of bias temperature instability (BTI) in MOSFETs, were shown to be at best a rough approximation of the real underlying distributions. Based on an analytic description of activation energy (AE) maps, the principles of the horizontal and the vertical extraction methods of an apparent activation energy were presented. This led to analytic approximations for these activation energies, which clearly demonstrated their dependency on several measurement parameters and their partial insignificance.

In Section 4.2, the prominent recoverable component of BTI in SiC power MOSFETs was investigated using four different commercially-available devices of different designs. It was shown that the measurement of a device parameter itself, such as the threshold voltage ( $V_{th}$ ), already affects the outcome of the measurement. For  $V_{th}$ , this could easily reach several hundreds of millivolts. A similar impact of the recoverable component on the measurement of the transfer characteristic was systematically investigated based on a gate-pulsed transfer characteristic, which represents the more application-relevant measurement technique with respect to the impact of the recoverable component. Hereby, no significant advantage of any device design was found. However, changes in pulse voltage and bias affected the measured drain-source current by more than 10%. In this context, device conditioning with negative gate-source voltage ( $V_{GS}$ ) pulses was shown to accelerate the return to thermal equilibrium by two orders of magnitude.

A central part of this work was a detailed investigation of GSI, a recently revealed degradation mechanism in SiC MOSFETs, that was provided in Section 4.3. GSI occurs upon extensive switching of  $V_{GS}$  between inversion and accumulation, while keeping both drain and source terminals grounded. Based on measurements at different switching frequencies, it was shown that the observed drift in  $V_{th}$  is a superposition of two components, associated with the two concurrently occurring mechanisms of BTI and GSI. It was shown that the GSI component depends solely on the number of switching cycles and that their relation is roughly linear. This exclusive dependence on the number of switching cycles was not only valid for the GSI component of the threshold voltage shift ( $\Delta V_{th}$ ), but the entire device characteristic, including the capacitance-voltage (CV) and conductance-voltage (GV) curves. Gate switching stress (GSS) caused a  $V_{GS}$ -dependent shift of the CV curve which indicated the creation of fast acceptor-like interface defects. They in turn cause the observed  $\Delta V_{th}$  once they get charged by electrons. Furthermore, it was found that GSI requires switching between inversion and accumulation, that it appears to be athermal and that it is affected by the transition time of  $V_{GS}$ . In addition to that, the impact of undershoots was shown to be significant and basically equal to a full switch to the voltage level of the undershoot. Finally, GSI appears to have no impact on the hysteresis. Based on these observations, it was concluded that GSI is most likely caused by REDRs and not by enhanced electron trapping due to a locally enhanced electric field, as recently suggested. A model based on this mechanism yielded good agreement with the measured  $\Delta V_{th}$  and agrees with all experimental observations.

Another central part of this work was presented in Section 4.4, which investigated light emission in the visible spectral range that occurs under the same conditions as GSI. This work demonstrated for the first time the detection and analysis of this light in fully-processed SiC power MOSFETs. The emitted photons originate from the 4H-SiC/SiO<sub>2</sub> interface and are created



by defect-assisted electron-hole recombination. By detecting the emitted light from a fully-processed SiC power MOSFET through the substrate and the epitaxial layer, almost unperturbed detection was achieved. This approach did not only allow to image the spatial distribution of the light emission on the active area of the power MOSFET, but also to characterize it with respect to its intensity and both its spectral and temporal distribution. A setup based on a silicon-photomultiplier (SiPM) allowed to detect the light emitted by single  $V_{GS}$ -transitions, which was on the order of a few hundred photons. It further enabled to temporally localize the light emission both at the rising and the falling transitions, determine its dependence on the voltage levels and relate that to the transient  $\Delta V_{th}$ . Additionally, a pump-probe-scheme enabled the tracking of recovery of the involved trapped charges and its correlation to  $\Delta V_{th}$ . This correlation between  $\Delta V_{th}$  and the light intensity was also found in a long-term stress experiment. Optical spectroscopy then provided the spectral distribution of the emitted light, which could be compared to density functional theory (DFT) calculations from literature. Overall, the measurements indicated recombination of trapped electrons and holes with their respective partners from the valence and conduction bands. A highlight of this work was the use of time-gated spectroscopy, which gave even deeper insights and changed the understanding of the underlying mechanism. Separately studying the light emission from the rising and falling transitions led to the extraction of two spectral components of which all observed emission spectra were composed. Based on their human-perceived color, these components were referred to as red and blue components. Using a quantum mechanical model and subsequent fitting of the emission spectrum, the red component could be assigned to a transition involving vibrational sidebands of a local vibrational mode (LVM) of 220 meV, which most probably originates from a carbon cluster-like defect that participates in donor-acceptor-pair (DAP) recombination. The blue component was similar to the light emission of the forward biased body diode. Although this component rather behaved like a donor-like defect close to the valence band, literature indicated that this component might be caused by DAP recombination as well. Again, a correlation between the transient  $\Delta V_{th}$  and the total light emission was found. Furthermore, the emission spectrum was independent of both the switching frequency and the duty cycle. An analysis of the transition time dependence of the two spectral components revealed similarities to CP experiments and confirmed the postulated mechanisms. Last but not least, it was possible to measure the time evolution of both components over an entire  $V_{GS}$  period revealing a longer decay time of the blue component.

Finally, similarities between GSI and field-effect stimulated light emission were discussed and a plausible relation between the two mechanisms was suggested. Indeed, both effects might be related to the same underlying defects.

## 5.2 Outlook

In particular the findings on the degradation mechanism GSI and the method of field-effect stimulated optical spectroscopy have contributed to significant advancement in the field of reliability physics of SiC MOSFETs. This work could be continued by following the questions and ideas listed below.

- *How does continuous switching during an experiment using time-gated optical spectroscopy affect the outcome of the optical measurement?* The trapping kinetics at  $V_{GS}$ -transitions during

continuous switching might differ from the kinetics occurring at  $V_{GS}$ -transitions in double pulses since during continuous switching, the device cannot return to thermal equilibrium.

- *What can be learned from inducing electron-hole pairs at the interface by laser excitation, either above or below bandgap, e.g. by multiphoton absorption?* GSI and light emission were shown to be caused by defect-assisted electron-hole recombination at the interface. In this work, electrons and holes are supplied by switching the device between inversion and accumulation. However, electron-hole pairs could also be supplied by laser excitation, which would allow to investigate the trapping kinetics at various bias conditions without the necessity to use gate switching. In addition to using direct band-to-band excitation, multiphoton excitation could even allow to obtain spatial resolution by creating electron-hole pairs only in the focal point of the excitation beam. Using a pulsed laser might even allow to temporally study the defect kinetics.
- *Temperature dependence of field-effect stimulated light emission using time-gated spectroscopy.* Although some efforts have been conducted in this direction by using conventional spectroscopy [MFJ9], [MFC9], time-gated spectroscopy might provide deeper insights into the exact trapping kinetics at the interface, because it allows to distinguish between the different spectral components occurring at the rising and falling transitions. Furthermore, it would allow to investigate the competition between the radiative and non-radiative pathways, which might allow to further prove and deepen the understanding presented in the course this work.
- *Correlation between transient  $\Delta V_{th}$ , field-effect stimulated light emission, GSI, and CP experiments in the same technology.* This work provided a good foundation to further drive these topics and evaluate how the presented effects are related in detail. A mechanism that could link both effects was proposed in Section 4.4.8. Several correlations have been presented, but a detailed correlation particularly between light emission and GSI on the same technology is still missing. Different technologies featuring different interfaces for the channel could be compared.

The list of questions and ideas above is certainly not complete. Using optical spectroscopy in conjunction with conventional electrical techniques can provide unprecedented information and possibilities to study the nature of defects at the interface between the semiconductor and the insulator of a MOSFET. Such a methodology is not limited to SiC technology. Provided that a suitable detection is possible, this could in principle be extended to any other technology. The obtained information becomes particularly powerful with respect to comparison with results from theoretical ab-initio calculations based on DFT.

# References

- [1] The Royal Swedish Academy of Sciences, *The Nobel prize in physics 2021*, press release, Oct. 2021.
- [2] P. Arias, N. Bellouin, E. Coppola, R. Jones, G. Krinner, J. Marotzke, V. Naik, M. Palmer, G.-K. Plattner, J. Rogelj, M. Rojas, J. Sillmann, T. Storelvmo, P. Thorne, B. Trewin, K. A. Rao, B. Adhikary, R. Allan, K. Armour, G. Bala, R. Barimalala, S. Berger, J. Canadell, C. Cassou, A. Cherchi, W. Collins, W. Collins, S. Connors, S. Corti, F. Cruz, F. Dentener, C. Dereczynski, A. D. Luca, A. D. Niang, F. Doblus-Reyes, A. Dosio, H. Douville, F. Engelbrecht, V. Eyring, E. Fischer, P. Forster, B. Fox-Kemper, J. Fuglestedt, J. Fyfe, N. Gillett, L. Goldfarb, I. Gorodetskaya, J. Gutierrez, R. Hamdi, E. Hawkins, H. Hewitt, P. Hope, A. Islam, C. Jones, D. Kaufman, R. Kopp, Y. Kosaka, J. Kossin, S. Krakovska, J.-Y. Lee, J. Li, T. Mauritsen, T. Maycock, M. Meinshausen, S.-K. Min, P. Monteiro, T. Ngo-Duc, F. Otto, I. Pinto, A. Pirani, K. Raghavan, R. Ranasinghe, A. Ruane, L. Ruiz, J.-B. Sallée, B. Samset, S. Sathyendranath, S. Seneviratne, A. Sörensson, S. Szopa, I. Takayabu, A.-M. Tréguier, B. van den Hurk, R. Vautard, K. von Schuckmann, S. Zaehle, X. Zhang, and K. Zickfeld, "2021: Technical summary," in *Climate Change 2021: The Physical Science Basis. Contribution of Working Group I to the Sixth Assessment Report of the Intergovernmental Panel on Climate Change*, V. Masson-Delmotte, P. Zhai, A. Pirani, S. Connors, C. Péan, S. Berger, N. Caud, Y. Chen, L. Goldfarb, M. Gomis, M. Huang, K. Leitzell, E. Lonnoy, J. Matthews, T. Maycock, T. Waterfield, O. Yelekçi, R. Yu, and B. Zhou, Eds., United Kingdom and New York, NY, USA: Cambridge University Press, 2021, pp. 33–144. DOI: 10.1017/9781009157896.002.
- [3] F. Creutzig, P. Jochem, O. Y. Edelenbosch, L. Mattauch, D. P. van Vuuren, D. McCollum, and J. Minx, "Transport: A roadblock to climate change mitigation?" *Science*, vol. 350, no. 6263, pp. 911–912, Nov. 2015. DOI: 10.1126/science.aac8033.
- [4] F. Creutzig, P. Agoston, J. C. Goldschmidt, G. Luderer, G. Nemet, and R. C. Pietzcker, "The underestimated potential of solar energy to mitigate climate change," *Nature Energy*, vol. 2, no. 9, Aug. 2017, Art. no. 17140. DOI: 10.1038/nenergy.2017.140.
- [5] R. J. Barthelmie and S. C. Pryor, "Potential contribution of wind energy to climate change mitigation," *Nature Climate Change*, vol. 4, no. 8, pp. 684–688, Jun. 2014. DOI: 10.1038/nclimate2269.
- [6] L. Berga, "The role of hydropower in climate change mitigation and adaptation: A review," *Engineering*, vol. 2, no. 3, pp. 313–318, Sep. 2016. DOI: 10.1016/j.eng.2016.03.004.

- [7] M. Jafari, A. Botterud, and A. Sakti, "Decarbonizing power systems: A critical review of the role of energy storage," *Renewable and Sustainable Energy Reviews*, vol. 158, Apr. 2022, Art. no. 112077. DOI: 10.1016/j.rser.2022.112077.
- [8] V. F. Pires, E. Romero-Cadaval, D. Vinnikov, I. Roasto, and J. Martins, "Power converter interfaces for electrochemical energy storage systems – a review," *Energy Conversion and Management*, vol. 86, pp. 453–475, Oct. 2014. DOI: 10.1016/j.enconman.2014.05.003.
- [9] R. Keyes, "Figure of merit for semiconductors for high-speed switches," *Proceedings of the IEEE*, vol. 60, no. 2, pp. 225–225, 1972. DOI: 10.1109/proc.1972.8593.
- [10] E. O. Johnson, "Physical limitations on frequency and power parameters of transistors," in *IRE International Convention Record*, IEEE, Mar. 1965, pp. 163–177. DOI: 10.1109/IRECON.1965.1147520.
- [11] T. Laska, "A Si IGBT review and outlook in competition to WBG power devices," in *Components of Power Electronics and their Applications 2023; ETG Symposium*, VDE, Jun. 2023.
- [12] K. Shenai, "High-density power conversion and wide-bandgap semiconductor power electronics switching devices," *Proceedings of the IEEE*, vol. 107, no. 12, pp. 2308–2326, Dec. 2019. DOI: 10.1109/jproc.2019.2948554.
- [13] B. Baliga, "Power semiconductor device figure of merit for high-frequency applications," *IEEE Electron Device Letters*, vol. 10, no. 10, pp. 455–457, Oct. 1989. DOI: 10.1109/55.43098.
- [14] F. Li, F. Roccaforte, G. Greco, P. Fiorenza, F. L. Via, A. Pérez-Tomas, J. E. Evans, C. A. Fisher, F. A. Monaghan, P. A. Mawby, and M. Jennings, "Status and prospects of cubic silicon carbide power electronics device technology," *Materials*, vol. 14, no. 19, Oct. 2021, Art. no. 5831. DOI: 10.3390/ma14195831.
- [15] B. Hull, S. Allen, Q. Zhang, D. Gajewski, V. Pala, J. Richmond, S. Ryu, M. O'Loughlin, E. V. Brunt, L. Cheng, A. Burk, J. Casady, D. Grider, and J. Palmour, "Reliability and stability of SiC power MOSFETs and next-generation SiC MOSFETs," in *2014 IEEE Workshop on Wide Bandgap Power Devices and Applications*, IEEE, Oct. 2014, pp. 139–142. DOI: 10.1109/wipda.2014.6964641.
- [16] L. Zhang, X. Yuan, X. Wu, C. Shi, J. Zhang, and Y. Zhang, "Performance evaluation of high-power SiC MOSFET modules in comparison to Si IGBT modules," *IEEE Transactions on Power Electronics*, vol. 34, no. 2, pp. 1181–1196, Feb. 2019. DOI: 10.1109/tpel.2018.2834345.
- [17] E. Acheson, "Carborundum: Its history, manufacture and uses," *Journal of the Franklin Institute*, vol. 136, no. 3, pp. 194–203, Sep. 1893. DOI: 10.1016/0016-0032(93)90311-h.
- [18] R. Szymanowitz, "Edward goodrich acheson," *Journal of Chemical Education*, vol. 33, no. 3, pp. 113–115, Mar. 1956. DOI: 10.1021/ed033p113.
- [19] E. Acheson, "Carborundum: Its history, manufacture and uses," *Journal of the Franklin Institute*, vol. 136, no. 4, pp. 279–289, Oct. 1893. DOI: 10.1016/0016-0032(93)90369-6.

- [20] H. Moissan, "Étude du siliciure de carbone de la météorite de cañon diablo," *Comptes-rendus Académie des Sciences (Paris)*, vol. 140, pp. 405–406, 1905.
- [21] H. C. Bumpus, "RECORD OF MEETINGS OF THE NEW YORK ACADEMY OF SCIENCES. january, 1905, to december, 1905.," *Annals of the New York Academy of Sciences*, vol. 17, no. 1, pp. 563–657, Mar. 1906. DOI: 10.1111/j.1749-6632.1906.tb56908.x.
- [22] N. Zheludev, "The life and times of the LED — a 100-year history," *Nature Photonics*, vol. 1, no. 4, pp. 189–192, Apr. 2007. DOI: 10.1038/nphoton.2007.34.
- [23] H. J. Round, "A note on carborundum," *Electrical World*, vol. XLIX, no. 6, p. 309, 1907. DOI: 10.1142/9789814503464\_0116.
- [24] O. V. Losev, "Luminous carborundum [silicon carbide] detector and detection with crystals," *Telegrafiya i Telefoniya bez Provodov*, vol. 44, pp. 485–494, 1927.
- [25] E. Loebner, "Subhistories of the light emitting diode," *IEEE Transactions on Electron Devices*, vol. 23, no. 7, pp. 675–699, Jul. 1976. DOI: 10.1109/t-ed.1976.18472.
- [26] J. A. Lely, "Sublimation process for manufacturing silicon carbide crystals," U.S. Patent 2 854 364, Sep. 1958.
- [27] T. Kimoto, "Bulk and epitaxial growth of silicon carbide," *Progress in Crystal Growth and Characterization of Materials*, vol. 62, no. 2, pp. 329–351, Jun. 2016. DOI: 10.1016/j.pcrysgrow.2016.04.018.
- [28] Y. Tairov and V. Tsvetkov, "Investigation of growth processes of ingots of silicon carbide single crystals," *Journal of Crystal Growth*, vol. 43, no. 2, pp. 209–212, Mar. 1978. DOI: 10.1016/0022-0248(78)90169-0.
- [29] Y. Tairov and V. Tsvetkov, "General principles of growing large-size single crystals of various silicon carbide polytypes," *Journal of Crystal Growth*, vol. 52, no. 1, pp. 146–150, Apr. 1981. DOI: 10.1016/0022-0248(81)90184-6.
- [30] R. F. Davis, C. H. Carter, and C. E. Hunter, "Sublimation of silicon carbide to produce large, device quality single crystals of silicon carbide," U.S. Patent RE 34 861, Feb. 1995.
- [31] L. F. Wallace, "Silicon carbide unipolar transistor," U.S. Patent 3 254 280, May 1966.
- [32] J. W. Palmour, "Metal-insulator-semiconductor capacitor formed on silicon carbide," U.S. Patent 4 875 083, Oct. 1989.
- [33] J. W. Palmour, "Power MOSFET in silicon carbide," U.S. Patent 5 506 421, Apr. 1996.
- [34] A. O. Adan, D. Tanaka, L. Burgyan, and Y. Kakizaki, "The current status and trends of 1,200-V commercial silicon-carbide MOSFETs: Deep physical analysis of power transistors from a designer's perspective," *IEEE Power Electronics Magazine*, vol. 6, no. 2, pp. 36–47, Jun. 2019. DOI: 10.1109/mpe1.2019.2909592.
- [35] W. Muench, P. Hoeck, and E. Pettenpaul, "Silicon carbide field-effect and bipolar transistors," in *1977 International Electron Devices Meeting, IRE, 1977*, pp. 337–339. DOI: 10.1109/iedm.1977.189248.
- [36] J. A. Edmond, "Blue light emitting diode formed in silicon carbide," U.S. Patent 5 027 168, Jun. 1991.

## REFERENCES

- [37] L. G. Matus, J. A. Powell, and C. S. Salupo, "High-voltage 6H-SiC p-n junction diodes," *Applied Physics Letters*, vol. 59, no. 14, pp. 1770–1772, Sep. 1991. DOI: 10.1063/1.106195.
- [38] T. Kimoto, T. Urushidani, S. Kobayashi, and H. Matsunami, "High-voltage (>1 kV) SiC Schottky barrier diodes with low on-resistances," *IEEE Electron Device Letters*, vol. 14, no. 12, pp. 548–550, Dec. 1993. DOI: 10.1109/55.260785.
- [39] A. Itoh, T. Kimoto, and H. Matsunami, "High performance of high-voltage 4H-SiC Schottky barrier diodes," *IEEE Electron Device Letters*, vol. 16, no. 6, pp. 280–282, Jun. 1995. DOI: 10.1109/55.790735.
- [40] H. Li, S. Dimitrijevic, H. B. Harrison, and D. Sweatman, "Interfacial characteristics of N<sub>2</sub>O and NO nitrided SiO<sub>2</sub> grown on SiC by rapid thermal processing," *Applied Physics Letters*, vol. 70, no. 15, pp. 2028–2030, Apr. 1997. DOI: 10.1063/1.118773.
- [41] G. Chung, C. Tin, J. Williams, K. McDonald, R. Chanana, R. Weller, S. Pantelides, L. Feldman, O. Holland, M. Das, and J. Palmour, "Improved inversion channel mobility for 4H-SiC MOSFETs following high temperature anneals in nitric oxide," *IEEE Electron Device Letters*, vol. 22, no. 4, pp. 176–178, Apr. 2001. DOI: 10.1109/55.915604.
- [42] M. Holz, G. Hultsch, T. Scherg, and R. Rupp, "Reliability considerations for recent Infineon SiC diode releases," *Microelectronics Reliability*, vol. 47, no. 9–11, pp. 1741–1745, Sep. 2007. DOI: 10.1016/j.microrel.2007.07.031.
- [43] R. Callanan, A. Agarwal, A. Burk, M. Das, B. Hull, F. Husna, A. Powell, J. Richmond, S.-H. Ryu, and Q. Zhang, "Recent progress in SiC DMOSFETs and JBS diodes at Cree," in *2008 34th Annual Conference of IEEE Industrial Electronics*, IEEE, Nov. 2008, pp. 2885–2890. DOI: 10.1109/iecon.2008.4758417.
- [44] B. Callanan, "CPWR-AN08 – Application considerations for silicon carbide MOSFETs," Cree, Inc., Tech. Rep., Jan. 2011.
- [45] T. Nakamura, Y. Nakano, M. Aketa, R. Nakamura, S. Mitani, H. Sakairi, and Y. Yokotsuji, "High performance SiC trench devices with ultra-low Ron," in *2011 International Electron Devices Meeting*, IEEE, Dec. 2011, pp. 1–3. DOI: 10.1109/iedm.2011.6131619.
- [46] L. Abbatelli, M. Macaudo, and G. Catalisano, "Fully SiC based high efficiency boost converter," in *2014 IEEE Applied Power Electronics Conference and Exposition - APEC 2014*, IEEE, Mar. 2014, pp. 1835–1837. DOI: 10.1109/apec.2014.6803555.
- [47] L. Abbatelli, M. Macaudo, G. Catalisano, A. Boscarato, and D. Kohout, "Cost benefits on high frequency converter system based on SiC MOSFET approach," in *PCIM Europe 2014*, VDE, May 2014, pp. 1–5.
- [48] M. Treu, R. Rupp, P. Blaschitz, K. Ruschenschmidt, T. Sekinger, P. Friedrichs, R. Elpelt, and D. Peters, "Strategic considerations for unipolar SiC switch options: JFET vs. MOSFET," in *2007 IEEE Industry Applications Annual Meeting*, IEEE, Sep. 2007, pp. 324–330. DOI: 10.1109/07ias.2007.10.
- [49] M. Schulz, L. de Lillo, L. Empringham, and P. Wheeler, "Pushing power density limits using SiC-JFet-based matrix converter," in *PCIM Europe 2011*, May 2011, pp. 464–470.

- [50] D. Heer, D. Domes, and D. Peters, "Switching performance of a 1200 V SiC-Trench-MOSFET in a low-power module," in *PCIM Europe 2016*, VDE, May 2016, pp. 1–7.
- [51] K. Daviau and K. Lee, "High-pressure, high-temperature behavior of silicon carbide: A review," *Crystals*, vol. 8, no. 5, May 2018, Art. no. 217. DOI: 10.3390/cryst8050217.
- [52] C. Kittel, *Introduction to solid state physics*, 8th ed. Wiley, 2005, ISBN: 0-471-41526-X.
- [53] D. Schwarzenbach, "Note on Bravais–Miller indices," *Journal of Applied Crystallography*, vol. 36, no. 5, pp. 1270–1271, Sep. 2003. DOI: 10.1107/s0021889803014778.
- [54] F. Bechstedt, P. Käckell, A. Zywietz, K. Karch, B. Adolph, K. Tenelsen, and J. Furthmüller, "Polytypism and properties of silicon carbide," *physica status solidi (b)*, vol. 202, no. 1, pp. 35–62, Jul. 1997. DOI: 10.1002/1521-3951(199707)202:1<35::aid-pssb35>3.0.co;2-8.
- [55] T. Kimoto and J. A. Cooper, *Fundamentals of Silicon Carbide Technology: Growth, Characterization, Devices and Applications, Growth, Characterization, Devices and Applications*. Wiley-IEEE Press, 2014, ISBN: 978-1-118-31352-7.
- [56] G. Pensl and W. Choyke, "Electrical and optical characterization of SiC," *Physica B: Condensed Matter*, vol. 185, no. 1-4, pp. 264–283, Apr. 1993. DOI: 10.1016/0921-4526(93)90249-6.
- [57] V. Ivády, J. Davidsson, N. T. Son, T. Ohshima, I. A. Abrikosov, and A. Gali, "Identification of Si-vacancy related room-temperature qubits in 4H silicon carbide," *Physical Review B*, vol. 96, no. 16, Oct. 2017, Art. no. 161114. DOI: 10.1103/physrevb.96.161114.
- [58] R. Nagy, M. Niethammer, M. Widmann, Y.-C. Chen, P. Udvarhelyi, C. Bonato, J. U. Hassan, R. Karhu, I. G. Ivanov, N. T. Son, J. R. Maze, T. Ohshima, Ö. O. Soykal, Á. Gali, S.-Y. Lee, F. Kaiser, and J. Wrachtrup, "High-fidelity spin and optical control of single silicon-vacancy centres in silicon carbide," *Nature Communications*, vol. 10, Apr. 2019, Art. no. 1954. DOI: 10.1038/s41467-019-09873-9.
- [59] E. Sörman, N. T. Son, W. M. Chen, O. Kordina, C. Hallin, and E. Janzén, "Silicon vacancy related defect in 4H and 6H SiC," *Physical Review B*, vol. 61, no. 4, pp. 2613–2620, Jan. 2000. DOI: 10.1103/physrevb.61.2613.
- [60] K. Momma and F. Izumi, "VESTA 3 for three-dimensional visualization of crystal, volumetric and morphology data," *Journal of Applied Crystallography*, vol. 44, no. 6, pp. 1272–1276, Oct. 2011. DOI: 10.1107/s0021889811038970.
- [61] A. Bauer, J. Kräußlich, L. Dressler, P. Kuschnerus, J. Wolf, K. Goetz, P. Käckell, J. Furthmüller, and F. Bechstedt, "High-precision determination of atomic positions in crystals: The case of 6H- and 4H-SiC," *Physical Review B*, vol. 57, no. 5, pp. 2647–2650, Feb. 1998. DOI: 10.1103/physrevb.57.2647.
- [62] R. F. Adamsky and K. M. Merz, "Synthesis and crystallography of the wurtzite form of silicon carbide," *Zeitschrift für Kristallographie - Crystalline Materials*, vol. 111, no. 1-6, pp. 350–361, Nov. 1959. DOI: 10.1524/zkri.1959.111.16.350.
- [63] R. Iwanowski, K. Fronc, W. Paszkowicz, and M. Heinonen, "XPS and XRD study of crystalline 3C-SiC grown by sublimation method," *Journal of Alloys and Compounds*, vol. 286, no. 1-2, pp. 143–147, May 1999. DOI: 10.1016/s0925-8388(98)00994-3.

- [64] V. V. Afanas'ev, M. Bassler, G. Pensl, M. J. Schulz, and E. S. von Kamienski, "Band offsets and electronic structure of SiC/SiO<sub>2</sub> interfaces," *Journal of Applied Physics*, vol. 79, no. 6, pp. 3108–3114, Mar. 1996. DOI: 10.1063/1.361254.
- [65] W. Choyke and G. Pensl, "Physical properties of SiC," *MRS Bulletin*, vol. 22, no. 3, pp. 25–29, Mar. 1997. DOI: 10.1557/s0883769400032723.
- [66] W. Taha, "Comparative study on silicon carbide (SiC) polytypes in high voltage devices," in *2021 International Conference on Sustainable Energy and Future Electric Transportation (SEFET)*, IEEE, Jan. 2021, pp. 1–6. DOI: 10.1109/sefet48154.2021.9375815.
- [67] H. M. Hobgood, M. Brady, W. Brixius, G. Fechko, R. Glass, D. Henshall, J. R. Jenny, R. Leonard, D. Malta, S. G. Müller, V. F. Tsvetkov, and C. H. C. Jr., "Status of large diameter SiC crystal growth for electronic and optical applications," *Materials Science Forum*, vol. 338-342, pp. 3–8, May 2000. DOI: 10.4028/www.scientific.net/msf.338-342.3.
- [68] D. Snyder, V. Heydemann, W. Everson, and D. L. Barrett, "Large diameter PVT growth of bulk 6H SiC crystals," *Materials Science Forum*, vol. 338-342, pp. 9–12, May 2000. DOI: 10.4028/www.scientific.net/msf.338-342.9.
- [69] S. Müller, R. Glass, H. Hobgood, V. Tsvetkov, M. Brady, D. Henshall, J. Jenny, D. Malta, and C. Carter, "The status of SiC bulk growth from an industrial point of view," *Journal of Crystal Growth*, vol. 211, no. 1-4, pp. 325–332, Apr. 2000. DOI: 10.1016/s0022-0248(99)00835-0.
- [70] G. Dhanaraj, X. Huang, M. Dudley, V. Prasad, and R.-H. Ma, "6 - Silicon carbide crystals — Part I: Growth and characterization," in *Crystal Growth Technology*, K. Byrappa, T. Ohachi, W. Michaeli, H. Warlimont, and E. Weber, Eds. Elsevier, 2003, pp. 181–232, ISBN: 978-0-8155-1453-4. DOI: 10.1016/b978-081551453-4.50008-7.
- [71] Q.-S. Chen, V. Prasad, H. Zhang, and M. Dudley, "7 - Silicon carbide crystals — Part II: Process physics and modeling," in *Crystal Growth Technology*, K. Byrappa, T. Ohachi, W. Michaeli, H. Warlimont, and E. Weber, Eds. Elsevier, 2003, pp. 233–269, ISBN: 978-0-8155-1453-4. DOI: 10.1016/b978-081551453-4.50009-9.
- [72] R. Glass, D. Henshall, V. Tsvetkov, and J. C.H. Carter, "SiC seeded crystal growth," *physica status solidi (b)*, vol. 202, no. 1, pp. 149–162, Jul. 1997. DOI: 10.1002/1521-3951(199707)202:1<149::aid-pssb149>3.0.co;2-m.
- [73] R. Yakimova and E. Janzén, "Current status and advances in the growth of SiC," *Diamond and Related Materials*, vol. 9, no. 3-6, pp. 432–438, Apr. 2000. DOI: 10.1016/s0925-9635(99)00219-8.
- [74] K. Semmelroth, M. Krieger, G. Pensl, H. Nagasawa, R. Püsche, M. Hundhausen, L. Ley, M. Nerding, and H. P. Strunk, "Growth of 3C-SiC bulk material by the modified Lely method," *Materials Science Forum*, vol. 457-460, pp. 151–156, Jun. 2004. DOI: 10.4028/www.scientific.net/msf.457-460.151.
- [75] W. S. Yoo, S. Nishino, and H. Matsunami, "Polytype change of silicon carbide at high temperatures," in *Amorphous and Crystalline Silicon Carbide II. Springer Proceedings in Physics*, vol. 43, Springer Berlin Heidelberg, 1989, pp. 35–39. DOI: 10.1007/978-3-642-75048-9\_6.



- [76] U. Starke, J. Schardt, J. Bernhardt, M. Franke, and K. Heinz, "Stacking transformation from hexagonal to cubic SiC induced by surface reconstruction: A seed for heterostructure growth," *Physical Review Letters*, vol. 82, no. 10, pp. 2107–2110, Mar. 1999. DOI: 10.1103/physrevlett.82.2107.
- [77] S. Nishino, J. A. Powell, and H. A. Will, "Production of large-area single-crystal wafers of cubic SiC for semiconductor devices," *Applied Physics Letters*, vol. 42, no. 5, pp. 460–462, Mar. 1983. DOI: 10.1063/1.93970.
- [78] P. Neudeck, D. Larkin, J. Starr, J. Powell, C. Salupo, and L. Matus, "Greatly improved 3C-SiC p-n junction diodes grown by chemical vapor deposition," *IEEE Electron Device Letters*, vol. 14, no. 3, pp. 136–139, Mar. 1993. DOI: 10.1109/55.215136.
- [79] H. Matsunami and T. Kimoto, "Step-controlled epitaxial growth of SiC: High quality homoepitaxy," *Materials Science and Engineering: R: Reports*, vol. 20, no. 3, pp. 125–166, Aug. 1997. DOI: 10.1016/s0927-796x(97)00005-3.
- [80] T. Kimoto, H. Nishino, W. S. Yoo, and H. Matsunami, "Growth mechanism of 6H-SiC in step-controlled epitaxy," *Journal of Applied Physics*, vol. 73, no. 2, pp. 726–732, Jan. 1993. DOI: 10.1063/1.353329.
- [81] D. Larkin, "An overview of SiC epitaxial growth," *MRS Bulletin*, vol. 22, no. 3, pp. 36–41, Mar. 1997. DOI: 10.1557/s0883769400032747.
- [82] D. J. Larkin, P. G. Neudeck, J. A. Powell, and L. G. Matus, "Site-competition epitaxy for controlled doping of CVD silicon carbide," in *Proceedings of the 5th International Institute of Physics Conference, No. 137: Silicon Carbide and Related Materials*, 1994, pp. 51–54.
- [83] P. Pirouz and A. Galeckas, "Degradation of SiC bipolar devices: A review of likely causes and recent advances in its understanding," *ECS Transactions*, vol. 41, no. 8, pp. 225–236, Oct. 2011. DOI: 10.1149/1.3631500.
- [84] S. O. Kasap, *Optoelectronics and Photonics Principles and Practices, Principles and Practices*, Second ed. Pearson Education Limited, 2013, p. 544, ISBN: 978-0-273-77417-4.
- [85] C. Persson and U. Lindelfelt, "Relativistic band structure calculation of cubic and hexagonal SiC polytypes," *Journal of Applied Physics*, vol. 82, no. 11, pp. 5496–5508, Dec. 1997. DOI: 10.1063/1.365578.
- [86] J. Serrano, J. Strempler, M. Cardona, M. Schwoerer-Böhning, H. Requardt, M. Lorenzen, B. Stojetz, P. Pavone, and W. J. Choyke, "Lattice dynamics of 4H-SiC by inelastic x-ray scattering," *Materials Science Forum*, vol. 433-436, pp. 257–260, Sep. 2003. DOI: 10.4028/www.scientific.net/msf.433-436.257.
- [87] E. A. Jackson, *Equilibrium Statistical Mechanics*. Dover Publications, 2000, ISBN: 978-0-486-41185-9.
- [88] D. W. Feldman, J. H. Parker, W. J. Choyke, and L. Patrick, "Phonon dispersion curves by Raman scattering in SiC, polytypes 3C, 4H, 6H, 15R, and 21R," *Physical Review*, vol. 173, no. 3, pp. 787–793, Sep. 1968. DOI: 10.1103/physrev.173.787.

- [89] J. Serrano, J. Strempler, M. Cardona, M. Schwoerer-Böhning, H. Requardt, M. Lorenzen, B. Stojetz, P. Pavone, and W. J. Choyke, "Determination of the phonon dispersion of zinc blende (3C) silicon carbide by inelastic x-ray scattering," *Applied Physics Letters*, vol. 80, no. 23, pp. 4360–4362, May 2002. DOI: 10.1063/1.1484241.
- [90] M. D. McCluskey, "Local vibrational modes of impurities in semiconductors," *Journal of Applied Physics*, vol. 87, no. 8, pp. 3593–3617, Apr. 2000. DOI: 10.1063/1.372453.
- [91] T. Egilsson, A. Henry, I. G. Ivanov, J. L. Lindström, and E. Janzén, "Photoluminescence of electron-irradiated 4H-SiC," *Physical Review B*, vol. 59, no. 12, pp. 8008–8014, Mar. 1999. DOI: 10.1103/physrevb.59.8008.
- [92] J. Steeds, G. Evans, L. Danks, S. Furkert, W. Voegeli, M. Ismail, and F. Carosella, "Transmission electron microscope radiation damage of 4H and 6H SiC studied by photoluminescence spectroscopy," *Diamond and Related Materials*, vol. 11, no. 12, pp. 1923–1945, Dec. 2002. DOI: 10.1016/s0925-9635(02)00212-1.
- [93] G. A. Evans, J. W. Steeds, L. Ley, M. Hundhausen, N. Schulze, and G. Pensl, "Identification of carbon interstitials in electron-irradiated 6H-SiC by use of a  $^{13}\text{C}$  enriched specimen," *Physical Review B*, vol. 66, no. 3, Jul. 2002, Art. no. 035204. DOI: 10.1103/physrevb.66.035204.
- [94] J. W. Steeds, G. Evans, S. Furkert, L. Ley, M. Hundhausen, N. Schulze, and G. Pensl, "Identification of dumb-bell shaped interstitials in electron irradiated 6H SiC by photoluminescence spectroscopy," *Materials Science Forum*, vol. 433-436, pp. 305–308, Sep. 2003. DOI: 10.4028/www.scientific.net/msf.433-436.305.
- [95] A. Mattausch, M. Bockstedte, O. Pankratov, J. W. Steeds, S. Furkert, J. Hayes, W. Sullivan, and N. G. Wright, "High energy local vibrational modes of carbon aggregates in SiC: Experimental and theoretical insight," *Materials Science Forum*, vol. 527-529, pp. 465–468, Oct. 2006. DOI: 10.4028/www.scientific.net/msf.527-529.465.
- [96] J. W. Steeds and W. Sullivan, "Identification of antisite carbon split-interstitial defects in 4H-SiC," *Physical Review B*, vol. 77, no. 19, May 2008, Art. no. 195204. DOI: 10.1103/physrevb.77.195204.
- [97] F. Yan, R. P. Devaty, W. J. Choyke, A. Gali, T. Kimoto, T. Ohshima, and G. Pensl, "Anharmonic vibrations of the dicarbon antisite defect in 4H-SiC," *Applied Physics Letters*, vol. 100, no. 13, Mar. 2012, Art. no. 132107. DOI: 10.1063/1.3699269.
- [98] A. Mattausch, M. Bockstedte, and O. Pankratov, "Interstitials in SiC: A model for the  $\text{D}_{\text{II}}$  center," *Physica B: Condensed Matter*, vol. 308-310, pp. 656–659, Dec. 2001. DOI: 10.1016/s0921-4526(01)00782-7.
- [99] A. Gali, P. Deák, P. Ordejón, N. T. Son, E. Janzén, and W. J. Choyke, "Aggregation of carbon interstitials in silicon carbide: A theoretical study," *Physical Review B*, vol. 68, no. 12, Sep. 2003, Art. no. 125201. DOI: 10.1103/physrevb.68.125201.
- [100] P. Li, P. Udvarhelyi, S. Li, B. Huang, and A. Gali, "Carbon cluster emitters in silicon carbide," *Physical Review B*, vol. 108, no. 8, Aug. 2023, Art. no. 085201. DOI: 10.1103/PhysRevB.108.085201.
- [101] A. Mattausch, M. Bockstedte, and O. Pankratov, "Structure and vibrational spectra of carbon clusters in SiC," *Physical Review B*, vol. 70, no. 23, Dec. 2004, Art. no. 235211. DOI: 10.1103/physrevb.70.235211.

- [102] M. Bockstedte, A. Mattausch, and O. Pankratov, "Ab initio study of the annealing of vacancies and interstitials in cubic SiC: Vacancy-interstitial recombination and aggregation of carbon interstitials," *Physical Review B*, vol. 69, no. 23, p. 235 202, Jun. 2004. DOI: 10.1103/physrevb.69.235202.
- [103] O. Ibrahim, N. Z. Yahaya, N. Saad, and K. Y. Ahmed, "Development of observer state output feedback for phase-shifted full bridge DC-DC converter control," *IEEE Access*, vol. 5, pp. 18 143–18 154, 2017. DOI: 10.1109/access.2017.2745417.
- [104] X. She, A. Q. Huang, O. Lucia, and B. Ozpineci, "Review of silicon carbide power devices and their applications," *IEEE Transactions on Industrial Electronics*, vol. 64, no. 10, pp. 8193–8205, Oct. 2017. DOI: 10.1109/tie.2017.2652401.
- [105] F. Jung, S. d. A. Pinheiro, C. T. Paz, M. Fiorin, and T. Dequigiovani, "DC-DC converter for photovoltaic systems," in *2016 12th IEEE International Conference on Industry Applications (INDUSCON)*, IEEE, Nov. 2016, pp. 1–8. DOI: 10.1109/INDUSCON.2016.7874524.
- [106] M. G. H. Aghdam and T. Thiringer, "Comparison of SiC and Si power semiconductor devices to be used in 2.5 kW DC/DC converter," in *2009 International Conference on Power Electronics and Drive Systems (PEDS)*, IEEE, Nov. 2009, pp. 1035–1040. DOI: 10.1109/peds.2009.5385745.
- [107] M. Grieb, M. Noborio, D. Peters, A. J. Bauer, P. Friedrichs, T. Kimoto, and H. Ryssel, "Comparison of the threshold-voltage stability of SiC MOSFETs with thermally grown and deposited gate oxides," *Materials Science Forum*, vol. 645–648, pp. 681–684, Apr. 2010. DOI: 10.4028/www.scientific.net/msf.645-648.681.
- [108] R. Siemieniec, D. Peters, R. Esteve, W. Bergner, D. Kuck, T. Aichinger, T. Basler, and B. Zippelius, "A SiC trench MOSFET concept offering improved channel mobility and high reliability," in *2017 19th European Conference on Power Electronics and Applications (EPE'17 ECCE Europe)*, IEEE, Sep. 2017, pp. 1–13. DOI: 10.23919/epe17ecceurope.2017.8098928.
- [109] H. Yano, H. Nakao, T. Hatayama, Y. Uraoka, and T. Fuyuki, "Increased channel mobility in 4H-SiC UMOSFETs using on-axis substrates," *Materials Science Forum*, vol. 556–557, pp. 807–810, Sep. 2007. DOI: 10.4028/www.scientific.net/msf.556-557.807.
- [110] Y. Nanen, M. Kato, J. Suda, and T. Kimoto, "Effects of nitridation on 4H-SiC MOSFETs fabricated on various crystal faces," *IEEE Transactions on Electron Devices*, vol. 60, no. 3, pp. 1260–1262, Mar. 2013. DOI: 10.1109/ted.2012.2236333.
- [111] R. H. Fowler and L. Nordheim, "Electron emission in intense electric fields," *Proceedings of the Royal Society A*, vol. 119, no. 781, pp. 173–181, May 1928. DOI: 10.1098/rspa.1928.0091.
- [112] R. K. Chanana, K. McDonald, M. Di Ventra, S. T. Pantelides, L. C. Feldman, G. Y. Chung, C. C. Tin, J. R. Williams, and R. A. Weller, "Fowler–Nordheim hole tunneling in p-SiC/SiO<sub>2</sub> structures," *Applied Physics Letters*, vol. 77, no. 16, pp. 2560–2562, Oct. 2000. DOI: 10.1063/1.1318229.

- [113] D. Peters, R. Siemieniec, T. Aichinger, T. Basler, R. Esteve, W. Bergner, and D. Kueck, "Performance and ruggedness of 1200V SiC — trench — MOSFET," in *2017 29th International Symposium on Power Semiconductor Devices and IC's (ISPSD)*, IEEE, May 2017, pp. 239–242. DOI: 10.23919/ispsd.2017.7988904.
- [114] S. Sabri, E. V. Brunt, A. Barkley, B. Hull, M. O'Loughlin, A. Burk, S. Allen, and J. Palmour, "New generation 6.5 kV SiC power MOSFET," in *2017 IEEE 5th Workshop on Wide Bandgap Power Devices and Applications (WiPDA)*, IEEE, Oct. 2017, pp. 246–250. DOI: 10.1109/wipda.2017.8170555.
- [115] M. Saggio, A. Guarnera, E. Zanetti, S. Rascunà, A. Frazzetto, D. Salinas, F. Giannazzo, P. Fiorenza, and F. Roccaforte, "Industrial approach for next generation of power devices based on 4H-SiC," *Materials Science Forum*, vol. 821-823, pp. 660–666, Jun. 2015. DOI: 10.4028/www.scientific.net/msf.821-823.660.
- [116] K. Breifelder and D. Messina, Eds., *IEEE 100 The Authoritative Dictionary of IEEE Standards Terms, The authoritative dictionary of IEEE standards terms*, Seventh ed. New York: Standards Information Network, IEEE Press, 2000, ISBN: 0-7381-2601-2.
- [117] T. Aichinger and M. Schmidt, "Gate-oxide reliability and failure-rate reduction of industrial SiC MOSFETs," in *2020 IEEE International Reliability Physics Symposium (IRPS)*, IEEE, Apr. 2020, pp. 1–6. DOI: 10.1109/irps45951.2020.9128223.
- [118] K. P. Cheung, "SiC power MOSFET gate oxide breakdown reliability — current status," in *2018 IEEE International Reliability Physics Symposium (IRPS)*, IEEE, Mar. 2018, pp. 1–5. DOI: 10.1109/IRPS.2018.8353545.
- [119] R. Singh and A. R. Hefner, "Reliability of SiC MOS devices," *Solid-State Electronics*, vol. 48, no. 10–11, pp. 1717–1720, Oct. 2004. DOI: 10.1016/j.sse.2004.05.005.
- [120] B. Schlund, C. Messick, J. Suehle, and P. Chaparala, "A new physics-based model for time-dependent-dielectric-breakdown," in *IEEE 1995 International Integrated Reliability Workshop. Final Report*, IEEE, Oct. 1995, pp. 72–80. DOI: 10.1109/IRWS.1995.493579.
- [121] Z. Chbili, A. Matsuda, J. Chbili, J. T. Ryan, J. P. Campbell, M. Lahbabi, D. E. Ioannou, and K. P. Cheung, "Modeling early breakdown failures of gate oxide in SiC power MOSFETs," *IEEE Transactions on Electron Devices*, vol. 63, no. 9, pp. 3605–3613, Sep. 2016. DOI: 10.1109/TED.2016.2586483.
- [122] E. Van Brunt, D. J. Lichtenwalner, R. Leonard, A. Burk, S. Sabri, B. Hull, S. Allen, and J. W. Palmour, "Reliability assessment of a large population of 3.3 kV, 45 A 4H-SiC MOSFETs," in *2017 29th International Symposium on Power Semiconductor Devices and IC's (ISPSD)*, IEEE, May 2017, pp. 251–254. DOI: 10.23919/ISPSD.2017.7988907.
- [123] Z. Chbili, K. P. Cheung, J. P. Campbell, J. Chbili, M. Lahbabi, D. E. Ioannou, and K. Matocha, "Time dependent dielectric breakdown in high quality SiC MOS capacitors," *Materials Science Forum*, vol. 858, pp. 615–618, May 2016. DOI: 10.4028/www.scientific.net/MSF.858.615.
- [124] M. Gurfinkel, J. C. Horst, J. S. Suehle, J. B. Bernstein, Y. Shapira, K. S. Matocha, G. Dunne, and R. A. Beaupre, "Time-dependent dielectric breakdown of 4H-SiC/SiO<sub>2</sub> MOS capacitors," *IEEE Transactions on Device and Materials Reliability*, vol. 8, no. 4, pp. 635–641, Dec. 2008. DOI: 10.1109/TDMR.2008.2001182.

- [125] M. Beier-Möbius and J. Lutz, "Breakdown of gate oxide of 1.2 kV SiC-MOSFETs under high temperature and high gate voltage," in *PCIM Europe 2016; International Exhibition and Conference for Power Electronics, Intelligent Motion, Renewable Energy and Energy Management*, VDE, 2016, pp. 1–8.
- [126] J. Lee, C. Ih-Chin, and H. Chenming, "Modeling and characterization of gate oxide reliability," *IEEE Transactions on Electron Devices*, vol. 35, no. 12, pp. 2268–2278, 1988. DOI: 10.1109/16.8802.
- [127] M. Skowronski and S. Ha, "Degradation of hexagonal silicon-carbide-based bipolar devices," *Journal of Applied Physics*, vol. 99, no. 1, Jan. 2006, Art. no. 011101. DOI: 10.1063/1.2159578.
- [128] A. O. Konstantinov and H. Bleichner, "Bright-line defect formation in silicon carbide injection diodes," *Applied Physics Letters*, vol. 71, no. 25, pp. 3700–3702, Dec. 1997. DOI: 10.1063/1.120486.
- [129] P. Bergman, H. Lendenmann, P. Å. Nilsson, U. Lindefelt, and P. Skytt, "Crystal defects as source of anomalous forward voltage increase of 4H-SiC diodes," *Materials Science Forum*, vol. 353–356, pp. 299–302, Jan. 2001. DOI: 10.4028/www.scientific.net/MSF.353-356.299.
- [130] H. Lendenmann, F. Dahlquist, N. Johansson, R. Söderholm, P. Å. Nilsson, P. Bergman, and P. Skytt, "Long term operation of 4.5kV PiN and 2.5kV JBS diodes," *Materials Science Forum*, vol. 353–356, pp. 727–730, Jan. 2001. DOI: 10.4028/www.scientific.net/MSF.353-356.727.
- [131] H. Lendenmann, F. Dahlquist, P. Bergman, H. Bleichner, and C. Hallin, "High-power SiC diodes: Characteristics, reliability and relation to material defects," *Materials Science Forum*, vol. 389–393, pp. 1259–1264, Apr. 2002. DOI: 10.4028/www.scientific.net/MSF.389-393.1259.
- [132] A. Agarwal, H. Fatima, S. Haney, and S.-H. Ryu, "A new degradation mechanism in high-voltage SiC power MOSFETs," *IEEE Electron Device Letters*, vol. 28, no. 7, pp. 587–589, Jul. 2007. DOI: 10.1109/LED.2007.897861.
- [133] A. Galeckas, J. Linnros, and P. Pirouz, "Recombination-enhanced extension of stacking faults in 4H-SiC p-i-n diodes under forward bias," *Applied Physics Letters*, vol. 81, no. 5, pp. 883–885, Jul. 2002. DOI: 10.1063/1.1496498.
- [134] K. Maeda and S. Takeuchi, "Chapter 54 Enhancement of dislocation mobility in semiconducting crystals by electronic excitation," in *Dislocations in Solids*, F. Nabarro and M. Duesbery, Eds. Elsevier, 1996, vol. 10, pp. 443–504, ISBN: 978-0-444-82370-0. DOI: 10.1016/S1572-4859(96)80009-X.
- [135] J. J. Sumakeris, P. Bergman, M. K. Das, C. Hallin, B. A. Hull, E. Janzén, H. Lendenmann, M. J. O'Loughlin, M. J. Paisley, S. Y. Ha, M. Skowronski, J. W. Palmour, and C. H. Carter Jr., "Techniques for minimizing the basal plane dislocation density in SiC epilayers to reduce  $V_f$  drift in SiC bipolar power devices," *Materials Science Forum*, vol. 527–529, pp. 141–146, Oct. 2006. DOI: 10.4028/www.scientific.net/MSF.527-529.141.

- [136] Y. Miura and Y. Matukura, "Investigation of silicon-silicon dioxide interface using MOS structure," *Japanese Journal of Applied Physics*, vol. 5, no. 2, Feb. 1966, Art. no. 180. DOI: 10.1143/JJAP.5.180.
- [137] K. O. Jeppson and C. M. Svensson, "Negative bias stress of MOS devices at high electric fields and degradation of MNOS devices," *Journal of Applied Physics*, vol. 48, no. 5, pp. 2004–2014, May 1977. DOI: 10.1063/1.323909.
- [138] J. H. Stathis, S. Mahapatra, and T. Grasser, "Controversial issues in negative bias temperature instability," *Microelectronics Reliability*, vol. 81, pp. 244–251, Feb. 2018. DOI: 10.1016/j.microrel.2017.12.035.
- [139] T. Grasser, B. Kaczer, W. Goes, H. Reisinger, T. Aichinger, P. Hehenberger, P.-J. Wagner, F. Schanovsky, J. Franco, M. T. Luque, and M. Nelhiebel, "The paradigm shift in understanding the bias temperature instability: From reaction–diffusion to switching oxide traps," *IEEE Transactions on Electron Devices*, vol. 58, no. 11, pp. 3652–3666, Nov. 2011. DOI: 10.1109/ted.2011.2164543.
- [140] T. Grasser, "Stochastic charge trapping in oxides: From random telegraph noise to bias temperature instabilities," *Microelectronics Reliability*, vol. 52, no. 1, pp. 39–70, Jan. 2012. DOI: 10.1016/j.microrel.2011.09.002.
- [141] B. Kaczer, T. Grasser, J. Martin-Martinez, E. Simoen, M. Aoulaiche, P. J. Roussel, and G. Groeseneken, "NBTI from the perspective of defect states with widely distributed time scales," in *2009 IEEE International Reliability Physics Symposium (IRPS)*, IEEE, Apr. 2009, pp. 55–60. DOI: 10.1109/irps.2009.5173224.
- [142] T. Grasser, B. Kaczer, W. Goes, T. Aichinger, P. Hehenberger, and M. Nelhiebel, "A two-stage model for negative bias temperature instability," in *2009 IEEE International Reliability Physics Symposium (IRPS)*, IEEE, Apr. 2009, pp. 33–44. DOI: 10.1109/irps.2009.5173221.
- [143] W. Goes, Y. Wimmer, A.-M. El-Sayed, G. Rzepa, M. Jech, A. Shluger, and T. Grasser, "Identification of oxide defects in semiconductor devices: A systematic approach linking DFT to rate equations and experimental evidence," *Microelectronics Reliability*, vol. 87, pp. 286–320, Aug. 2018. DOI: 10.1016/j.microrel.2017.12.021.
- [144] H. Reisinger, T. Grasser, W. Gustin, and C. Schlunder, "The statistical analysis of individual defects constituting NBTI and its implications for modeling DC- and AC-stress," in *2010 IEEE International Reliability Physics Symposium (IRPS)*, IEEE, May 2010, pp. 7–15. DOI: 10.1109/irps.2010.5488858.
- [145] K. Zhao, J. H. Stathis, B. P. Linder, E. Cartier, and A. Kerber, "PBTI under dynamic stress: From a single defect point of view," in *2011 International Reliability Physics Symposium (IRPS)*, IEEE, Apr. 2011, pp. 1–9. DOI: 10.1109/IRPS.2011.5784502.
- [146] H. Reisinger, T. Grasser, K. Ermisch, H. Nielen, W. Gustin, and C. Schlunder, "Understanding and modeling AC BTI," in *2011 International Reliability Physics Symposium (IRPS)*, IEEE, Apr. 2011, pp. 1–8. DOI: 10.1109/irps.2011.5784542.
- [147] T. Grasser, P.-J. Wagner, H. Reisinger, T. Aichinger, G. Pobegen, M. Nelhiebel, and B. Kaczer, "Analytic modeling of the bias temperature instability using capture/emission time maps," in *2011 International Electron Devices Meeting (IEDM)*, IEEE, Dec. 2011, pp. 1–4. DOI: 10.1109/iedm.2011.6131624.

- [148] G. Rzepa, J. Franco, B. O'Sullivan, A. Subirats, M. Simicic, G. Hellings, P. Weckx, M. Jech, T. Knobloch, M. Waltl, P. Roussel, D. Linten, B. Kaczer, and T. Grasser, "Comphy — a compact-physics framework for unified modeling of BTI," *Microelectronics Reliability*, vol. 85, pp. 49–65, Jun. 2018. DOI: 10.1016/j.microrel.2018.04.002.
- [149] K. Puschkarsky, T. Grasser, T. Aichinger, W. Gustin, and H. Reisinger, "Review on SiC MOSFETs high-voltage device reliability focusing on threshold voltage instability," *IEEE Transactions on Electron Devices*, vol. 66, no. 11, pp. 4604–4616, Nov. 2019. DOI: 10.1109/ted.2019.2938262.
- [150] M. Bassler, V. Afanas'ev, G. Pensl, and M. Schulz, "Degradation of 6H SiC MOS capacitors operated at high temperatures," *Microelectronic Engineering*, vol. 48, no. 1–4, pp. 257–260, Sep. 1999. DOI: 10.1016/S0167-9317(99)00382-2.
- [151] M. J. Marinella, D. K. Schroder, T. Isaacs-Smith, A. C. Ahyi, J. R. Williams, G. Y. Chung, J. W. Wan, and M. J. Loboda, "Evidence of negative bias temperature instability in 4H-SiC metal oxide semiconductor capacitors," *Applied Physics Letters*, vol. 90, no. 25, Jun. 2007, Art. no. 253508. DOI: 10.1063/1.2748327.
- [152] J. Berens, M. Weger, G. Pobegen, T. Aichinger, G. Rescher, C. Schleich, and T. Grasser, "Similarities and differences of BTI in SiC and Si power MOSFETs," in *2020 IEEE International Reliability Physics Symposium (IRPS)*, IEEE, Apr. 2020, pp. 1–7. DOI: 10.1109/irps45951.2020.9129259.
- [153] G. Pobegen and T. Grasser, "Efficient characterization of threshold voltage instabilities in SiC nMOSFETs using the concept of capture-emission-time maps," *Materials Science Forum*, vol. 740-742, pp. 757–760, Jan. 2013. DOI: 10.4028/www.scientific.net/msf.740-742.757.
- [154] K. Puschkarsky, H. Reisinger, T. Aichinger, W. Gustin, and T. Grasser, "Threshold voltage hysteresis in SiC MOSFETs and its impact on circuit operation," in *2017 IEEE International Integrated Reliability Workshop (IIRW)*, IEEE, Oct. 2017, pp. 1–5. DOI: 10.1109/iirw.2017.8361232.
- [155] K. Puschkarsky, H. Reisinger, T. Aichinger, W. Gustin, and T. Grasser, "Understanding BTI in SiC MOSFETs and its impact on circuit operation," *IEEE Transactions on Device and Materials Reliability*, vol. 18, no. 2, pp. 144–153, Jun. 2018. DOI: 10.1109/tdmr.2018.2813063.
- [156] C. Schleich, J. Berens, G. Rzepa, G. Pobegen, G. Rescher, S. Tyaginov, T. Grasser, and M. Waltl, "Physical modeling of bias temperature instabilities in SiC MOSFETs," in *2019 IEEE International Electron Devices Meeting (IEDM)*, IEEE, Dec. 2019, pp. 1–4. DOI: 10.1109/iedm19573.2019.8993446.
- [157] G. Rescher, G. Pobegen, T. Aichinger, and T. Grasser, "On the subthreshold drain current sweep hysteresis of 4H-SiC nMOSFETs," in *2016 IEEE International Electron Devices Meeting (IEDM)*, IEEE, Dec. 2016, pp. 1–4. DOI: 10.1109/iedm.2016.7838392.
- [158] S. T. Pantelides, S. Wang, A. Franceschetti, R. Buczko, M. Di Ventra, S. N. Rashkeev, L. Tsetseris, M. Evans, I. Batyrev, L. C. Feldman, S. Dhar, K. McDonald, R. A. Weller, R. Schrimpf, D. Fleetwood, X. Zhou, J. R. Williams, C. C. Tin, G. Chung, T. Isaacs-Smith, S. Wang, S. Pennycook, G. Duscher, K. Van Benthem, and L. Porter, "Si/SiO<sub>2</sub> and SiC/SiO<sub>2</sub> interfaces for MOSFETs – Challenges and advances," *Materials Science*

- Forum*, vol. 527–529, pp. 935–948, Oct. 2006. DOI: 10.4028/www.scientific.net/MSF.527–529.935.
- [159] A. Vasilev, M. Jech, A. Grill, G. Rzepa, C. Schleich, S. Tyaginov, A. Makarov, G. Pobegen, T. Grasser, and M. Waltl, “TCAD modeling of temperature activation of the hysteresis characteristics of lateral 4H-SiC MOSFETs,” *IEEE Transactions on Electron Devices*, vol. 69, no. 6, pp. 3290–3295, Jun. 2022. DOI: 10.1109/ted.2022.3166123.
- [160] W. Shockley and W. T. Read, “Statistics of the recombinations of holes and electrons,” *Physical Review*, vol. 87, no. 5, pp. 835–842, Sep. 1952. DOI: 10.1103/physrev.87.835.
- [161] R. N. Hall, “Electron-hole recombination in germanium,” *Physical Review*, vol. 87, no. 2, pp. 387–387, Jul. 1952. DOI: 10.1103/PhysRev.87.387.
- [162] C.-t. Sah, R. Noyce, and W. Shockley, “Carrier generation and recombination in p-n junctions and p-n junction characteristics,” in *Proceedings of the IRE*, vol. 45, IEEE, Sep. 1957, pp. 1228–1243. DOI: 10.1109/JRPROC.1957.278528.
- [163] F. Heiman and G. Warfield, “The effects of oxide traps on the MOS capacitance,” *IEEE Transactions on Electron Devices*, vol. 12, no. 4, pp. 167–178, Apr. 1965. DOI: 10.1109/T-ED.1965.15475.
- [164] T. Tewksbury and H.-S. Lee, “Characterization, modeling, and minimization of transient threshold voltage shifts in MOSFETs,” *IEEE Journal of Solid-State Circuits*, vol. 29, no. 3, pp. 239–252, Mar. 1994. DOI: 10.1109/4.278345.
- [165] F. B. McLean, “A direct tunneling model of charge transfer at the insulator-semiconductor interface in MIS devices,” *US Gov. Rep. HDL-TR-1765*, Oct. 1976.
- [166] A. Lelis, D. Habersat, R. Green, and N. Goldsman, “SiC MOSFET oxide-trap two-way tunneling model,” in *2011 International Semiconductor Device Research Symposium (ISDRS)*, IEEE, Dec. 2011, pp. 1–2. DOI: 10.1109/ISDRS.2011.6135139.
- [167] A. J. Lelis, D. B. Habersat, R. Green, and N. Goldsman, “Two-way tunneling model of oxide trap charging and discharging in SiC MOSFETs,” *Materials Science Forum*, vol. 717–720, pp. 465–468, May 2012. DOI: 10.4028/www.scientific.net/MSF.717–720.465.
- [168] J. Campbell, J. Qin, K. Cheung, L. Yu, J. Suehle, A. Oates, and K. Sheng, “Random telegraph noise in highly scaled nMOSFETs,” in *2009 IEEE International Reliability Physics Symposium (IRPS)*, IEEE, 2009, pp. 382–388. DOI: 10.1109/IRPS.2009.5173283.
- [169] T. Grasser, B. Kaczer, W. Goes, H. Reisinger, T. Aichinger, P. Hehenberger, P.-J. Wagner, F. Schanovsky, J. Franco, P. Roussel, and M. Nelhiebel, “Recent advances in understanding the bias temperature instability,” in *2010 International Electron Devices Meeting (IEDM)*, IEEE, Dec. 2010, pp. 1–4. DOI: 10.1109/IEDM.2010.5703295.
- [170] B. Ruch, M. Jech, G. Pobegen, and T. Grasser, “Applicability of Shockley-Read-Hall theory for interface states,” *IEEE Transactions on Electron Devices*, vol. 68, no. 4, pp. 2092–2097, Apr. 2021. DOI: 10.1109/TED.2021.3049760.
- [171] C. H. Henry and D. V. Lang, “Nonradiative capture and recombination by multi-phonon emission in GaAs and GaP,” *Physical Review B*, vol. 15, no. 2, pp. 989–1016, Jan. 1977. DOI: 10.1103/PhysRevB.15.989.



- [172] J. Bourgoin and M. Lannoo, *Point Defects in Semiconductors II: Experimental Aspects*. Springer Berlin Heidelberg, 1983, ISBN: 978-3-642-81832-5. DOI: 10.1007/978-3-642-81832-5.
- [173] A. M. Stoneham, "Non-radiative transitions in semiconductors," *Reports on Progress in Physics*, vol. 44, no. 12, pp. 1251–1295, Dec. 1981. DOI: 10.1088/0034-4885/44/12/001.
- [174] K. Müller, "Reaction paths on multidimensional energy hypersurfaces," *Angewandte Chemie International Edition in English*, vol. 19, no. 1, pp. 1–13, Jan. 1980. DOI: 10.1002/anie.198000013.
- [175] P. F. Barbara, T. J. Meyer, and M. A. Ratner, "Contemporary issues in electron transfer research," *The Journal of Physical Chemistry*, vol. 100, no. 31, pp. 13 148–13 168, Jan. 1996. DOI: 10.1021/jp9605663.
- [176] R. A. Marcus, "On the theory of oxidation-reduction reactions involving electron transfer. I," *The Journal of Chemical Physics*, vol. 24, no. 5, pp. 966–978, May 1956. DOI: 10.1063/1.1742723.
- [177] The Royal Swedish Academy of Sciences, *The Nobel prize in physics 1992*, press release, Oct. 1992.
- [178] M. Kirton and M. Uren, "Noise in solid-state microstructures: A new perspective on individual defects, interface states and low-frequency ( $1/f$ ) noise," *Advances in Physics*, vol. 38, no. 4, pp. 367–468, Jan. 1989. DOI: 10.1080/00018738900101122.
- [179] C. Schleich, D. Waldhor, T. Knobloch, W. Zhou, B. Stampfer, J. Michl, M. Waltl, and T. Grasser, "Single- versus multi-step trap assisted tunneling currents — Part I: Theory," *IEEE Transactions on Electron Devices*, vol. 69, no. 8, pp. 4479–4485, Aug. 2022. DOI: 10.1109/TED.2022.3185966.
- [180] W. Heitler and F. London, "Wechselwirkung neutraler Atome und homöopolare Bindung nach der Quantenmechanik," *Zeitschrift für Physik*, vol. 44, no. 6–7, pp. 455–472, Jun. 1927. DOI: 10.1007/BF01397394.
- [181] M. Born and R. Oppenheimer, "Zur Quantentheorie der Molekeln," *Annalen der Physik*, vol. 389, no. 20, pp. 457–484, Jan. 1927. DOI: 10.1002/andp.19273892002.
- [182] K. Fukui, "Formulation of the reaction coordinate," *The Journal of Physical Chemistry*, vol. 74, no. 23, pp. 4161–4163, Nov. 1970. DOI: 10.1021/j100717a029.
- [183] M. D. Newton, "Quantum chemical probes of electron-transfer kinetics: The nature of donor-acceptor interactions," *Chemical Reviews*, vol. 91, no. 5, pp. 767–792, Jul. 1991. DOI: 10.1021/cr00005a007.
- [184] F. Schanovsky, W. Gös, and T. Grasser, "Multiphonon hole trapping from first principles," *Journal of Vacuum Science & Technology B, Nanotechnology and Microelectronics: Materials, Processing, Measurement, and Phenomena*, vol. 29, no. 1, Jan. 2011, Art. no. 01A201. DOI: 10.1116/1.3533269.
- [185] D. T. Gillespie, *Markov Processes – An Introduction for Physical Scientists*. Elsevier, 1992, ISBN: 978-0-122-83955-9. DOI: 10.1016/c2009-0-22215-x.
- [186] O. C. Ibe, *Markov processes for stochastic modeling*, 2nd ed. London: Elsevier, 2013, 11 pp., ISBN: 978-0-12-407795-9.

- [187] J. D. Weeks, J. C. Tully, and L. C. Kimerling, "Theory of recombination-enhanced defect reactions in semiconductors," *Physical Review B*, vol. 12, no. 8, pp. 3286–3292, Oct. 1975. DOI: 10.1103/physrevb.12.3286.
- [188] L. Kimerling, "Recombination enhanced defect reactions," *Solid-State Electronics*, vol. 21, no. 11-12, pp. 1391–1401, Nov. 1978. DOI: 10.1016/0038-1101(78)90215-0.
- [189] D. V. Lang, "Recombination-enhanced reactions in semiconductors," *Annual Review of Materials Science*, vol. 12, no. 1, pp. 377–398, Aug. 1982. DOI: 10.1146/annurev.ms.12.080182.002113.
- [190] H. Sumi, "Dynamic defect reactions induced by multiphonon nonradiative recombination of injected carriers at deep levels in semiconductors," *Physical Review B*, vol. 29, no. 8, pp. 4616–4630, Apr. 1984. DOI: 10.1103/physrevb.29.4616.
- [191] H. Sumi, "Phonon-kick mechanism for defect reactions enhanced by electronic excitation," *Journal of Physics C: Solid State Physics*, vol. 17, no. 34, pp. 6071–6086, Dec. 1984. DOI: 10.1088/0022-3719/17/34/009.
- [192] D. V. Lang and L. C. Kimerling, "Observation of recombination-enhanced defect reactions in semiconductors," *Physical Review Letters*, vol. 33, no. 8, pp. 489–492, Aug. 1974. DOI: 10.1103/PhysRevLett.33.489.
- [193] O. K. Rice and H. C. Ramsperger, "Theories of unimolecular gas reactions at low pressures," *Journal of the American Chemical Society*, vol. 49, no. 7, pp. 1617–1629, Jul. 1927. DOI: 10.1021/ja01406a001.
- [194] O. K. Rice and H. C. Ramsperger, "Theories of unimolecular gas reactions at low pressures. II," *Journal of the American Chemical Society*, vol. 50, no. 3, pp. 617–620, Mar. 1928. DOI: 10.1021/ja01390a002.
- [195] J. Franck and E. G. Dymond, "Elementary processes of photochemical reactions," *Transactions of the Faraday Society*, vol. 21, pp. 536–542, 1926. DOI: 10.1039/TF9262100536.
- [196] E. Condon, "A theory of intensity distribution in band systems," *Physical Review*, vol. 28, no. 6, pp. 1182–1201, Dec. 1926. DOI: 10.1103/PhysRev.28.1182.
- [197] E. U. Condon, "Nuclear motions associated with electron transitions in diatomic molecules," *Physical Review*, vol. 32, no. 6, pp. 858–872, Dec. 1928. DOI: 10.1103/PhysRev.32.858.
- [198] P. A. M. Dirac, "The quantum theory of the emission and absorption of radiation," *Proceedings of the Royal Society A*, vol. 114, no. 767, pp. 243–265, Mar. 1927. DOI: 10.1098/rspa.1927.0039.
- [199] E. Fermi, *Nuclear Physics: A Course Given by Enrico Fermi at the University of Chicago*, Rev. ed., reprint. Chicago: Univ. of Chicago Press, 1950, 248 pp., ISBN: 978-0-226-24365-8.
- [200] C. L. Hammer and T. A. Weber, "Time-dependent perturbation theory," *Journal of Mathematical Physics*, vol. 6, no. 10, pp. 1591–1606, Oct. 1965. DOI: 10.1063/1.1704699.

- [201] S. E. Schwartz, "The Franck-Condon principle and the duration of electronic transitions," *Journal of Chemical Education*, vol. 50, no. 9, Sep. 1973, Art. no. 608. DOI: 10.1021/ed050p608.
- [202] L. Razinkovas, M. W. Doherty, N. B. Manson, C. G. V. de Walle, and A. Alkauskas, "Vibrational and vibronic structure of isolated point defects: The nitrogen-vacancy center in diamond," *Physical Review B*, vol. 104, no. 4, Jul. 2021, Art. no. 045303. DOI: 10.1103/physrevb.104.045303.
- [203] P. M. Morse, "Diatomic molecules according to the wave mechanics. II. Vibrational levels," *Physical Review*, vol. 34, no. 1, pp. 57–64, Jul. 1929. DOI: 10.1103/physrev.34.57.
- [204] J. P. Dahl and M. Springborg, "The Morse oscillator in position space, momentum space, and phase space," *The Journal of Chemical Physics*, vol. 88, no. 7, pp. 4535–4547, Apr. 1988. DOI: 10.1063/1.453761.
- [205] W. Demtröder, *Experimentalphysik 3*. Springer Berlin Heidelberg, 2016, ISBN: 978-3-662-49094-5. DOI: 10.1007/978-3-662-49094-5.
- [206] P. V. Sushko, S. Mukhopadhyay, A. S. Mysovsky, V. B. Sulimov, A. Taga, and A. L. Shluger, "Structure and properties of defects in amorphous silica: New insights from embedded cluster calculations," *Journal of Physics: Condensed Matter*, vol. 17, no. 21, S2115–S2140, May 2005. DOI: 10.1088/0953-8984/17/21/007.
- [207] M. de Jong, L. Seijo, A. Meijerink, and F. T. Rabouw, "Resolving the ambiguity in the relation between Stokes shift and Huang–Rhys parameter," *Physical Chemistry Chemical Physics*, vol. 17, no. 26, pp. 16959–16969, 2015. DOI: 10.1039/C5CP02093J.
- [208] K. Huang and A. Rhys, "Theory of light absorption and non-radiative transitions in F-centres," *Proceedings of the Royal Society of London. Series A*, vol. 204, no. 1078, pp. 406–423, Dec. 1950. DOI: 10.1098/rspa.1950.0184.
- [209] M. A. Reshchikov, "Mechanisms of thermal quenching of defect-related luminescence in semiconductors," *physica status solidi (a)*, vol. 218, no. 1, 2021, Art. no. 2000101. DOI: 10.1002/pssa.202000101.
- [210] A. G. Wintle, "Thermal quenching of thermoluminescence in quartz," *Geophysical Journal International*, vol. 41, no. 1, pp. 107–113, Apr. 1975. DOI: 10.1111/j.1365-246X.1975.tb05487.x.
- [211] F. Seitz, "An interpretation of crystal luminescence," *Transactions of the Faraday Society*, vol. 35, pp. 74–85, 1939. DOI: 10.1039/TF9393500074.
- [212] R. W. Gurney and N. F. Mott, "Luminescence in solids," *Transactions of the Faraday Society*, vol. 35, pp. 69–73, 1939. DOI: 10.1039/TF9393500069.
- [213] J. Michl, A. Grill, D. Waldhoer, W. Goes, B. Kaczer, D. Linten, B. Parvais, B. Govoreanu, I. Radu, M. Wlatl, and T. Grasser, "Efficient modeling of charge trapping at cryogenic temperatures — Part I: Theory," *IEEE Transactions on Electron Devices*, vol. 68, no. 12, pp. 6365–6371, Dec. 2021. DOI: 10.1109/TED.2021.3116931.
- [214] A. Kerber and E. Cartier, "Bias temperature instability characterization methods," in *Bias Temperature Instability for Devices and Circuits*, T. Grasser, Ed. Springer New York, Sep. 2013, pp. 3–31, ISBN: 978-1-4614-7909-3. DOI: 10.1007/978-1-4614-7909-3\_1.

- [215] C. Sah, "Characteristics of the metal-oxide-semiconductor transistors," *IEEE Transactions on Electron Devices*, vol. 11, no. 7, pp. 324–345, Jul. 1964. DOI: 10.1109/T-ED.1964.15336.
- [216] S. Sun and J. Plummer, "Electron mobility in inversion and accumulation layers on thermally oxidized silicon surfaces," *IEEE Journal of Solid-State Circuits*, vol. 15, no. 4, pp. 562–573, Aug. 1980. DOI: 10.1109/JSSC.1980.1051439.
- [217] H.-G. Lee, S.-Y. Oh, and G. Fuller, "A simple and accurate method to measure the threshold voltage of an enhancement-mode MOSFET," *IEEE Transactions on Electron Devices*, vol. 29, no. 2, pp. 346–348, Feb. 1982. DOI: 10.1109/T-ED.1982.20707.
- [218] H. Reisinger, O. Blank, W. Heinrigs, A. Muhlhoff, W. Gustin, and C. Schlunder, "Analysis of NBTI degradation- and recovery-behavior based on ultra fast VT-measurements," in *2006 IEEE International Reliability Physics Symposium Proceedings (IRPS)*, IEEE, 2006, pp. 448–453. DOI: 10.1109/relphy.2006.251260.
- [219] T. Kimoto, "High-voltage SiC power devices for improved energy efficiency," *Proceedings of the Japan Academy, Series B*, vol. 98, no. 4, pp. 161–189, Apr. 2022. DOI: 10.2183/pjab.98.011.
- [220] T. L. Tewksbury, "Relaxation effects in MOS devices due to tunnel exchange with near-interface oxide traps," Ph.D. dissertation, Massachusetts Institute of Technology, 1992.
- [221] E. H. Nicollian and A. Goetzberger, "MOS conductance technique for measuring surface state parameters," *Applied Physics Letters*, vol. 7, no. 8, pp. 216–219, Oct. 1965. DOI: 10.1063/1.1754385.
- [222] E. H. Nicollian and A. Goetzberger, "The Si-SiO<sub>2</sub> interface - electrical properties as determined by the metal-insulator-silicon conductance technique," *Bell System Technical Journal*, vol. 46, no. 6, pp. 1055–1133, Jul. 1967. DOI: 10.1002/j.1538-7305.1967.tb01727.x.
- [223] R. Castagné and A. Vapaille, "Description of the SiO<sub>2</sub>-Si interface properties by means of very low frequency MOS capacitance measurements," *Surface Science*, vol. 28, no. 1, pp. 157–193, Nov. 1971. DOI: 10.1016/0039-6028(71)90092-6.
- [224] *Keysight Technologies - Impedance measurement handbook - A guide to measurement technology and techniques*, 6th ed., Keysight Technologies, Inc., Nov. 2016.
- [225] T. Grasser, B. O'Sullivan, B. Kaczer, J. Franco, B. Stampfer, and M. Watzl, "CV stretch-out correction after bias temperature stress: Work-function dependence of donor-/acceptor-like traps, fixed charges, and fast states," in *2021 IEEE International Reliability Physics Symposium (IRPS)*, IEEE, Mar. 2021, pp. 1–6. DOI: 10.1109/irps46558.2021.9405184.
- [226] D. K. Schroder, *Semiconductor material and device characterization*. John Wiley, 2005, ISBN: 978-0-471-73906-7.
- [227] H. Yoshioka, T. Nakamura, and T. Kimoto, "Accurate evaluation of interface state density in SiC metal-oxide-semiconductor structures using surface potential based on depletion capacitance," *Journal of Applied Physics*, vol. 111, no. 1, Jan. 2012, Art. no. 014502. DOI: 10.1063/1.3673572.

- [228] S. V. Walstra and C.-T. Sah, "Extension of the McNutt-Sah method for measuring thin oxide thicknesses of MOS devices," *Solid-State Electronics*, vol. 42, no. 4, pp. 671–673, Apr. 1998. DOI: 10.1016/S0038-1101(97)00202-5.
- [229] M. J. McNutt and C. T. Sah, "Determination of the MOS oxide capacitance," *Journal of Applied Physics*, vol. 46, no. 9, pp. 3909–3913, Sep. 1975. DOI: 10.1063/1.322138.
- [230] L. E. Black, *New Perspectives on Surface Passivation: Understanding the Si-Al<sub>2</sub>O<sub>3</sub> Interface*. Springer International Publishing, 2016. DOI: 10.1007/978-3-319-32521-7.
- [231] K. Puschkarsky, T. Grasser, T. Aichinger, W. Gustin, and H. Reisinger, "Understanding and modeling transient threshold voltage instabilities in SiC MOSFETs," in *2018 IEEE International Reliability Physics Symposium (IRPS)*, IEEE, Mar. 2018, pp. 1–10. DOI: 10.1109/irps.2018.8353560.
- [232] B. Kaczer, V. Arkhipov, R. Degraeve, N. Collaert, G. Groeseneken, and M. Goodwin, "Disorder-controlled-kinetics model for negative bias temperature instability and its experimental verification," in *2005 IEEE International Reliability Physics Symposium, 2005. Proceedings. 43rd Annual.*, IEEE, 2005, pp. 381–387. DOI: 10.1109/re1phy.2005.1493117.
- [233] T. Grasser, P.-J. Wagner, P. Hehenberger, W. Goes, and B. Kaczer, "A rigorous study of measurement techniques for negative bias temperature instability," *IEEE Transactions on Device and Materials Reliability*, vol. 8, no. 3, pp. 526–535, Sep. 2008. DOI: 10.1109/tdmr.2008.2002353.
- [234] J. Brugler and P. Jespers, "Charge pumping in MOS devices," *IEEE Transactions on Electron Devices*, vol. 16, no. 3, pp. 297–302, Mar. 1969. DOI: 10.1109/T-ED.1969.16744.
- [235] G. Groeseneken, H. Maes, N. Beltran, and R. D. Keersmaecker, "A reliable approach to charge-pumping measurements in MOS transistors," *IEEE Transactions on Electron Devices*, vol. 31, no. 1, pp. 42–53, Jan. 1984. DOI: 10.1109/t-ed.1984.21472.
- [236] D. Bauza, "Rigorous analysis of two-level charge pumping: Application to the extraction of interface trap concentration versus energy profiles in metal-oxide-semiconductor transistors," *Journal of Applied Physics*, vol. 94, no. 5, pp. 3239–3248, Aug. 2003. DOI: 10.1063/1.1595138.
- [237] A. B. Elliot, "The use of charge pumping currents to measure surface state densities in MOS transistors," *Solid-State Electronics*, vol. 19, no. 3, pp. 241–247, Mar. 1976. DOI: 10.1016/0038-1101(76)90169-6.
- [238] T. Aichinger and M. Nelhiebel, "Characterization of MOSFET interface states using the charge pumping technique," in *Hot Carrier Degradation in Semiconductor Devices*, T. Grasser, Ed. Springer International Publishing, Oct. 2015, pp. 231–255, ISBN: 978-3-319-08994-2. DOI: 10.1007/978-3-319-08994-2\_8.
- [239] P. J. Macfarlane and R. E. Stahlbush, "Characterization of light emission from 4H and 6H SiC MOSFETs," in *MRS Proceedings*, Art. no. 49, vol. 640, Springer Science and Business Media LLC, 2000. DOI: 10.1557/proc-640-h4.9.
- [240] R. E. Stahlbush and P. J. Macfarlane, "Light emission from interface traps and bulk defects in SiC MOSFETs," *Journal of Electronic Materials*, vol. 30, no. 3, pp. 188–195, Mar. 2001. DOI: 10.1007/s11664-001-0014-2.

- [241] R. Stahlbush, P. Macfarlane, J. Williams, G. Chung, L. Feldman, and K. McDonald, "Light emission from 4H SiC MOSFETs with and without NO passivation," *Micro-electronic Engineering*, vol. 59, no. 1-4, pp. 393–398, Nov. 2001. DOI: 10.1016/s0167-9317(01)00674-8.
- [242] *Product data sheet, SiPM – silicon photomultiplier, WL series*, KETEK GmbH, Hofer Str. 3, 81737 Munich, Germany, Jan. 2021.
- [243] F. Acerbi and S. Gundacker, "Understanding and simulating SiPMs," *Nuclear Instruments and Methods in Physics Research Section A: Accelerators, Spectrometers, Detectors and Associated Equipment*, vol. 926, pp. 16–35, May 2019. DOI: 10.1016/j.nima.2018.11.118.
- [244] S. Gundacker and A. Heering, "The silicon photomultiplier: Fundamentals and applications of a modern solid-state photon detector," *Physics in Medicine & Biology*, vol. 65, no. 17, Aug. 2020, Art. no. 17TR01. DOI: 10.1088/1361-6560/ab7b2d.
- [245] D. Renker and E. Lorenz, "Advances in solid state photon detectors," *Journal of Instrumentation*, vol. 4, no. 04, Apr. 2009, Art. no. P04004. DOI: 10.1088/1748-0221/4/04/P04004.
- [246] *CCS series spectrometer operation manual, 2.1*, Thorlabs GmbH, Jul. 2018.
- [247] J. Kölzer, C. Boit, A. Dallmann, G. Deboy, J. Otto, and D. Weinmann, "Quantitative emission microscopy," *Journal of Applied Physics*, vol. 71, no. 11, R23–R41, Jun. 1992. DOI: 10.1063/1.350466.
- [248] G. Deboy and J. Kolzer, "Fundamentals of light emission from silicon devices," *Semiconductor Science and Technology*, vol. 9, no. 5, pp. 1017–1032, May 1994. DOI: 10.1088/0268-1242/9/5/004.
- [249] E. Inuzuka and H. Suzuki, "Emission microscopy in semiconductor failure," in *Conference Proceedings. 10th Anniversary. IMTC/94. Advanced Technologies in I & M. 1994 IEEE Instrumentation and Measurement Technology Conference (Cat. No.94CH3424-9)*, IEEE, 1994, pp. 1492–1496. DOI: 10.1109/IMTC.1994.352178.
- [250] R. Newman, "Visible light from a silicon p – n junction," *Physical Review*, vol. 100, no. 2, pp. 700–703, Oct. 1955. DOI: 10.1103/PhysRev.100.700.
- [251] A. G. Chynoweth and K. G. McKay, "Photon emission from avalanche breakdown in silicon," *Physical Review*, vol. 102, no. 2, pp. 369–376, Apr. 1956. DOI: 10.1103/PhysRev.102.369.
- [252] S. Tam and C. Hu, "Hot-electron-induced photon and photocarrier generation in silicon MOSFET's," *IEEE Transactions on Electron Devices*, vol. 31, no. 9, pp. 1264–1273, Sep. 1984. DOI: 10.1109/T-ED.1984.21698.
- [253] M. Herzog and F. Koch, "Hot-carrier light emission from silicon metal-oxide-semiconductor devices," *Applied Physics Letters*, vol. 53, no. 26, pp. 2620–2622, Dec. 1988. DOI: 10.1063/1.100177.
- [254] N. C. Das, W. S. Khokle, and S. D. Mohanty, "Visible light emission from silicon MOSFETs," *Solid-State Electronics*, vol. 28, no. 10, pp. 967–977, Oct. 1985. DOI: 10.1016/0038-1101(85)90027-9.

- [255] I. De Wolf and M. Rasras, "Spectroscopic photon emission microscopy: A unique tool for failure analysis of microelectronics devices," *Microelectronics Reliability*, vol. 41, no. 8, pp. 1161–1169, Aug. 2001. DOI: 10.1016/S0026-2714(01)00104-4.
- [256] M. Denais, V. Huard, C. Parthasarathy, G. Ribes, F. Perrier, N. Revil, and A. Bravaix, "Interface traps and oxide traps under NBTI and PBTI in advanced CMOS technology with a 2nm gate-oxide," in *IEEE International Integrated Reliability Workshop Final Report*, IEEE, 2003, pp. 1–6. DOI: 10.1109/irws.2003.1283289.
- [257] S. Rangan, N. Mielke, and E. Yeh, "Universal recovery behavior of negative bias temperature instability [PMOSFETs]," in *IEEE International Electron Devices Meeting 2003*, IEEE, 2003, pp. 1–4. DOI: 10.1109/iedm.2003.1269294.
- [258] A. K. Sinha and T. E. Smith, "Kinetics of the slow-trapping instability at the Si/SiO<sub>2</sub> interface," *Journal of The Electrochemical Society*, vol. 125, no. 5, pp. 743–746, May 1978. DOI: 10.1149/1.2131539.
- [259] S. Chakravarthi, A. Krishnan, V. Reddy, C. F. Machala, and S. Krishnan, "A comprehensive framework for predictive modeling of negative bias temperature instability," in *2004 IEEE International Reliability Physics Symposium (IRPS)*, IEEE, Apr. 2004, pp. 273–282. DOI: 10.1109/relphy.2004.1315337.
- [260] A. A. Katsetos, "Negative bias temperature instability (NBTI) recovery with bake," *Microelectronics Reliability*, vol. 48, no. 10, pp. 1655–1659, Oct. 2008. DOI: 10.1016/j.microrel.2008.04.012.
- [261] M. Cioni, P. Fiorenza, F. Roccaforte, M. Saggio, S. Cascino, A. Messina, V. Vinciguerra, M. Calabretta, and A. Chini, "Identification of interface states responsible for VTH hysteresis in packaged SiC MOSFETs," in *2022 IEEE International Reliability Physics Symposium (IRPS)*, IEEE, Mar. 2022, pp. 1–6. DOI: 10.1109/IRPS48227.2022.9764543.
- [262] T. Grasser, K. Rott, H. Reisinger, M. Walzl, F. Schanovsky, and B. Kaczer, "NBTI in nanoscale MOSFETs—the ultimate modeling benchmark," *IEEE Transactions on Electron Devices*, vol. 61, no. 11, pp. 3586–3593, Nov. 2014. DOI: 10.1109/ted.2014.2353578.
- [263] G. Rzepa, W. Goes, G. Rott, K. Rott, M. Karner, C. Kernstock, B. Kaczer, H. Reisinger, and T. Grasser, "Physical modeling of NBTI: From individual defects to devices," in *2014 International Conference on Simulation of Semiconductor Processes and Devices (SISPAD)*, IEEE, Sep. 2014, pp. 81–84. DOI: 10.1109/sispad.2014.6931568.
- [264] G. Pobegen and T. Grasser, "On the distribution of NBTI time constants on a long, temperature-accelerated time scale," *IEEE Transactions on Electron Devices*, vol. 60, no. 7, pp. 2148–2155, Jul. 2013. DOI: 10.1109/ted.2013.2264816.
- [265] M. Alam, H. Kufluoglu, D. Varghese, and S. Mahapatra, "A comprehensive model for PMOS NBTI degradation: Recent progress," *Microelectronics Reliability*, vol. 47, no. 6, pp. 853–862, Jun. 2007. DOI: 10.1016/j.microrel.2006.10.012.
- [266] M. Alam and S. Mahapatra, "A comprehensive model of PMOS NBTI degradation," *Microelectronics Reliability*, vol. 45, no. 1, pp. 71–81, Jan. 2005. DOI: 10.1016/j.microrel.2004.03.019.

- [267] G. Pobegen, T. Aichinger, M. Nelhiebel, and T. Grasser, "Understanding temperature acceleration for NBTI," in *2011 International Electron Devices Meeting (IEDM)*, IEEE, Dec. 2011, pp. 1–4. DOI: 10.1109/iedm.2011.6131623.
- [268] T. Grasser, H. Reisinger, P.-J. Wagner, F. Schanovsky, W. Goes, and B. Kaczer, "The time dependent defect spectroscopy (TDDS) for the characterization of the bias temperature instability," in *2010 IEEE International Reliability Physics Symposium (IRPS)*, IEEE, 2010, pp. 16–25. DOI: 10.1109/irps.2010.5488859.
- [269] Y. Illarionov, A. Smith, S. Vaziri, M. Ostling, T. Mueller, M. Lemme, and T. Grasser, "Hot-carrier degradation and bias-temperature instability in single-layer graphene field-effect transistors: Similarities and differences," *IEEE Transactions on Electron Devices*, vol. 62, no. 11, pp. 3876–3881, Nov. 2015. DOI: 10.1109/ted.2015.2480704.
- [270] K. Puschkarsky, H. Reisinger, C. Schlünder, W. Gustin, and T. Grasser, "Fast acquisition of activation energy maps using temperature ramps for lifetime modeling of BTI," in *2018 48th European Solid-State Device Research Conference (ESSDERC)*, IEEE, Sep. 2018, pp. 218–221. DOI: 10.1109/essderc.2018.8486855.
- [271] T. Grasser, "The capture/emission time map approach to the bias temperature instability," in *Bias Temperature Instability for Devices and Circuits*, T. Grasser, Ed. Springer New York, Sep. 2013, pp. 447–481, ISBN: 978-1-4614-7909-3. DOI: 10.1007/978-1-4614-7909-3\_17.
- [272] K. Puschkarsky, H. Reisinger, C. Schlünder, W. Gustin, and T. Grasser, "Voltage-dependent activation energy maps for analytic lifetime modeling of NBTI without time extrapolation," *IEEE Transactions on Electron Devices*, vol. 65, no. 11, pp. 4764–4771, Nov. 2018. DOI: 10.1109/ted.2018.2870170.
- [273] T. Aichinger, G. Rescher, and G. Pobegen, "Threshold voltage peculiarities and bias temperature instabilities of SiC MOSFETs," *Microelectronics Reliability*, vol. 80, pp. 68–78, Jan. 2018. DOI: 10.1016/j.microrel.2017.11.020.
- [274] D. B. Habersat, A. J. Lelis, and R. Green, "Towards a robust approach to threshold voltage characterization and high temperature gate bias qualification," in *2020 IEEE International Reliability Physics Symposium (IRPS)*, IEEE, Apr. 2020, pp. 1–4. DOI: 10.1109/irps45951.2020.9128227.
- [275] J. Berens, G. Pobegen, G. Rescher, T. Aichinger, and T. Grasser, "NH<sub>3</sub> and NO + NH<sub>3</sub> annealing of 4H-SiC trench MOSFETs: Device performance and reliability," *IEEE Transactions on Electron Devices*, vol. 66, no. 11, pp. 4692–4697, Nov. 2019. DOI: 10.1109/ted.2019.2941723.
- [276] G. Rescher, G. Pobegen, T. Aichinger, and T. Grasser, "Comprehensive evaluation of bias temperature instabilities on 4H-SiC MOSFETs using device preconditioning," *Materials Science Forum*, vol. 924, pp. 671–675, Jun. 2018. DOI: 10.4028/www.scientific.net/msf.924.671.
- [277] G. Rescher, G. Pobegen, T. Aichinger, and T. Grasser, "Preconditioned BTI on 4H-SiC: Proposal for a nearly delay time-independent measurement technique," *IEEE Transactions on Electron Devices*, vol. 65, no. 4, pp. 1419–1426, Apr. 2018. DOI: 10.1109/ted.2018.2803283.



- [278] C. Strenger, V. Uhnevionak, A. Burenkov, A. J. Bauer, V. Mortet, E. Bedel-Pereira, F. Cristiano, M. Krieger, and H. Ryssel, "Correlation of interface characteristics to electron mobility in channel-implanted 4H-SiC MOSFETs," *Materials Science Forum*, vol. 740-742, pp. 537–540, Jan. 2013. DOI: 10.4028/www.scientific.net/msf.740-742.537.
- [279] "JEP183A – Guidelines for measuring the threshold voltage ( $V_T$ ) of SiC MOSFETs," Joint Electron Device Engineering Council (JEDEC), JEDEC Publication, Jan. 2023.
- [280] "JEP184 – Guideline for evaluating bias temperature instability of silicon carbide metal-oxide-semiconductor devices for power electronic conversion," Joint Electron Device Engineering Council (JEDEC), JEDEC Publication, Mar. 2021.
- [281] A. Kar, S. S. Ahmad, G. Narayanan, and M. Sengupta, "Design, performance evaluation, fabrication and testing of a SiC MOSFET gate driver," in *2017 IEEE International Conference on Signal Processing, Informatics, Communication and Energy Systems (SPICES)*, IEEE, Aug. 2017, pp. 1–6. DOI: 10.1109/SPICES.2017.8091311.
- [282] Y. Ren, X. Yang, F. Zhang, K. Wang, W. Chen, L. Wang, and Y. Pei, "A compact gate control and voltage-balancing circuit for series-connected SiC MOSFETs and its application in a DC breaker," *IEEE Transactions on Industrial Electronics*, vol. 64, no. 10, pp. 8299–8309, Oct. 2017. DOI: 10.1109/tie.2017.2711579.
- [283] H. Jiang, X. Zhong, G. Qiu, L. Tang, X. Qi, and L. Ran, "Dynamic gate stress induced threshold voltage drift of silicon carbide MOSFET," *IEEE Electron Device Letters*, vol. 41, no. 9, pp. 1284–1287, Sep. 2020. DOI: 10.1109/led.2020.3007626.
- [284] AN2018-09 – *Guidelines for CoolSiC™ MOSFET gate drive voltage window*, 2019-05-064, Infineon Technologies AG, 2018.
- [285] M. Regardi, Y. Zhihui, I. Voss, P. Salmen, T. Aichinger, R. Elpelt, and P. Friedrichs, "How Infineon controls and assures the reliability of SiC based power semiconductors," Infineon Technologies AG, Whitepaper, Aug. 2020.
- [286] D. B. Habersat and A. J. Lelis, "AC-stress degradation and its anneal in SiC MOSFETs," *IEEE Transactions on Electron Devices*, vol. 69, no. 9, pp. 5068–5073, Sep. 2022. DOI: 10.1109/ted.2022.3190815.
- [287] "JEP195 – Guideline for evaluating gate switching instability of silicon carbide metal-oxide-semiconductor devices for power electronic conversion," Joint Electron Device Engineering Council (JEDEC), JEDEC Publication, Feb. 2023.
- [288] T. Grasser, B. Kaczer, H. Reisinger, P.-J. Wagner, and M. Toledano-Luque, "On the frequency dependence of the bias temperature instability," in *2012 IEEE International Reliability Physics Symposium (IRPS)*, IEEE, Apr. 2012, pp. 1–7. DOI: 10.1109/irps.2012.6241938.
- [289] K. Puschkarsky, H. Reisinger, G. A. Rott, C. Schlunder, W. Gustin, and T. Grasser, "An efficient analog compact NBTI model for stress and recovery based on activation energy maps," *IEEE Transactions on Electron Devices*, vol. 66, no. 11, pp. 4623–4630, Nov. 2019. DOI: 10.1109/ted.2019.2941889.
- [290] J. Stathis and S. Zafar, "The negative bias temperature instability in MOS devices: A review," *Microelectronics Reliability*, vol. 46, no. 2-4, pp. 270–286, Feb. 2006. DOI: 10.1016/j.microrel.2005.08.001.

- [291] X. Zhong, H. Jiang, G. Qiu, L. Tang, H. Mao, X. Chao, X. Jiang, J. Hu, X. Qi, and L. Ran, "Bias temperature instability of silicon carbide power MOSFET under AC gate stresses," *IEEE Transactions on Power Electronics*, vol. 37, no. 2, pp. 1998–2008, Feb. 2022. DOI: 10.1109/tpe1.2021.3105272.
- [292] X. Zhong, H. Jiang, L. Tang, X. Qi, P. Jiang, and L. Ran, "Gate stress polarity dependence of AC bias temperature instability in silicon carbide MOSFETs," *IEEE Transactions on Electron Devices*, vol. 69, no. 6, pp. 3328–3333, Jun. 2022. DOI: 10.1109/ted.2022.3164641.
- [293] A. J. Lelis and D. B. Habersat, "AC-stress degradation in SiC MOSFETs," *Materials Science Forum*, vol. 1092, pp. 151–155, Jun. 2023. DOI: 10.4028/p-y82029.
- [294] B. Ullmann, M. Jech, K. Puschkarsky, G. A. Rott, M. Waltl, Y. Illarionov, H. Reisinger, and T. Grasser, "Impact of mixed negative bias temperature instability and hot carrier stress on MOSFET characteristics — Part I: Experimental," *IEEE Transactions on Electron Devices*, vol. 66, no. 1, pp. 232–240, Jan. 2019. DOI: 10.1109/ted.2018.2873419.
- [295] M. Jech, B. Ullmann, G. Rzepa, S. Tyaginov, A. Grill, M. Waltl, D. Jabs, C. Jungemann, and T. Grasser, "Impact of mixed negative bias temperature instability and hot carrier stress on MOSFET characteristics — Part II: Theory," *IEEE Transactions on Electron Devices*, vol. 66, no. 1, pp. 241–248, Jan. 2019. DOI: 10.1109/ted.2018.2873421.
- [296] M. Jech, G. Rott, H. Reisinger, S. Tyaginov, G. Rzepa, A. Grill, D. Jabs, C. Jungemann, M. Waltl, and T. Grasser, "Mixed hot-carrier/bias temperature instability degradation regimes in full  $\{V_G, V_D\}$  bias space: Implications and peculiarities," *IEEE Transactions on Electron Devices*, vol. 67, no. 8, pp. 3315–3322, Aug. 2020. DOI: 10.1109/ted.2020.3000749.
- [297] H. Jiang, X. Qi, G. Qiu, X. Zhong, L. Tang, H. Mao, Z. Wu, H. Chen, and L. Ran, "A physical explanation of threshold voltage drift of SiC MOSFET induced by gate switching," *IEEE Transactions on Power Electronics*, vol. 37, no. 8, pp. 8830–8834, Aug. 2022. DOI: 10.1109/tpe1.2022.3161678.
- [298] N. Paulter, D. Larson, and J. Blair, "The IEEE standard on transitions, pulses, and related waveforms, Std-181-2003," *IEEE Transactions on Instrumentation and Measurement*, vol. 53, no. 4, pp. 1209–1217, Aug. 2004. DOI: 10.1109/tim.2004.831470.
- [299] B. C. Bittel, P. M. Lenahan, J. T. Ryan, J. Fronheiser, and A. J. Lelis, "Spin dependent charge pumping in SiC metal-oxide-semiconductor field-effect-transistors," *Applied Physics Letters*, vol. 99, no. 8, Aug. 2011, Art. no. 083504. DOI: 10.1063/1.3630024.
- [300] A. Salinaro, G. Pobegen, T. Aichinger, B. Zippelius, D. Peters, P. Friedrichs, and L. Frey, "Charge pumping measurements on differently passivated lateral 4H-SiC MOSFETs," *IEEE Transactions on Electron Devices*, vol. 62, no. 1, pp. 155–163, Jan. 2015. DOI: 10.1109/ted.2014.2372874.
- [301] B. Ruch, G. Pobegen, M. Rosch, R. K. Vytla, and T. Grasser, "Charge pumping of low-voltage silicon trench powers MOSFETs," *IEEE Transactions on Device and Materials Reliability*, vol. 19, no. 1, pp. 133–139, Mar. 2019. DOI: 10.1109/tdmr.2019.2891794.

- [302] C. T.-K. Lew, V. K. Sewani, T. Ohshima, J. C. McCallum, and B. C. Johnson, "Charge pumping electrically detected magnetic resonance of silicon carbide power transistors," *Journal of Applied Physics*, vol. 134, no. 5, Aug. 2023, Art. no. 055703. DOI: 10.1063/5.0167650.
- [303] D. Scholten, J. Baringhaus, D. Krebs, and S. Noll, "Hypothesis to explain threshold drift due to dynamic bipolar gate stress," *Materials Science Forum*, vol. 1090, pp. 159–164, May 2023. DOI: 10.4028/p-bt3i95.
- [304] L. Storasta, F. H. C. Carlsson, J. P. Bergman, and E. Janzén, "Observation of recombination enhanced defect annealing in 4H-SiC," *Applied Physics Letters*, vol. 86, no. 9, Feb. 2005, Art. no. 091903. DOI: 10.1063/1.1811381.
- [305] L. Storasta, F. Carlsson, P. Bergman, and E. Janzén, "Recombination enhanced defect annealing in 4H-SiC," *Materials Science Forum*, vol. 483–485, pp. 369–372, May 2005. DOI: 10.4028/www.scientific.net/msf.483-485.369.
- [306] S. K. Lai, "Two-carrier nature of interface-state generation in hole trapping and radiation damage," *Applied Physics Letters*, vol. 39, no. 1, pp. 58–60, Jul. 1981. DOI: 10.1063/1.92514.
- [307] E. Rosenbaum, Z. Liu, and C. Hu, "The effects of oxide stress waveform on MOSFET performance," in *International Electron Devices Meeting 1991*, IEEE, Dec. 1991, pp. 719–722. DOI: 10.1109/iedm.1991.235322.
- [308] E. Rosenbaum, Z. Liu, and C. Hu, "Silicon dioxide breakdown lifetime enhancement under bipolar bias conditions," *IEEE Transactions on Electron Devices*, vol. 40, no. 12, pp. 2287–2295, Dec. 1993. DOI: 10.1109/16.249477.
- [309] Y. Mutha, R. Lal, and V. R. Rao, "Physical mechanisms for pulsed AC stress degradation in thin gate oxide MOSFETs," in *Proceedings of the 9th International Symposium on the Physical and Failure Analysis of Integrated Circuits*, IEEE, Jul. 2002, pp. 250–253. DOI: 10.1109/ipfa.2002.1025673.
- [310] S. Zhu, A. Nakajima, T. Ohashi, and H. Miyake, "Enhancement of BTI degradation in pMOSFETs under high-frequency bipolar gate bias," *IEEE Electron Device Letters*, vol. 26, no. 6, pp. 387–389, Jun. 2005. DOI: 10.1109/1ed.2005.848075.
- [311] S. C. Kang, S. M. Kim, U. Jung, Y. Kim, W. Park, and B. H. Lee, "Interface state degradation during AC positive bias temperature instability stress," *Solid-State Electronics*, vol. 158, pp. 46–50, Aug. 2019. DOI: 10.1016/j.sse.2019.05.006.
- [312] T. Grasser, B. Kaczer, B. O'Sullivan, G. Rzepa, B. Stampfer, and M. Wärtl, "The mysterious bipolar bias temperature stress from the perspective of gate-sided hydrogen release," in *2020 IEEE International Reliability Physics Symposium (IRPS)*, IEEE, Apr. 2020, pp. 1–6. DOI: 10.1109/irps45951.2020.9129198.
- [313] T. Grasser, M. Wärtl, W. Goes, Y. Wimmer, A.-M. El-Sayed, A. Shluger, and B. Kaczer, "On the volatility of oxide defects: Activation, deactivation, and transformation," in *2015 IEEE International Reliability Physics Symposium (IRPS)*, IEEE, Apr. 2015, pp. 1–8. DOI: 10.1109/IRPS.2015.7112739.

- [314] T. Grasser, M. Walzl, Y. Wimmer, W. Goes, R. Kosik, G. Rzepa, H. Reisinger, G. Pobegen, A. El-Sayed, A. Shluger, and B. Kaczer, "Gate-sided hydrogen release as the origin of "permanent" NBTI degradation: From single defects to lifetimes," in *2015 IEEE International Electron Devices Meeting (IEDM)*, IEEE, Dec. 2015, pp. 1–4. DOI: 10.1109/iedm.2015.7409739.
- [315] T. Grasser, M. Walzl, G. Rzepa, W. Goes, Y. Wimmer, A.-M. El-Sayed, A. L. Shluger, H. Reisinger, and B. Kaczer, "The "permanent" component of NBTI revisited: Saturation, degradation-reversal, and annealing," in *2016 IEEE International Reliability Physics Symposium (IRPS)*, IEEE, Apr. 2016, pp. 1–8. DOI: 10.1109/irps.2016.7574504.
- [316] T. Grasser, M. Walzl, K. Puschkarsky, B. Stampfer, G. Rzepa, G. Pobegen, H. Reisinger, H. Arimura, and B. Kaczer, "Implications of gate-sided hydrogen release for post-stress degradation build-up after BTI stress," in *2017 IEEE International Reliability Physics Symposium (IRPS)*, IEEE, Apr. 2017, pp. 1–6. DOI: 10.1109/irps.2017.7936334.
- [317] A.-M. El-Sayed, Y. Wimmer, W. Goes, T. Grasser, V. V. Afanas'ev, and A. L. Shluger, "Theoretical models of hydrogen-induced defects in amorphous silicon dioxide," *Physical Review B*, vol. 92, no. 1, Jul. 2015, Art. no. 014107. DOI: 10.1103/PhysRevB.92.014107.
- [318] A. Mattausch, M. Bockstedte, O. Pankratov, J. W. Steeds, S. Furkert, J. M. Hayes, W. Sullivan, and N. G. Wright, "Thermally stable carbon-related centers in 6H-SiC: Photoluminescence spectra and microscopic models," *Physical Review B*, vol. 73, no. 16, Apr. 2006, Art. no. 161201. DOI: 10.1103/PhysRevB.73.161201.
- [319] A. Stesmans, "Dissociation kinetics of hydrogen-passivated  $P_b$  defects at the (111) Si/SiO<sub>2</sub> interface," *Physical Review B*, vol. 61, no. 12, pp. 8393–8403, Mar. 2000. DOI: 10.1103/PhysRevB.61.8393.
- [320] V. Huard, M. Denais, and C. Parthasarathy, "NBTI degradation: From physical mechanisms to modelling," *Microelectronics Reliability*, vol. 46, no. 1, pp. 1–23, Jan. 2006. DOI: 10.1016/j.microrel.2005.02.001.
- [321] C. Wilhelmer, D. Waldhoer, M. Jech, A.-M. B. El-Sayed, L. Cvitkovich, M. Walzl, and T. Grasser, "Ab initio investigations in amorphous silicon dioxide: Proposing a multi-state defect model for electron and hole capture," *Microelectronics Reliability*, vol. 139, Dec. 2022, Art. no. 114801. DOI: 10.1016/j.microrel.2022.114801.
- [322] M. Vinay, L. Sang, J. Tong, O. Perlman, R. Daw, C. Galasso, M. Su, D. Querlioz, L. Tian, A. Vasylenkova, Y.-C. Chen, and C. Huang, "Editors' choice 2023," *Communications Engineering*, vol. 2, Dec. 2023, Art. no. 96. DOI: 10.1038/s44172-023-00151-7.
- [323] R. Weingärtner, P. J. Wellmann, M. Bickermann, D. Hofmann, T. L. Straubinger, and A. Winnacker, "Determination of charge carrier concentration in n- and p-doped SiC based on optical absorption measurements," *Applied Physics Letters*, vol. 80, no. 1, pp. 70–72, Jan. 2002. DOI: 10.1063/1.1430262.
- [324] C. Xu, S. Wang, G. Wang, J. Liang, S. Wang, L. Bai, J. Yang, and X. Chen, "Temperature dependence of refractive indices for 4H- and 6H-SiC," *Journal of Applied Physics*, vol. 115, no. 11, Mar. 2014, Art. no. 113501. DOI: 10.1063/1.4868576.

- [325] N. Wiener, *Extrapolation, Interpolation, and Smoothing of Stationary Time Series: With Engineering Applications*. The MIT Press, Aug. 1949, ISBN: 978-0-262-25719-0. DOI: 10.7551/mitpress/2946.001.0001.
- [326] T. Bretz, J. Kemp, L. Middendorf, C. Peters, J. Schumacher, R. Engel, R. Smida, and D. Veberic, "SiPMs – a revolution for high dynamic range applications," in *Proceedings of 35th International Cosmic Ray Conference — PoS(ICRC2017)*, Sissa Medialab, Aug. 2017, pp. 1–8. DOI: 10.22323/1.301.0472.
- [327] J. W. Cooley and J. W. Tukey, "An algorithm for the machine calculation of complex Fourier series," *Mathematics of Computation*, vol. 19, no. 90, pp. 297–301, 1965. DOI: 10.1090/S0025-5718-1965-0178586-1.
- [328] T. Grasser, K. Rott, H. Reisinger, P. Wagner, W. Goes, F. Schanovsky, M. Walzl, M. Toledano-Luque, and B. Kaczer, "Advanced characterization of oxide traps: The dynamic time-dependent defect spectroscopy," in *2013 IEEE International Reliability Physics Symposium (IRPS)*, IEEE, Apr. 2013, pp. 1–7. DOI: 10.1109/irps.2013.6531957.
- [329] J. Cabanillas-Gonzalez, G. Grancini, and G. Lanzani, "Pump-probe spectroscopy in organic semiconductors: Monitoring fundamental processes of relevance in optoelectronics," *Advanced Materials*, vol. 23, no. 46, pp. 5468–5485, Oct. 2011. DOI: 10.1002/adma.201102015.
- [330] J. Mooney and P. Kambhampati, "Get the basics right: Jacobian conversion of wavelength and energy scales for quantitative analysis of emission spectra," *The Journal of Physical Chemistry Letters*, vol. 4, no. 19, pp. 3316–3318, Oct. 2013. DOI: 10.1021/jz401508t.
- [331] B. Armstrong, "Spectrum line profiles: The Voigt function," *Journal of Quantitative Spectroscopy and Radiative Transfer*, vol. 7, no. 1, pp. 61–88, Jan. 1967. DOI: 10.1016/0022-4073(67)90057-X.
- [332] A. Belafhal, "The shape of spectral lines: Widths and equivalent widths of the Voigt profile," *Optics Communications*, vol. 177, no. 1–6, pp. 111–118, Apr. 2000. DOI: 10.1016/S0030-4018(00)00564-2.
- [333] C. F. Gauß, *Theoria motus corporum coelestium in sectionibus conicis solem ambientium auctore Carolo Friderico Gauss*. Frid. Perthes et I. H. Besser, 1809.
- [334] A. Alkauskas, M. D. McCluskey, and C. G. V. de Walle, "Tutorial: Defects in semiconductors—combining experiment and theory," *Journal of Applied Physics*, vol. 119, no. 18, May 2016, Art. no. 181101. DOI: 10.1063/1.4948245.
- [335] P. Deák, J. M. Knaup, T. Hornos, C. Thill, A. Gali, and T. Frauenheim, "The mechanism of defect creation and passivation at the SiC/SiO<sub>2</sub> interface," *Journal of Physics D: Applied Physics*, vol. 40, no. 20, pp. 6242–6253, Oct. 2007. DOI: 10.1088/0022-3727/40/20/s09.
- [336] F. Devynck, A. Alkauskas, P. Broqvist, and A. Pasquarello, "Charge transition levels of carbon-, oxygen-, and hydrogen-related defects at the SiC/SiO<sub>2</sub> interface through hybrid functionals," *Physical Review B*, vol. 84, no. 23, Dec. 2011, Art. no. 235320. DOI: 10.1103/physrevb.84.235320.

- [337] W. Kohn and L. J. Sham, "Self-consistent equations including exchange and correlation effects," *Physical Review*, vol. 140, no. 4A, A1133–A1138, Nov. 1965. DOI: 10.1103/PhysRev.140.A1133.
- [338] E. E. Salpeter and H. A. Bethe, "A relativistic equation for bound-state problems," *Physical Review*, vol. 84, no. 6, pp. 1232–1242, Dec. 1951. DOI: 10.1103/PhysRev.84.1232.
- [339] J. Winkler, J. Homoth, and I. Kallfass, "Utilization of parasitic and luminescence from power and semiconductor and devices for current and sensing," in *PCIM Europe 2018*, IEEE, 2018, pp. 1–8.
- [340] J. Winkler, J. Homroth, and I. Kallfass, "Study on transient and light emission and of SiC and power MOSFETs and regarding the sensing and of source-drain and currents in hard-switched and power electronic and applications," in *PCIM Europe 2019*, 2019, pp. 1–8.
- [341] J. Winkler, J. Homoth, and I. Kallfass, "Electroluminescence-based junction temperature measurement approach for SiC power MOSFETs," *IEEE Transactions on Power Electronics*, vol. 35, no. 3, pp. 2990–2998, Mar. 2020. DOI: 10.1109/tpe1.2019.2929426.
- [342] S. Kalker, C. H. van der Broeck, and R. W. D. Doncker, "Utilizing electroluminescence of SiC MOSFETs for unified junction-temperature and current sensing," in *2020 IEEE Applied Power Electronics Conference and Exposition (APEC)*, IEEE, Mar. 2020, pp. 1098–1105. DOI: 10.1109/apec39645.2020.9124517.
- [343] L. A. Ruppert, M. Laumen, and R. W. D. Doncker, "Utilizing the electroluminescence of SiC MOSFETs as degradation sensitive optical parameter," in *24th European Conference on Power Electronics and Applications (EPE'22 ECCE Europe)*, IEEE, 2022, pp. 1–9.
- [344] H. Mustroph, "Potential-energy surfaces, the Born-Oppenheimer approximations, and the Franck-Condon principle: Back to the roots," *ChemPhysChem*, vol. 17, no. 17, pp. 2616–2629, Jun. 2016. DOI: 10.1002/cphc.201600243.
- [345] M. Lax, "The Franck-Condon principle and its application to crystals," *The Journal of Chemical Physics*, vol. 20, no. 11, pp. 1752–1760, Nov. 1952. DOI: 10.1063/1.1700283.
- [346] E. U. Condon, "Coupling of electronic and nuclear motions in diatomic molecules," in *Proceedings of the National Academy of Sciences*, vol. 13, Jun. 1927, pp. 462–466. DOI: 10.1073/pnas.13.6.462.
- [347] N. Kuznetsov and A. Zubrilov, "Deep centers and electroluminescence in 4H SiC diodes with a p-type base region," *Materials Science and Engineering: B*, vol. 29, no. 1-3, pp. 181–184, Jan. 1995. DOI: 10.1016/0921-5107(94)04035-3.
- [348] P. B. Klein, B. V. Shanabrook, S. W. Huh, A. Y. Polyakov, M. Skowronski, J. J. Sumakeris, and M. J. O'Loughlin, "Lifetime-limiting defects in n- 4H-SiC epilayers," *Applied Physics Letters*, vol. 88, no. 5, Jan. 2006, Art. no. 052110. DOI: 10.1063/1.2170144.
- [349] F. Fabbri, D. Natalini, A. Cavallini, T. Sekiguchi, R. Nipoti, and F. Moscatelli, "Comparison between cathodoluminescence spectroscopy and capacitance transient spectroscopy on Al<sup>+</sup> ion implanted 4H-SiC p<sup>+</sup>/n diodes," *Superlattices and Microstructures*, vol. 45, no. 4-5, pp. 383–387, Apr. 2009. DOI: 10.1016/j.spmi.2008.10.024.

- [350] S. Bishop, C. Reynolds, J. Molstad, F. Stevie, D. Barnhardt, and R. Davis, "On the origin of aluminum-related cathodoluminescence emissions from sublimation grown 4H-SiC(11 $\bar{2}$ 0)," *Applied Surface Science*, vol. 255, no. 13-14, pp. 6535–6539, Apr. 2009. DOI: 10.1016/j.apsusc.2009.02.036.
- [351] A. Fissel, W. Richter, J. Furthmüller, and F. Bechstedt, "On the nature of the D<sub>1</sub>-defect center in SiC: A photoluminescence study of layers grown by solid-source molecular-beam epitaxy," *Applied Physics Letters*, vol. 78, no. 17, pp. 2512–2514, Apr. 2001. DOI: 10.1063/1.1367883.
- [352] P. Bouguer, *Essai d'optique sur la gradation de la lumière*. Claude Jombert, 1729.
- [353] J. H. Lambert, *Photometria sive de mensura et gradibus luminis, colorum et umbrae*. umptibus vidvae E. Klett, typis CP Detleffsen, 1760.
- [354] Beer, "Bestimmung der Absorption des rothen Lichts in farbigen Flüssigkeiten," *Annalen der Physik*, vol. 162, no. 5, pp. 78–88, Jan. 1852. DOI: 10.1002/andp.18521620505.
- [355] S. Deng, C. Xiao, J. Yuan, D. Ma, J. Li, N. Yang, and H. He, "Thermal boundary resistance measurement and analysis across SiC/SiO<sub>2</sub> interface," *Applied Physics Letters*, vol. 115, no. 10, Sep. 2019, Art. no. 101603. DOI: 10.1063/1.5111157.
- [356] M. Bockstedte, A. Mattausch, and O. Pankratov, "Ab initio study of the migration of intrinsic defects in 3C-SiC," *Physical Review B*, vol. 68, no. 20, Nov. 2003, Art. no. 205201. DOI: 10.1103/PhysRevB.68.205201.
- [357] J. W. Steeds, S. Furkert, J. Hayes, and W. Sullivan, "Low temperature annealing of optical centres in 4H SiC," *Materials Science Forum*, vol. 457-460, pp. 637–640, Jun. 2004. DOI: 10.4028/www.scientific.net/msf.457-460.637.
- [358] Y. Kagoyama, M. Okamoto, T. Yamasaki, N. Tajima, J. Nara, T. Ohno, H. Yano, S. Harada, and T. Umeda, "Anomalous carbon clusters in 4H-SiC/SiO<sub>2</sub> interfaces," *Journal of Applied Physics*, vol. 125, no. 6, Feb. 2019, Art. no. 065302. DOI: 10.1063/1.5066356.
- [359] Z. Zhang, Z. Wang, Y. Guo, and J. Robertson, "Carbon cluster formation and mobility degradation in 4H-SiC MOSFETs," *Applied Physics Letters*, vol. 118, no. 3, Jan. 2021, Art. no. 031601. DOI: 10.1063/5.0037241.
- [360] X. Shen, M. P. Oxley, Y. Puzyrev, B. R. Tuttle, G. Duscher, and S. T. Pantelides, "Excess carbon in silicon carbide," *Journal of Applied Physics*, vol. 108, no. 12, Dec. 2010, Art. no. 123705. DOI: 10.1063/1.3517142.
- [361] T. Zheleva, A. Lelis, G. Duscher, F. Liu, I. Levin, and M. Das, "Transition layers at the SiO<sub>2</sub>/SiC interface," *Applied Physics Letters*, vol. 93, no. 2, Jul. 2008, Art. no. 022108. DOI: 10.1063/1.2949081.
- [362] T. L. Biggerstaff, C. L. Reynolds, T. Zheleva, A. Lelis, D. Habersat, S. Haney, S.-H. Ryu, A. Agarwal, and G. Duscher, "Relationship between 4H-SiC/SiO<sub>2</sub> transition layer thickness and mobility," *Applied Physics Letters*, vol. 95, no. 3, Jul. 2009, Art. no. 032108. DOI: 10.1063/1.3144272.

- [363] G. Gruber, C. Gspan, E. Fisslthaler, M. Dienstleder, G. Pobegen, T. Aichinger, R. Meszaros, W. Grogger, and P. Hadley, "Impact of the NO anneal on the microscopic structure and chemical composition of the Si-face 4H-SiC/SiO<sub>2</sub> interface," *Advanced Materials Interfaces*, vol. 5, no. 12, Apr. 2018, Art. no. 1800022. DOI: 10.1002/admi.201800022.
- [364] J. Woerle, B. C. Johnson, R. Stark, M. Camarda, and U. Grossner, "Fast defect mapping at the SiO<sub>2</sub>/SiC interface using confocal photoluminescence," *Materials Science Forum*, vol. 1062, pp. 389–394, May 2022. DOI: 10.4028/p-78192c.
- [365] B. Johnson, J. Woerle, D. Haasmann, C.-K. Lew, R. Parker, H. Knowles, B. Pingault, M. Atature, A. Gali, S. Dimitrijevic, M. Camarda, and J. McCallum, "Optically active defects at the SiC/SiO<sub>2</sub> interface," *Physical Review Applied*, vol. 12, no. 4, Oct. 2019, Art. no. 044024. DOI: 10.1103/physrevapplied.12.044024.
- [366] Y. Abe, T. Umeda, M. Okamoto, R. Kosugi, S. Harada, M. Haruyama, W. Kada, O. Hanaizumi, S. Onoda, and T. Ohshima, "Single photon sources in 4H-SiC metal-oxide-semiconductor field-effect transistors," *Applied Physics Letters*, vol. 112, no. 3, Jan. 2018, Art. no. 031105. DOI: 10.1063/1.4994241.
- [367] A. Lohrmann, N. Iwamoto, Z. Bodrog, S. Castelletto, T. Ohshima, T. Karle, A. Gali, S. Prawer, J. McCallum, and B. Johnson, "Single-photon emitting diode in silicon carbide," *Nature Communications*, vol. 6, Jul. 2015, Art. no. 7783. DOI: 10.1038/ncomms8783.
- [368] A. Lohrmann, S. Castelletto, J. R. Klein, T. Ohshima, M. Bosi, M. Negri, D. W. M. Lau, B. C. Gibson, S. Prawer, J. C. McCallum, and B. C. Johnson, "Activation and control of visible single defects in 4H-, 6H-, and 3C-SiC by oxidation," *Applied Physics Letters*, vol. 108, no. 2, Jan. 2016, Art. no. 021107. DOI: 10.1063/1.4939906.
- [369] J. Woerle, B. C. Johnson, C. Bongiorno, K. Yamasue, G. Ferro, D. Dutta, T. A. Jung, H. Sigg, Y. Cho, U. Grossner, and M. Camarda, "Two-dimensional defect mapping of the SiO<sub>2</sub>/4H-SiC interface," *Physical Review Materials*, vol. 3, no. 8, Aug. 2019, Art. no. 084602. DOI: 10.1103/physrevmaterials.3.084602.
- [370] N. Alyabyeva, J. Ding, M. Sauty, J. Woerle, Y. Jousseau, G. Ferro, J. C. McCallum, J. Peretti, B. C. Johnson, and A. C. H. Rowe, "Nanoscale mapping of sub-gap electroluminescence from step-bunched, oxidized 4H-SiC surfaces," *physica status solidi (b)*, vol. 260, no. 5, Nov. 2022, Art. no. 2200356. DOI: 10.1002/pssb.202200356.
- [371] Y. Yamagishi and Y. Cho, "Nanosecond microscopy of capacitance at SiO<sub>2</sub>/4H-SiC interfaces by time-resolved scanning nonlinear dielectric microscopy," *Applied Physics Letters*, vol. 111, no. 16, Oct. 2017, Art. no. 163103. DOI: 10.1063/1.4999794.



# List of Publications

## Scientific Journals

- [MFJ1] C. Schleich, D. Waldhoer, K. Waschneck, M. W. Feil, H. Reisinger, T. Grasser, and M. Walzl, "Physical modeling of charge trapping in 4H-SiC DMOSFET technologies," *IEEE Transactions on Electron Devices*, vol. 68, no. 8, pp. 4016–4021, Aug. 2021. DOI: 10.1109/ted.2021.3092295.
- [MFJ2] M. W. Feil, M. Weger, H. Reisinger, T. Aichinger, A. Kabakow, D. Waldhör, A. Jakowetz, S. Prigann, G. Pobegen, W. Gustin, M. Walzl, M. Bockstedte, and T. Grasser, "Time-gated optical spectroscopy of field-effect stimulated recombination via interfacial point defects in fully-processed silicon carbide power MOSFETs," *Physical Review Applied*, 2024, **accepted**. DOI: 10.48550/ARXIV.2404.13463.
- [MFJ3] M. W. Feil, K. Puschkarsky, W. Gustin, H. Reisinger, and T. Grasser, "On the physical meaning of single-value activation energies for BTI in Si and SiC MOSFET devices," *IEEE Transactions on Electron Devices*, vol. 68, no. 1, pp. 236–243, Jan. 2021. DOI: 10.1109/ted.2020.3036321.
- [MFJ4] M. W. Feil, A. Huerner, K. Puschkarsky, C. Schleich, T. Aichinger, W. Gustin, H. Reisinger, and T. Grasser, "The impact of interfacial charge trapping on the reproducibility of measurements of silicon carbide MOSFET device parameters," *Crystals*, vol. 10, no. 12, Dec. 2020, Art. no. 1143. DOI: 10.3390/cryst10121143.
- [MFJ5] M. W. Feil, K. Waschneck, H. Reisinger, J. Berens, T. Aichinger, S. Prigann, G. Pobegen, P. Salmen, G. Rescher, D. Waldhör, A. Vasilev, W. Gustin, M. Walzl, and T. Grasser, "Gate switching instability in silicon carbide MOSFETs—Part I: Experimental," *IEEE Transactions on Electron Devices*, vol. 71, no. 7, pp. 4210–4217, Jul. 2024. DOI: 10.1109/TED.2024.3397636.
- [MFJ6] T. Grasser, M. W. Feil, K. Waschneck, H. Reisinger, J. Berens, D. Waldhör, A. Vasilev, M. Walzl, T. Aichinger, M. Bockstedte, W. Gustin, and G. Pobegen, "Gate switching instability in silicon carbide MOSFETs—Part II: Modeling," *IEEE Transactions on Electron Devices*, vol. 71, no. 7, pp. 4218–4226, Jul. 2024. DOI: 10.1109/TED.2024.3397629.
- [MFJ7] P. Salmen, M. Feil, K. Waschneck, H. Reisinger, G. Rescher, I. Voss, M. Sievers, and T. Aichinger, "Gate-switching-stress test: Electrical parameter stability of SiC

- MOSFETs in switching operation," *Microelectronics Reliability*, vol. 135, Aug. 2022, Art. no. 114575. DOI: 10.1016/j.microrel.2022.114575.
- [MFJ8] M. W. Feil, H. Reisinger, A. Kabakow, T. Aichinger, C. Schleich, A. Vasilev, D. Waldhör, M. Walzl, W. Gustin, and T. Grasser, "Electrically stimulated optical spectroscopy of interface defects in wide-bandgap field-effect transistors," *Communications Engineering*, vol. 2, Jan. 2023, Art. no. 5. DOI: 10.1038/s44172-023-00053-8.
- [MFJ9] M. Weger, M. W. Feil, M. V. Orden, J. Cottom, M. Bockstedte, and G. Pobegen, "Temperature-dependent electroluminescence of a gate pulsed silicon carbide metal-oxide-semiconductor field-effect transistor: Insight into interface traps," *Journal of Applied Physics*, vol. 134, no. 3, Jul. 2023, Art. no. 034503. DOI: 10.1063/5.0152337.
- [MFJ10] H. Huang, Y. Li, Y. Tong, E.-P. Yao, M. W. Feil, A. F. Richter, M. Döblinger, A. L. Rogach, J. Feldmann, and L. Polavarapu, "Spontaneous crystallization of perovskite nanocrystals in nonpolar organic solvents: A versatile approach for their shape-controlled synthesis," *Angewandte Chemie International Edition*, vol. 58, no. 46, pp. 16 558–16 562, Sep. 2019. DOI: 10.1002/anie.201906862.
- [MFJ11] H. Huang, M. W. Feil, S. Fuchs, T. Debnath, A. F. Richter, Y. Tong, L. Wu, Y. Wang, M. Döblinger, and B. Nickel, "Growth of perovskite CsPbBr<sub>3</sub> nanocrystals and their formed superstructures revealed by in situ spectroscopy," *Chemistry of Materials*, vol. 32, no. 20, pp. 8877–8884, Sep. 2020. DOI: 10.1021/acs.chemmater.0c02467.
- [MFJ12] D. Vila-Liarte, M. W. Feil, A. Manzi, J. L. Garcia-Pomar, H. Huang, M. Döblinger, L. M. Liz-Marzán, J. Feldmann, L. Polavarapu, and A. Mihi, "Templated-assembly of CsPbBr<sub>3</sub> perovskite nanocrystals into 2D photonic supercrystals with amplified spontaneous emission," *Angewandte Chemie International Edition*, vol. 59, no. 40, pp. 17 750–17 756, Aug. 2020. DOI: 10.1002/anie.202006152.

## Conference Proceedings

- [MFC1] A. Vasilev, M. W. Feil, C. Schleich, B. Stampfer, G. Rzepa, G. Pobegen, T. Grasser, and M. Walzl, "Oxide and interface defect analysis of lateral 4H-SiC MOSFETs through CV characterization and TCAD simulations," *Materials Science Forum*, vol. 1090, pp. 119–126, May 2023. DOI: 10.4028/p-k93y93.
- [MFC2] M. W. Feil, K. Waschneck, H. Reisinger, J. Berens, T. Aichinger, P. Salmen, G. Rescher, W. Gustin, and T. Grasser, "Towards understanding the physics of gate switching instability in silicon carbide MOSFETs," in *2023 IEEE International Reliability Physics Symposium (IRPS)*, IEEE, Mar. 2023, pp. 1–10. DOI: 10.1109/irps48203.2023.10117740.
- [MFC3] M. W. Feil, H. Reisinger, A. Kabakow, T. Aichinger, W. Gustin, and T. Grasser, "Optical emission correlated to bias temperature instability in SiC MOSFETs," in *2022 IEEE International Reliability Physics Symposium (IRPS)*, IEEE, Mar. 2022, pp. 1–9. DOI: 10.1109/irps48227.2022.9764584.

- 
- [MFC4] M. W. Feil, K. Waschneck, H. Reisinger, P. Salmen, G. Rescher, T. Aichinger, W. Gustin, and T. Grasser, "On the frequency dependence of the gate switching instability in silicon carbide MOSFETs," *Materials Science Forum*, vol. 1092, pp. 109–117, Jun. 2023. DOI: 10.4028/p-6g5v7s.
- [MFC5] M. W. Feil, K. Waschneck, H. Reisinger, J. Berens, T. Aichinger, S. Prigann, G. Pobegen, P. Salmen, G. Rescher, W. Gustin, and T. Grasser, "Recent developments in understanding the gate switching instability in silicon carbide MOSFETs," in *2023 IEEE International Integrated Reliability Workshop (IIRW)*, IEEE, Oct. 2023, pp. 1–9. DOI: 10.1109/iirw59383.2023.10477632.
- [MFC6] T. Grasser, M. Feil, K. Waschneck, H. Reisinger, J. Berens, D. Waldhoer, A. Vasilev, M. Waltl, T. Aichinger, M. Bockstedte, W. Gustin, and G. Pobegen, "A recombination-enhanced-defect-reaction-based model for the gate switching instability in SiC MOSFETs," in *2024 IEEE International Reliability Physics Symposium (IRPS)*, IEEE, Apr. 2024, pp. 1–7. DOI: 10.1109/IRPS48228.2024.10529465.
- [MFC7] P. Salmen, M. W. Feil, K. Waschneck, H. Reisinger, G. Rescher, and T. Aichinger, "A new test procedure to realistically estimate end-of-life electrical parameter stability of SiC MOSFETs in switching operation," in *2021 IEEE International Reliability Physics Symposium (IRPS)*, IEEE, Mar. 2021, pp. 1–7. DOI: 10.1109/irps46558.2021.9405207.
- [MFC8] T. Aichinger, M. W. Feil, and P. Salmen, "Assessing, controlling and understanding parameter variations of SiC power MOSFETs in switching operation," *Key Engineering Materials*, vol. 947, pp. 69–75, May 2023. DOI: 10.4028/p-13016n.
- [MFC9] M. Weger, D. Biermeier, M. W. Feil, J. Cottom, M. Bockstedte, and G. Pobegen, "Electroluminescence spectra of a gate switched MOSFET at cryogenic and room temperatures agree with ab initio calculations of 4H-SiC/SiO<sub>2</sub>-interface defects," *Materials Science Forum*, vol. 1091, pp. 15–23, Jun. 2023. DOI: 10.4028/p-050q7w.
- [MFC10] A. Huerner, P. Sochor, Q. Sun, M. W. Feil, and R. Elpelt, "Influence of turn-off gate-voltage undershoots on the turn-on behavior of SiC MOSFETs," in *PCIM Europe 2022; International Exhibition and Conference for Power Electronics, Intelligent Motion, Renewable Energy and Energy Management*, VDE VERLAG GMBH, May 2022, pp. 1–8. DOI: 10.30420/565822038.
- [MFC11] A. Huerner, P. Sochor, M. Feil, and R. Elpelt, "Influence of the threshold-voltage hysteresis on the switching properties of SiC MOSFETs," in *PCIM Europe digital days 2021; International Exhibition and Conference for Power Electronics, Intelligent Motion, Renewable Energy and Energy Management*, VDE VERLAG GMBH, May 2021, pp. 1–8.
- [MFC12] C. Schleich, M. W. Feil, D. Waldhoer, A. Vasilev, T. Grasser, and M. Waltl, "Lifetime projection of bipolar operation of SiC DMOSFET," *Materials Science Forum*, vol. 1091, pp. 73–77, Jun. 2023. DOI: 10.4028/p-9i494d.
- [MFC13] A. Martin, P.-L. Pham, H. Nielen, and M. W. Feil, "Restrictive antenna rules limiting PID degradation for MOS transistors with connected MIM-capacitors," in *2023 IEEE International Integrated Reliability Workshop (IIRW)*, IEEE, Oct. 2023, pp. 1–6. DOI: 10.1109/iirw59383.2023.10477710.

- [MFC14] S. Prigann, M. W. Feil, H. Reisinger, J. Bissinger, M. Strasser, M. Walzl, J. Schlipf, T. Kaya, L. Bartholomäus, W. Gustin, and T. Basler, "Prompt shift of on-state resistance in LDMOS devices: Causes, recovery, and reliability implications," in *2024 IEEE 36th International Symposium on Power Semiconductor Devices and ICs (ISPSD)*, **accepted**, 2024.


## Patents

- [MFP1] T. Aichinger, M. W. Feil, A. Kabakow, and H. Reisinger, "Semiconductor device having an optical device degradation sensor," U.S. Patent 11 940 489 B2, Mar. 2024.

## Master Thesis

- [MFT1] M. W. Feil, "Amplified spontaneous emission from perovskite nanocrystals assembled into electronic and optical superlattices," M.S. thesis, Ludwig Maximilian University Munich, Munich, Germany, Aug. 2019.

# Curriculum Vitae

|                    |   |
|--------------------|---|
| Name               | Maximilian Wolfgang Feil  |
| Date of Birth      | [REDACTED]  |
| Place of Birth     | [REDACTED]  |
| Nationality        | [REDACTED]  |
| Publication Record | Google Scholar  |
| ORCID              | 0000-0002-5383-5402  |



## Education

|               |  |
|---------------|--|
| since 10/2019 | <b>PhD Candidate</b><br>at the Institute for Microelectronics, Vienna University of Technology, Vienna, Austria<br><br>Thesis: "Radiative and Non-Radiative Phenomena During Gate-Switching in Silicon Carbide Power MOSFETs", Supervisor: Univ.Prof. Dipl.-Ing. Dr.techn. Tibor Grasser   |
| 09/2019       | <b>Master of Science in Physics</b><br>at the Ludwig Maximilian University Munich, Munich, Germany<br><br>Thesis: "Amplified Spontaneous Emission from Perovskite Nanocrystals Assembled into Electronic and Optical Superlattices" at the Chair for Photonics and Optoelectronics, Nano-Institute Munich, Supervisor: Prof. Dr. Jochen Feldmann |
| 09/2017       | <b>Bachelor of Science in Physics</b><br>at the Ludwig Maximilian University Munich, Munich, Germany<br><br>Thesis: "Calibration of a coordinate measuring machine for optical computer-aided surveying of microstructured anode surfaces" at the Chair of Experimental Elementary Particle Physics, Supervisor: Prof. Dr. Otmar Biebel          |

## Employment

|                      |  |
|----------------------|--|
| since 04/2024        | <b>Staff Engineer Technology and Process Development</b> – SiC Central R&D at Infineon Technologies Austria AG, Villach, Austria |
| 10/2019 –<br>03/2024 | <b>PhD Candidate</b> – Quality Management, Reliability & Qualification at Infineon Technologies AG, Neubiberg, Germany           |
| 07/2017 –<br>06/2018 | <b>Working Student</b> – Chair of Elementary Particle Physics at Ludwig Maximilian University Munich, Garching, Germany          |

## Awards

|      |  |
|------|--|
| 2023 | <b>Best Student Paper Award</b><br>of the IEEE 2023 International Reliability Physics Symposium (IRPS) for the paper “Towards Understanding the Physics of Gate Switching Instability in Silicon Carbide MOSFETs” [MFC2]                   |
| 2023 | <b>Editors’ Choice 2023</b> [322]<br>of the journal Communications Engineering (Springer Nature Limited) for the paper “Electrically stimulated optical spectroscopy of interface defects in wide-bandgap field-effect transistors” [MFJ8] |

## Talks on Conferences

|         |  |
|---------|--|
| 10/2023 | IEEE International Integrated Reliability Workshop (IIRW) ( <b>Invited</b> ) |
| 03/2023 | IEEE International Reliability Physics Symposium (IRPS)                      |
| 09/2022 | International Conference on Silicon Carbide and Related Materials (ICSCRM)   |
| 03/2022 | IEEE International Reliability Physics Symposium (IRPS)                      |
| 03/2019 | 83rd Annual Meeting of DPG and DPG Spring Meeting 2019                       |

## Magazine Articles

|         |  |
|---------|--|
| 11/2021 | T. Aichinger, J. Berens, M.W. Feil, “Gate-Oxid-Zuverlässigkeit bei SiC-MOSFETs – Alterung unter Kontrolle,” <i>Elektronik</i> , 23 |
|---------|--|

## Reviewing Activities

|               |  |
|---------------|--|
| since 03/2023 | IEEE Transactions on Device and Materials Reliability (TDMR)               |
| since 12/2022 | International Conference on Silicon Carbide and Related Materials (ICSCRM) |
| since 05/2021 | IEEE Electron Device Letters (EDL)   |
| since 03/2021 | IEEE Transactions on Electron Devices (TED)                                |